
Long term hydrological change, the El Niño/Southern Oscillation and biomass burning in the tropics

Submitted by Lilo Maria Ketí Henke to the University of Exeter
as a thesis for the degree of
Doctor of Philosophy in Geography

December 2016

This thesis is available for Library use on the understanding that it is copyright material and that no quotation from the thesis may be published without proper acknowledgement.

I certify that all material in this thesis which is not my own work has been identified and that no material has previously been submitted and approved for the award of a degree by this or any other University.

Signature:

Acknowledgements

Doing this PhD has been a difficult and long process, but I have been pulled through by many beautiful people along the way. I have been very lucky with my supervisors, who have helped me immeasurably. Dr. F. Hugo Lambert, whose endless enthusiasm and confidence in me has helped me push through the many challenges, and Prof. Dan Charman, who has always managed to make sense of the mess and has helped me see the bigger picture. I am incredibly grateful for their kindness, advice and support.

The day-to-day of PhD life has been improved infinitely by my fellow Geographers; it has been a pleasure sharing the ups and downs, working together and procrastinating together. Those who have finished before me have been an inspiration. Those who are still here; if I can do it, you definitely can too! I want to say a particular thanks to Andy and Holly for the various birthday fruits, and always seeing the positive in every situation I complain about. Also a shout out to my yoga kids for getting me into the office at 8am, and Chris for some delicious vegan fuel. These, and many other gifts, have kept me relatively sane.

Living in the South West has been a treat. I will never forget the incredible landscapes and beautiful adventures I have experienced here. I owe a huge thank you to all those friends who have taken me along and have joined me on whatever walk I could think of. Thanks to Jarrah and AD for making the trek to come visit me down here several times (and giving me an occasional escape from these distant lands in return), and reminding me that there is real life outside the PhD bubble.

Finally, I would never have made it here without the love and support of my family. I miss them more than anything.

Abstract

Rapidly rising levels of atmospheric greenhouse gases including carbon dioxide and methane since the industrial revolution have drawn scientific attention to the importance of the global carbon cycle to the climate (Cubasch et al., 2013). Tropical peatlands, the majority of which are located in the Indonesian region, are a major source of uncertainty in the carbon cycle as the relationships between carbon accumulation and hydrological changes remain poorly understood (Hergoualc'h & Verchot, 2011, Page et al., 2011). An important driver of carbon emissions in tropical peatlands is fire, which in the Indonesian region is strongly influenced on interannual timescales by the El Niño/Southern Oscillation (ENSO). However, it is not clear how ENSO and fire have varied at decadal to centennial scales over the past two millennia. This thesis explores long term tropical hydrological variability and ENSO-like climate change from palaeorecords and their interactions with fire. Using a wide range of instrumental, proxy and model datasets and a novel reconstruction method, two separate reconstructions of long-term ENSO-like climate change are produced based on precipitation and temperature data. These show no evidence of a difference between the ENSO-like behaviour of precipitation and temperature. There is limited evidence for a difference in long-term ENSO-like state between the Medieval Climate Anomaly and the Little Ice Age. Reconstructions of hydrological variability and biomass burning in the Indonesian region suggest that precipitation and fire have been positively correlated over the past 2,000 years, which is contrary to the modern-day relationship on ENSO timescales. This throws up questions of long-term versus short-term interactions and feedbacks between fire, climate and vegetation. It is likely that anthropogenic activity in the Indonesian region has significantly altered the stability of the fire regime. Further research combining proxy data, climate and fire models, and using more robust statistical analysis is necessary to untangle the natural and anthropogenic driving factors at different time resolutions.

Contents

Acknowledgements	2
Abstract	3
List of Figures	9
List of Tables	11
Abbreviations and units	13
1 Introduction	19
1.1 Aims and objectives	22
1.1.1 Method development and hypothesis foundations	22
1.1.2 Tropical hydrological change and ENSO	23
1.1.3 Links between tropical hydrological change and fire	23
1.2 Thesis structure	24
2 Long term climate variability, fire and the carbon cycle	27
2.1 Introduction	27
2.2 The hydrological cycle	28
2.3 Long term climatic changes in the Pacific Basin	31
2.3.1 The tropical Pacific Ocean and ENSO	31
2.3.2 Glacial-interglacial cycles	34
2.3.3 The Holocene	34
2.3.3.1 Early to Mid-Holocene	35
2.3.3.2 Mid to Late Holocene	38
2.3.3.3 Last millennium	38
2.3.4 Outstanding issues	40
2.4 Fire in the tropics	41
2.4.1 Fire mechanisms	42
2.4.2 ENSO and fire	42
2.4.3 Recent ENSO-fire links in the Indonesian region	43

2.4.4	Ignition: lightning and ENSO	44
2.4.5	Palaeo-evidence of fire behaviour	45
2.4.6	Modelling fire	45
2.5	Tropical peatlands and the global carbon cycle	47
2.5.1	Tropical peatland development	47
2.5.2	The carbon cycle in tropical peatlands	48
2.5.2.1	CO ₂ sequestration and burial	48
2.5.2.2	CO ₂ efflux from aerobic respiration	50
2.5.2.3	Fluvial organic C transport	50
2.5.2.4	CH ₄ from anaerobic respiration	50
2.5.2.5	Biomass burning	52
2.6	Summary	54
3	Method development and hypothesis foundations	55
3.1	Introduction	55
3.2	Multiproxy reconstruction methods	56
3.2.1	EOF analysis	60
3.2.2	Selecting EOFs: 20CRv2c	63
3.2.3	Selecting EOFs: GCMs	65
3.2.3.1	Full field comparison	67
3.2.3.2	Proxy field comparison	68
3.2.4	Sparse PC reconstructions	69
3.3	Linking temperature, precipitation and ENSO	72
3.3.1	20CRv2c temperature vs. precipitation	73
3.3.2	GCM temperature vs. precipitation	74
3.3.3	Indonesian P vs. ENSO	74
3.4	Pseudoproxies	77
3.4.1	Proxy System Models	79
3.4.2	Pseudo-tree ring widths using VS-Lite	80
3.4.3	Signal-to-noise ratios	84
3.5	Proxy transformations	86
3.5.1	Minimax and Z-score transformations	87
3.5.2	Box-Cox transformation	88
3.5.3	Inverse transform sampling	89
3.6	Smoothing methods	90
3.6.1	Binning	90
3.6.2	LOWESS smoothing	91
3.6.3	GAM and GAMM spline fitting	94
3.6.3.1	GAM	94
3.6.3.2	GAMM	97
3.6.4	Summary	99
4	El Niño-like climate change in the tropics and subtropics over the past two millennia	101

4.1	Introduction	101
4.2	Data description	106
4.2.1	Study region	106
4.2.2	Proxy records	106
4.2.3	Modern climate datasets	107
4.2.4	General circulation model simulations	107
4.3	Methodology	108
4.3.1	GCM data	109
4.3.2	Pseudoproxies	109
4.3.3	Calibration: network creation	111
4.3.4	Validation: network evaluation	112
4.3.5	Proxy ENSO ensemble	114
4.3.6	LIA-MCA difference analysis	115
4.4	Results: ENSO reconstructions	116
4.4.1	Comparing precipitation and temperature	121
4.5	Discussion	123
4.5.1	Reflections on the method	128
4.6	Conclusions	130
5	Precipitation and fire in the Indonesian region over the past two millennia	133
5.1	Introduction	133
5.2	Data and methods	136
5.2.1	Data selection	136
5.2.2	Data transformation	137
5.2.3	Compositing and smoothing	138
5.2.4	Statistical fire - precipitation models	139
5.3	Results and discussion	140
5.3.1	Data characteristics	140
5.3.1.1	Vegetation	141
5.3.1.2	Precipitation regimes	142
5.3.2	Temporal trends	143
5.3.2.1	ENSO and the ITCZ	144
5.3.3	Fire and precipitation interactions	146
5.4	Fire-climate interactions over different timescales	151
5.5	Humans and fire	154
5.6	Conclusions	156
6	Conclusion	159
6.1	Revisiting aims and objectives	159
6.1.1	Methodological issues in palaeoclimatology	160
6.1.2	Long-term ENSO-like precipitation and temperature	163
6.1.3	Long-term Indonesian precipitation and fire	166
6.2	Moving forward: untangling fire mechanisms using models	170

6.3	Concluding remarks	172
A	Proxy data used in Chapter 4	175
A.1	Proxy data details	175
A.2	Precipitation records	178
A.3	Temperature records	181
B	Proxy data used in Chapter 5	193
B.1	Charcoal records	193
B.2	Precipitation records	197
C	R scripts	199
C.1	VS-Lite bugs and corrections	199
C.2	Inverse Transform Sampling (ITS)	200
D	Data acknowledgements	203

List of Figures

2.1	IPCC projected precipitation vs. temperature	29
2.2	T and P anomalies during La Niña (cold) and El Niño (warm) events	33
2.3	ITCZ influence on ENSO development	37
2.4	Global peatland records since the Last Glacial Maximum	49
2.5	Daily mean fire CO ₂ emissions across Indonesia in Sept-Oct 2015	53
3.1	20CRv2c and GCM precipitation EOFs	68
3.2	20CRv2c and GCM temperature EOFs	69
3.3	GCM precipitation vs. temperature (detrended)	75
3.4	GCM precipitation vs. temperature (undetrended)	76
3.5	20CRv2c TRW correlation maps	82
3.6	GCM TRW correlation maps	83
3.7	GCM TRW correlation boxplots	84
3.8	Binwidth effect	92
3.9	Bin placement effect	92
3.10	Pre-binning effect	94
3.11	LOWESS half-window effect	95
4.1	Network creation process diagram	114
4.2	Precipitation ENSO ensembles	117
4.3	Temperature ENSO ensembles	118
4.4	Within-ensemble correlations	119
4.5	Precipitation EOF with proxy locations	120
4.6	Temperature EOF with proxy locations	121
4.7	Difference between the means of the MCA and LIA	122
4.8	Precipitation – temperature correlations	122
4.9	Sensitivity to MCA and LIA definitions	123
5.1	Potential vegetation map	141
5.2	Map of record starting ages	142
5.3	Composite curves	145
5.4	2ka GAM vs. GAMM	148
5.5	21ka P-E, MAT and charcoal GAMs	150
5.6	GA(M)M results	152
5.7	HYDE3.1 simulations	156

6.1	Indonesian peat and forest cover change	173
6.2	Fire history data sources	174

List of Tables

3.1	Proxy types	59
3.2	EOF–ENSO correlation	65
3.3	20CRv2c vs. GCMs	67
3.4	Sparse 20CRv2c vs. GCMs	70
3.5	Model sparse PCs	73
3.6	Modern day precipitation vs. ENSO	77
3.7	Proxy SNRs	85
5.1	Charcoal vegetation summary	143
5.2	ANOVA results	147
5.3	GA(M)M summaries	149
A.1	Precipitation proxy details	180
A.2	Temperature proxy details	190
B.1	Charcoal records	196
B.2	Precipitation records	197

Abbreviations and units

20CRv2c	20th Century Reanalysis Project version 2c
AD	Anno Domini
AMOC	Atlantic Meridional Overturning Circulation
ARIMA	Autoregressive Integrated Moving Average
ASM	Australian Summer Monsoon
BP	Before Present (present taken as AD 1950)
C	Carbon
CCSM4	Community Climate System Model 4
CDF	Cumulative Distribution Function
CFR	Climate Field Reconstruction
CH₄	Methane
CMIP5	Coupled Model Intercomparison Project Phase 5
CO₂	Carbon dioxide
CPS	Composite Plus Scaling
DGVM	Dynamic Global Vegetation Model
DOC	Dissolved Organic Carbon
EASM	East Asian Summer Monsoon
EEP	Eastern Equatorial Pacific
EH	Early Holocene
EKF	Ensemble Kalman Filter
ENSO	El Niño/Southern Oscillation
EOF	Empirical Orthogonal Function
ESM	Earth System Model

FireMIP	Fire Modeling Intercomparison Project
GAM	Generalised Additive Model
GAMM	Generalised Additive Mixed Model
GCD	Global Charcoal Database
GCM	General Circulation Model
GCV	Generalised Cross Validation
GFED	Global Fire Emissions Database
GHG	Greenhouse Gas
GLM	Generalised Linear Model
GLMM	Generalised Linear Mixed Model
GPCP	Global Precipitation Climatology Project
GPWG	Global Paleofire Working Group
HadISST	Hadley Centre Global Sea Ice and Sea Surface Temperature
INFERNO	INteractive Fire and Emission algoRithm for Natural environments
IPCC	Intergovernmental Panel on Climate Change
ITCZ	Intertropical Convergence Zone
ITS	Inverse Transform Sampling
JULES	Joint UK Land Environment Simulator
LH	Late Holocene
LIA	Little Ice Age
LOWESS	LOcally WEighted Scatterplot Smoothing
MCA	Medieval Climate Anomaly
MEI.ext	Extended Multivariate ENSO Index
MH	Middle Holocene
NAO	North Atlantic Oscillation
NH	Northern Hemisphere
NINO3.4	East Central Tropical Pacific SST (5°N–5°S, 170–120°W)
NOAA	National Oceanic and Atmospheric Administration
P	Precipitation
PC	Principal Component
P–E	Precipitation–Evaporation

PMIP3	Palaeoclimate Intercomparison Project 3
POC	Particulate Organic Carbon
PSM	Proxy System Model
PWC	Pacific Walker Circulation
RCP	Representative Concentration Pathways
REML	REstricted/REsidual Maximum Likelihood
RMSE	Root Mean Squared error
SH	Southern Hemisphere
SLP	Sea Level Pressure
SNR	Signal-to-Noise Ratio
SOI	Southern Oscillation Index
SPCZ	South Pacific Convergence Zone
SSS	Sea Surface Salinity
SST	Sea Surface Temperature
T	Temperature
THC	Thermohaline Circulation
TRW	Tree Ring Width
VS	Vaganov-Shashkin
WATCH	Integrated Project WATer and Global CHange
WPWP	Western Pacific Warm Pool
Gt	Gigatonne (10⁹ tonnes)
kyr	Thousand years
Mha	Megahectare (10⁶ hectares)
Tg	Teragram (10¹² grams)

Voor Papa

Tua culpa.

Chapter 1

Introduction

Rapidly rising levels of atmospheric greenhouse gases including carbon dioxide (CO₂) and methane (CH₄) since the industrial revolution have drawn scientific attention to the importance of the global carbon cycle to the climate (Cubasch et al., 2013). The threat of disastrous impacts of climate change on nature and current and future human populations (Hansen et al., 2013) highlights the importance of understanding how the balance of carbon sinks and sources will be affected by projected changes in global temperatures and the hydrological cycle. This is necessary for producing effective global climate models, but also has ramifications for environmental and economic management strategies (Braconnot et al., 2011, Cattau et al., 2016, Le Quéré et al., 2009). Altered climate states (whether natural or human induced) directly and indirectly invoke responses in terrestrial and marine systems. These responses may be disproportionately strong when the systems are close to some threshold or 'tipping point' (Lenton et al., 2008), such that a small change in climate can cause major shifts in the carbon cycle, which then feeds back into further climate change. For example, carbon emissions from tropical peatlands can increase dramatically if the drought threshold for fire occurrence is exceeded. The fact that the relationships between carbon accumulation and hydrological changes remain poorly understood make tropical peatlands a major source of uncertainty in the carbon cycle (Hergoualc'h & Verchot, 2011, Page et al., 2011).

On a global scale, the hydrological cycle is regulated by the global energy budget. Regionally, this gets expressed in different ways depending on a combination of factors such as land-sea contrasts, wind regimes, and oceanic circulation

patterns. The net hydrological response to a change in temperature is also dependent on the type of forcing (e.g. CO₂ versus incoming solar radiation), which further complicates the picture (Held & Soden, 2006).

Nevertheless, there are several regional precipitation regimes such as monsoon systems and the coupled ocean-atmosphere El Niño/Southern Oscillation (ENSO) system. The latter is a main source of interannual climate variability, causing shifts in precipitation and sea surface temperatures (SSTs) across the equatorial Pacific Basin, and significantly affecting global temperatures (NOAA/OAR/ESRL PSD, 2011). It is associated with a latitudinal shift in the Intertropical Convergence Zone (ITCZ) at ENSO (monthly to annual) timescales. However, such shifts have also been observed over longer (centennial to millennial) timescales. The long-term latitudinal migrations of the ITCZ can potentially create long-term ENSO-like states, where the mean climate displays prolonged El Niño-like or La Niña-like behaviour (cf Rustic et al., 2015). The effects of short-term versus long-term changes in the tropical hydrological regimes linked to ENSO and the ITCZ are not well understood, despite their important role in modulating changes in biomass and greenhouse gas emissions in these regions. Gaining a stronger understanding of these precipitation regimes is thus paramount to our ability to accurately project the role of tropical peatlands in the global carbon cycle under different climate scenarios.

The use of climate proxy records (such as tree rings, sediment cores and coral records) to extend the hydrological record further back in time is crucial to separating the roles of various forcing mechanisms and natural (stochastic) variability, and ultimately to facilitating the prediction of future hydrological changes under elevated carbon dioxide (CO₂) concentrations (Jones & Mann, 2004). However, the interpretation of such indirect measures continues to be an issue in the palaeoclimate community. Not only is the often low signal-to-noise ratio (SNR) a hindrance, but issues such as identifying and quantifying the relationship between a proxy measure and climatic parameters, and the assumption that such relations observed in the modern day have remained unchanged through time, can add substantial error margins (Dee et al., 2015, Evans et al., 2013). Long-term changes in the hydrological cycle are therefore still poorly understood.

The global carbon cycle, which is a dominant driver of climate change, has close

linkages with the hydrological cycle through interactions with vegetation and microbial processes which regulate CO₂ and CH₄ fluxes (Hooijer et al., 2010, Mitra et al., 2005). This is particularly pertinent in tropical peatlands, where moisture availability is more influential than temperature. These ecosystems are currently a substantial carbon sink (Yu et al., 2011, 2010) but are potentially highly vulnerable to hydrological climate change as the bulk of the tropical peat carbon is located in South East Asia. If future changes in strength or frequency of precipitation lead to more extreme weather conditions, this could lead to a destabilisation of the carbon stores and create a positive feedback loop contributing to global climate change (Page et al., 2013).

One of the most dramatic modulators of the tropical carbon cycle is fire, which can cause the release of vast quantities of carbon from tropical peatlands within a very short timespan (Page et al., 2002). These wildfires are often accompanied by thick haze and have significant negative impacts on local and regional economies and health (Field, 2004, Heil & Goldammer, 2001, Wang, 2004). Anthropogenic activities have intensified fire activity in tropical peatland regions, but there is also evidence for a significant relationship between fire and hydrological regimes, particularly ENSO (Page et al., 2002, van der Werf et al., 2008, Wooster et al., 2012). The net impact depends on the extent to which peatlands are sensitive to hydrological change, which is as yet undefined, and to what extent this relationship is driven by human activity. Current research on these various drivers is still limited, and it is unclear how relationships evident at seasonal to interannual scales translate to longer-term variability in fire and carbon cycling in these regions. Such concerns, as well as related pressures on biodiversity and land degradation are serious considerations for governments and regulatory bodies responsible for regulating peatland management, conservation and restoration policies, as well as the wider effort to combat global climate change and reducing CO₂ emissions.

While palaeoclimatological research based on proxy records provides valuable information on long-term climatic changes, and research into climate dynamics using instrumental and model data is crucial for attributing and projecting changes in Earth System processes, these disciplines in isolation cannot produce a complete picture of the past, current and future climate. The combination of such approaches is increasingly being employed (e.g. Brücher et al., 2014, Donders

et al., 2008, Russon et al., 2013), creating new opportunities for mutual cross-validation of results as well as providing a more comprehensive context in which to place observed trends and patterns.

The work presented in this thesis has come forth from the broad issues summarised above. The main topics addressed in the following chapters are the tropical hydrological cycle and its interactions with fire regimes in the Indonesian region, and our ability to reconstruct these processes for the past two millennia. This has implications for carbon cycling in tropical peatlands, which plays a significant role globally. The methods used in palaeoclimatology to draw from, and contribute to, our understanding of climate dynamics underpins the manner in which these issues are examined, and how they are proposed to be resolved.

1.1 Aims and objectives

The main aim of this thesis is to evaluate long-term tropical hydrological processes and their impacts on the carbon cycle through links with fire regimes. A secondary aim is to explore new methods for selecting and combining proxy records into a synthesised reconstruction. Chapter 3 initially lays the methodological foundations and provides preliminary results that underpin the hypotheses in the main two results Chapters 4 and 5. The objectives for each of these three chapters are outlined below.

1.1.1 Method development and hypothesis foundations

This chapter serves to provide essential background knowledge for the following two chapters. It introduces various mathematical and statistical techniques that are employed throughout the thesis, allowing for more concise method descriptions in Chapters 4 and 5. It also presents the results of various analyses that serve as starting points for the hypotheses challenged in the other chapters. As such, the main objectives of this chapter are to:

- Describe the mathematical foundations underpinning the methodologies applied in the thesis

- Test modern-day relationships between temperature, precipitation and ENSO in the tropical-subtropical latitudes and the Indonesian region
- Introduce pseudoproxy experiment methods and describe their application in the thesis

1.1.2 Tropical hydrological change and ENSO

This chapter describes a new statistical method to create multiproxy reconstructions using EOF-based weighting. It presents two reconstructions of long-term ENSO-like climate change, one derived from temperature proxies and one from precipitation proxies. This chapter addresses the following two questions:

1. Do temperature and precipitation proxies show consistent long-term ENSO behaviour over the last millennium?
2. Do the Little Ice Age (LIA) and the Medieval Climate Anomaly (MCA) differ significantly in their mean ENSO-like state?

1.1.3 Links between tropical hydrological change and fire

This chapter explores long-term links between fire and precipitation in the Indonesian region. It applies established methods to charcoal and precipitation proxies to create reconstructions of hydrological change and biomass burning over the Indonesian region. These are used to answer the following questions:

1. Is there a significant correlation between precipitation and biomass burning in the Indonesian region over the past two millennia?
2. Does this long-term correlation correspond with the short-term relationship between ENSO and fire activity evident in the modern satellite record?

1.2 Thesis structure

This thesis is presented in six chapters broadly structured around the three sets of objectives outlined above.

Chapter 2 is a literature review providing background and context for the research presented in the rest of the thesis. It initially reviews the physics of the hydrological cycle before considering long-term hydrological changes in the tropical Pacific at different timescales. It then goes on to explore the role of tropical peatlands in the global carbon cycle and the interlinkages between hydrological changes and fire in these regions.

Chapter 3 serves as a foundation for the next two chapters. It provides background on the main statistical methods employed in this thesis, along with justifications for their use. It also describes the preliminary experiments that were conducted to test the effectiveness of these methods, or to support the hypotheses underpinning the data chapters. It is written such that it can be largely interpreted independently from the data chapters; to this end, some datasets are described here. Throughout this chapter, reference is made to appropriate sections in the data chapters where the methods are applied, and more specific detail on their application (and additional datasets used) is given in the data chapters.

The two main studies are described in Chapters 4 and 5, which are intended for publication in academic journals and are roughly structured as such. Chapter 4 introduces an EOF weighting based method for creating separate multiproxy temperature and precipitation reconstructions of (spatially) ENSO-like climate change in the tropics. Using reanalysis, model and proxy datasets, this methodology builds an ensemble of 'optimal' proxy networks using bootstrapped 'pseudoproxy' experiments designed to maximise the ability of the proxy networks to capture the desired ENSO-like pattern. The resultant two proxy reconstructions are then compared for similarity, particularly over the LIA and MCA, to explore long-term ENSO-like change in the tropical climate system and potential decoupling between temperature and precipitation responses. An adapted version of Chapter 4 has been published in *Climate of the Past* (Henke et al., 2017).

Chapter 5 shifts the focus from the entire tropical and subtropical zone to the Indonesian region, which holds the majority of the world's tropical peat and is

strongly affected by ENSO-induced hydrological variability. This chapter explores the links between precipitation and fire regimes, which play an important role in carbon cycling in this region, and examines how these relationships change at different timescales.

The thesis is concluded with a brief synthesis of the data in Chapter 6, revisiting the thesis aims and objectives. Finally, this chapter discusses recent advances in peatland and fire modelling, and outlines some potential modelling experiments to further the exploration of possible drivers behind changing relationships between tropical hydrological variability, biomass burning and carbon cycling at different timescales.

Chapter 2

Long term climate variability, fire and the carbon cycle

2.1 Introduction

The global climate has undergone drastic changes on glacial and millennial timescales. The Earth's changing orbital configurations, known as Milankovitch cycles, play a major role in modulating the amount and spatial distribution of incoming solar radiation, which is the main input of energy into the climate system. These variations in available energy not only affect global temperatures, but also strongly influence patterns of atmospheric and oceanic circulation, affecting wind regimes, upwelling and deep-water formation, and the hydrological cycle. The resultant climatic states are complicated by numerous feedback mechanisms that work to amplify or dampen different processes, as well as internal stochasticity inherent to the chaotic nature of the climate system. Large hydrological regimes such as ENSO dominate regional precipitation patterns, and are thus of more immediate relevance to understanding regional environmental changes. Particularly in the tropics, hydrological regimes have a significant influence on the global carbon cycle through modulation of CH₄ and CO₂ sequestration and production in wetlands, forests and other terrestrial ecosystems. The impact of moisture-modulated fire regimes and key ecosystems such as tropical peatlands is especially important. This literature review covers four broad topics relevant to the work in this thesis: 1) the hydrological cycle, 2) long term climatic changes in the Pacific Basin with a

focus on the El Niño/Southern Oscillation (ENSO), 3) the role of fire in the tropics, and 4) tropical peatlands and their role in the global carbon cycle.

2.2 The hydrological cycle

Recent and future changes in climate are often referred to as ‘global warming’, implying a rise in global temperatures. However, it is probably associated changes in the hydrological cycle that pose the greatest human societal, economic and health threat (Allen & Ingram, 2002). The global hydrological cycle is a complex system with a range of forcings which act on varying time scales. At its most fundamental level, however, it is driven by the Sun. Incoming solar radiation (insolation) heats up the surface of the oceans, triggering evaporation and thus increasing the moisture content of the overlying air. As the warm, moist air rises and cools, the water vapour saturation threshold is exceeded and the moisture condenses out to form clouds. These then return the moisture to the Earth through precipitation. Variable heating zonally, meridionally and between continents and oceans, combined with the Earth’s axial rotation, create a complex network of dominant atmospheric circulation cells such as the Hadley cells. Changes in atmospheric pressures and water vapour saturation levels due to these large-scale circulation patterns ultimately regulate weather patterns. Wind regimes sustained by these cells, such as the mid-latitude jet stream and equatorial trade winds, can in turn affect ocean circulation patterns by driving surface currents which alter sea surface temperature (SST) gradients and can promote or suppress upwelling of cold deep waters.

The global atmospheric energy budget balances atmospheric radiative cooling with latent heat, released by precipitation, and sensible heating. A direct increase in temperature, for example through increased insolation, is thus accompanied by an increase in precipitation (Collins et al., 2013). The impact of increased atmospheric CO₂ concentrations, however, is two-fold (Allen & Ingram, 2002, Andrews et al., 2010, Bala et al., 2009, Bony et al., 2013, Held & Soden, 2006). On the short term, the increased atmospheric opacity due to the CO₂ (i.e. reduced radiative cooling) diminishes the strength of the hydrological cycle. On the other hand, the long-term CO₂-induced temperature increase acts to increase precipitation.

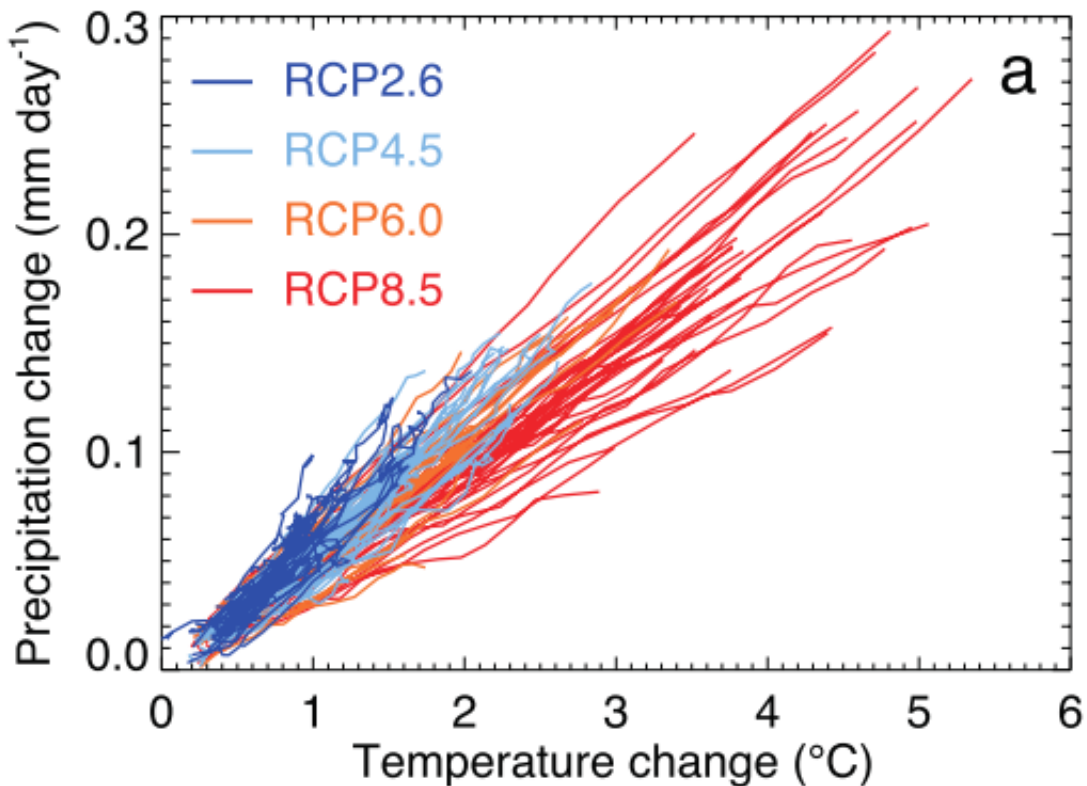


FIGURE 2.1: Figure taken from Collins et al. (2013): “Global mean precipitation (mm day^{-1}) versus temperature ($^{\circ}\text{C}$) changes relative to 1986–2005 baseline period in CMIP5 model concentrations-driven projections for the four RCPs for means over decadal periods starting in 2006 and overlapped by 5 years (2006–2015, 2011–2020, up to 2091–2100), each line representing a different model (one ensemble member per model)”.

Multi-model projections of 21st century climate change for the four Intergovernmental Panel on Climate Change (IPCC) Representative Concentration Pathways (RCPs) agree on a strong positive correlation between global mean precipitation and temperature (Figure 2.1).

This modelled relationship between projected precipitation and temperature change has also been found on geological time scales. During the Last Glacial Maximum ~ 22 thousand years before present (kyr BP; where present is defined as AD 1950), for example, the global climate was much more arid than the current one, as large amounts of water were locked up in land and sea ice (Hegerl et al., 2007). Since the beginning of the Holocene (~ 10 kyr BP) a number of proxy and model studies (cf Shin et al., 2006, Wanner et al., 2008) suggest that regional climates regimes have undergone significant changes. Roughly speaking, the post-glacial global climate warmed until a Mid-Holocene (MH; ~ 6 kyr BP) maximum, after

which temperatures declined again to the modern values (Hegerl et al., 2007). During the MH, the Earth's altered orbital configuration meant that the Northern Hemisphere (NH) seasonal cycle was amplified while the Southern Hemisphere (SH) experienced reduced seasonality (Duplessy et al., 2005, Shin et al., 2006). The Intertropical Convergence Zone (ITCZ) is a zone of low level atmospheric convergence which lies over the warmest water, and creates substantial positive precipitation anomalies. It follows a seasonal migratory pattern, moving southwards towards the Equator during the Boreal winter and retreating northwards during the summer months. The different seasonality during the MH led to a northward shift of the ITCZ (Haug et al., 2001, Shin et al., 2006, Wanner et al., 2008), as well as strengthening monsoon systems over Africa and Asia (Duplessy et al., 2005, Wanner et al., 2008). However, regional precipitation change is much more complex, which is reflected in much higher variability in model projections of regional precipitation compared to temperature (Collins et al., 2013). This is partly due to the additional impact of temperature, moisture availability and CO₂ on atmospheric circulation patterns, such as the ITCZ, which strongly influence regional precipitation.

The forcing mechanisms under anthropogenic climate change may have substantially different effects compared to the 'natural' forcings that dominated hydrological change in the past, and which cannot be distinguished in the relatively short instrumental datasets. This highlights the importance of producing palaeohydrological records, as they provide crucial information on long-term natural variability and change in climate, and associated responses of the various aspects of the carbon cycle. Such a long-term context, where anthropogenic influence was negligible, provides a baseline from which it becomes possible to identify how recent human activity has altered climatic behaviour. The differential response of the hydrological cycle, globally as well as regionally, to different forcings such as insolation and greenhouse gases (GHGs) is important because it also affects the way in which dominant climatic oscillations will behave. Perhaps the most notable large-scale and highly influential interaction between atmosphere and ocean is the ENSO system in the tropical Pacific region, which is discussed in more detail in the following section.

2.3 Long term climatic changes in the Pacific Basin

The tropical Pacific Ocean plays a very important role in the climate system's internal variability, as it is the largest provider of moisture to the atmosphere (Lea et al., 2000). This has implications for meridional energy transport, thereby linking changes at the equator to high-latitude climates (Turney et al., 2004). This section provides a brief overview of the long-term climatic changes and variability in the Pacific Basin based on proxy reconstructions, with a focus on the Holocene and concludes with some discussion of outstanding issues regarding data interpretation.

2.3.1 The tropical Pacific Ocean and ENSO

The global climate is characterised by a range of modes of climate variability, which are recognisable, often (quasi-)oscillatory, patterns associated with specific regional effects. They are often defined through empirical orthogonal function (EOF) analysis (see Section 3.2.1), which identifies the spatial pattern and temporal variation of the dominant oscillations in a gridded dataset. Climate modes vary in spatial extent, temporal frequency of their oscillation, and strength. The seasonal cycle, for example, is the most globally pervasive climate mode and operates on sub-annual timescales. The thermohaline circulation (THC), in contrast, works on millennial timescales.

ENSO is centred in the Pacific Basin and is the most influential interannual oscillation mode in the modern climate. It is a coupled atmosphere-ocean circulation pattern that links the Pacific Walker Circulation (PWC) and associated equatorial easterlies to the SST gradient across the equatorial Pacific basin. The Southern Oscillation Index (SOI) represents the atmospheric component and is defined as the difference in sea level pressure anomalies between Tahiti and Darwin, while El Niño refers to the changes in equatorial Pacific SSTs. The equatorial western Pacific is home to the so-called Western Pacific Warm Pool (WPWP), whereas upwelling of cold, nutrient-rich deep water along the Americas creates the Eastern Equatorial Pacific (EEP) Cold Tongue extending from the coast westwards. Under 'cold' (La Niña) conditions, the equatorial easterlies converge over the Maritime

Continent (the region between the Indian and Pacific Oceans including Indonesia, Borneo, New Guinea, the Philippines, Malaysia), leading to large volumes of moisture to be precipitated out (Figure 2.2a & 2.2c). During 'warm' (El Niño) events, the equatorial thermohaline gradient slackens, upwelling reduces and the cold tongue becomes less pronounced (Figure 2.2b & 2.2d). Weakened easterlies or westerly wind bursts cause the main region of convergence to shift eastwards away from the coast, causing anomalously dry conditions in Oceania and (South) East Asia and anomalously wet conditions over the central Pacific. While the ENSO source region is restricted to the equatorial Pacific basin, it shows strong correlations (i.e. teleconnections) with other, remote, climate oscillations such as the North Atlantic Oscillation (NAO; Trouet et al., 2009, 2012) and monsoonal behaviours over Asia (Conroy et al., 2008) and Africa (Ivanochko et al., 2005).

Spectral analyses of instrumental and proxy records for the Holocene reveal an interannual variability with a period of 2-7 years (Cane, 2005). Proxy, instrumental and modelling studies have hypothesised links between ENSO and global and remote regional climate variability on interannual (Klein et al., 1999, Wang et al., 1999), decadal (Nelson et al., 2011), centennial (Mann et al., 2005, Trouet et al., 2012) and millennial (Cane, 2005, Ivanochko et al., 2005, Moy et al., 2002, Shin et al., 2006) timescales. Regardless, the variability in ENSO-like states on centennial and longer time scales is still not fully understood. Evidence from a range of proxy archives is needed to evaluate the role of ENSO-like long-term climate change to understand past changes as well as to gain a better understanding of possible future changes due to increased radiative forcing from GHG emissions. The following sections summarise the available evidence for tropical Pacific hydrological change and variability during different stages of the past.

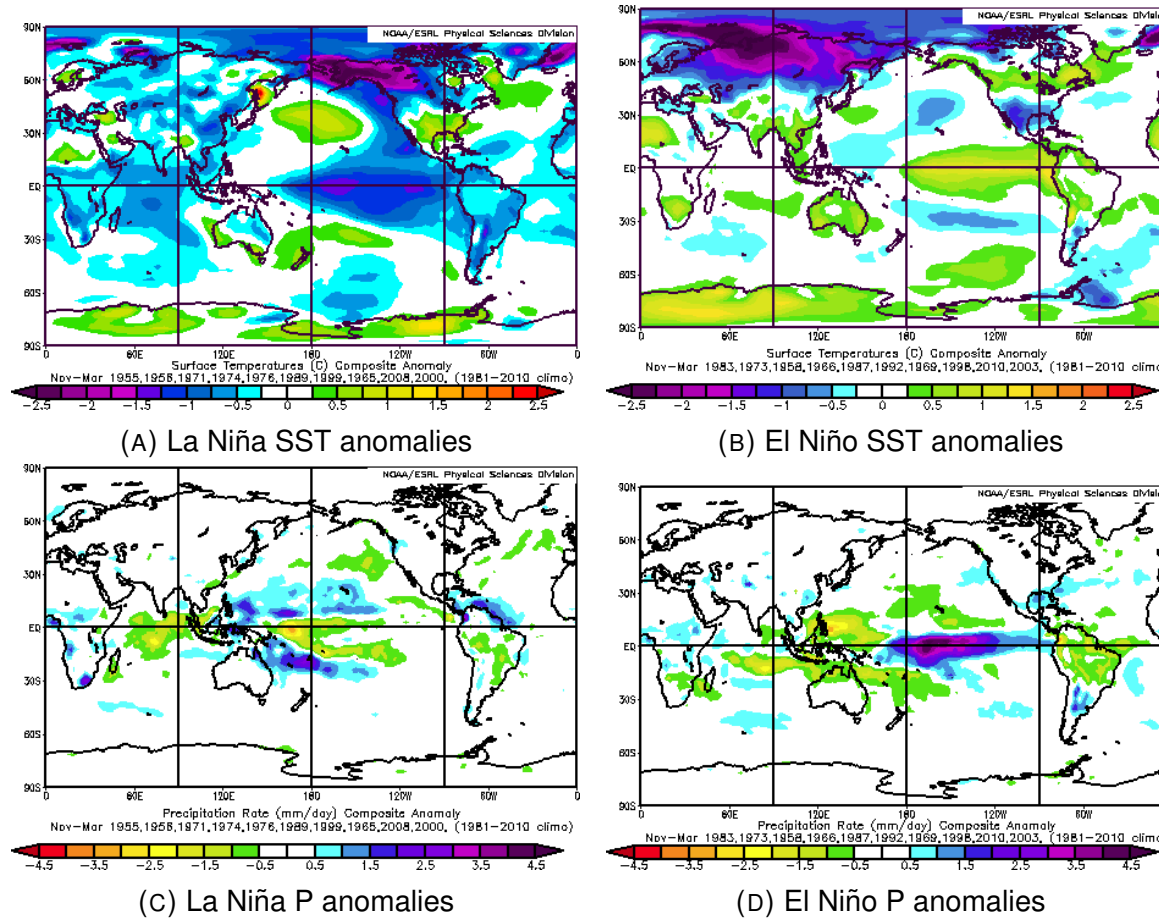


FIGURE 2.2: ENSO-induced surface temperature ($^{\circ}\text{C}$) and precipitation rate (mm/day) composite anomalies based on winter (November-March) anomalies with respect to 1981-2010. El Niño years are 1983, 1973, 1958, 1966, 1987, 1992, 1998, 2003 and 2010; La Niña years are 1995, 1958, 1965, 1971, 1974, 1976, 1989, 1999, 2000, and 2008. Scales run from -4.5 to +4.5 except for (B), which runs from -2.5 to +2.5. Figures adapted from NOAA/OAR/ESRL PSD (2011).

2.3.2 Glacial-interglacial cycles

Numerous studies of proxy records from a range of locations have found significant temporal variability in the amplitude and, to some extent, frequency of ENSO events over the last glacial-interglacial cycle. Based on geochemical analysis of fossil corals in Papua New Guinea, Tudhope et al. (2001) conclude that an ENSO-like pattern in the Pacific basin has been a persistent feature of the climate system for at least the last 130 kyr, although its strength has varied substantially. Several modelling studies, supported by proxy evidence, indicate a multi-millennial spectral peak in ENSO variability in the tropical Pacific basin linked to precessional forcing which alters the seasonal distribution of insolation (Clement, 1999, Turney et al., 2004). Moreover, there is strong evidence for a link between zonal equatorial Pacific SST gradients and glacial-interglacial cycles (Lea et al., 2000) as well as glacial Dansgaard-Oeschger (D-O) cycles (Ivanochko et al., 2005, Stott et al., 2002) and Holocene Bond cycles (Moy et al., 2002, Wanner et al., 2008), although the exact nature and directionality of these relationships is still disputed. Tudhope et al. (2001) suggest some form of “glacial dampening” mechanism brought on by glacial climatic states which acts to diminish the amplitude of ENSO events, leading to La Niña-like glacials. Conversely, other work suggests that ENSO is a possible driver of glacial-interglacial cycles and other abrupt climate changes by regulating poleward heat transport (Turney et al., 2004), tropical GHG emissions (Ivanochko et al., 2005, Stott et al., 2002, Visser et al., 2003), and affecting the strength of the North Atlantic meridional overturning circulation (AMOC; Partin et al., 2007, Turney et al., 2004). The interactions are likely to be multi-directional and non-linear, with feedbacks in the tropical Pacific both influencing and being influenced by higher-latitude climate processes (Partin et al., 2007).

2.3.3 The Holocene

There is an increasing body of research that points towards significant changes in ENSO behaviour since the last deglaciation approximately 12 kyr BP. While most modelling studies show relatively smooth insolation-driven transitions in ENSO behaviour (Donders et al., 2008) many proxy records suggest more extreme and sudden changes, with conspicuous shifts in ENSO activity centred at ~5 kyr BP (Donders et al., 2005, Haug et al., 2001, Koutavas et al., 2006, Moy et al., 2002,

Rodbell, 1999, Tudhope et al., 2001) and ~ 3 -4 kyr BP (Donders et al., 2005, Koutavas et al., 2006). Evidence for more recent changes over the last millennium is available in both proxy and instrumental records, but there is as yet no consensus over the mean climatological state nor strength of ENSO during this period (Conroy et al., 2010, Yan et al., 2011b).

2.3.3.1 Early to Mid-Holocene

Most ENSO reconstructions for the Early Holocene (EH; ~ 10 -8 kyr BP) and MH (~ 7 -4 kyr BP) display low ENSO variance (Donders et al., 2008, Haug et al., 2001, Rodbell, 1999, Tudhope et al., 2001). Studies on storm-derived clastic laminae in lake sediments from Ecuador, which record moderate to strong ENSO events (Moy et al., 2002, Rodbell, 1999), show a lack of variance in the ENSO band prior to 7 kyr BP, suggestive of a weak ENSO. Clement (1999) and Clement et al. (2000) use the Zebiak-Cane ENSO model (Zebiak & Cane, 1987) to demonstrate that the orbital configurations are sufficiently influential to force the climatic trends found in these proxy archives. In their simulations, the increased insolation in boreal summer and decreased insolation in boreal winter during the EH/MH reinforces the zonal SST gradient in the equatorial Pacific, thus repressing the evolution of warm events and keeping the mean global climate in a La Niña-like state (Barron & Anderson, 2011, Clement et al., 2000). The model employed by Clement et al. (2000) predicts a significant overall reduction in amplitude, fewer seasonal and interannual cold events, and a lower frequency of warm events prior to ~ 6 kyr. Several proxy-based studies provide support for an increased EH/MH zonal SST gradient, with cooler conditions in the East Pacific Cold Tongue (Carré et al., 2005, Stott et al., 2004) and warmer conditions in the Warm Pool (Koutavas et al., 2006).

Cane (2005) highlights the role of the positioning of the ITCZ in modulating millennial-scale ENSO variability. Instrumental records show that El Niño events are accompanied by a mean southward shift of the ITCZ over the Pacific Basin (Deser & Wallace, 1990, Haug et al., 2001). Figure 2.3 is a schematic of the influence of the ITCZ position on the coupled ocean-atmosphere system in the Pacific in response to a uniform increase in SST such as by insolation. In April, the ITCZ lies closer to the Equator, causing uniform heating of the atmosphere over the Pacific Basin. In

October, Equatorial heating of the atmosphere is only amplified by the ITCZ in the West Pacific, driving a positive feedback of the background easterly wind regime and encouraging the westward expansion of the Cold Tongue characteristic of a La Niña-like state. In response to the orbitally-induced shift in seasonality, the NH received more summer insolation during the EH and MH, which resulted in a more northerly mean position of the ITCZ, consequently diminishing the likelihood of ENSO anomalies building up. As Boreal winter insolation gradually increased and summer insolation decreased, the ITCZ is likely to have migrated southward over the Holocene. Marine sediment titanium and iron concentration data measurements over the last 14 kyr in the Cariaco Basin, Venezuela, indeed indicate a progressive southward shift of the Atlantic ITCZ throughout the Holocene (Haug et al., 2001). Similar conclusions are drawn regarding the Asian ITCZ from a multi-proxy reconstruction of the Arabian Sea Summer Monsoon (ASSM) in the Somali Basin (Ivanochko et al., 2005), supporting the notion of an orbitally-induced global atmospheric adjustment (Koutavas et al., 2006). This southward migration of the ITCZ drove the system to a mean state closer to that of modern-day April (i.e. an El Niño-like state; Fig 2.3), thus increasing over time the probability of warm ENSO events developing.

However, several studies contest the notion of a weak ENSO during the first half of the Holocene. Based on changes in C/N, grain size and silt abundance in lake sediments from Galápagos, Conroy et al. (2008) deduce a cool, dry background state in the tropical East Pacific between 9.2-9 kyr BP paired with a higher number of El Niño events. More evidence of high interannual variability during the EH comes from $\delta^{18}O$ -derived temperature reconstructions in three individual molluscs from the Cold Tongue (Carré et al., 2005). These discrete but seasonally-resolved records, dated between 8.9-7.9 kyr BP, all show significant $\delta^{18}O$ excursions interpreted as strong El Niño events. Sr/Ca temperature reconstructions on two EH (8.92 and 7.73 kyr BP) fossil corals from the Huon Peninsula, Indonesia, also indicate large temperature variability strikingly similar to modern-day SST variations linked to ENSO (McCulloch et al., 1996). The short length of the records in both studies preclude evaluation of the persistence of high variability phases or ENSO frequency, however, and possible seasonality-driven impacts on SST complicate the inference of ENSO-related temperature changes (Carré et al., 2005). McCulloch et al. (1996) report Warm Pool SSTs 2-3°C lower than modern values over this period, apparently in conflict with the insolation hypothesis (Clement et al.,

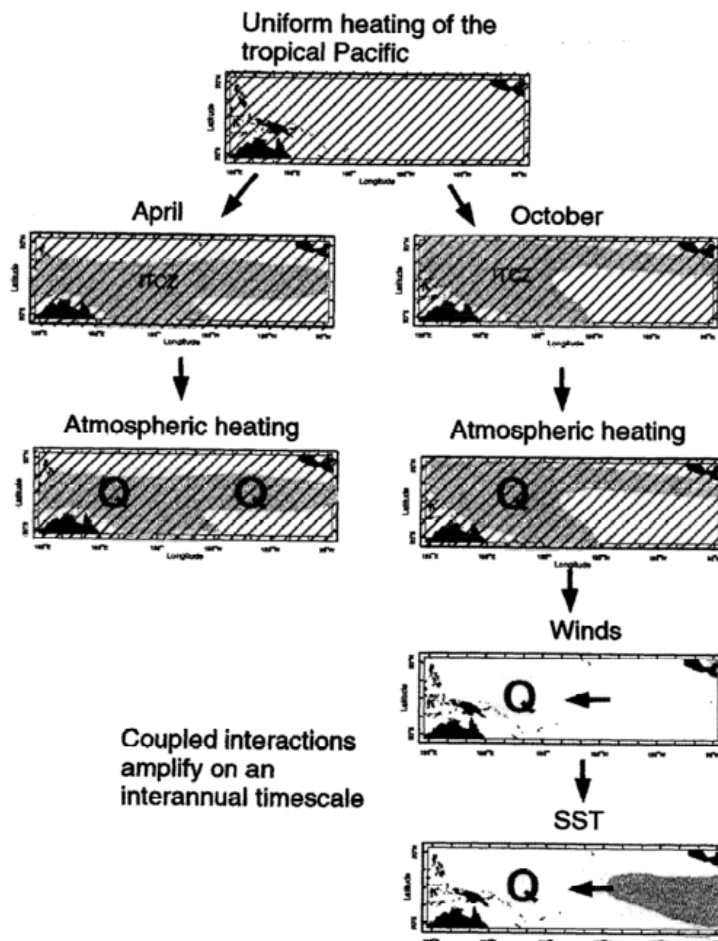


FIGURE 2.3: Schematic of the influence of the ITCZ on ENSO development in the tropical Pacific basin (figure from Clement, 1999). Cross-hatching indicates heating or a positive SST anomaly, shading indicates the position of the ITCZ, and “Q” indicates atmospheric heating. See 2.3.3.1 for detail.

2000) and the proxy reconstructions cited above (Carré et al., 2005, Koutavas et al., 2006, Stott et al., 2004). The authors postulate that the drastically lower EH sea level could have led to significantly altered oceanic and atmospheric currents, leading to lower SSTs in the Huon Peninsula. The oceans experienced rapid post-glacial sea level rise up to ~ 6 kyr BP (Wanner et al., 2008), which led to large changes to coastal outlines, the submergence of several land bridges and the establishment of new oceanic straits. This conclusion highlights that locally and globally altered oceanic currents and changes to mesoscale teleconnections related to these physical changes present potentially serious complications to the interpretation of ENSO proxy records prior to ~ 6 kyr BP (Carré et al., 2005, Wanner et al., 2008).

2.3.3.2 Mid to Late Holocene

The period around $\sim 6-5$ kyr BP is highlighted in many studies as the onset of the modern-day ENSO regime (cf Donders et al., 2005, 2008, Moy et al., 2002, Rodbell, 1999, and references therein). This roughly coincides with the estimated switch-over of peak insolation from NH summer to NH winter at ~ 5.7 kyr BP (Barron & Anderson, 2011) and the ITCZ crossing the equatorial West Pacific at ~ 5 kyr BP (Partin et al., 2007). Rodbell (1999) note a shift in the periodicity of (assumed ENSO-related) storm-derived clastic depositions from ≥ 15 years during the EH to a dominance in the 2-8.5 years band at ~ 5 kyr BP, which is consistent with modern ENSO periodicity. The climatic response in regions outside the ENSO source areas is somewhat more ambiguous, however. Pollen analysis in Florida, which shows strong teleconnections with modern ENSO, indicates that the onset of peat formation started at ~ 5.2 kyr BP in response to higher moisture availability (Donders et al., 2005). This is followed by five distinct wet pulses between $\sim 5-2$ kyr BP with a main transition from wet prairie to swamp between 3.5-2 kyr BP, suggestive of an existent but subdued ENSO, and/or weakened teleconnections. In a review of circum-Pacific proxy records, Donders et al. (2008) find that climatic conditions in modern-day strongly teleconnected regions (including regions in the Americas, Australia and Asia) are still responding to changes in the ENSO source region in a non-linear fashion at ~ 4 kyr BP. Northeast Pacific proxy records display a stepwise north to south increase in ENSO variability and strength at ~ 4.2 , 3.2 and 2 kyr BP (Barron & Anderson, 2011). The authors suggest that the influence of ENSO progressively moved northward after gaining strength in the MH. Carré et al. (2005), Gomez et al. (2004), Nelson et al. (2011) similarly invoke altered Holocene atmospheric circulation to explain extra-equatorial Pacific climatic transitions during the LH.

2.3.3.3 Last millennium

The climate of the last millennium has experienced significant upheavals, including the Medieval Climate Anomaly (MCA) and the Little Ice Age (LIA). These two periods are based on NH climate variability, and are generally defined to fall within ca. AD 900-1300 and AD 1300-1850, respectively (Jones & Mann, 2004). The global nature of these concepts is disputed (Neukom et al., 2014), but there has

nevertheless been much debate linked to the dominant ENSO state of the climate over these periods. Nelson et al. (2011) note an increase in multi-decadal wet/dry cycles over the Pacific Northwest since ~ 6 kyr BP culminating in a maximum in the past 1000 years, and point to the intensification of ENSO as principal driver. The decadal- to centennial-scale shifts in ENSO strength within this latter period of peak intensity are subject to disagreement. The MCA appears to have been preceded by a peak in ENSO activity; a lake sedimentation record in Ecuador displays a peak in the frequency of medium to strong ENSO events at AD ~ 750 (Moy et al., 2002), while proxy records of basin ventilation in the Warm Pool suggest a more ENSO-like mean state or stronger and/or more frequent events at AD 800 compared to the preceding ~ 1.5 kyr (Langton et al., 2008). Both studies note a reduction in ENSO activity during the MCA, characteristic of more La Niña-like conditions, followed by a peak at the start of the LIA around ca. AD 1200 (Moy et al., 2002) to AD 1250 (Langton et al., 2008). This is in agreement with the more northerly (i.e. more La Niña-like) position of the Atlantic ITCZ during the MCA compared to the LIA reported by Haug et al. (2001). They propose a link between with climatic processes in the Northern mid-latitudes, such as a strengthened AMOC and a more positive NAO. Trouet et al. (2009, 2012) further explore this potential positive feedback loop between ENSO, NAO and AMOC, which they postulate may have led to a sustained phase-locking of the oceanic and atmospheric states during the MCA.

After the peak in ENSO activity at the initiation of the LIA, Moy et al. (2002) and Langton et al. (2008) both report a steady decline to modern times. A precipitation reconstruction from stalagmites in Madagascar going back to AD 1550 shows high amplitude fluctuations during AD 1575-1770, including decadal and longer droughts (Brook et al., 1999). The authors associate these dry periods with low SSTs in the Cold Tongue, high SOI and low ENSO event frequency, and conclude that the LIA was characterised by highly fluctuating climate conditions ending in AD 1770. The lack of coverage of older periods precludes comparison of the dominant climate state between the LIA and the MCA. Further evidence for high variability during the LIA comes from the ITCZ reconstruction by Haug et al. (2001), which displays three southerly excursions between AD 1450-1850. Similarly, based on records of North Atlantic storminess and NAO, Trouet et al. (2009, 2012) argue for a comparatively less La Niña-like state in the LIA with more intense North Atlantic storms than during the MCA.

Interestingly, a reconstruction of the Southern Oscillation Index (SOI) based on two precipitation proxies from opposite sides of the Pacific (Yan et al., 2011b) suggests an El Niño-dominated MCA (which they define as AD 1000-1300) and a La Niña-dominated LIA (defined as AD 1400-1850). Based on this reconstruction and additional comparisons with other precipitation and temperature proxy reconstructions of ENSO from the WPWP and EEP Cold Tongue, the authors highlight an apparent discrepancy in the interpretation of precipitation-based and SST-based proxies. The latter indicate cooler, warmer and warmer conditions in the western, central and eastern tropical Pacific, respectively, in the LIA compared to the MCA – a pattern characteristic of El Niño. The precipitation proxies, on the other hand, show comparatively more, less and less rainfall over the respective regions. The authors describe two theoretical frameworks of oceanic and atmospheric responses to basin-wide heating (i.e. insolation) which support the different conclusions, one driven by oceanic processes and one based on atmospheric energy and moisture availability. However, they fail to reconcile the conflicting results.

In summary, the behaviour of ENSO is shown to have varied substantially throughout the Holocene. It is generally thought that ENSO gradually increased in strength during the EH, reaching its modern-day periodicity ca. 6-5 kyr BP (Clement, 1999, Rodbell, 1999). During the latter part of the Holocene, event frequency and magnitude continued to increase, strengthening teleconnections with extra-tropical regions in a non-linear fashion (Barron & Anderson, 2011). The directionality of ENSO-like climate change over the past millennium is contested, with an apparent divide between temperature and precipitation sensitive proxies in their reconstruction of ENSO activity during the MCA and LIA (Yan et al., 2011b).

2.3.4 Outstanding issues

Although much progress has been made in understanding the causes and feedbacks that control the tropical Pacific climate, there are still several issues that need to be addressed. It is generally understood that orbital forcing and associated shifts in the ITCZ play a major role in ENSO activity, but there is ambiguity over the relative influence on event magnitude and event frequency as evidenced

by conflicting proxy reconstructions (Carré et al., 2005, Rodbell, 1999). Interactions with other large-scale climate processes (such as ice melt, variability in THC and AMOC strength, monsoon systems and other dominant atmospheric circulation patterns) must be carefully considered and evaluated when interpreting potentially ambiguous proxy records. For example, $\delta^{18}O$ can be influenced by salinity as well as temperature (Langton et al., 2008, Russon et al., 2013). The dominant interannual spectral density of ENSO calls for the use of high-resolution proxy records to be able to identify both magnitude and frequency of ENSO events. More research is needed to establish which combinations of mean states (warm vs. cool) and ENSO intensity (high vs. low variability) are possible, and when they have occurred. Moreover, the assumption of stationarity in relation to atmospheric and oceanic teleconnections must be approached with caution, especially for reconstructions prior to ~ 6 kyr BP (Wanner et al., 2008). Changes in such climatic linkages may account for some of the differences between marine and terrestrial proxy reconstructions, and could also affect the relevance of indirect (i.e. not SST or P) inferences of ENSO activity (Langton et al., 2008).

Hydrological change and variability is salient for regulating the global carbon cycle in various ways, including its effect on net ecosystem productivity, aerobic and anaerobic respiration, and fire incidences. Peatlands, particularly in the tropics, are sensitive to hydrological changes and can switch from being carbon (C) sinks to C sources accordingly. The following section explores the links between carbon fluxes in tropical peatlands and the hydrological cycle.

2.4 Fire in the tropics

Fire has been an integral part of the natural climate system for hundreds of millions of years (Scott & Glasspool, 2006), influencing the atmospheric composition and terrestrial ecosystems (Power et al., 2010). As described in 2.5.2.5, it plays an important role in the C cycle of tropical peatlands. This section explores the role of fire in the tropics in more detail, first briefly outlining the main drivers of fire activity before assessing links with ENSO and evaluating evidence of fire behaviour in the Indonesian region. It concludes with a brief introduction to fire modelling and the recently established Fire Model Intercomparison Project (FireMIP).

2.4.1 Fire mechanisms

There are four main climatic controllers of fire occurrence: fuel availability, fuel moisture, vegetation distribution and ignition source (Kloster et al., 2015). The fuel availability, or load, is determined by the flammability of the vegetation types present, the amount of fallen and dead organic matter, and the density of the vegetation. The fuel moisture is impacted by the amount of precipitation and water table levels, as well as by vegetation density (especially the canopy) and composition. Vegetation distribution refers to the types of vegetation present and their spatial composition, which has implications for flammability and how easily fire can spread. The two main sources of ignition are lightning and humans. Interactions between the four factors lead to non-linear relationships with fire, with the implication that different regions will experience different changes in their fire regimes in response to the same climatic changes. Where fuel load is the limiting factor, an increase in precipitation may lead to an increase in fire as vegetation growth is encouraged. Contrastingly, if moisture is the limiting factor, fire is more likely to increase under drought conditions. Fires are generally ignited naturally only by lightning; all other natural ignition sources such as volcanic activity are usually rare and/or extremely localised. Human activity is a major source of ignition in the modern day, mostly for the purposes of land clearance and agriculture. There is evidence that humans have played a role in global fire modulation since at least 6000 years ago (Power et al., 2008), although climate appears to have been the driving factor at least on the global scale (Marlon et al., 2013). However, disentangling human and climatic impacts in palaeorecords can be problematic as climate, vegetation and fire patterns likely influenced human movement as much as human activity altered vegetation and fire trends (Haberle & Ledru, 2001).

2.4.2 ENSO and fire

As discussed in 2.3.1, ENSO events are linked to significant anomalies in temperature, precipitation and wind patterns, which have implications for global and regional fire regimes. A reduction in precipitation can lead to a decrease in fuel moisture and increased fuel availability due to heightened vegetation die-back. High precipitation intensity, on the other hand, can be paired with more thunderstorms and hence a higher risk of ignition by lightning. Moreover, it can also

increase fuel availability through enhanced plant growth. Temperature indirectly alters moisture and fuel availability through its effect on evaporation and vegetation growth rates, as well as changing atmospheric stratification and convective instability. Changes in wind regimes have various implications for fire. Firstly, stronger winds can exacerbate the spread of existing fires leading to larger burning areas. Moreover, the depth of convection influences the probability of lightning, with deep convection being equally, if not more, important to the formation of lightning compared to the presence of storms in some regions.

2.4.3 Recent ENSO-fire links in the Indonesian region

The Indonesian Maritime Continent is an interesting case for exploring ENSO-fire relationships for a number of reasons. Firstly, this region plays a significant role in the global carbon cycle as it hosts the majority of tropical peatlands storing up to an estimated 50 gigatonnes of carbon (GtC; Page et al., 2002, Yu et al., 2010, see also 2.5). Secondly, it is strongly affected by ENSO, as illustrated by the severe droughts brought on by the extreme 1997-1998 El Niño event (Page et al., 2002) and more recently by the 2015-2016 El Niño - which gained the pet name of “Godzilla” for its strength (Kintisch, 2016). This decrease in precipitation also appears to be accompanied by more lightning (Chronis et al., 2008, Dowdy, 2016, Hamid, 2001, Kumar & Kamra, 2012, Sători et al., 2009, Sători & Zieger, 1999) thus potentially making the region particularly vulnerable to fire during ENSO events. Evidence from satellite data (including MODIS, TRMM VIRS and ATSR, AVHRR GAC) for recent decades indicates a strong positive correlation between El Niño and fire incidence over Indonesia (Fuller & Murphy, 2006, Giglio et al., 2010, Wooster et al., 2012), with corresponding increases in CO₂ emissions (Field et al., 2009, van der Werf et al., 2008).

However, the recent fire trends in Indonesia are strongly influenced by human activity. Biomass burning for agricultural (e.g. slash and burn) or land-clearing purposes are major sources of wildfire ignitions. Peatland draining and intensive logging reduce ambient and soil moisture, thus increasing drought sensitivity and increasing potential fuel load (Field et al., 2009, Fuller & Murphy, 2006, van der Werf et al., 2008). The question remains to what extent ENSO-like climate change drives multidecadal to centennial fire regimes in Indonesia.

2.4.4 Ignition: lightning and ENSO

Various studies have found significant relationships between ENSO events and lightning, albeit to varying degrees and regional patterns. A review by Williams (2005) finds reported global increases in lightning during El Niño events compared to La Niña events ranging between ~ 10 -100%. Using Schumann Resonance data (extremely low frequency electromagnetic spectrum peaks excited by lightning activity) covering two El Niño and two La Niña years between 1994-1999, (Sátori & Zieger, 1999) show a meridional oscillation of ~ 4 -8° latitude in the global position of lightning activity, moving southwards during El Niño years and northwards during La Niña years. Over the Maritime Continent, several studies point to an increase in lightning activities during El Niño years despite the accompanying negative precipitation anomalies. Hamid (2001) finds a $\sim 75\%$ increase in lightning activity during the 1997-1998 strong El Niño event compared to the following (La Niña) year, concentrated over land and coastal areas on Indonesia. (Sátori et al., 2009) point out a land-ocean contrast with the Pacific Ocean receiving anomalously little lightning and the Maritime Continent experiencing anomalously high flash rates during El Niño years. Other analyses over Southeast Asia (Kumar & Kamra, 2012, Sátori et al., 2009, Yoshida et al., 2007) similarly show higher lightning incidence during El Niño with the increase concentrated over land. Various authors have speculated that the land–sea contrast in terms of temperature and pressure is responsible for the increase in lightning over the Maritime Continent during El Niño events, as it leads to stronger updraft, deeper cloud formation, and ultimately more intense convective storms which are conducive to lightning (Chronis et al., 2008, Hamid, 2001, Price, 2009, Yoshida et al., 2007).

The paucity of long-term lightning data makes it difficult to make inferences of past decadal or centennial variability. However, several modelling studies predict an increase in global lightning in a warmer world, which could further exacerbate the region's human-induced vulnerability to fire.

2.4.5 Palaeo-evidence of fire behaviour

Past fire histories are mainly derived from charcoal preserved in sediments, fire scars visible in tree rings, and more recently from satellite data. From the Global Charcoal Database (GCD, <http://www.gpwg.org/gpwgdb.html>), global (Marlon et al., 2008, 2013, Power et al., 2008) and regional (Mooney et al., 2011) fire activity reconstructions have been made for various periods since the Last Glacial Maximum.

Several studies have examined the climatic influence on global and regional fire regimes over the Holocene ($\sim 10,000$ yr BP). Charcoal records from Indonesia, Papua New Guinea and Central and South America (Haberle & Ledru, 2001) show increased fire incidence on both sides of the Pacific around 5 kyr BP, which coincides with the onset of the modern-day ENSO regime (Section 2.3.3.1). Over the past millennium, there is evidence for synchronous fire regimes over the Americas, both within South and Central America (Grau & Veblen, 2000, Román-Cuesta et al., 2014, 2003), within North America (Grissino-Mayer & Swetnam, 2000, Swetnam, 1990, 1993, Swetnam & Betancourt, 1990), as well as between South/Central America and North America (Kitzberger et al., 2001).

Kitzberger et al. (2001) examined forest fire trends in the Southwestern United States and Northern Patagonia, which both experience anomalously high temperatures and low precipitation during La Niña events. Using documentary records and tree rings going back to AD 1650, they found that decadal-scale fire trends were similar in both regions. Moreover, SST and SOI patterns preceding major fire years strongly suggest that the switching from El Niño to La Niña predisposes these regions to fire. This indicates that high climate variability, such as is produced by an active ENSO cycle, plays a significant role in fire occurrence.

2.4.6 Modelling fire

The complex nature of fire processes and their interaction with terrestrial ecosystems, climate and humans has made it difficult to model (Ward et al., 2012) and thus fire is often not represented in models. At the same time, its important role in these systems calls for its inclusion in dynamic global vegetation models (DGVMs) and earth system models (ESMs) to improve our understanding of past and future

variability in fire and its role in the global C budget (Le Quéré et al., 2009). Past attempts to model fire behaviour include relatively simple empirical models that inform fire danger indices such as McArthur's Forest Fire Danger Index (McArthur et al., 1967) and the Canadian Forest Fire Weather Index (Forestry Canada Fire Danger Group, 1992) that take hourly to daily weather information. While easy to calculate, these are calibrated to specific environments and do not provide actual predictions of fire activity, making them unsuitable for large-scale modelling purposes.

At the other end of the spectrum lie the highly complex and dynamic process-based fire models, which evaluate fire occurrence, fire spread and burnt area, combustion and mortality, and the fire-related emissions individually. The high detail of these models makes them potentially very accurate and widely applicable, as they are rooted in physical processes. However, these processes are not always well understood yet and the level of detail varies between models. Consequently there is disagreement over the parametrisation of variables such as anthropogenic ignition or fire suppression (Kloster et al., 2015, Li et al., 2013b, Pfeiffer et al., 2013) and vegetation type and cover (Arora & Boer, 2005, Li et al., 2013b). This leads to significant discrepancies among models (Hantson et al., 2016b, Settele et al., 2014), between models and satellite data (Kantzas et al., 2013, Pfeiffer et al., 2013, Prentice et al., 2011), and between models and charcoal-derived palaeofire data (Kloster et al., 2012).

A middle ground of sorts is occupied by more sophisticated statistical models that evaluate spatially robust relationships between fire behaviour and climate variables (cf Chen et al., 2016, Krawchuk & Moritz, 2011). There is potential for inclusion of such models in DGVMs as they model the individual fire processes implicitly rather than explicitly and consequently require fewer inputs (Fletcher, 2014). However, the variables used are not always modelled by DGVMs (e.g. fire season severity; Chen et al., 2011) and the transferability of regionally determined relationships to other regions is contentious (Lehmann et al., 2014).

A recent endeavour seeks to produce substantial improvements in fire modelling through the creation of the Fire Model Intercomparison Project (Hantson et al., 2016a,b). This project sets out a comprehensive framework for evaluating and comparing different fire models over a number of scenarios with set parameters. Similar efforts by the climate modelling community such as the Coupled Model

Intercomparison Project (CMIP5; Taylor et al., 2012) and the Paleoclimate Model Intercomparison Project (PMIP3; Braconnot et al., 2011) have led to a better understanding of the fundamental characteristics that cause models to behave differently (Bellenger et al., 2014, Kim & Yu, 2012). An example of the issues that FireMIP may help resolve is the poor representation of tropical fire activity, particularly in moist tropical forests (Fletcher et al., 2013, Prentice et al., 2011).

2.5 Tropical peatlands and the global carbon cycle

Although peatlands only cover 3% of the global land surface (Yu et al., 2011), they form a substantial C store. Recent data syntheses (Page et al., 2011, Yu et al., 2011, 2010) estimate that they store 600 GtC (gigatonnes of carbon, 10^9) globally, of which ~ 50 -88.6 GtC is located in the tropics. Within this latitudinal zone, Southeast Asia holds 68-77%. However, data for the tropics are still relatively sparse and its carbon budget dynamics are very poorly understood (Yu et al., 2010). Peatlands have been a highly variable, but persistent, C sink throughout the Holocene, but there is uncertainty over their behaviour under projected climatic and land use changes. It is important to gain a better understanding of the interactions between natural internal processes, climate feedbacks and anthropogenic disturbances in order to be able to form a more accurate picture of their future evolution and contributions to climate change. Such knowledge has ramifications for climate projections as well as current and future efforts of peatland preservation, management and restoration.

2.5.1 Tropical peatland development

Tropical peat development was initiated much earlier than boreal and temperate peat, with evidence from Indonesia of peatland presence for at least the last ~ 33 kyr (Figure 2.4d; Anshari et al., 2004); basal dates for northern peatlands, in contrast, peak around 11-9 kyr BP (Figure 2.4b; Yu et al., 2010). During the Holocene, tropical peat initiation peaks between 8-4 kyr BP, albeit with a gap at 5.5 kyr BP, after which initiation declines until the present (Yu et al., 2010). Most of this peatland is located in South East Asia. Tropical peat carbon accumulation rates

are low before 13 kyr BP, then rise to a peak at 5-4 kyr BP; the last 2,000 years are also characterised by an increase in tropical peat accumulation (Yu et al., 2010), which can partly be explained by the lack of complete decomposition of surface peats. Most peat accumulation appears to have occurred during periods of warm climates, more specifically when summer insolation is at a maximum and seasonality is greatest (Yu et al., 2010). Regionally in the tropics, these conditions drive peat accumulation and expansion through modulating the intensity of the summer monsoon, sea level changes, and ENSO intensity (Dommain et al., 2011, Yu et al., 2010).

2.5.2 The carbon cycle in tropical peatlands

Peatlands are active contributors to the global C cycle, but are still poorly understood and thus often neglected in C budgets and models. There are five main pathways through which C is taken up and emitted by peatlands (Hooijer et al., 2010, Mitra et al., 2005): i) net CO₂ sequestration by vegetation and burial of organic material, ii) CO₂ release through respiration and decomposition, iii) fluvial organic C export, iv) anaerobic respiration of methane (CH₄), and v) CO₂ and other emissions from biomass burning. Each of these is briefly discussed below, with particular reference to tropical peatlands.

2.5.2.1 CO₂ sequestration and burial

The above-ground vegetation in peatlands removes atmospheric CO₂ through photosynthesis and stores this in the form of biomass, as well as transferring it to the soils as roots and plant litter. The high water table characteristic of peatlands slows down decomposition of organic matter, as oxygen supply to decomposable substrate is low and microbial respiration is inhibited (Davidson & Janssens, 2006). Instead, layers of organic C accumulate and get buried, forming a potential long-term reserve. Although tropical peatlands appeared less active sinks overall throughout the Holocene, their accumulation rates increased to $\sim 50 \text{ g C m}^{-2} \text{ yr}^{-1}$ in the last two millennia (Figure 2.4e); northern peatlands, in contrast, reached a peak accumulation rate in the EH and currently sequester at a rate of around $25 \text{ g C m}^{-2} \text{ yr}^{-1}$ (Figure 2.4c; Yu et al., 2011, 2010).

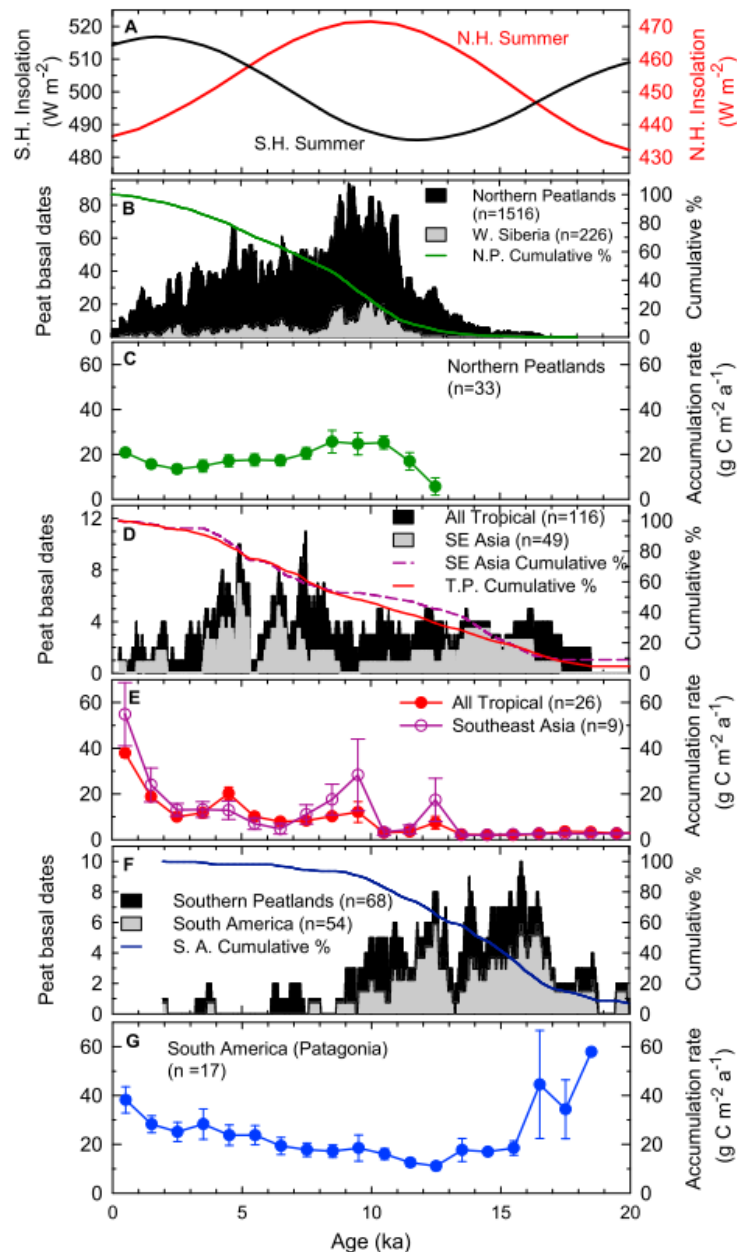


FIGURE 2.4: Global peatland records since the Last Glacial Maximum (figure from Yu et al., 2010). Horizontal axis units are kyr BP. a) Summer insolation changes in the NH and SH. Changes at the Equator follow the NH pattern, but moving between 380-410 $W m^{-2}$ (Donders et al., 2008); b) northern peatlands basal dates; c) northern peatlands accumulation rates; d) tropical peatlands basal dates; e) tropical peatlands accumulation rates; f) southern peatlands basal dates; g) southern peatlands accumulation rates. See Yu et al. (2010) for data sources.

2.5.2.2 CO₂ efflux from aerobic respiration

Aerobic root respiration and microbial decomposition, which lead to CO₂ emissions, occur when the water table is below the peat surface. Most pristine peatlands are waterlogged, limiting the potential for CO₂ release from aerobic biomass decomposition. However, drainage and drought conditions can lower the groundwater level considerably. Between 1985 and 2006, approximately 47% of the 27.1 Mha of peatland in South East Asia had been logged and largely drained (Hooijer et al., 2010) to satisfy the growing demand for timber and to make way for agricultural activities such as palm oil plantations and the failed Mega Rice Project in Indonesia (Hirano et al., 2007, van der Werf et al., 2008). Droughts, in South East Asia usually attributable to El Niño conditions, can further lower the water table, exposing a larger cross section of peat for a longer period of time (Hirano et al., 2007). Hooijer et al. (2010) derived a linear relationship between water table depth and CO₂ emissions from peatlands based on a number of emission studies; the resultant relationship suggests that every 10 cm lowering in water table depth causes an increase in peatland emissions by 9.1 tCO₂ ha⁻¹ yr⁻¹.

2.5.2.3 Fluvial organic C transport

In addition to CO₂ release from respiration and biomass burning, fluvial transport of particulate organic C (POC) and dissolved organic C (DOC) is another, often somewhat overlooked, C flux in peatlands (Hooijer et al., 2010). A recent study by Moore et al. (2013) finds that peatland degradation leads to long-term destabilisation of the C store, reporting an increase of 50% in the fluvial C flux compared to pristine peatland. Moreover, most of this additional C is sourced from ancient peat as opposed to recent plant material from undisturbed peatlands. They conclude that including fluvial organic C transport in the C budget increases C loss estimates by 22% in disturbed peatlands.

2.5.2.4 CH₄ from anaerobic respiration

The waterlogged conditions in peatlands encourage anaerobic respiration, leading to methanogenesis. CH₄ is released through ebullition, flux through vascular plant stems, and molecular diffusion across the air-water interface (Gedney

et al., 2004, Keller, 2011). The CH₄ exchange is highly variable both spatially and temporally and is linked primarily to water table depth, soil temperature, and decomposable substrate characteristics (Gedney et al., 2004, Limpens et al., 2008). Hodson et al. (2011) use a simple peatland CH₄ model to estimate that 44% of recent (1950-2000) interannual variability in global CH₄ is from tropical peatlands. They find that tropical ($R^2 = 0.56$) and global ($R^2 = 0.39$) peatland CH₄ emissions are well correlated with the Multivariate ENSO Index (MEI) over the studied period, with an average decrease in emissions of 9 ± 3 Tg CH₄ yr⁻¹ during strong El Niño years, and a mean increase of 8 ± 4 Tg CH₄ yr⁻¹ for strong La Niña years.

Empirical (Yu et al., 2011, 2010) and modelling (Singarayer et al., 2011) data suggest that tropical peatlands have also made a significant contribution to global atmospheric CH₄ concentrations throughout the Holocene. A modelling study of CH₄ emissions under projected future climate change (IPCC-TAR IS92a scenario) finds an approximate doubling of global peatland CH₄ emissions by 2100 in response to GHG-induced warming, which is comparable to projected anthropogenic CH₄ emissions (Gedney et al., 2004). Most of these modelled emission increases are likely due to northern extra tropical sources, however, as relative humidity and water table depth appear to be a more dominant factor than temperature in the tropics (Melling et al., 2005). Biomass burning does cause CH₄ release as well, but these emissions are likely small compared to any changes due to precipitation/moisture variability (Gedney et al., 2004, Melling et al., 2005, Singarayer et al., 2011).

Recent papers suggest that an elevated atmospheric CO₂ concentration in itself can alter CH₄ emissions through several pathways: a) increasing labile C availability through higher plant productivity, b) increased root oxygen loss which stimulates CH₄ oxidation (i.e. conversion to CO₂), and c) changing the plant community structure (Boardman et al., 2011, Keller, 2011). This has ramifications for future peatland emissions, but the interactions and feedbacks between temperature, precipitation, CO₂ and CH₄ are still not completely understood (Gedney et al., 2004, Hooijer et al., 2010, Keller, 2011, Li et al., 2007, Wooster et al., 2012).

2.5.2.5 Biomass burning

Although natural fires do occur, most fires in South East Asian peatlands are due to human activities, managed burning being used by local farmers as well as large corporations as a standard method of land clearance (Page et al., 2002). The high C concentration of peatlands and their overlying vegetation imply these natural C sinks are easily turned into substantial C sources during fire events. Not only do tropical peat swamp forests represent a substantial above-ground C stock, fire can penetrate deeply into the thick peat that has accumulated over millennia. In a study covering 2.5 Mha of peatland in Central Kalimantan, Indonesia, Page et al. (2002) estimated peat was removed to an average depth of 0.51 m in the areas affected during the extensive fire events in 1997.

Drainage and ENSO-related drought increase the vulnerability of peatlands to fire as these conditions can allow the peat to dry out to a flammable state. Studies of satellite data and fire activity in South East Asia (Page et al., 2002, van der Werf et al., 2008, Wooster et al., 2012) show that ENSO-induced precipitation anomalies significantly contributed to patterns of fire activity since 1980, in conjunction with land use change. Page et al. (2002) estimate that peat and biomass burning during the extreme El Niño year 1997 in Indonesia alone released the equivalent of 13-40% of total annual global C emissions from fossil fuels. Using a mix of satellite data spanning 2000-2006 and modelling approaches, van der Werf et al. (2008) find that fire-induced C fluxes were 30 times higher during the 2006 El Niño year than the 2000 La Niña year. The most recent El Niño (2015-2016) was accompanied by the highest fire CO₂ emissions since 1997, with an estimated average emission rate of 11.3 Tg day⁻¹ between September-October 2015; this exceeds the contemporary fossil fuel CO₂ emission rate of the entire European Union (Huijnen et al., 2016). As Figure 2.5 indicates, areas with the highest emissions were on or near peatlands. Over the entire Maritime Southeast Asia region, roughly 38% of total burnt area was on peatlands ($0.8 \pm 0.3 \times 10^6$ out of $2.11 \pm 1.0 \times 10^6$ ha; Huijnen et al., 2016, Randerson et al., 2015). Since peatlands store C that has been accumulated over millennia, and they tend to be covered by dense (often slow growing) tropical forests, these fire emissions will be unlikely to be offset by subsequent regrowth (Huijnen et al., 2016, Jaenicke et al., 2008, Kurnianto et al., 2015).

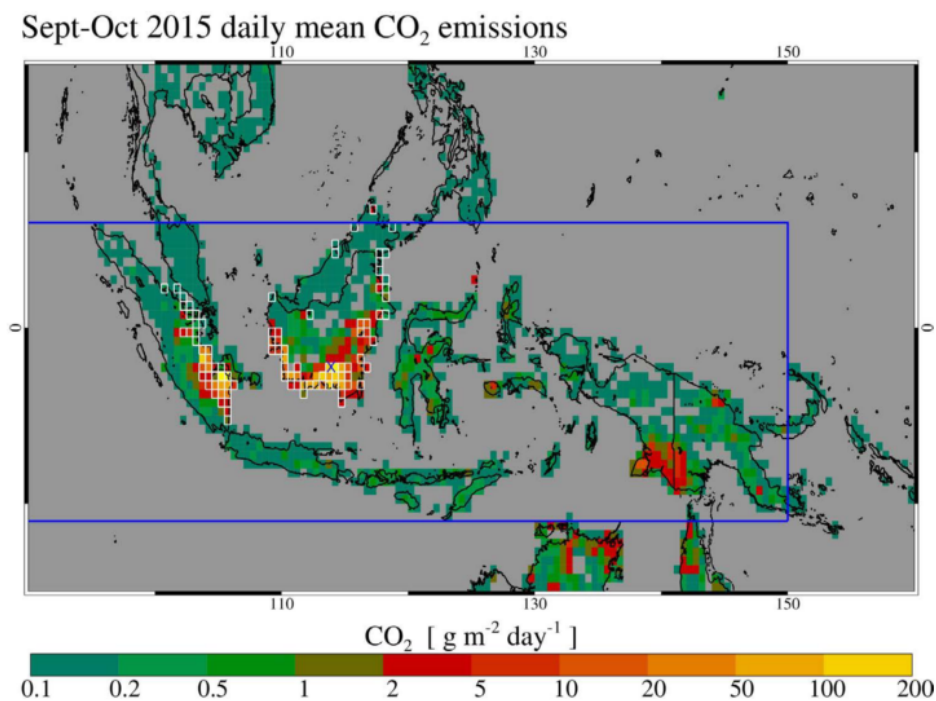


FIGURE 2.5: Daily mean CO₂ emissions from peat and vegetation fires across Indonesia from September-October 2015 (figure from Huijnen et al., 2016). Grid cells containing peat soils are outlined in white.

An examination of 11 climate models included in the IPCC AR4 (Li et al., 2007) suggests a future decrease of dry season precipitation over South East Asia, as well as larger interannual variability. If accurate, these projected changes will further decrease the capacity of tropical peatlands to store C and possibly turn significant areas into net C sources.

While it is clear that peatlands are a significant player in the global C cycle, they are still ignored in most global climate models. The underlying processes regulating C uptake and release are highly complex, with multiple pathways and feedbacks. Lack of sufficient data in the tropics is a major stumbling block for producing accurate estimates of past and present C budget developments, which limits the possibility to disentangle different forcings, drivers and feedbacks that have contributed. More research is required to understand how tropical peatlands will respond to projected changes in climate as well as the on-going anthropogenic degradation.

2.6 Summary

This literature review has shown the importance of the tropical hydrological cycle and ENSO in relation to tropical fire regimes and C cycling in tropical peatlands. Hydrological patterns have been non-stationary throughout the Holocene, including robust features like ENSO. The response of the global hydrological cycle varies depending on the nature of the forcing mechanisms, which is important for understanding how it will change in the future. Changes in precipitation are paramount in modulating fire activity in the tropics, as demonstrated by the strong relationship between ENSO state and biomass burning at interannual scales. Fire behaviour is very complex, however, with strong feedbacks on vegetation dynamics and fuel characteristics. There is a need for a better understanding of the natural dynamics fire outside the influence of humans, and to assess these interactions at longer timescales not captured by instrumental data. These hydrological changes and fire activity are of global importance in tropical peatlands, which are largely located in the ENSO-sensitive Indonesian region and hold substantial amounts of C. The lack of knowledge on fire behaviour and associated C cycling in this region over longer timescales hinders the accurate assessment and modelling of the global C cycle, which is important for accurate projections of climate change. These main findings provide the foundation for the motivations of this project outlined in 1.1.

Chapter 3

Method development and hypothesis foundations

3.1 Introduction

Palaeoclimatological research is severely constrained by the availability and quality of data, which poses unique challenges in terms of interpretation and extrapolation of results to other regions or time periods. While much progress has been made in applying more statistically robust techniques to palaeo-data in order to accurately characterise the various sources of uncertainty as well as to maximise the amount of information extracted from the available data (cf Emile-Geay & Tingley, 2016, Mann et al., 2007, Tingley et al., 2012), there is still scope for improvement within the community. The work presented in this thesis is a combination of methodological development and data exploration in the palaeo context, both of which are underpinned by a substantial amount of mathematical and statistical analyses. Achieving this necessitates thorough evaluation of the relative strengths and limitations of various techniques, and selecting the most appropriate ones given the constraints of the data. This chapter describes the mathematical foundations underpinning the methodologies applied in the thesis, equipping the reader with the necessary understanding and providing justifications for methodological choices made throughout. Particular attention is paid to the concept of pseudoproxy experiments, which is arguably one of the most

promising avenues for improving palaeo-data interpretation. To lay the groundwork for the hypotheses tested in Chapters 4 and 5, some preliminary analyses are also presented here. The overarching theme of long-term versus short-term tropical climate change and variability is addressed in this chapter by examining modern-day interannual relationships between temperature, precipitation and ENSO in the tropical-subtropical latitudes and the Indonesian region. This provides a backdrop with which the palaeo-data can be compared to interrogate the robustness of natural relationships between climate variables and fire behaviour, and to start untangling the possible role of human influence on recent and future climate change and wildfire risk.

This chapter first introduces multiproxy reconstruction methods (Section 3.2), describing background analyses and tests for the methods applied in Chapter 4. Section 3.3 investigates relationships between temperature, precipitation, and ENSO in observational and model data, providing baseline expectations that inform the hypotheses of Chapters 4 and 5. The concepts of pseudoproxies and proxy system models are introduced in 3.4, accompanied by details on their implementation in Chapter 4. Sect 3.5 discusses various data transformation techniques applied in Chapters 4 and 5, followed by smoothing methods in 3.6.

3.2 Multiproxy reconstruction methods

There are no meteorological measurements of the climate beyond the most recent ~400 years, before the advent of thermometers (Manley, 1974), rain gauges (Wallace, 1997) and ship logs (Freeman et al., 2016). Instead, we rely on climate proxies, which are naturally occurring physical or biological processes that are measurably and reliably influenced by environmental factors. Common examples include: trees whose tree rings vary in density, width or even isotopic composition in response to moisture availability and/or temperature; corals that produce seasonal or annual layers reflecting the seawater isotopic composition (which in turn can be altered by temperature, ocean currents and precipitation); and varved lakes where changes in influx (due to source area or precipitation-induced runoff) affect the grain size of inflowing sediments. Table 3.1 provides an overview of the most common proxy types, their characteristics, examples of models used to interpret them (see Section 3.4.1) and known limitations. This table is by no

means exhaustive, but serves to provide the reader with a flavour of the breadth of available proxy data sources and their strengths and limitations.

It is common in the palaeoclimatology community to create reconstructions of climatic phenomena by combining two or more proxy records to capture spatial covariability. For example, Briffa et al. (2001) employ a large network of tree ring records to reconstruct hemispheric and global temperature anomalies over the past two millennia. Other global reconstructions combine different types of proxies (Mann et al., 2008, Shi et al., 2013), which expands the available network of records but introduces other complications due to differences in aspects such as proxy units and resolution. In addition to hemispheric-scale reconstructions, various authors have attempted to reconstruct regional climate change and modes of variability such as the NAO (Trouet et al., 2009, 2012), the PDO (D'Arrigo & Wilson, 2006, MacDonald & Case, 2005), and monsoon regimes (Clemens & Prell, 2003, Yang et al., 2016). The methods used for combining the proxy records are diverse, depending on the objective and the nature of the proxy network. For example, Conroy et al. (2010) use two proxy records (Galápagos lake sediment in the EEP and marine sediment in the WPWP) to reconstruct the zonal Pacific SST gradient over the past 1.2kyr; the proxy series are converted to degrees Celsius via calibrations with instrumental data, and then differenced to calculate the gradient. This is similar to the method of Yan et al. (2011b) for creating a proxy SOI (SOI_{pr}) from two precipitation records, except that they assign empirically determined weights to the two records. Studies with larger multiproxy networks usually employ more complex methods, often based on some form of regression (e.g. MacDonald & Case, 2005, Mann et al., 2009, Yang et al., 2016) or principal components analysis (PCA) (e.g. Griffiths et al., 2016, McGregor et al., 2010). The method developed in Chapter 4 is largely inspired by the study by Yan et al. (2011b). It extends their application of normalising and weighting records to a larger network of proxies, assigning weights based on the expected strength of the ENSO signal at each location. This also links to PCA in the form of empirical orthogonal function (EOF) analysis, which is a variation of PCA that is more explicitly spatial as well as temporal.

Sensor	Var	Domain	Archive	Observation	Resolution	Length	PSM	Limitations
trees	T(t), M(t)	terrestrial temperate	wood	ring width, ring density	seasonal to annual	dyr to kyr	Vaganov et al. (2011), Tolwinski-Ward et al. (2011)	divergence problem for temperature, potential for biological influence, spatially limited
	T(t), M(t)	terrestrial tropical	wood	stable isotopes	seasonal to annual	dyr to kyr	Dee et al. (2015), Roden et al. (2000), Barbour et al. (2004), Evans (2007)	
corals	SST(t), SSS(t)	marine trop- ical	colony	stable isotopes, skeletal density, fluorescence, elemental ratios	seasonal to annual	dyr to cent.	Thompson et al. (2011), Dee et al. (2015)	assumption violation of stable $\delta^{18}O_{sw}$, short records, potential for biological influence
lakes	P(t), runoff	terrestrial	sediment	grain size, elemental ratios, trace metal concentrations, sediment lamination	annual to decadal	dyr to kyr	empirical, e.g. Shanahan et al. (2007), Tierney et al. (2010)	often low temporal resolution and large dating error
	T(x,t), P(x,t), SSS(t)		vegetation	pollen relative abundance, pollen assemblages, PFTs	annual to decadal	dyr to kyr	modern analogue technique, artificial neural network, empirical, Parnell et al. (2016)	lack of modern analogues, differential preservation of pollen species
oceans	SST(x), SST(x,t), U(x), N(x,t), U(x,t), pCO_2	marine	sediment	stable isotopes, species assemblages, pollen assemblages, PFTs, trace metal concentrations, elemental ratios, biomarkers	Annual to centennial	dyr to Myr	empirical calibration, Tierney & Tingley (2014), Parnell et al. (2016)	poor age control, often low temporal resolution and large dating error
ice sheets	T(t), A(t), U(x,t)	terrestrial high lati- tudes, high elevations	ice	stable isotopes, dust deposition rates, fraction of melting ice, accumulation rates, salt/acid concentrations, trace gases	seasonal to decadal	dyr to Myr	Dee et al. (2015), Vuille et al. (2003), Hurley et al. (2016)	spatially limited, difficult to date melt water and precipitation accumulation data, tropical glacier controls poorly understood

Continued on next page

Table 3.1 – continued from previous page

Sensor	Var	Domain	Archive	Observation	Resolution	Length	PSM	Limitations
caves	D(t), P(t)	terrestrial	speleothem	stable isotopes, elemental ratios	seasonal to millennial	dyr to Myr	Dee et al. (2015), Stoll et al. (2012), Baker et al. (2012), Truebe et al. (2010), Partin et al. (2013)	requires understanding of overlying geology and water-rock interactions, possible but poorly understood non-climatic influences
rocks	T(t)	terrestrial	bore hole	temperature-depth profiles	decadal to centennial	cent. to kyr	Goto & Yamano (2010)	sensitivity to assumptions needed to convert the temperature profiles to surface temperature changes, non-climatic factors (e.g. land use change) change the soil thermal properties
historical docu- ments	T(t), P(t), SST(t), SLP(t)	all	diaries, ship logs, paint- ings, early instruments		daily to decadal	months to cent.		can be highly subjective or non-realistic (especially diaries and paintings), ship logs are spatially limited, requires calibration between different types of measuring methods

TABLE 3.1: Overview of the most common sources of proxy data and their characteristics. The response of a “Sensor” to one or more environmental variables “Var” is imprinted in the “Archive”, and is extracted for analysis through an “Observation” (Evans et al., 2013). T is temperature, M is moisture, SST is sea surface temperature, SSS is sea surface salinity, P is precipitation, U is wind, N is nutrient concentration, pCO_2 is partial pressure of CO_2 , A is atmospheric aerosol concentration, D is drip rate, and SLP is sea level pressure; t indicates time and x indicates spatial distribution. “Resolution” is the usual temporal resolution, while “Length” indicates the usual order of years captured by the archive; dyr is decennial, $cent.$ is centennial, kyr is millennial, Myr is million years.

“PSM” provides models available for interpreting the proxy, and “Limitations” lists the main known issues for the proxy.

This section details the mathematics of EOF analysis (Section 3.2.1) and describes its application in this thesis (Section 3.2.4). It then discusses the EOF selection procedure for modern-day (reanalysis) and model data.

3.2.1 EOF analysis

Empirical Orthogonal Function (EOF) analysis decomposes a spatiotemporal dataset into stationary time-varying coefficients. For a dataset of spatial resolution $x \times y$ and n time steps, it produces n maps (EOFs) of $x \times y$. The first map (EOF1) captures the largest fraction of variance of the original data. Each subsequent map maximises the amount of remaining variance captured, whilst being completely uncorrelated (orthogonal) to all preceding maps. Every EOF map is accompanied by a principal component (PC) timeseries of length n , which describes how the magnitude and sign of the EOF pattern varies over n . The first few EOFs can usually be attributed to physical dynamical phenomena such as seasonality or a longer term regional mode of variation such as ENSO. By only retaining the leading EOFs, a dataset can be ‘cleaned’ of the (assumed) random noise captured by the lower-order EOFs. As ENSO is globally the most influential source of interannual variability, it is likely to be captured in the first EOF of an annual temperature or precipitation dataset and its corresponding PC, both at a global level and more strongly in the tropical-subtropical region. Prior to EOF calculation, the dataset can be temporally detrended to remove any linear trend. Throughout this chapter, both undetrended and detrended versions of the datasets are evaluated to explore the effect of this detrending.

The EOF calculations performed in this thesis are based on the EOF manual by Björnsson & Venegas (1997) and run in R. It approaches EOFs as an eigenvalue problem (as opposed to a singular value decomposition (SVD) approach). The data are contained in a matrix \mathbf{F} , with time (n) in rows and location (p) in columns such that each column p can be seen as a timeseries of length n at location p . The data matrices used in this thesis are highly non-square; with a resolution of $2^\circ \times 3^\circ$, there are 16200 locations p for only 1000 timesteps n . To reduce the computational load, a slightly adapted version of EOF analysis is performed based on producing a reduced covariance matrix. The main mathematics

is outlined below, while more background of the mathematical reasoning behind this can be found in Björnsson & Venegas (1997).

For standard EOF analysis, the first step is to calculate the covariance matrix \mathbf{R} of size $[p \times p]$:

$$\mathbf{R} = \mathbf{F}^T \mathbf{F} \quad (3.1)$$

where \mathbf{F}^T is the transpose of \mathbf{F} . The EOFs and corresponding PCs are then found by solving the eigenproblem:

$$\mathbf{R}\mathbf{C} = \mathbf{C}\mathbf{\Lambda} \quad (3.2)$$

The eigenvalues λ_i of \mathbf{R} are contained in the diagonal matrix $\mathbf{\Lambda}$, and when divided by the trace of $\mathbf{\Lambda}$ represent the fraction of total variance in \mathbf{R} explained by each corresponding eigenvector. The eigenvectors are the column vectors c_i of \mathbf{C} , and represent the EOFs (i.e. the spatial patterns).

In this scenario, \mathbf{R} , \mathbf{C} and $\mathbf{\Lambda}$ are all of size $[p \times p]$. As p in this thesis is very large, this creates computational issues. To avoid this, a reduced covariance matrix \mathbf{L} of size $[n \times n]$ is calculated instead:

$$\mathbf{L} = \mathbf{F}\mathbf{F}^T \quad (3.3)$$

The eigenproblem for \mathbf{L} is found by multiplying Eqn. 3.2 by \mathbf{F} and defining a new matrix \mathbf{B} :

$$\mathbf{F}\mathbf{R}\mathbf{C} = \mathbf{F}\mathbf{C}\mathbf{\Lambda} \quad (3.4)$$

$$\mathbf{F}\mathbf{F}^T \mathbf{F}\mathbf{C} = \mathbf{F}\mathbf{C}\mathbf{\Lambda} \quad (3.5)$$

$$\mathbf{L}\mathbf{F}\mathbf{C} = \mathbf{F}\mathbf{C}\mathbf{\Lambda} \quad (3.6)$$

$$\therefore \mathbf{L}\mathbf{B} = \mathbf{B}\mathbf{\Lambda} \quad (3.7)$$

The interpretation of Eqn. 3.7 is the same as Eqn. 3.2, so the eigenvalues of \mathbf{L} contained in $\mathbf{\Lambda}$ are the same as those of \mathbf{R} . However, solving Eqn. 3.7 gives a $\mathbf{\Lambda}$ of size $[n \times n]$, which is much less intensive to compute. To find the corresponding EOFs of \mathbf{R} , we calculate:

$$\mathbf{D} = \mathbf{F}^T \mathbf{B} \quad (3.8)$$

where column vectors \mathbf{d}_i of matrix \mathbf{D} are proportional to the EOFs by a factor of $\frac{1}{\sqrt{\lambda_i}}$. EOF $_i$ is thus found by calculating $\frac{\mathbf{d}_i}{\sqrt{\lambda_i}}$. This is not important if the EOFs are normalised, however, as is done in this thesis.

The corresponding PCs are calculated by doing a matrix multiplication of the original data \mathbf{F} $[n \times p]$ with the eigenvectors of \mathbf{D} $[p \times n]$ to obtain a matrix \mathbf{T} $[n \times n]$ in which column vector \mathbf{t}_i is the PC timeseries for EOF $_i$:

$$\mathbf{t}_i = \mathbf{F} \mathbf{d}_i \quad (3.9)$$

The fraction of variance v captured by each EOF is calculated by dividing eigenvalue λ_i by the sum of all λ (i.e. the trace of $\mathbf{\Lambda}$):

$$\mathbf{v}_i = \frac{\lambda_i}{\sum_{i=1}^n \lambda_i} \quad (3.10)$$

There are various selection rules to determine which EOFs to retain, depending on the purpose of the EOF analysis. *Dominant variance* rules focus on the size of the eigenvalues (i.e. the amount of variance captured), and can be used to determine a cut-off point for significant EOFs. *Time-history* rules look for non-stochastic PCs, which can be similarly applied to find a cut-off point, or to compare to a known timeseries. Finally, *space-map* rules focus on the spatial patterns of the EOFs, and are useful for comparing to known or expected patterns (see Björnsson & Venegas, 1997, and references therein for more detail). As the aim in this thesis is to find the most ENSO-like EOF (i.e. comparing to a known entity), a combination of time-history and space-map rules were used. The implementation of these selection procedures is described in the following Sections.

3.2.2 Selecting EOFs: 20CRv2c

The Twentieth Century Reanalysis Project Version 2c (20CRv2c) is the longest global dataset of atmospheric circulation available, spanning AD 1851-2014. It combines observations of surface and sea level pressure, sea surface temperature and sea ice distribution with output from a numerical weather prediction model. The latter implements a ‘deterministic’ Ensemble Kalman Filter (EKF) to assimilate the data and estimate the state of the entire atmosphere along with uncertainties in the estimate. Sea surface temperature boundary conditions are based on the Simple Ocean Data Assimilation with Sparse Input version 2 (SO-DAsi.2; Giese et al., 2016), sea ice concentration boundary conditions on monthly COBE-SST sea ice (Hirahara et al., 2014). 20CRv2c has a spatial resolution of 2° latitude \times 2° longitude \times 24 vertical pressure levels, and a temporal resolution of 6 hours.

It has been demonstrated that the 20CRv2c is competent at representing the global tropospheric circulation as well as the mean state and variability of the hydroclimate – for a detailed description and evaluation of the product see Compo et al. (2011). The monthly mean surface air temperature and precipitation rate datasets were downloaded from the NOAA/OAR/ESRL PSD web site (<http://www.esrl.noaa.gov/psd/>). The 20CRv2c data were regridded to $2^\circ \times 3^\circ$ to be comparable to the model data described below (Section 3.2.3). The climatology (for the period 1851-2014) was removed to produce monthly anomalies with respect to the long term mean, and these were then averaged to annual resolution. The conversion to anomalies is performed to ensure identical treatment of the reanalysis, model and proxy data in all analyses presented in this thesis. Since these datasets do not share a common measurement unit, this conversion makes them more directly comparable (see also 3.5). The calculation of annual means was done because the focus in this thesis is on long-term changes rather than seasonal variability. An added benefit of reducing the temporal resolution is the reduction in computational cost. The spatial and temporal availability of instrumental temperature data is better than that of precipitation, which means that the temperature data in 20CRv2c are more completely based on observations, and precipitation is more reliant on model output; its spatial pattern is constrained by observations, however (Compo et al., 2011).

For the purpose of this thesis, the global 20CRv2c dataset was cropped to the tropical-subtropical region (40°S–40°N); this is the study area of Chapter 4. All of the following analyses using 20CRv2c were performed on this reduced dataset, unless otherwise specified.

A time-history selection approach (Section 3.2.1) was used to determine which 20CRv2c EOF pattern was most representative of ENSO, by comparing their associated timeseries (PCs) for both temperature and precipitation fields to three ENSO indices:

- **NINO3.4** calculated from SST anomalies in the Equatorial Pacific region of 5°N–5°S, 120°–170°W (http://www.esrl.noaa.gov/psd/gcos_wgsp/Timeseries/Nino34/);
- **Southern Oscillation Index (SOI)** calculated from the difference in sea level pressure (SLP) between Tahiti and Darwin, and is inversely linked to ENSO state (i.e. negative SOI during El Niño). (<http://www.cpc.ncep.noaa.gov/data/indices/soi>);
- **Extended Multivariate ENSO Index (MEI.ext)** is calculated from a combination of SLP and SST (Wolter & Timlin, 2011, <http://www.esrl.noaa.gov/psd/enso/mei.ext/table.ext.html>).

Results for the highest scoring PCs are shown in Table 3.2. Correlations with all three indices were extremely high for temporally detrended PC1 ($R^2 > 0.61$, $p < 0.001$) and undetrended PC2 ($R^2 > 0.62$, $p < 0.001$). This is in line with expectations, as the global warming trend overtakes ENSO in the undetrended PC1 as the strongest source of temporal variability. All further tests and analyses presented in this thesis were consequently performed using these EOFs and PCs to represent ENSO-like spatiotemporal variability in 20CRv2c. The variance captured (Eqn. 3.10) by the undetrended and detrended EOFs is 11.6% and 17.0% respectively for precipitation, and 9.75% and 13.23% respectively for temperature.

ENSO index	P_{detrend} (PC1)	P (PC2)	T_{detrend} (PC1)	T (PC2)
NINO3.4	0.88	0.88	0.89	0.88
MEIext	0.85	0.86	0.9	0.88
SOI	-0.78	-0.79	-0.81	-0.81

TABLE 3.2: Correlations (Pearson product-moment correlation coefficient R) between ENSO indices and 20CRv2c precipitation (P) and temperature (T) PCs, using detrended and undetrended data. Only the PCs with the highest correlations are shown here, and are identified in brackets.

3.2.3 Selecting EOFs: GCMs

Having confirmed the observed relationship between ENSO-like precipitation and temperature change, we now turn to an exploration of the expected links as simulated by state-of-the-art climate models. General circulation models (GCMs) are excellent test-beds for developing methods and exploring dynamical processes and links. In this thesis, GCMs are used to investigate expected temperature vs. precipitation behaviour and links (Section 3.3.2), as well as developing and testing the EOF-based reconstruction method introduced in 3.2.4, and expanded on in Chapter 4. This section evaluates the ability of six GCMs to simulate the ENSO pattern.

There are several comprehensive modelling projects with the aim of improving comparability between GCMs produced by different teams. GCMs taking part in these projects perform a set of simulations with standardised forcings and boundary conditions. The following six GCMs (followed by their climate modelling groups in brackets) were included:

- CCSM4 (National Center for Atmospheric Research)
- GISS-E2-R (NASA Goddard Institute for Space Studies)
- MPI-ESM-P (Max-Planck-Institut für Meteorologie/Max Planck Institute for Meteorology)
- IPSL-CM5A-LR (Institut Pierre-Simon Laplace)
- BCC-CSM1-1 (Beijing Climate Center, China Meteorological Administration)

- MIROC-ESM (Atmosphere and Ocean Research Institute (The University of Tokyo), National Institute for Environmental Studies, and Japan Agency for Marine-Earth Science and Technology)

In this thesis, the pre-industrial control (piControl; pre-1850 parameters, no external forcings) and historical (AD 1850–~2000) runs from the Coupled Model Intercomparison Project 5 (CMIP5; Taylor et al., 2012) were used, in addition to the last millennium (past1000; AD 850–1850) runs from the Paleoclimate Model Intercomparison Project 3 (PMIP3; Braconnot et al., 2012, 2011). The six models were selected on the basis of all three runs being available. Monthly precipitation and temperature datasets were downloaded, and all datasets were regridded to $2^\circ \times 3^\circ$ to enable comparison among models and with the 20CRv2c datasets. As with 20CRv2c (Section 3.2.2), all model datasets were cropped to the tropical-subtropical study region and the monthly values were converted to annual anomalies.

All current GCMs are deficient in their ability to simulate many aspects of the modern day ENSO, often overestimating the western extent of the Pacific Cold Tongue and failing to correctly simulate central Pacific precipitation anomalies, ENSO feedbacks, and ENSO amplitude (Bellenger et al., 2014, Collins, 2005, van Oldenborgh et al., 2005). These biases vary between models as well as among model runs. To examine the ability of the six GCMs to simulate ENSO, they were compared to the ENSO-like EOFs identified in the 20CRv2c data. Since the ENSO oscillation is a stochastic process, GCM-simulated ENSO-like PC time-series cannot be directly compared to the ENSO indices as done with 20CRv2c (Section 3.2.2). Therefore, a direct comparison of the spatial patterns (in other words, a space-map approach) is the most appropriate way to select the most ENSO-like EOFs in GCMs.

EOF analysis was performed on all 18 GCM runs, and the first three EOFs were retained for comparison with the 20CRv2c ENSO-like EOFs. The EOF maps were converted to vectors to enable Pearson product-moment correlation analysis.

3.2.3.1 Full field comparison

Five of the six GCMs showed strongest similarity with the 20CRv2c ENSO-like EOF in their EOF1. The only exception was BCC-CSM1-1 precipitation, which showed stronger correlations in EOF2. R -values range between 0.34-0.76 (precipitation) and 0.49-0.78 (temperature) for detrended and undetrended EOFs, over all three time periods (Table 3.3). The undetrended EOFs are shown in Figures 3.1 and 3.2 for illustration.

P_{detrend}	piC	h	1k	P	piC	h	1k
BCC-CSM1-1 (EOF2)	0.58	0.59	0.59	BCC-CSM1-1 (EOF2)	0.64	0.65	0.65
GISS-E2-R	0.76	0.72	0.75	GISS-E2-R	0.76	0.74	0.75
MIROC-ESM	0.48	0.57	0.49	MIROC-ESM	0.50	0.52	0.52
MPI-ESM-P	0.44	0.40	0.42	MPI-ESM-P	0.39	0.35	0.36
IPSL-CM5A-LR	0.39	0.39	0.38	IPSL-CM5A-LR	0.35	0.35	0.34
CCSM4	0.73	0.73	0.74	CCSM4	0.68	0.69	0.69
T_{detrend}	piC	h	1k	T	piC	h	1k
BCC-CSM1-1	0.67	0.50	0.71	BCC-CSM1-1	0.68	0.45	0.70
GISS-E2-R	0.68	0.67	0.58	GISS-E2-R	0.71	0.54	0.67
MIROC-ESM	0.60	0.59	0.56	MIROC-ESM	0.63	0.49	0.59
MPI-ESM-P	0.72	0.68	0.73	MPI-ESM-P	0.75	0.72	0.76
IPSL-CM5A-LR	0.66	0.65	0.63	IPSL-CM5A-LR	0.72	0.70	0.70
CCSM4	0.73	0.70	0.73	CCSM4	0.77	0.75	0.78

TABLE 3.3: Correlations (Pearson product-moment correlation coefficient R) between 20CRv2c and GCM EOFs, using detrended and undetrended data. All results are for EOF1, which had the highest correlation except for BCC-CSM1-1, which had higher correlations for P EOF2. piC refers to piControl, h refers to historical, and 1k is past1000.

Since the piControl and past1000 run should not (and do not) contain an anthropogenic global warming trend, it is unsurprising that EOF1 is consistently the most ENSO-like (excepting BCC-CSM1-1). However, it is interesting that EOF1 also shows highest correlation for the undetrended historical run, which theoretically should contain the global warming signal. This suggests that the ENSO amplitude is perhaps larger in the models than in the reanalysis data such that it takes dominance over the warming trend, or conversely the warming trend is smaller in these models. Correlations are slightly higher for most (but not all) GCMs using the detrended data. Based on this comparison, the three GCMs

with overall best representation of the precipitation-ENSO signal are GISS-E2-R, CCSM4 and BCC-CSM1-1 (in EOF 2) or MIROC-ESM (in EOF1). The best models for temperature are CCSM4, MPI-ESM-P and IPSL-CM5A-LR.

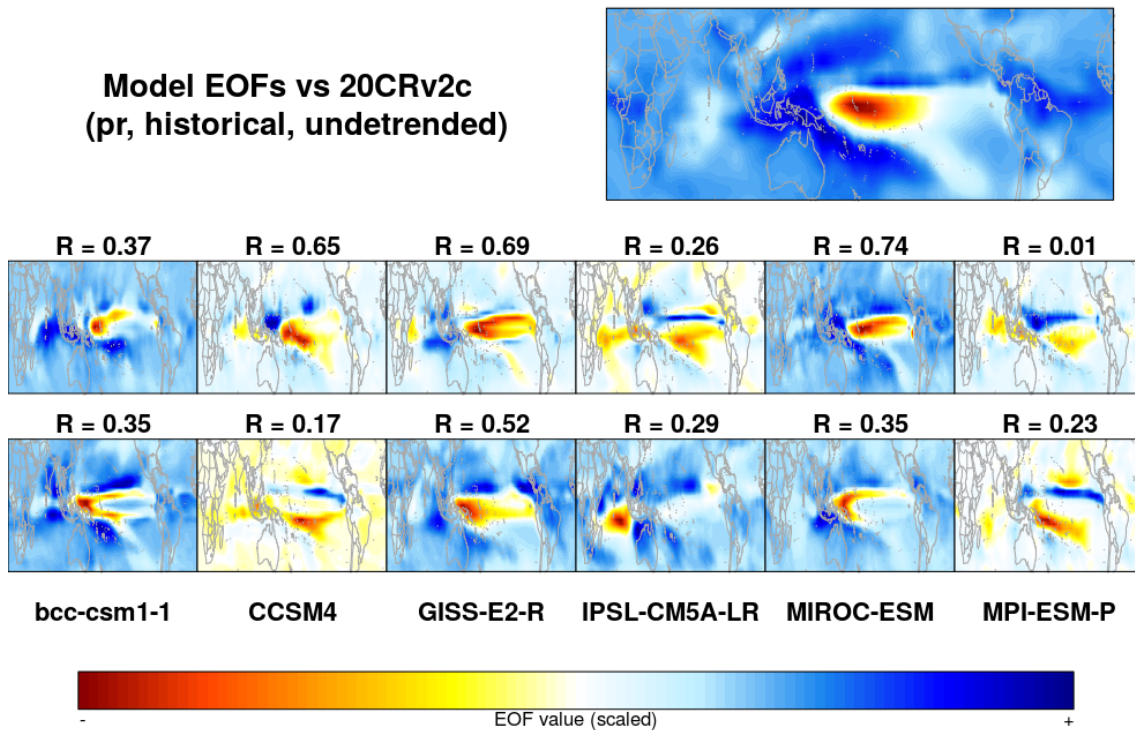


FIGURE 3.1: Comparisons of 20CRv2c EOF1 (top right) with undetrended precipitation EOF1 (middle row) and EOF2 (bottom row) of the historical runs of six GCMs. R -values are shown above each EOF map. Note that the directionality of the colour scale is arbitrary; it is merely an indication of the relative difference within the spatial pattern. In this case it is directed to reflect El Niño-like conditions.

3.2.3.2 Proxy field comparison

While the full-field comparison is informative for the overall performance of the models, it does not necessarily identify the models that are optimal at the locations of the proxies employed in Chapter 4 (see also Appendix A for a complete list of proxy records). Therefore the correlation analysis was repeated, extracting the EOF values at real proxy locations only. A subset of proxies was used here; the full methodology described in Chapter 4 applies a more sophisticated approach to proxy selection. The results are displayed in Table 3.4. In the sparse (proxy) case,

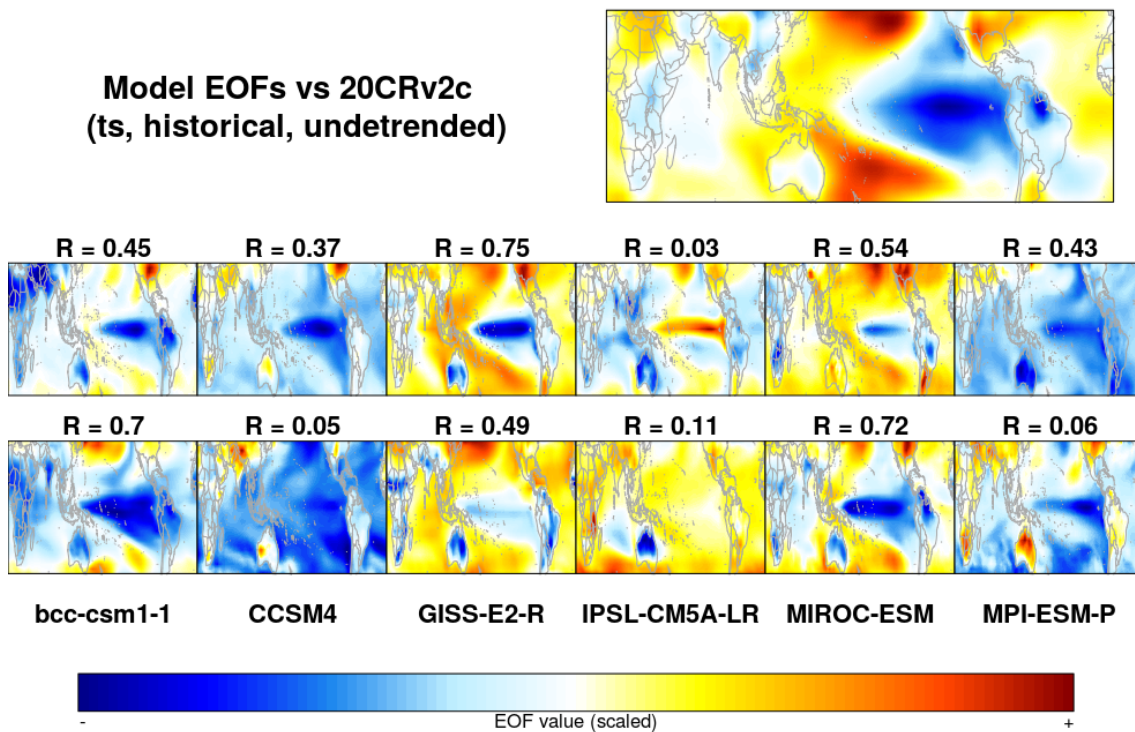


FIGURE 3.2: As Figure 3.1 but for temperature.

the top three models for precipitation are the same, but BCC-CSM1-1 is strongest in EOF1 (not EOF2 as was the case in the full field scenario). For temperature, MPI-ESM-P and IPSL-CM5A-LR remain in the top three, but CCSM4 is surpassed by BCC-CSM1-1. The correlations overall are much lower in the sparse temperature scenario compared to the full field, and compared to the sparse precipitation correlations. This is likely a reflection of the suboptimal locations of most of the temperature proxies, with the majority lying outside the regions of high ENSO sensitivity.

3.2.4 Sparse PC reconstructions

Equation 3.9 in 3.2.1 shows how the temporal evolution (PC) of a mode of oscillation can be reconstructed using the EOF and the original dataset. By substituting F in Eqn. 3.9 with a dataset from a different time period, we can estimate how this mode behaved outside the original time bounds. Assuming we had a perfect dataset of temperature or precipitation for the past two millennia, this principle

P_{detrrend}	piC	h	1k	P	piC	h	1k
BCC-CSM1-1	0.58	0.59	0.57	BCC-CSM1-1	0.60	0.58	0.58
GISS-E2-R	0.81	0.74	0.82	GISS-E2-R	0.75	0.68	0.78
MIROC-ESM	0.13*	0.28	0.09*	MIROC-ESM	0.10*	0.23*	0.11*
MPI-ESM-P	0.51	0.49	0.50	MPI-ESM-P	0.52	0.49	0.51
IPSL-CM5A-LR	0.35	0.37	0.42	IPSL-CM5A-LR	0.40	0.39	0.47
CCSM4	0.83	0.83	0.82	CCSM4	0.79	0.81	0.79
T_{detrrend}	piC	h	1k	T	piC	h	1k
BCC-CSM1-1	0.44	0.17	0.52	BCC-CSM1-1	0.73	0.51	0.75
GISS-E2-R	0.10*	0.17	0.05	GISS-E2-R	0.24	0.26	0.33
MIROC-ESM	0.00*	0.05*	0.06*	MIROC-ESM	0.26	0.05*	0.35
MPI-ESM-P	0.31	0.26	0.32	MPI-ESM-P	0.57	0.56	0.57
IPSL-CM5A-LR	0.46	0.38	0.48	IPSL-CM5A-LR	0.66	0.58	0.70
CCSM4	0.26	0.14	0.30	CCSM4	0.50	0.38	0.54

TABLE 3.4: As Table 3.3 but at proxy locations. All results (including BCC-CSM1-1 precipitation) are for EOF1. Starred R -values are not significant ($p > 0.05$). piC refers to piControl, h refers to historical, and 1k is past1000.

could then be applied to evaluate how the strength of the modern-day ENSO pattern varied over this time period. However, palaeoclimate data tends to be incomplete both temporally and spatially. This leads us to the proposal of a 'sparse' PC reconstruction, using spatiotemporally incomplete palaeoproxy data to derive a best estimate.

The sparse PC reconstruction is essentially a weighted sums approach, where proxy timeseries are weighted based on the relative strength of the EOF at their respective locations, and summed to obtain a single timeseries. The relative weights are calculated by scaling the EOF values for all included timeseries such that the absolute sum of the weights is 1 at each timestep. This accounts for the fact that the number of locations with proxy data may vary over the reconstructed period as proxies drop in and out. The weight w at proxy location i can thus be considered an indication of the *relative* sensitivity of location i to the ENSO-like EOF pattern, which changes depending on the number of proxies n available at each timestep t , and their associated EOF values d :

$$\mathbf{w}_{i,t} = \frac{d_{i,t}}{\sum_{i=1}^n |d_{i,t}|} \quad (3.11)$$

The resultant vector \mathbf{w}_i is thus the weighting series for proxy location i (equivalent to the n^{th} value in eigenvector \mathbf{d}_i). The n proxy series are multiplied by their corresponding \mathbf{w}_i , and finally are summed to create a single reconstruction series:

$$\mathbf{s} = \sum_{i=1}^n \mathbf{p}_i \mathbf{w}_i \quad (3.12)$$

where \mathbf{s} is the sparse PC (sparse equivalent of t_i in Eqn. 3.9), and \mathbf{p}_i is the corresponding proxy timeseries (equivalent to column vector \mathbf{f}_i of original dataset \mathbf{F}).

This can be compared to the method employed by Yan et al. (2011b), who used two precipitation proxies located off the coast of Indonesia (marine sediment $\delta^{18}O_{\text{sw}}$; Oppo et al., 2009) and in the Galápagos islands (lake sediment %sand; Conroy et al., 2008) to reconstruct the SOI over the past 2000 years. The two proxies are normalised, then weighted to maximise correlation with the instrumental SOI (1955-1997), which results in weights of 0.67 for Indonesia and 0.33 for the Galápagos. Finally the two weighted series are summed to create a proxy SOI (SOI_{pr}). Although the authors use weighting based on a temporal series rather than a spatial pattern, the underlying concept is identical. The sparse PC reconstruction employed in this thesis (Chapter 4) can thus be seen as an extension of the method presented in Yan et al. (2011b) by incorporating more than two proxy records for more extensive spatial coverage, and using two climate variables (temperature and precipitation) as proxy targets. Performing the EOF-based sparse PC reconstruction method using only the two proxies used in Yan et al. (2011b) and an ENSO-like EOF derived from 20CRv2 results in very similar weights (0.6 and 0.4 respectively), and a timeseries virtually indistinguishable from the one produced by Yan et al. (2011b).

The effectiveness of the sparse PC reconstruction was initially tested using GCM data. Using model data from real proxy locations (Section 3.2.3.2 and Appendix A), a sparse PC was created, which was then compared to the full PC using Pearson's product moment correlation. As a preliminary experiment of the effect of proxy selection, two sets of proxies were used for temperature: one without tree rings, and one including the tree rings from the Mann et al. (2009) database. The sparse PCs were able to reproduce the full PC with varying accuracy (Table 3.5). The model BCC-CSM1-1 consistently performs worse than the others,

particularly for the historical and past1000 run in temperature. This may be linked to the lack of a clear ENSO signal in the first EOF (Section 3.2.3). The range of R -values (excluding BCC-CSM1-1) is 0.61–0.89 (0.14–0.89) for temperature without tree rings, 0.10–0.65 (-0.07–0.65) with tree rings, and 0.67–0.84 (0.36–0.84) for precipitation. It is notable that the temperature reconstructions with tree rings consistently perform worse. This is a strong indication that the selection of proxies is an important consideration, and that quantity does not equate to quality. Overall, however, these model sparse PC reconstructions suggest that with the right proxy network, it is possible to reconstruct the full PC with considerable accuracy.

Several aspects of real proxy data degrade this correlation. Firstly, the incomplete temporal coverage of proxy records is detrimental to the ability of proxies to reconstruct the PC. Moreover, low temporal resolution of some proxies degrades the ability to reproduce higher-frequency variability. Finally, many proxies have multivariate responses to climate, i.e. they are sensitive to more than one climatic variable (T, P, SSS, etc.). This confounds the signal of interest and thus increases noise levels. Sections 3.4.1 and 3.4.3 deal with these issues in more detail. It is important to reiterate that the sparse PC method aims to reconstruct the given EOF pattern, which here is the modern-day ENSO pattern. If the spatial characteristics of ENSO changed over time, this is not captured by this method.

3.3 Linking temperature, precipitation and ENSO

Before exploring relationships between climate and ENSO in the past, looking at modern-day and model data can provide indications of expected links and potential explanations. In preparation for the two studies presented in this thesis (Chapters 4 and 5), a thorough examination of links between precipitation, temperature, ENSO-like EOFs, and ENSO indices, was carried out. Four types of data were compared: observational, reanalysis, satellite, and model data. This section presents these comparisons with references to their relevance elsewhere in the thesis.

T no TR	piC	h	1k
CCSM4	0.82	0.80	0.75
BCC-CSM1-1	0.70	0.14	0.68
GISS-E2-R	0.77	0.61	0.70
MIROC-ESM	0.87	0.63	0.71
MPI-ESM-P	0.89	0.86	0.86
IPSL-CM5A-LR	0.88	0.72	0.86
T with TR	piC	h	1k
CCSM4	0.65	0.62	0.38
BCC-CSM1-1	0.44	0.11	-0.07
GISS-E2-R	0.49	0.31	0.10
MIROC-ESM	0.48	0.56	0.36
MPI-ESM-P	0.57	0.54	0.36
IPSL-CM5A-LR	0.49	0.34	0.28
P	piC	h	1k
CCSM4	0.82	0.81	0.84
BCC-CSM1-1	0.47	0.53	0.36
GISS-E2-R	0.72	0.69	0.69
MIROC-ESM	0.81	0.67	0.73
MPI-ESM-P	0.82	0.67	0.82
IPSL-CM5A-LR	0.76	0.80	0.75

TABLE 3.5: Correlations between full PC and reconstructed sparse PC six models. 'no TR' and 'with TR' refers to temperature proxy sets including and excluding the Mann et al. (2009) tree ring dataset (see Appendix A for proxy record information). piC refers to piControl, h refers to historical, and 1k is past1000.

3.3.1 20CRv2c temperature vs. precipitation

In addition to creating a proxy SOI (SOI_{pr}), Yan et al. (2011b) discuss apparent differences in the temperature and precipitation signals of ENSO in proxy records. They compare a range of ENSO reconstructions derived from proxies sensitive to temperature and to precipitation, and suggest that during the LIA and MCA the two sets show opposing behaviour. This stands in contrast to our current dynamical understanding of ENSO mechanisms, as we would expect both expressions of ENSO (precipitation and temperature) to behave similarly, not in opposing directions. This apparent discrepancy highlighted by Yan et al. (2011b) thus informs a key research hypothesis explored in Chapter 4 (see 1.1.2 and 4.1).

Using the ENSO-like EOFs identified in 20CRv2c, we inspect the modern-day

relationship between the ENSO signature in precipitation and temperature. The ENSO-like PCs are highly correlated, both for detrended ($R = 0.86$, $p < 0.001$) and undetrended ($R = 0.87$, $p < 0.001$) data. Observations of the present day thus also do not display the behaviour found by Yan et al. (2011b). This raises the question of how ENSO-like climate change is expressed in temperature and precipitation at different timescales, which is an issue explored in more depth in Chapter 4, and expanded to links between precipitation and fire regimes in Chapter 5.

3.3.2 GCM temperature vs. precipitation

Having identified the ENSO-like EOFs for the GCMs (Section 3.2.3), it is possible to similarly evaluate the coherence of precipitation and temperature ENSO-like variability in the model world. Results are in Figures 3.3 (detrended data) and 3.4 (undetrended data).

All models show high correlation between the ENSO-like temperature and precipitation PC ($R > 0.55$, $p < 0.001$) over all model runs, and using detrended and undetrended data. The high agreement between modelled temperature and rainfall expressions of ENSO is further confirmation of the observed relationship (Section 3.3.1) and the physical-dynamical expectation.

3.3.3 Indonesian P vs. ENSO

In Chapter 5, the focus shifts from the entire tropics and subtropics (40°S–40°N; Chapter 4) to the Indonesian region (100–200°E, 30°S–15°N). Here the interest lies in relationships between temperature, precipitation, ENSO and biomass burning. As for the entire tropics, comparisons are first done using modern-day data. Precipitation in Indonesia is known to be strongly influenced by ENSO on interannual timescales (Hendon, 2003). The study region of Chapter 5 encompasses some areas outside Indonesia, including the northern part of Australia and some of Southeast Asia. To explore the relationship between rainfall and ENSO over Indonesia and the wider study region, the regionally averaged modern-day precipitation data were compared to the three ENSO indices listed

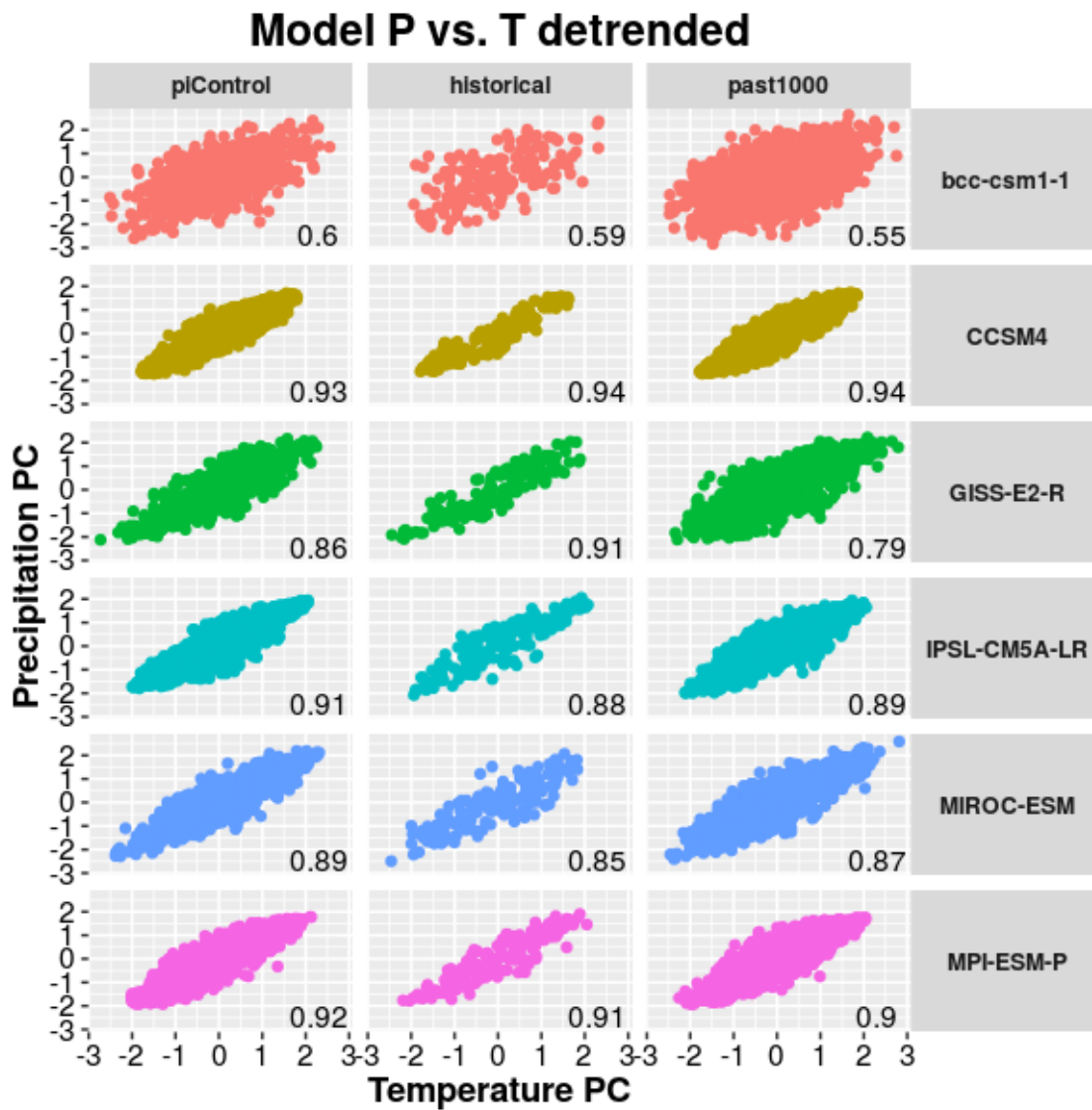


FIGURE 3.3: Comparison of ENSO-like precipitation and temperature in six GCMs over three model runs. R -values are shown in the bottom-right corner of each plot. PCs are PC1 for all models except for BCC-CSM1-1, which uses precipitation PC2 (Section 3.2.3).

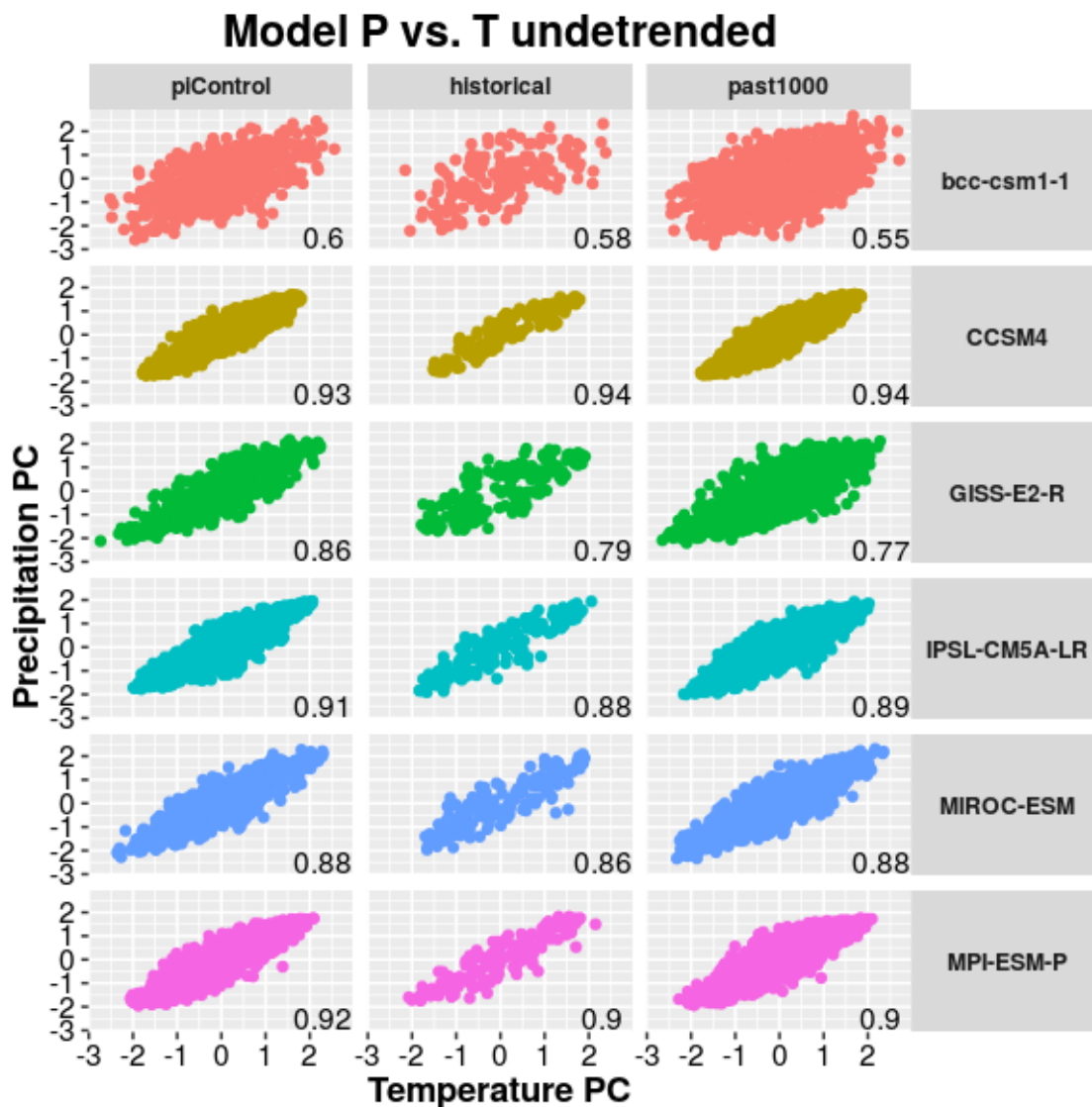


FIGURE 3.4: As Figure 3.3 but for undetrended data.

in 3.2.2 at annual resolution. In addition to the 20CRv2c precipitation data, the same comparison was done using data from the Global Precipitation Climatology Project (GPCP version 2.2; Adler et al., 2003, Huffman et al., 2009, data are available at <http://www.esrl.noaa.gov/psd/data/gridded/data.gpcp.html#>). This dataset, spanning AD 1979–2015, combines surface based and satellite precipitation observations at a resolution of $2.5^{\circ} \times 2.5^{\circ}$. As it does not rely on model infilling as 20CRv2c does, it is arguably a more accurate picture of modern precipitation. It is not used in the rest of this thesis, however, due to its short timespan (<30 years).

The GPCP data, reduced to annual resolution and averaged over Indonesia (90–145°E, 12°S–7°N), are significantly ($p < 0.05$) correlated with all three indices (Table 3.6). 20CRv2c shows similarly significant correlations, except for the MEI.ext, which is insignificant ($p > 0.05$). For the wider study region of Chapter 5 (100–200°E, 30°S–15°N), both datasets are significantly correlated with the MEI.ext and SOI, but GPCP shows an insignificant correlation with NINO3.4. The 20CRv2c correlation for NINO3.4 is also very low compared to the other indices, suggesting that the atmospheric influence of ENSO is stronger than the oceanic component over this region. Overall, these results confirm that on annual timescales, precipitation over the Indonesian region is significantly reduced during El Niño events in the modern day.

Region	Dataset	MEI.ext	NINO3.4	SOI
Indonesia	20CRv2c	-0.16*	-0.63	0.27
	GPCP	-0.85	-0.59	0.88
Study region	20CRv2c	-0.48	-0.22	0.37
	GPCP	-0.76	-0.16*	0.67

TABLE 3.6: Correlations (Pearson product-moment correlation coefficient R) between regionally averaged annual precipitation and ENSO indices for Indonesia and the study region of Chapter 5 (see text for coordinates). Starred R -values are insignificant ($p > 0.05$).

3.4 Pseudoproxies

Section 3.2 introduces the concept of multiproxy reconstructions, and provides an initial glimpse into using model data to test methods and hypotheses using simulated proxies (Section 3.2.4). This section expands on the use of such simulated (or pseudo) proxies, and describes in more detail the techniques used in this thesis to create more realistic pseudoproxies.

For a proxy record to be useful, it is paramount that the impact of the environmental driver of interest on the proxy is strong enough so as not to be obscured by non-climatic noise (e.g. changes related to the age of the proxy organism). Moreover, the relationship must be understood well enough to interpret the proxy – is it linear, does it saturate at high levels, is there a lower limit? Is it univariate

or do multiple factors influence the proxy? Another constraint on the utility of a proxy record is the way it is measured (how high is the resolution? Are measurements contiguous, discrete, aggregate?) and dated (how many dating tie-points are there? What is the accuracy of the method? What assumptions are made about sedimentation/accretion/growth rates when making the age model?).

Proxy reconstructions contain errors from various stages. A single proxy contains errors from the proxy response to the climatic variable (e.g. response of a tree to higher temperatures), to how this is translated into a physical manifestation that can be measured (tree ring width), and to how this is observed (ring counting). This includes dating errors, biological or other non-climate influences, local environmental processes, nonlinear and/or multivariate responses to climate, sampling methods, and measurement error (Dee et al., 2015, Evans et al., 2013). In a multiproxy reconstruction, there are additional errors through spatial and temporal sampling sparsity and the representativeness of calibration targets. In other words, having proxies in the right locations and recording at the right temporal resolution matters, and the observational data that the network is calibrated to must be assumed to be truly representative of the climate phenomenon back in time.

Pseudoproxies enable us to test these assumptions and the effectiveness of methods using more realistic (i.e. spatiotemporally imperfect) data. They emulate the limitations of real proxy data, and can be altered in any way desirable to evaluate the impact of one or multiple error sources. Pseudoproxies are generally created from observational or model data by extracting timeseries (at random or at real proxy locations), and degrading the signal to reflect errors in the real proxy data. Their power lies in the fact that the 'true' target climate is known (i.e. the dataset the timeseries is extracted from), which enables concrete comparisons with the pseudoproxy reconstructions.

The complexity of pseudoproxies ranges from adding stochastic (white Gaussian) noise to reduce the signal-to-noise (SNR) ratio, to applying complex transformations to simulate nonlinearities and multivariate responses; the latter is described more detail in 3.4.1. The basic process of using pseudoproxies to evaluate the effectiveness of a method, as is done in Chapter 4, follows the format:

1. Sample from realistic proxy locations

2. Degrade the signal
3. Apply reconstruction method to reproduce 'true' climate
4. Compare to known model/observational target dataset

In the method applied in 4, pseudoproxies are used to select the optimal combination of proxies for use in the actual reconstruction. As such, having pseudoproxies with realistic SNRs, temporal resolution and length is important. The process of applying realistic temporal resolution and length is described in 4 as it is relatively straightforward. The following sections will describe and discuss the more complex issues of dealing with multivariate and nonlinear responses (Sects. 3.4.1 and 3.4.2) and SNR (Section 3.4.3).

3.4.1 Proxy System Models

An important recent development in the pseudoproxy community is the development of proxy system models (PSMs). These models attempt to characterise and simulate the processes that link the climate, the proxy and its measurement, providing a mechanistic understanding of how to interpret the proxy record and the various sources of error. This goes beyond the use of empirical transfer functions, which have been widely used for decades (Sachs et al., 1977). Rather than relying on such empirical equations derived from spatial correlations between proxies and climate, PSMs are forward models – i.e. the underlying physical processes are understood and constrained realistically (Evans et al., 2013). This enables a better understanding of nonlinear and multivariate responses of proxy records to environmental stimuli, and therefore provides a more realistic pseudoproxy testing ground for characterising error sources.

Several PSMs have been developed to deal with different proxy types, including models of coral $\delta^{18}O$ (Thompson et al., 2011), ice core $\delta^{18}O$ (cf Vuille et al., 2003), speleothem dripwater $\delta^{18}O$ (cf Truebe et al., 2010), and tree ring widths (Section 3.4.2; Evans et al., 2014, Tolwinski-Ward et al., 2013, 2011, Vaganov et al., 2011). Due to the *ad hoc* creation of PSMs, they can be difficult to implement and combine in different programming environments. A recent endeavour has attempted to address this issue by creating an integrated framework (PRYSM; Dee

et al., 2015) into which the various PSMs can be assimilated for consistency and ease of use.

Many proxies employed in Chapter 4 are isotopic ratios, which require isotope-enabled GCMs to simulate them. While there are several such models available (Xi, 2014, and references therein), none of the GCMs used in this thesis (Section 3.2.3) provide this. The nature of the method set out in Chapter 4 requires the availability of the different model runs (historical, past1000), as well as a combination of different models. Since this cannot be provided by isotope-enabled GCMs, the use of PSMs is limited to non-isotopic proxies in this thesis.

3.4.2 Pseudo-tree ring widths using VS-Lite

There is a wealth of tree ring proxies located within the study region of Chapter 4, with a very high concentration in North America (Appendix A). As modelling these does not require isotope-enabled GCMs, we explore the use of PSM-derived tree ring widths for use in Chapter 4. VS-Lite (Breitenmoser et al., 2014, Evans et al., 2014, Tolwinski-Ward et al., 2013, 2011) is a simplified version of the full Vaganov-Shashkin (VS) model (Vaganov et al., 2011, 2006). The full model simulates climate-induced tree ring growth using daily temperature, light, and soil moisture as inputs coupled with a representation of cambial activity and wood formation. VS-Lite uses monthly climatic data input and does not incorporate the (mechanistic) cell-level biological processes. It retains the (parametric) climatic threshold growth response functions and limiting factors, however, which capture the non-linear response of tree ring growth (Fritts, 2001). It is designed to run quickly with minimal inputs compared to the full model; the only requirements for running VS-Lite are latitude, monthly precipitation (or soil moisture) and monthly temperature inputs. If soil moisture is not provided, it is calculated from precipitation and temperature using the empirically tuned National Oceanic and Atmospheric Administration (NOAA) Climate Prediction Center “Leaky Bucket Model” (Huang et al., 1996, van den Dool, 2003). Through this model, empirical relationships are used to estimate evapotranspiration, runoff, and groundwater flow, which are then used in conjunction with precipitation and soil moisture at time $t - 1$ to calculate soil moisture at time t (Tolwinski-Ward et al., 2011).

MATLAB source code is freely available at the NOAA Paleoclimatology World Data Center (<ftp://ftp.ncdc.noaa.gov/pub/data/paleo/softlib/vs-lite/>); R source code (used in this thesis) can be found at <https://github.com/suztolwinskiward/VSLiteR>. Corrections to the R code are available in Appendix C.1 The tree ring width (TRW) datasets produced by VS-Lite include annual TRW as well as monthly moisture and temperature growth responses (gM and gT, respectively), which provide information on the limiting climatic factor on tree growth. The overall limiting factor is determined by the point-wise minimum over the growing season (May–September for NH, November–March for SH). More detail on the workings of VS-Lite can be found in Tolwinski-Ward et al. (2011).

A full TRW dataset was created using VS-Lite for the entire study region of Chapter 4 for 20CRv2c and each GCM, using their respective precipitation and temperature datasets. General characteristics of these datasets are described here. Figure 3.5 shows the correlation between the 20CRv2c TRW dataset and the original precipitation (top) and temperature (bottom) data, at tree ring proxy locations. Figure 3.6 shows the equivalent for each of the six GCMs. These correlations should be taken as an indication of how much these two climate variables contribute to the modelled TRW, rather than a direct indication of the sensitivity of TRW to the climate variables. TRW at the tree ring proxy locations is generally more strongly correlated with (i.e. more strongly influenced by) temperature than precipitation in both 20CRv2c and the GCMs. For most locations, TRW is positively correlated with temperature, and negatively correlated with precipitation (Figure 3.7). There is good agreement between the models in terms of median correlation and interquartile range, especially for temperature. IPSL-CM5A-LR deviates most from the others, giving weaker correlations for both precipitation and temperature. The negative correlation with precipitation is surprising, since an increase in moisture is often associated with increased tree growth. A possible explanation for the negative correlations observed here is if low precipitation tends to be accompanied by higher temperatures, and tree growth is mostly temperature limited. In this case, periods of high precipitation are associated with low tree growth due to the limiting effect of the accompanying low temperatures, rather than the direct effect of the moisture. This hypothesis is qualitatively supported by the strong positive correlations between TRW and temperature (Figure 3.7), although more in-depth analysis is needed to unpack these relationships further.

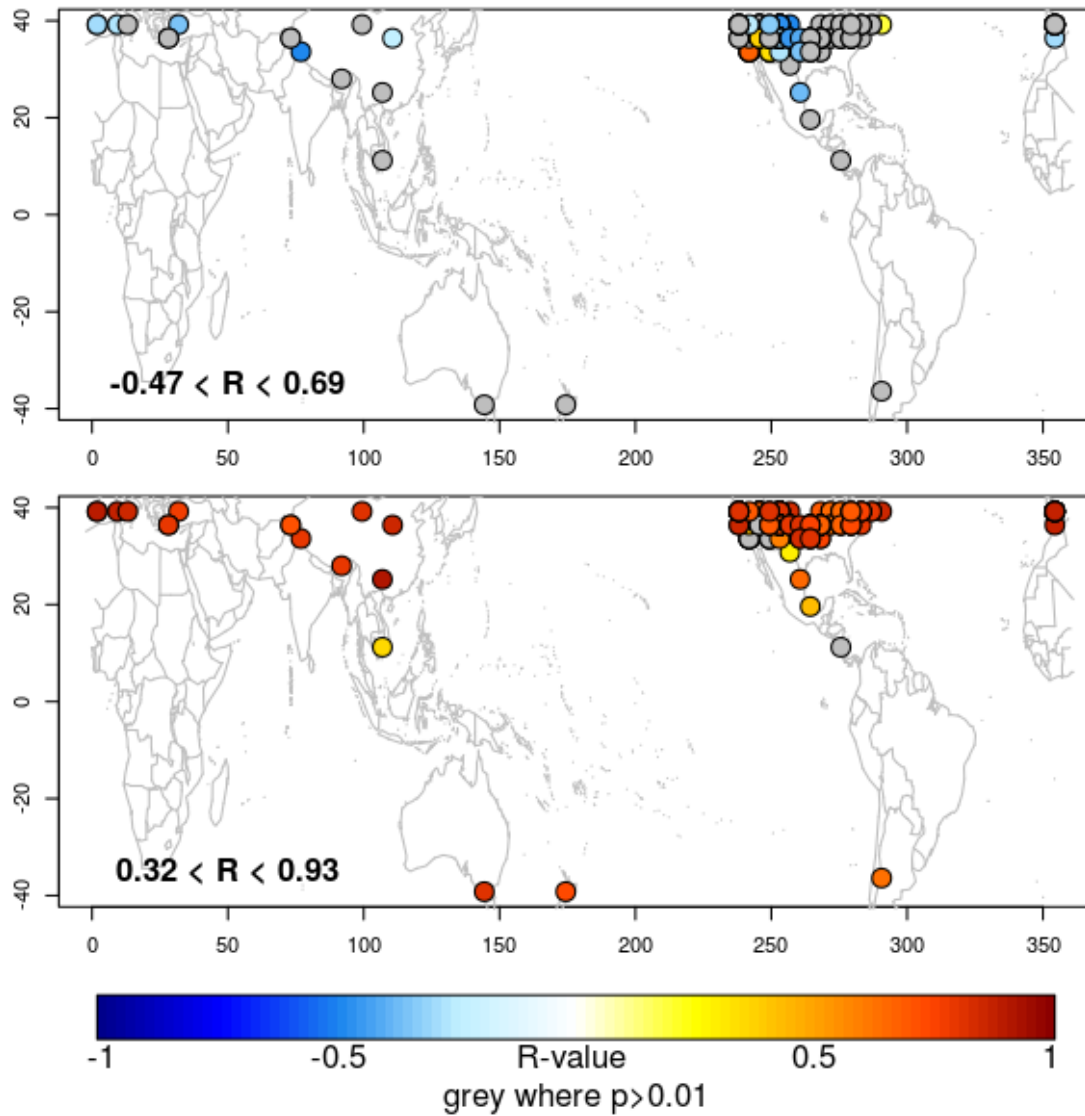


FIGURE 3.5: 20CRv2c TRW correlations with P (top) and T (bottom) at proxy tree ring locations (see Appendix A). The range in R -values is indicated in the bottom left corner. Locations where the correlation was insignificant are denoted by grey points.

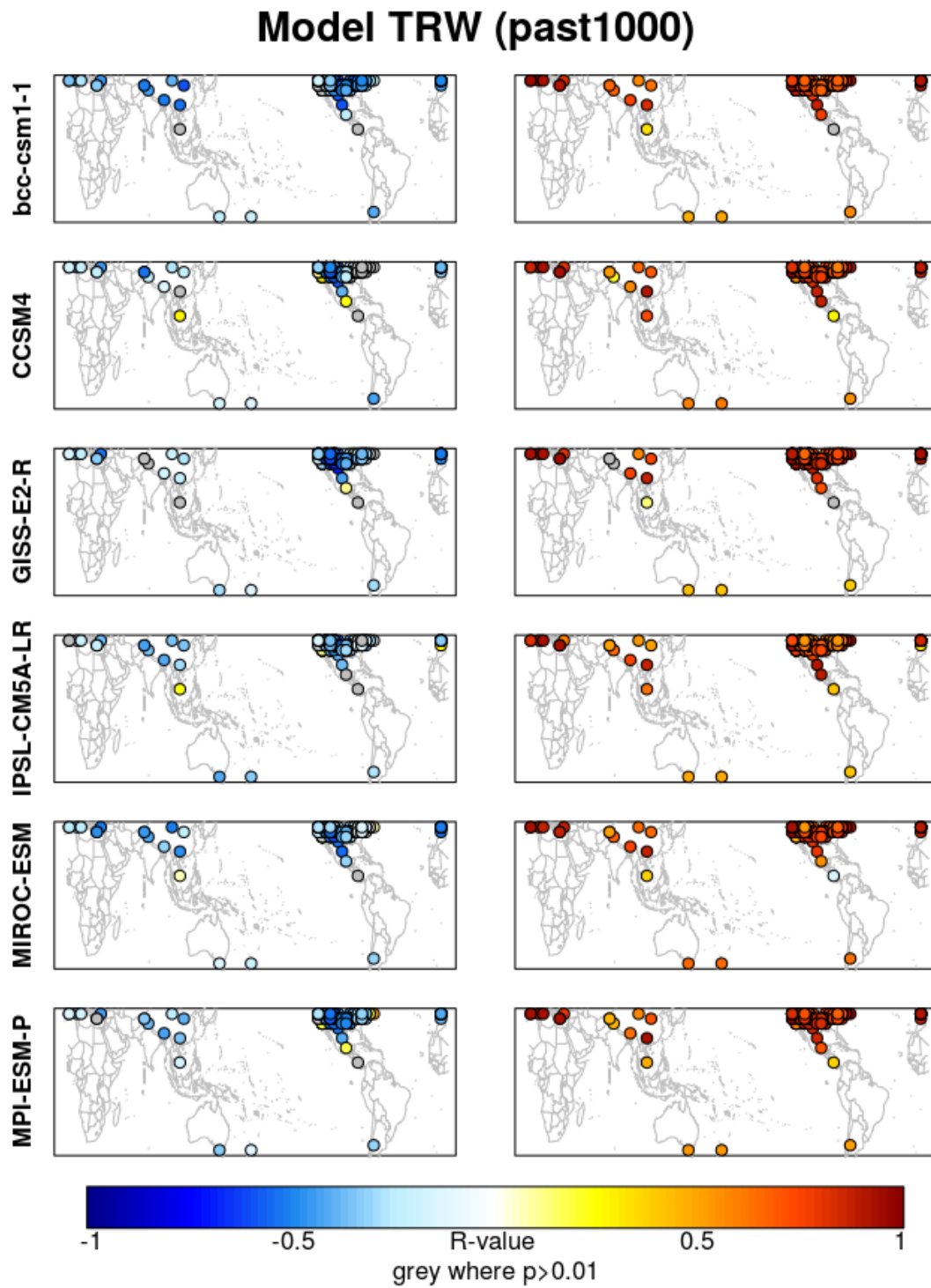


FIGURE 3.6: Model TRW correlations with P (left) and T (right) for the past1000 run of six GCMs at proxy tree ring locations (see Appendix A). Locations where the correlation was insignificant are denoted by grey points.

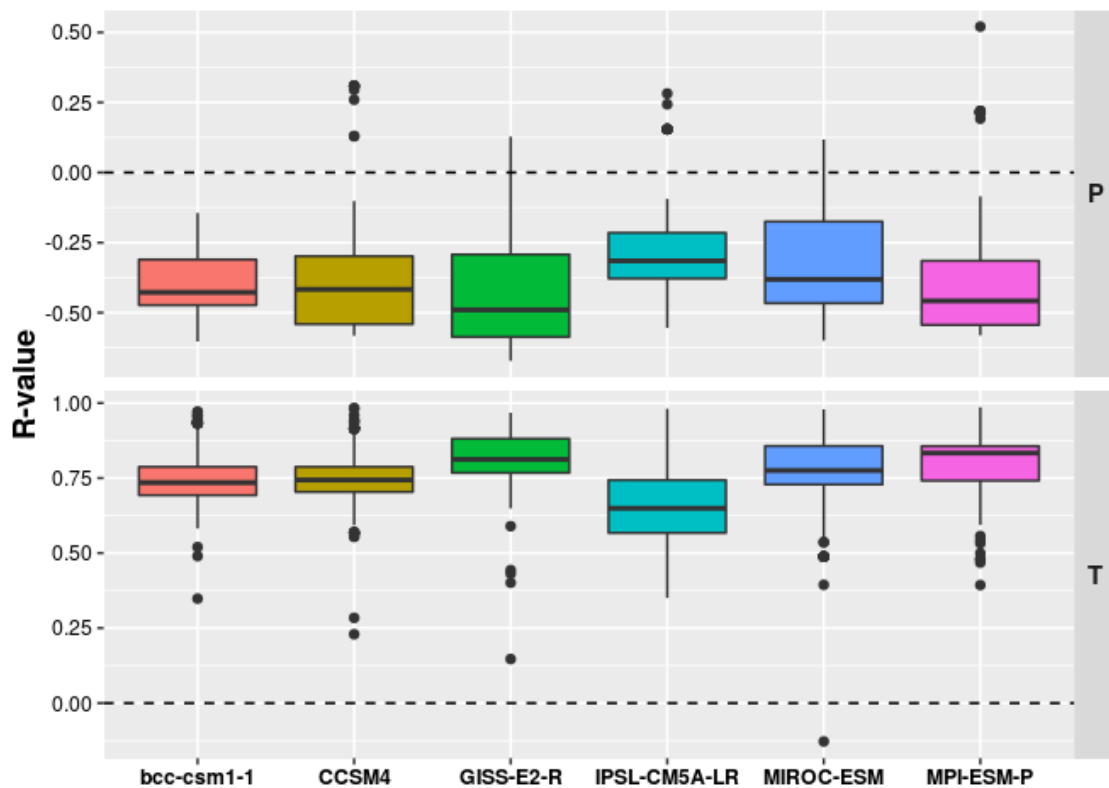


FIGURE 3.7: Overview of correlations of simulated TRW with raw precipitation (top) and temperature (bottom) data at proxy tree ring locations, across six GCMs. TRW is simulated using the past1000 run.

3.4.3 Signal-to-noise ratios

As 3.4 outlines, degradation of the signal is a crucial part of the pseudoproxy creation process. The most common approach is to reduce the signal-to-noise ratio (SNR) by adding some form of noise to the pure signal (i.e. observational/model timeseries). The noise structure can range from 'blue' (skewed to high-frequency) to 'white' to 'red' (skewed to low-frequency), but the most common type is white Gaussian noise (Smerdon, 2012). The noise serves to mimic non-climatic sources of variability in the observed proxy record that may obscure the climate signal.

The pseudoproxies created in Chapter 4 are based on a wide variety of proxy types. Every proxy record has a different SNR, determined by factors including location, proxy type, and local environment. Ideally, each corresponding pseudoproxy would be degraded accordingly, but this is not always feasible. Firstly, not all original publications of the proxy records provide information on the SNR.

Secondly, SNR may vary on different timescales, with some proxies preferentially reflecting climatic variability on seasonal, annual or decadal timescales (cf Felis et al., 2000, Linsley et al., 2006). Moreover, it is difficult to determine SNR for low-resolution records as instrumental records (the target datasets from which SNR would be calculated) are relatively short and thus poorly characterise the long-term variability captured by these low-resolution proxies. In lieu of individualised SNRs, it is therefore more expedient to implement a generic SNR to these proxies. Several studies suggest that an SNR value of 0.4 is a fairly conservative realistic value for most proxies (Mann, 2002, Smerdon, 2012).

A notable collection of SNR indications is the extensive coral dataset presented in Tierney et al. (2015), most of which is incorporated in the proxy dataset used in this thesis (Appendix A). The authors systematically compare coral proxy records to the Hadley Centre Global Sea Ice and Sea Surface Temperature (HadISST) dataset spanning 1900-1990, enabling the calculation of SNRs for each record. This coral dataset allows us to evaluate the appropriateness of the generic SNR value of 0.4. Table 3.7 provides a summary of the absolute coral R -values (excluding those which gave physically implausible values; see Tierney et al., 2015, and Appendix A). An SNR of 0.4 corresponds to an R -value of $\sim \pm 0.38$, which is comparable to the coral mean value of 0.44 in Table 3.7. This suggests that the generic SNR value is indeed a reasonable average. The caveat here is that the Tierney et al. (2015) database only represents coral records, which may not be representative of all other proxy types. The reported R -values of other proxies in our dataset tend to be higher (mean absolute R -value of 0.62; Table 3.7), which is closer to an SNR of 0.6. The estimate of 0.4 is thus a conservative estimate.

Proxy subset	Min	1st Qu	Med	Mean	3rd Qu	Max
Tierney et al. (2015)	0.10	0.28	0.44	0.41	0.56	0.72
Other reported	0.28	0.51	0.61	0.62	0.74	0.92
All	0.10	0.32	0.50	0.52	0.64	0.92

TABLE 3.7: Summary of R -values for proxy records used in this thesis. The Tierney et al. (2015) coral records are compared to HadISST; coral records with physically unrealistic (i.e. positive) values were excluded from the overview and the rest of this thesis. 'Other reported' refers to other proxy records for which an R -value is provided in the original publications; these values are thus calculated using a variety of observational datasets. 'All' is the combination of the above two proxy subsets.

3.5 Proxy transformations

As 3.4 illustrates, proxies are derived from a wide range of sources, each with individual strengths and limitations. When performing multiproxy analyses, it is important to ensure that all proxies are comparable. This generally means establishing a common unit, particularly when combining proxies from different archives. In practice this usually means standardising the records to unit-less anomalies with respect to a common period.

Another issue with proxy timeseries is that many are non-parametric in nature, which can pose many problems when interpreting and comparing them as it violates the assumption of normality integral to many statistical methods. There are various possible reasons behind this non-normality, including:

1. natural limits. Lake sediment influx cannot be negative, regardless of how strongly the climatic driving factor deviates.
2. saturation. Tree ring width may be primarily driven by temperature, but at optimal levels eventually other limiting factors (like nutrients) will prevent infinite growth.
3. non-linear response. A coral may grow fastest within a specific temperature range, but slow down at cooler or warmer temperatures, leading to a (potentially skewed) bell-shaped response curve.

To overcome this issue, the records can be 'normalised' to approach a Gaussian distribution.

Proxy temporal resolution is a third potentially significant aspect to consider in multiproxy syntheses. Two questions must be considered: what is the lowest proxy resolution available, and what is the resolution we are interested in? In this thesis, the two methods used to strike a balance between these two questions are binning – taking weighted or simple averages over discrete bins – and smoothing – applying a spline function to capture lower-frequency variations. Binning and smoothing methods also partly mitigate issues related to the accuracy of age estimates. In Chapter 4 the issue of dating error is further addressed by limiting proxy selection to those with a dating error of less than 60 years.

Section 3.5.1 sets out the standardisation methods used in this thesis, followed by a description of two methods used to 'Gaussianise' skewed proxy records (Sects. 3.5.2 and 3.5.3). Sections 3.6.1 and 3.6.2 expand on the issue of different temporal resolutions. Finally 3.6.3 explores general additive (mixed) models (GA(M)Ms), and provides justifications for the choices made in their application in Chapter 5.

3.5.1 Minimax and Z-score transformations

Since proxy sampling methods vary widely and values are reported in different units, multiproxy data must first be standardised. The two methods used in this thesis are minimax rescaling and Z-score conversion.

The former rescales the values of each record c to fall between 0 – 1:

$$c'_i = \frac{c_i - c_{min}}{c_{max} - c_{min}} \quad (3.13)$$

where c'_i is the minimax-transformed value of the i^{th} sample of c , and c_{min} and c_{max} are the maximum and minimum values of c respectively. As it ensures all values are positive, it enables the implementation of various further statistical techniques. In Chapter 5, it is applied to charcoal records in preparation for the Box-Cox transformation (Section 3.5.2).

The Z-score calculation is the conversion of data series to unit-less anomalies with respect to a specified period, over which the mean has a value of 0 and the standard deviation is 1:

$$z_i = \frac{c_i - \bar{c}_n}{\sigma_n} \quad (3.14)$$

where z_i is the Z-score for the i^{th} sample, \bar{c}_n is the mean of series c over the base period n , and σ_n is the standard deviation over the same base period. By setting the same base period for all proxies, they become comparable and can be combined. It is important to select a period that is long enough with respect to the

resolution of the proxies. If it is too short, there is a possibility that noise in the series will dominate the standard deviation, leading to a squashing or amplification of the series.

3.5.2 Box-Cox transformation

The Box-Cox power transformation (Box & Cox, 1964) is a statistical transformation method which serves to homogenise the variance of the data:

$$c_i^* = \begin{cases} \frac{(c_i + \alpha)^\lambda - 1}{\lambda} & \text{if } \lambda \neq 0 \\ \log(c_i + \alpha) & \text{if } \lambda = 0 \end{cases} \quad (3.15)$$

where c^* is the Box-Cox transformed series, α is a small positive constant to avoid singularity when c_i and the transformation parameter λ are both zero, and transformation parameter λ is estimated by maximum likelihood (Venables & Ripley, 2002).

While Box-Cox transformed series will have similar (Gaussian) distributions, they are only comparable when the value of λ is the same for each one (Power et al., 2008). This can be achieved by applying the minimax transformation described above (Section 3.5.1), and is implemented in Chapter 5.

The Box-Cox transformation is a popular method in many areas of data analysis (Sakia, 1992). It is the standard approach for normalising charcoal data used for palaeo-fire reconstructions (Blarquez et al., 2014, Daniau et al., 2012, Marlon, 2016, Power et al., 2008, Vanniere et al., 2011) and has also been applied in other palaeo-reconstruction procedures (cf Henley et al., 2011). Various alternatives and adaptations have been suggested to address limitations of the Box-Cox transformation (Sakia, 1992), including accommodating negative observations (Manly, 1976), dealing with approximately symmetric but long-tailed distributions (John & Draper, 1980), improving the robustness of the transformation parameter λ estimation procedure (Bickel & Doksum, 1981), and simpler transformations to focusing on variance, skewness or kurtosis individually (Withers & Nadarajah, 2013). An alternative method applied in this thesis (Chapter 4) is inverse transform sampling (ITS), which is described in the next section.

3.5.3 Inverse transform sampling

ITS is a simple non-parametric, quantile-based transform that can be applied to any data type (van Albada & Robinson, 2007). It is based on the fact that for any continuous variable, the cumulative distribution function (CDF) is uniformly distributed over $(0, 1)$ regardless of the distribution of the variable itself (Rosenblatt, 1952). The basic concept is to calculate the CDF of a variable and invert it. The transformation takes the following form for variable c :

$$y(c) = \mu + \sigma\sqrt{2}\text{erf}^{-1}[2P_x(x) - 1] \quad (3.16)$$

where μ is the desired mean, σ is the desired standard deviation, $P_x(x)$ is the indefinite integral of probability density $p_x(x)$, and erf is the error function:

$$\text{erf}(x) = \frac{2}{\sqrt{\pi}} \int_0^x e^{-t^2} dt \quad (3.17)$$

While there are more accurate Bayesian approaches for normalising variance, ITS is preferable when considering the trade-off between performance and ease of use (Emile-Geay & Tingley, 2016). It is less likely to be influenced by outliers than the Box-Cox transform and is non-parametric, making it more appropriate for a range of different proxy types. Regardless of the normalisation method applied, it must be kept in mind that the quality of transformed data will still be limited by the information held in the original series. If there is a natural upper or lower limit in the proxy response (e.g. no negative values of influx), the transformation will similarly lack information at these points. MATLAB source code for an ITS procedure developed by Emile-Geay & Tingley (2016) can be found at <https://github.com/CommonClimate/common-climate/blob/master/gaussianize.m>. For the analyses described in this thesis it was translated into R; this script is available in Appendix C.2.

3.6 Smoothing methods

When working with palaeodata, it is common to have samples that are unevenly spaced in time, either within a single record or between records. This can pose issues for certain statistical methods; high-resolution records may dominate the resultant reconstruction as they contribute more data points, while low-resolution records can impose a degree of artificial smoothing. Various smoothing methods are applied throughout this thesis, and are expounded in this section.

3.6.1 Binning

A straightforward approach to homogenise the resolution of a timeseries is to divide it into time-slices ('bins') of a set width and calculating the mean of all the values falling within the bin. The bins can be overlapping (e.g. 10-year bins defined every 5 years) or discrete (10-year bins every 10 years). The latter is also useful to reduce autocorrelation, and is used for that purpose in 5.2.4. The bin means can be calculated using a simple or weighted average. A simple average is a special form of weighted average, where every sample is assigned an equal weight of 1. When samples are unequally spaced, however, this may not be desirable. If, for example, one bin has many samples near one end of the bin, this would result in a skewed representation of the bin. Weighted averaging takes into account the distance of each sample from the centre of the bin, giving a more accurate estimate of the real mean. There are various ways to weight the samples, but a commonly used function is the tricube function (Cleveland, 1979):

$$W(z) = \begin{cases} (1 - |z|^3)^3 & |z| < 1 \\ 0 & |z| \geq 1 \end{cases} \quad (3.18)$$

where $z = (x_i - x)/h$, x_i is a data point along the time dimension within the window $(x - h, x + h)$, x is the centre of the bin, and h is the half-width of the bin. The tricube weight function assigns high weights to data points x_i near x , and low weights to points near the boundaries $x \pm h$.

The implementation of a binning procedure can also be used to synthesise multiple proxy records (e.g. Blarquez et al., 2014, Power et al., 2008). In this case,

the same bins are applied, and means are calculated, across all records to create a single binned series. This method assumes that all series are comparable, i.e. they are calibrated to the same period and have the same units. In terms of physical interpretation, it is also prudent to ensure that all timeseries are expected to show similar behaviour in the variable of interest; this can mean looking at the environmental homogeneity of the region, for example.

Other factors that influence the results of a binning procedure include bin width and the positioning of the bins. The effect of these two factors were explored using the precipitation and charcoal data used in Chapter 5. Using the `pfComposite` function from the `paleofire` package in R (Blarquez et al., 2014), the data were synthesised into binned composite curves with bin widths ranging between 10 and 200 years (Figure 3.8). The larger the bin width, the higher the degree of smoothing as more datapoints are averaged out per bin. When calculating correlations between the binned fire and precipitation series in Figure 3.8, the bin width has a strong impact on the statistical significance of the correlations regardless of the strength of those correlations. This is to be expected, as the degrees of freedom decreases with increased bin width.

To evaluate the effect of the start date of the bins, the same data were composited using 100-year bins but with shifting starting points; the upper boundary of the most recent bin was shifted from -50yrBP (i.e. bin centre at 0yrBP) to 100yrBP (centred at 150yrBP). Figure 3.9 shows the resultant composites. It is clear that the placement of the bins affects the strength of some peaks and troughs depending on which bin certain data points fall into. This effect becomes less visible as the bin width increases and the number of data points in each bin increases (not shown).

3.6.2 LOWESS smoothing

It is commonplace in palaeoclimatology to smooth data series in order to evaluate lower-frequency variability. While binning methods provide a form of smoothing, they may either artificially reduce variance as strongly deviating data points are 'lost' in the averaging process, or exaggerate excursions where an anomalous sample skews the bin average. A more sophisticated, widely used method for smoothing is the non-parametric LOcally WEighted Scatterplot Smoothing

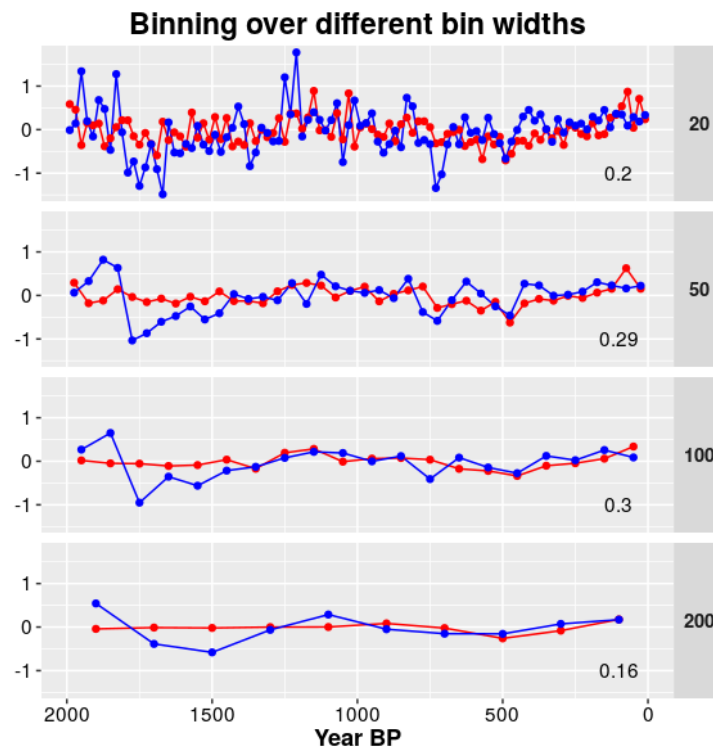


FIGURE 3.8: Binned precipitation (blue) and charcoal (red) composites using bin widths of 20, 50, 100 and 200 years. R -values of the correlation between the two series is shown in the bottom right hand corner of each plot.

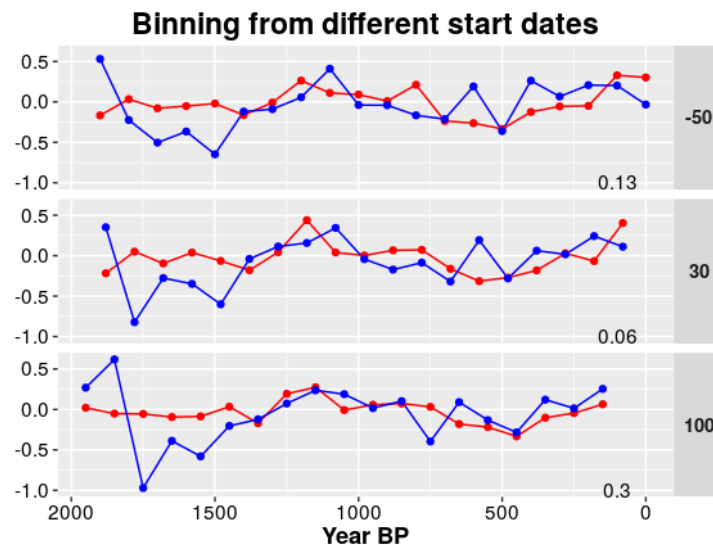


FIGURE 3.9: 100-year binned precipitation (blue) and charcoal (red) composites setting the start date of the most recent bin to -50yrBP, 30yrBP and 100yrBP. R -values of the correlation between the two series is shown in the bottom right hand corner of each plot.

(LOWESS) regression (Cleveland, 1979). This essentially applies a regression to a subset of the data determined by a smoother span (which indicates the fraction of data points to be included in each subset) or a window width (which indicates the timespan for each subset). In series with non-homogeneous sample distribution, these two will vary as high-resolution sections will result in more LOWESS estimations when using the smoother span.

For each subset, the data points are weighted according to their proximity to the target point (the window centre), and a linear weighted least squares regression is fitted. The final LOWESS curve is created by retaining the fitted value at each target point. Similar to the approach in 3.6.1, the weighting function can vary. The standard is a tricube weighting function (Eqn. 3.18), and is used in the analyses described in this thesis (Chapter 5).

The LOWESS procedure is flexible, as it is data-driven rather than relying on a pre-specified function like classical non-linear regressions do. As the locally fitted polynomial is usually of first or second degree, it is less prone to biases that plague other kernel methods (Hastie & Loader, 1993, Loader, 1999). However, the local fitting also means it is not mechanistic and the resultant regression cannot be transferred or extrapolated to other datasets. Moreover, the data density must be sufficient to provide a good smooth. It is thus important to (often empirically) select an appropriate smoothing window.

In Chapter 5, proxy precipitation and charcoal records are synthesised into smoothed composites. The data are first pre-binned to homogenise the temporal resolution (3.6.1) before being combined and LOWESS smoothed. The width of the pre-binning windows and the LOWESS smoothing window can both affect the resultant composites; pre-binning reduces the effective number of data points fed into the LOWESS, while the smoothing window alters the strength of the fit (i.e. the over- or under-smoothing). Figure 3.10 shows the effect of the pre-binning width. The same dataset is pre-binned to bins ranging from 5 to 100 years, and LOWESS smoothed using a 200-year window. As the bin width increases, the number of data points decreases and the smoothness of the LOWESS curve is degraded, suggesting increasing over-fitting. The curves also flatten out, suggesting the the larger bins over-smooth the data leading to loss of information. The effect of LOWESS smoothing window width is illustrated in Figure 3.11. Here the

data are pre-binned to 20 years and subsequently smoothed using windows ranging between 20 (essentially no smoothing) and 200. The smaller windows result in very spiky curves, indicating under-smoothing. In this case, a minimum window width of 50-60 years would be recommended, as this is where the curves become smooth. After this point it is a case of determining the resolution of interest, as larger windows highlight the robust lower-frequency trends.

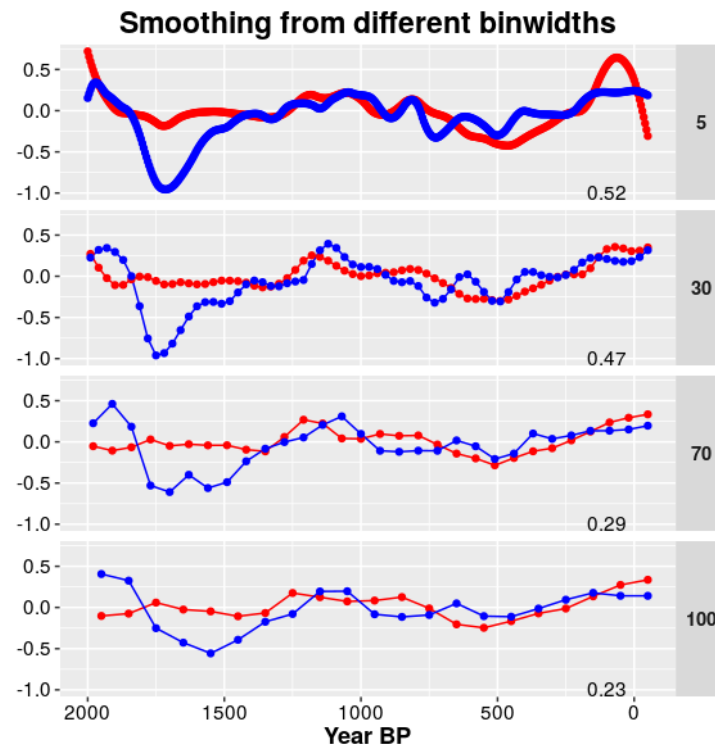


FIGURE 3.10: 200-year LOWESS smoothed precipitation (blue) and charcoal (red) curves using pre-binned data with bin widths of 5, 30, 70 and 100 years. R -values of the correlation between the two series is shown in the bottom right hand corner of each plot.

3.6.3 GAM and GMM spline fitting

3.6.3.1 GAM

A relatively recent smoothing technique to be used in the palaeocommunity is the generalised additive model (GAM; Hastie & Tibshirani, 1990, Wood, 2006). Combining properties of generalised linear models (GLMs) and additive models, it uses smoothing splines to relate predictor variables to the response variable. The

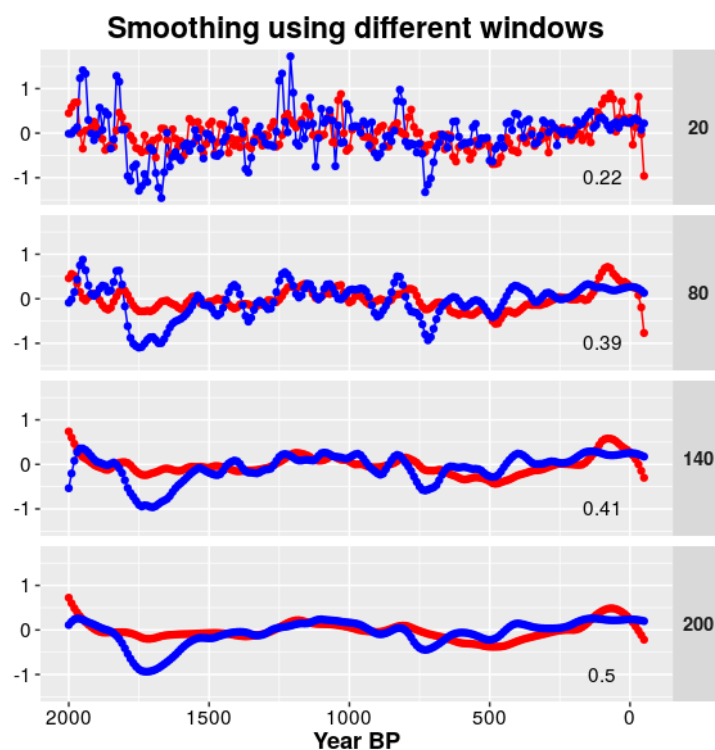


FIGURE 3.11: LOWESS smoothed precipitation (blue) and charcoal (red) curves using window widths of 20 (i.e. no smoothing), 80, 140 and 200 years. Original data are pre-binned to 20 years. R -values of the correlation between the two series is shown in the bottom right hand corner of each plot.

mathematical explanations below heavily derive from Hastie & Tibshirani (1990) and Wood (2006), unless otherwise indicated.

GLMs are an extension of regular least squares regressions, allowing for non-parametric relationships – i.e. data responses can be distributed non-normally. It does this by introducing a link function g , which transforms the response Y from a non-normal (e.g. logarithmic) distribution to a normal one. An ordinary linear regression is a special case of a GLM, with g being the identity function. A basic GLM takes the following form:

$$g(\mu_i) = \mathbf{X}_i\boldsymbol{\beta} \quad (3.19)$$

Where $\mu_i \equiv \mathbb{E}(Y_i)$, \mathbf{X} is a model matrix with i rows and the vector $\boldsymbol{\beta}$ contains unknown parameters. Response variable $Y_i \sim$ some exponential family distribution and is independent. In addition to Normal, the exponential family distribution

could be Poisson, Binomial, or Gamma.

GAMs are the additive equivalent of GLMs, generalising additive models to allow for non-parametric response distributions. The general structure of a GAM is:

$$g(\mu_i) = \mathbf{X}_i^* \boldsymbol{\theta} + \sum_{j=1}^p f_j(\mathbf{X}_j) + \varepsilon \quad (3.20)$$

Where

$$\mu_i \equiv \mathbb{E}(Y_i) \sim \text{some exponential family distribution} \quad (3.21)$$

In this case, model matrix \mathbf{X}^* contains any strictly parametric model components, and $\boldsymbol{\theta}$ is the corresponding parameter vector. Predictor variables \mathbf{X}_j are smoothed by arbitrary smoothing functions f_j . While GAMs provide more flexibility by only specifying ‘smooth functions’ rather than parametric relationships, it introduces two new considerations: how to represent the smooth functions, and the degree of smoothing.

The smoothing function is usually represented by a penalised regression spline. A spline is essentially a set of locally fitted polynomials joined together at ‘knots’ where they are equal in value and first two derivatives. The number and location of knots must be empirically determined; while different types of splines deal differently with knot placement, they are generally equally spaced either based on the range of x values, or based on quantiles. The number of knots controls the flexibility of the spline, modulating the degree of fitting to the data. Depending on the dataset, knot placement can also significantly impact the shape of the fitted model.

Once the number of knots is determined, the degree of smoothness is controlled by adding a penalty for the ‘wiggleness’ of a model by minimising:

$$\lambda \int_0^1 [f''(x)]^2 dx \quad (3.22)$$

The smoothing parameter λ determines the balance between model fit and smoothness; a low λ may result in undersmoothing, and a high λ may lead to oversmoothing. The choice of smoothing parameter can be determined in various ways including Akaike's information criterion (AIC), generalised cross validation (GCV) or, as is done in Chapter 5, residual/restricted maximum likelihood (REML) estimation. The latter takes a more Bayesian approach by treating smooth components as random effects to calculate maximum likelihood. For brevity, the mathematics of REML estimation will not be discussed further here (see Kimeldorf & Wahba, 1970, Wahba, 1985, for more detail); importantly, it has been shown that REML is preferable to GCV as it is less likely to get 'trapped' in local minima and to overfit (Reiss & Todd Ogden, 2009, Wood, 2011).

The smoothing spline employed in Chapter 5 is a low-rank thin plate regression spline (Wood, 2003), which is a truncated version of the full thin plate regression spline (Duchon, 1977) using eigendecomposition. The truncation makes it more computationally efficient for large datasets, and also avoids the issues of knot placement that plagues 'conventional' regression splines.

3.6.3.2 GAMM

Where data are autocorrelated, the fitting of a model becomes complicated as the assumption of homoscedasticity is violated. Straightforward correlation analysis (e.g. Pearson's product moment correlation) is likely to exaggerate the strength of the correlation and its significance, as it assumes a higher number of effective degrees of freedom than is truly the case. To overcome this issue, a generalised additive mixed models (GAMMs) can be implemented instead. GAMMs are more flexible than GAMs, as they can estimate random effects and include complex error structures (Shadish et al., 2014). Similar to a GAM being adapted from a GLM, a GAMM is adapted from a general linear mixed model (GLMM) containing random effects \mathbf{b} :

$$g(\mu_i^b) = \mathbf{X}_i\boldsymbol{\beta} + \mathbf{Z}_i\mathbf{b} \quad (3.23)$$

Where $\mu^b \equiv \mathbb{E}(\mathbf{y}|\mathbf{b})$, $\mathbf{b} \sim N(\mathbf{0}, \boldsymbol{\psi}_\theta)$, and $y_i|\mathbf{b} \sim$ some exponential family distribution and are independent. $\boldsymbol{\psi}_\theta$ is the covariance matrix of the random effects

contained in vector \mathbf{b} with corresponding parameter vector θ and model matrix \mathbf{Z} . A GAMM then takes the form:

$$g(\mu_i^b) = \mathbf{X}_i\boldsymbol{\beta} + \sum_{j=1}^p f_j(\mathbf{X}_j) + \mathbf{Z}_i\mathbf{b} + \phi_i \quad (3.24)$$

Where vector $\boldsymbol{\beta}$ contains fixed parameters with corresponding fixed effects model matrix \mathbf{X} , f_j are smooth functions of covariates \mathbf{X}_j , \mathbf{Z} is the random effects model matrix, and \mathbf{b} is the corresponding vector of random effects covariates as above. Residual errors are contained in $\phi_i \sim N(\mathbf{0}, \boldsymbol{\Lambda})$ with covariance matrix $\boldsymbol{\Lambda}$.

The conversion from GLMM to GAMM is conceptually relatively straightforward, as the smoothers f_j can be written as components of a mixed model, while treating their smoothing parameters λ as variance component parameters. To revert a GAMM into a GLMM, the (unpenalised) fixed effects component of each smooth is absorbed into $\mathbf{X}_i\boldsymbol{\beta}$, and the (penalised) random effects component is absorbed into $\mathbf{Z}_i\mathbf{b}$. The function `gamm` from the R package `mgcv` utilises this approach to solve GAMMs (Section 5.2.4; Wood, 2006, 2011). The mathematical details of how to convert the smooths to mixed model components can be found in Wood (2006).

In this thesis, GAMMs are employed to deal with autocorrelation in the data series, which can be modelled using an autoregressive integrated moving average (ARIMA) model. An ARIMA takes three arguments p , d and q , each addressing a different aspect of autocorrelation. The autoregressive (AR) part explains how the variable is regressed onto its own previous values with lag time p . The moving average (MA) explains regression errors that are composed of linearly combined error terms occurring at various times in the past, where q indicates the lags up to which there is non-zero autocorrelation. Integration d is the number of times the data has been differenced. The notation of an ARIMA model can be simplified from $\text{ARIMA}(p, d, q)$ when d (or d and either of the other two terms) is zero, by dropping the unused part from the acronym; $\text{ARIMA}(1, 0, 1)$ is identical to $\text{ARMA}(1, 1)$, and $\text{ARIMA}(1, 0, 0)$ is identical to $\text{AR}(1)$. The general $\text{ARMA}(p, q)$ model is defined as (Davison & Hinkley, 1997):

$$\phi_t = \sum_{i=1}^p \alpha_i \phi_{t-i} + \varepsilon_t + \sum_{i=1}^q \beta_i \varepsilon_{t-i} \quad (3.25)$$

Where α and β are the AR and MA model parameters respectively, p and q are the respective AR and MA model orders, and ε_t is again i.i.d $N(0, \sigma^2)$.

GA(M)Ms have been implemented in the palaeo-community, including on charcoal data by Marlon et al. (2013) and Daniau et al. (2012). The use of GA(M)Ms as presented in this thesis is inspired by these studies, which are discussed in more detail in Chapter 5.

3.6.4 Summary

This chapter has served to lay the mathematical and statistical foundations necessary to understand the implementation (and justifications for doing so) of the methods employed in this thesis. It also has examined fundamental relationships apparent in the modern-day climate which are explored in a long-term context over the past two millennia using proxy data in the next two chapters. The sparse PC reconstruction method is integral to the work presented in Chapter 4, as it is applied to create multi-proxy network ensembles for reconstructing ENSO-like climate change over the past 1,500 years. The discussion and evaluation of pseudoproxy creation using PSMs and signal-to-noise ratios has highlighted the importance of assessing various sources of uncertainty inherent to different proxy archives, which is further discussed in 4.3.2 and 4.5.1. The modern-day and modelled relationships between temperature, precipitation and ENSO assessed in 3.3 illustrate clearly the expected behaviours of these variables, and are the starting point for interpreting the relationships found in the precipitation and temperature palaeorecords analysed in Chapter 4, and the precipitation and fire proxies in Chapter 5. Finally, the descriptions and sensitivity tests of the various transformation and smoothing methods in 3.5 and 3.6 not only provide necessary mathematical understanding, but also serve to further illustrate the complexity of combining, comparing and interpreting proxy records. Issues including non-linearity, unit standardisation, and temporal and spatial resolution must be taken into account when working with multiple proxy series, but the choices made along the way can

have a substantial impact on the resultant reconstructions. The combined exploration and implementation of the methods discussed in this chapter provides a powerful new way to look at the research questions, improving our understanding of the results presented in the following two chapters and their robustness to data availability and quality.

Chapter 4

El Niño-like climate change in the tropics and subtropics over the past two millennia

A manuscript based on this chapter is published in *Climate of the Past* (Henke et al., 2017).

4.1 Introduction

The El Niño/Southern Oscillation (ENSO) is the most influential source of interannual variability in the modern climate. The ‘warm’ El Niño state is characterised by a weaker sea surface temperature (SST) gradient across the equatorial Pacific and a shift in precipitation from the western Pacific toward the central Pacific, while the ‘cool’ La Niña state is roughly the opposite. Although ENSO originates in the tropical Pacific, it has far-reaching effects through teleconnections on some regions in higher latitudes, and El Niño years are generally anomalously warm on a global scale. However, it is unclear whether there is a link between anomalously warm or cool periods and the two ENSO states on decadal to centennial timescales. Given the severe socio-economic consequences of ENSO events (Badjeck et al., 2010, Hjelle & Glass, 2000, Kovats et al., 2003, Page et al., 2002), and a warmer future under continued anthropogenic warming, it is

important to understand the ‘natural’ long-term ENSO and its interaction with the climate. It allows for an evaluation of the effects of anthropogenic impacts on recent and future ENSO behaviour (Bellenger et al., 2014, Collins, 2005, Guilyardi et al., 2009, Vecchi & Wittenberg, 2010).

Recent multi-model studies of projected changes in ENSO under anthropogenic warming suggest robust changes to ENSO-driven temperature and precipitation, including an increase in extreme El Niño (Cai et al., 2015a) and La Niña (Cai et al., 2015b) events, and changes in the ENSO SST pattern and ENSO-driven precipitation variability (Power et al., 2013b). However, most current general circulation models (GCMs) cannot simulate many aspects of the modern day ENSO accurately, often overestimating the western extent of the Pacific Cold Tongue and failing to correctly simulate central Pacific precipitation anomalies, ENSO feedbacks, and ENSO amplitude (Bellenger et al., 2014, Collins, 2005, van Oldenborgh et al., 2005). This translates into uncertainty over simulations of past ENSO-like climate change, calling for alternative sources of climatic information to supplement, complement and corroborate the model and instrumental data. This is done using proxy climate records such as tree rings, tropical ice cores, sediment cores and corals (Jones & Mann, 2004).

There are very few annually-resolved proxy records available longer than ~500 years (Mann et al., 2008). The issue with high-resolution proxies is that they tend to be short in length; trees and corals, for example, rarely live beyond a few centuries (Jones & Mann, 2004). Some such highly resolved records are available for the more distant past, but these generally offer snapshots rather than continuous records (Abram et al., 2009, Corrège et al., 2000, McCulloch et al., 1996). However, there are several long, lower-resolution proxy records of ENSO variability on decadal to millennial scales, often derived from lake sediments (cf Conroy et al., 2010), marine sediments (cf Barron & Anderson, 2011), or speleothems (cf Maupin et al., 2014). While these are unable to capture the interannual frequency and amplitude of individual ENSO episodes, they provide an insight into longer-term ENSO-like climate states and average ENSO behaviour. Although there are some endeavours to combine some low-resolution proxies, often to capture spatial gradients (Anderson, 2012, Conroy et al., 2010, Yan et al., 2011b), there has not, to our knowledge, been a comprehensive effort to systematically merge a large set of such low-resolution records to create a long-term reconstruction of ENSO-like climate variability. Doing this could shed light on the long-term stability

of ENSO and its links with the wider climate, for example by examining ENSO behaviour under different dominant cool or warm climate states, which in turn can inform our understanding of potential future ENSO-like changes in a warmer world.

A number of proxy, instrumental and modelling studies investigate links between ENSO and global climate variability on interannual (Klein et al., 1999, Wang et al., 1999), decadal (Nelson et al., 2011), centennial (Mann et al., 2005, Trouet et al., 2012) and millennial (Cane, 2005, Ivanochko et al., 2005, Moy et al., 2002, Shin et al., 2006) time-scales. A wide range of proxy records and modelling studies point to substantial shifts in the ENSO-like state of the climate linked to changes in solar variability on orbital time-scales (Barron & Anderson, 2011, Clement et al., 2001), movement of the Intertropical Convergence Zone (ITCZ; Carré et al., 2005, Gomez et al., 2004, Nelson et al., 2011, Partin et al., 2007) and changes in ocean circulation linked to sea level rise (McGregor et al., 2008, Wanner et al., 2008). In the more recent past, changes in solar irradiance and stratospheric aerosol loadings due to volcanic activity have played significant roles in modulating the hemispheric to global scale climate (Mann et al., 2009). The so-called Medieval Climate Anomaly (MCA; ca. AD 800–1200) and the Little Ice Age (LIA; ca. AD 1300–1850; Yan et al., 2011b) were periods of anomalously warm and cool conditions respectively, at least in the Northern Hemisphere (NH; Jones & Mann, 2004, Mann et al., 2009). These two periods are often used for exploring past behaviour of climatic phenomena as they represent relatively large and sustained excursions from the long-term mean. However, a comparison of a NH and SH temperature reconstruction (Neukom et al., 2014) and continental-scale temperature reconstructions (Consortium, 2013) find no evidence of a globally coherent MCA, and only partial evidence for a global LIA. Neither of these two studies focus specifically on the Equatorial tropics, leaving open the question of the strength of a potential MCA and/or LIA in these latitudes. This is potentially an important knowledge gap, as proxy evidence for the expression of ENSO-like climate change over these periods appears to be ambiguous. A range of proxies point to a more northerly ITCZ (Haug et al., 2001, Sachs et al., 2009, Tierney et al., 2010) during the MCA, which is characteristic of La Niña-like conditions and is in agreement with warming patterns found in multiproxy reconstructions of hemispheric and global scale temperature (cf Mann et al., 2009). Langton et al. (2008) similarly infer a reduction in El Niño-like activity during the MCA based on ocean

basin ventilation changes in Indonesia. In contrast, a Southern Oscillation Index reconstruction based on two proxy records (Yan et al., 2011b) shows an El Niño-like state during the MCA and a La Niña-like LIA. This seems to be supported by a number of other precipitation proxies from the West Pacific (Yan et al., 2011a) and East Pacific (Moy et al., 2002). Other precipitation proxies indicate a highly variable ENSO during the LIA, including two multidecadal droughts in Java (Crausbay et al., 2006), high amplitude rainfall fluctuations in Madagascar (Brook et al., 1999), and three southerly ITCZ excursions (Haug et al., 2001).

These discrepancies in long-term ENSO-like variations between proxy records raise two important questions. The current dynamical understanding of ENSO is underpinned by the strong relationship between temperature and rainfall observed today, and the relationships between the ENSO ‘source region’, the tropical Pacific, and teleconnected regions, which largely fall between 40°S and 40°N. As Yan et al. (2011b) highlight, however, temperature and precipitation proxies appear to disagree on the ENSO-like states of the MCA and the LIA. To what extent, therefore, does the modern-day precipitation–temperature relationship in the source and teleconnected regions continue to exist in the past? The second question concerns the relation of ENSO to the wider climate; is there a link between global temperatures and long-term ENSO state on multidecadal to centennial time-scales? A comparison between the MCA and the LIA can give some insight into this, and may hold some clues to what we can expect under anthropogenic climate change.

The use of proxy archives can contribute valuable insights on past climate variability by extending the instrumental records back in time, but substantial uncertainties remain. This is because all reconstructions have inherent limitations and ambiguities that must be identified and dealt with appropriately. These include resolution, dating errors, noise, limited and/or skewed spatial coverage, and non-linear responses to the climatic variable of interest (Jones et al., 2009). Various statistical techniques have been employed to create multiproxy reconstructions of climatological phenomena, broadly falling into the categories ‘composite plus scaling’ (CPS) or ‘climate field reconstruction’ (CFR) (Jones et al., 2009). CPS encompasses any method which involves combining standardised proxy records into a single reconstruction which is subsequently calibrated to a known time-series of the target variable (e.g. instrumental temperature record) to provide a quantitative estimate of the variable. CFRs, on the other hand, aim to reconstruct

large-scale spatial patterns of climatic change using covariance between proxies and instrumental data. Within both methods there is a wide variety of approaches; see Jones et al. (2009) for detailed descriptions and examples of both CPS and a range of CFR methods. The focus of this study – comparing the climate signals in temperature and precipitation proxy records separately – calls for a slightly different approach.

Here we create two new ENSO reconstructions, one derived from temperature proxies and one from precipitation proxies, using a new method for assessing the stability of the modern-day ENSO patterns in the source region and the wider teleconnected regions. In a fashion similar to e.g. Braganza et al. (2009), proxy records are not tuned to instrumental data other than a simple location-dependent weighting. While this precludes direct quantitative comparisons, it removes the bias towards high-frequency trends that stems from calibrating to the relatively short (~ 150 year) instrumental record (or indeed any short record; Cook et al., 1995, Jones & Mann, 2004). The method amplifies the ENSO component of proxy records and simultaneously attempts to quantify uncertainty related to noise and incomplete spatio-temporal data coverage, whilst maximising the use of a wide range of tropical proxies. With this, we aim to answer two questions:

1. Do temperature and precipitation proxies show consistent long-term ENSO behaviour over the last millennium?
2. Do the LIA and the MCA differ significantly in their mean ENSO state?

Section 4.2 provides a description of the proxy and instrumental/reanalysis data used in this study and a concise overview of the methodology is given in 4.3. The results and discussion of the findings are presented in 4.4 and 4.5 respectively before revisiting the research questions and making concluding remarks in 4.6.

4.2 Data description

4.2.1 Study region

The focus of this study is limited to the tropical-subtropical latitudes between 40°S – 40°N. This encompasses the ENSO source region (the equatorial Pacific Basin) and the major teleconnected regions (Wilson et al., 2010), and allows for a wider set of proxy records to be considered. This is significant as there is a dearth of proxy records in the most optimal region – the Pacific Basin – for capturing ENSO-like temperature and precipitation patterns.

4.2.2 Proxy records

For this study, a comprehensive effort was made to collect all published proxy precipitation and temperature records between 40°S – 40°N that cover the last 2000 years. The large majority of records were accessed from the NOAA Paleoclimatology and Pangea Databases (<https://www.ncdc.noaa.gov/data-access/paleoclimatology-discussion/datasets>). In addition, over 200 tree ring records were taken from the dataset used by Mann et al. (2008), and hence were subject to their criteria including length, intra-site signal coherence and sample density (see Appendix A for details). A set of coral records was taken from the dataset made available by Tierney et al. (2015); these were largely temperature proxies although some were assigned as precipitation proxies or excluded altogether based on information in the original publications (see Appendix A for details).

After collection, all records were screened for a maximum dating error of 60 years. Although somewhat arbitrary, this cut-off was decided by taking double the averaging binwidth of 30 years that was applied to the data prior to analysis (Section 4.3.3). This is a step towards addressing the issue of dating uncertainty whilst allowing a wider range of proxies to be utilised. Proxies with larger dating errors generally have lower (multi-annual to multi-decadal) resolution but are usually also much longer, and are arguably more useful for capturing long-term trends which may be less evident or reliable in annual-resolution proxies (cf Cook et al., 1995, Esper et al., 2002, Mann et al., 2008, on low-frequency trends in tree

rings). Other quality judgements regarding temporal resolution, record length and proxy location are accounted for by the method set out in 4.3.

4.2.3 Modern climate datasets

Instrumental climate data are the best available in terms of dating accuracy, calibration and physical basis (Jones & Mann, 2004). However, their spatial coverage is not complete and sharply decreases back in time. The nature of the method used in this study calls for full spatial coverage over a long period; therefore, re-analysis products are more suitable. These are combinations of instrumental and satellite data interpolated using models. The 20th Century Reanalysis Version 2c (20CRv2c) is the longest global dataset of atmospheric circulation available, spanning AD 1851-2014. It is based on surface pressure, temperature and sea ice distribution data, filled in with a ‘deterministic’ Ensemble Kalman Filter (EKF). It has a spatial resolution of 2°latitude × 2°longitude × 24 vertical pressure levels, and a temporal resolution of up to 6 hours. It has been demonstrated that the 20CRv2c is competent at representing the global tropospheric circulation as well as the mean state and variability of the hydroclimate – for a detailed description and evaluation of the product see Compo et al. (2011). The monthly mean surface air temperature and precipitation rate datasets were downloaded from the NOAA/OAR/ESRL PSD web site (<http://www.esrl.noaa.gov/psd/>). The 20CRv2c data were regridded to 2°×3° to be comparable to the model data described in 4.2.4. The climatology (for the period 1851-2014) was removed to produce monthly anomalies, which were then averaged to annual resolution.

4.2.4 General circulation model simulations

There are several comprehensive modelling projects with the aim of improving comparability between general circulation models (GCMs) produced by different teams. GCMs taking part in these projects perform a set of simulations with standardised forcings and boundary conditions. For this study, the pre-industrial control (piControl; pre-1850 parameters, no external forcings) and historical (AD 1850– 2000) runs from the Coupled Model Intercomparison Project 5 (CMIP5; Taylor et al., 2012) were used, in addition to the last millennium (past1000; AD

850–1850) runs from the Paleoclimate Model Intercomparison Project 3 (PMIP3; Braconnot et al., 2012, 2011). Of the six GCMs which have all three runs available, two were chosen for their similarity to 20CRv2c in terms of spatial ENSO representation (see 3.2.3) for precipitation (climate modelling groups in brackets):

- CCSM4 (National Center for Atmospheric Research)
- GISS-E2-R (NASA Goddard Institute for Space Studies)

And two for temperature:

- IPSL-CM5A-LR (Institut Pierre-Simon Laplace)
- BCC-CSM1-1 (Beijing Climate Center, China Meteorological Administration)

Similar to 20CRv2c, all model datasets were regridded to $2^\circ \times 3^\circ$ and converted to annual anomalies.

4.3 Methodology

The method developed in this study was used to create separate temperature and precipitation-based reconstructions of ENSO-like climate change made from weighted temperature and precipitation proxy records respectively. The weights were based on Empirical Orthogonal Function (EOF; 3.2.1) patterns derived from GCMs and 20CRv2c. The method consists of two stages: first, a temperature and a precipitation ensemble of ‘optimal’ proxy networks is created based on GCM-derived cross-validated ‘add-one-in’ pseudoproxy experiments; these networks are then applied to real proxy data to create a separate precipitation and temperature reconstruction of ENSO-like climate change over the past two millennia. This approach attempts to take into account the effects of proxy selection, the temporal limitations of individual proxies, and non-climatic noise. Each step is described in more detail below.

4.3.1 GCM data

For the creation of the network ensemble, GCM data was employed. The objective of the ‘add-one-in’ method is to create networks which accurately reconstruct the long-term (30-year averaged) ENSO signal. 20CRv2c covers less than 200 years, which is too short for meaningful evaluation of low-frequency change, particularly if the dataset is to be partitioned into calibration and validation sets. GCMs, meanwhile, offer much longer datasets. Although they cannot simulate the real temporal climate change and variability of the past 1000 years, they are still useful for the building of proxy network ensembles, which asks only that they simulate realistic modes of spatiotemporal variability (i.e. EOF patterns). For the pseudoproxy experiment, the past1000 runs from two different GCMs were used for calibration (GCM_{cal}) and validation (GCM_{val}). The precipitation and temperature calibration GCMs (GCM_{cal}) were CCSM4 and ISPL-CM5A-LR, respectively; the corresponding validation GCMs (GCM_{val}) were GISS-E2-R and BCC-CSM1-1.

For this study, the most ‘accurate’ GCM past1000 runs were selected, in the sense that their EOF values at proxy locations were most similar to the corresponding 20CRv2c values, which is the most realistic EOF pattern of modern-day ENSO available here. The process of evaluating the likeness of the EOFs is described in 3.2.3. The real modern ENSO pattern will be different again, as will the real ENSO pattern of the past 1–2 millennia. By calibrating and validating the networks on datasets with slightly varying realisations of this ENSO pattern, the sensitivity of the networks to these variations is tested. Moreover, using two 1000-year simulations (rather than dividing one simulation into a calibration and a validation partition) leaves more degrees of freedom, which is important as the 30-year averaging constitutes a significant reduction. Ideally, this process would be performed with multiple combinations of GCMs as calibration/validation candidates, but time restraints push this beyond the scope of this thesis.

4.3.2 Pseudoproxies

Pseudoproxies (see also 3.4) are simulated proxies that attempt to mimic various sources of uncertainty inherent in the real proxy records. This ranges from adding

white Gaussian noise with a prescribed signal-to-noise (SNR) ratio to approximate non-climatic random noise, to more sophisticated process-based additions that take into account effects such as dating error, nonlinear and multivariate responses of the proxy sensor to the climate variable, and sampling biases (Mann, 2002, Smerdon, 2012). The utility of any pseudoproxy exercise lies in the fact that the answer to the question is known, as it can be derived directly from the original model dataset. By putting the 'signal plus noise' pseudoproxies through a method to make a reconstruction of the signal, it allows for inferences about the stability and limitations of the method, estimates of uncertainties due to noise and other proxy record characteristics and, as highlighted by the method used here, it provides a way of objectively and systematically selecting the most appropriate data (see Smerdon, 2012, for an introduction to pseudoproxy experiments).

Ideally, all pseudoproxies in this study would be created from proxy system models (PSMs; e.g. Dee et al., 2015). However, as discussed in 3.4.1, this is beyond the scope of this thesis. As a compromise, all tree ring width (TRW) records in the proxy dataset used in this study were represented using VS-Lite derived pseudo-TRW series (see 3.4.2). For the rest of the proxies, the GCM raw temperature or precipitation series were used.

These precipitation, temperature and TRW series (taken from the real proxy locations) were firstly degraded by adding white Gaussian noise. The calculation of the signal-to-noise ratio for each record is described in 3.4.3.

After the addition of noise, the pseudoproxies were degraded further to reflect the length, timespan and resolution of the real proxies. Real proxies' temporal resolution between 0-1000 yrBP was applied; this period was chosen as it is the focus of this study. The resolution was recreated by assuming that each data point represents an average of the previous unsampled years; for example in a proxy with a 10-year resolution, data point i was recreated by taking the average over points $(i - 9) : i$.

4.3.3 Calibration: network creation

After screening proxy records, selecting GCMs and creating pseudoproxies, a pseudoproxy experiment was conducted to create an ‘optimal’ network ensemble. The calibration stage builds proxy networks in a stepwise manner by incrementally adding the proxy that maximally improves the quality of the network reconstruction. Using the GCM_{cal} past1000 dataset, a thousand proxy networks were created via an ‘add-one-in’ pseudoproxy algorithm that automatically builds a network based on how much each proxy improves the reconstructive power of the network (Figure 4.1). Similar to a forward stepwise regression procedure, GCM_{cal} -derived pseudoproxies are gradually added to a ‘base’ network of zero proxies, testing the quality of the network with each addition, until all proxies have been incorporated (Figure 4.1 a&b). The final ‘optimal’ network is that which performed best over all steps (Figure 4.1 c). By repeating the process 1000 times adding different random noise series to the pseudoproxies each iteration, it addresses the influence of stochastic processes on the ability of a proxy network to optimally reconstruct the large-scale ENSO pattern.

The reconstruction process itself is a weighted average approach, where the proxy weights are based on the ENSO-like EOF pattern of the GCM_{cal} past1000 run (for the add-one-in network building) or 20CRv2c (for the final reconstruction). All pseudoproxies were first subjected to inverse transform sampling (ITS; 3.5.3), before binning them into 30-year bins (using a simple average; see 3.6.1) to prevent high-resolution records from dominating the signal. This binwidth was chosen as the focus here is on long-term ENSO-like state rather than inter-annual variability, and it reflects the resolution of many individual low-frequency proxy reconstructions (cf Anderson, 2012, Makou et al., 2010, Rodysill et al., 2012, Yan et al., 2011a,b).

At each stage (for each interim network), the pseudoproxies c in the network (derived from GCM_{cal} past1000) were first converted to Z-scores (z ; see 3.5.1) with a common period (n) where all proxies contain data. For clarity, Eq. 3.14 for calculating Z-scores is repeated here:

$$z_i = \frac{c_i - \bar{c}_n}{\sigma_n} \quad (4.1)$$

where z_i is the Z-score for the i^{th} sample, \bar{c}_n is the mean of series c over the base period n , and σ_n is the standard deviation over the same base period. The length of n was ensured to be at least 100 years to reduce the influence of noise on \bar{c}_n and σ_n . In some cases, this requirement led to the rejection of one or more proxies as their length or position in time were not compatible with the other records. This process of normalisation is similar to the method used in Wilson et al. (2010). Proxies that fall in the same grid box were averaged after normalisation. This prevents overrepresentation of those locations, and improves their SNR by cancelling out some of the stochastic noise and amplifying their signal (Wang et al., 2014a).

Each normalised pseudoproxy z at location $[x, y]$ was multiplied by a scaled version of the EOF value at location $[x, y]$ (Eq. 3.11) and summed to create a single reconstruction series s (Eq. 3.12). More detail on this process can be found in 3.2.4. The quality of a network was assessed by comparing its s with the PC using the Pearson product-moment correlation R . The entire calibration process was repeated 1000 times, each time using pseudoproxies with newly generated noise iterations, resulting in 1000 proxy networks.

4.3.4 Validation: network evaluation

The validation stage tests the robustness of the networks using independent data. Validation was performed in two steps. First, the 1000 networks produced with the GCM_{cal} were used to make reconstructions using GCM_{val} past1000 data and the GCM_{cal} EOF. Using data from a different GCM ensures complete separation between the calibration and validation periods, and tests the sensitivity of the networks to the spatial stability of the EOF pattern, as the ENSO-like EOF from each model and from 20CRv2c is different. The switch from GCM_{cal} to GCM_{val} thus mirrors the switch between the GCMs and 20CRv2c. Each network was reconstructed 1000 times using GCM_{val} pseudoproxies, again adding different noise realisations for each iteration. Validation test scores (R) were calculated to check the quality of these validation reconstructions compared to the validation PC (calculated using EOF_{cal} and GCM_{val} past1000 data).

There are several measures of quality for validation statistics, the most common of which are the coefficient of determination R^2 , the reduction of error (RE) and the coefficient of efficiency (CE; Cook et al., 1994). Discussions on the relative merits

and pitfalls of these measures can be found in the literature (cf Cook et al., 1995, Emile-Geay et al., 2013a). Although CE is generally regarded as the appropriate indicator for low-frequency reconstructions (Bürger, 2007, Emile-Geay et al., 2013a), the nature of the method described here reduces its effectiveness as a measure of quality. The past1000 and piControl runs have little (or no) external forcing driving the simulation, hence they have very little low-frequency variability or trends. Moreover, the data are z-normalised at various stages, removing any differences in means. As the CE effectively tracks changes in the mean, this removal of the mean renders CE sensitive to spurious results. The diagnostic R was instead chosen as tests showed that it was more effective at picking high-quality reconstructions than CE and RMSE, though generally a high R value did correspond to high CE and low RMSE (not shown). R is essentially equivalent to using R^2 , but retains the ability to distinguish between positive and negative correlations.

The R -values from the 1000×1000 validation reconstructions (R_{val}) were then compared to critical values (R_{crit}) calculated for each network. Critical values for the validation test scores were calculated by repeating the first validation step but using the GCM_{val} piControl run. The piControl run contains no external forcing and so is essentially noise, but retains the inherent climatological spatial correlations. From these reconstructions, R_{crit} for each network was determined by taking the 95th percentile of the R -values of the corresponding 1000 reconstructions. Where $R_{val} > R_{crit}$, the network was retained; where $R_{val} < R_{crit}$, the network was deemed unfit and was discarded. Networks sensitive to the choice of dataset are thus weeded out. The remaining networks may not all be unique, further reducing the effective number of networks. Presumably, networks that occur multiple times are more effective proxy combinations; retaining the duplicates accordingly upweights these networks in the final reconstruction.

The combination of using pseudoproxies, the add-one-in approach and R_{crit} simultaneously accounts for proxy temporal resolution, spatial distribution and temporal coverage (i.e. proxy start and end dates), and gives an estimate of the uncertainty due to proxy noise. However, an important assumption is that the *signal* in all proxies is solely temperature or precipitation, and it is thus still a ‘best case’ estimate.

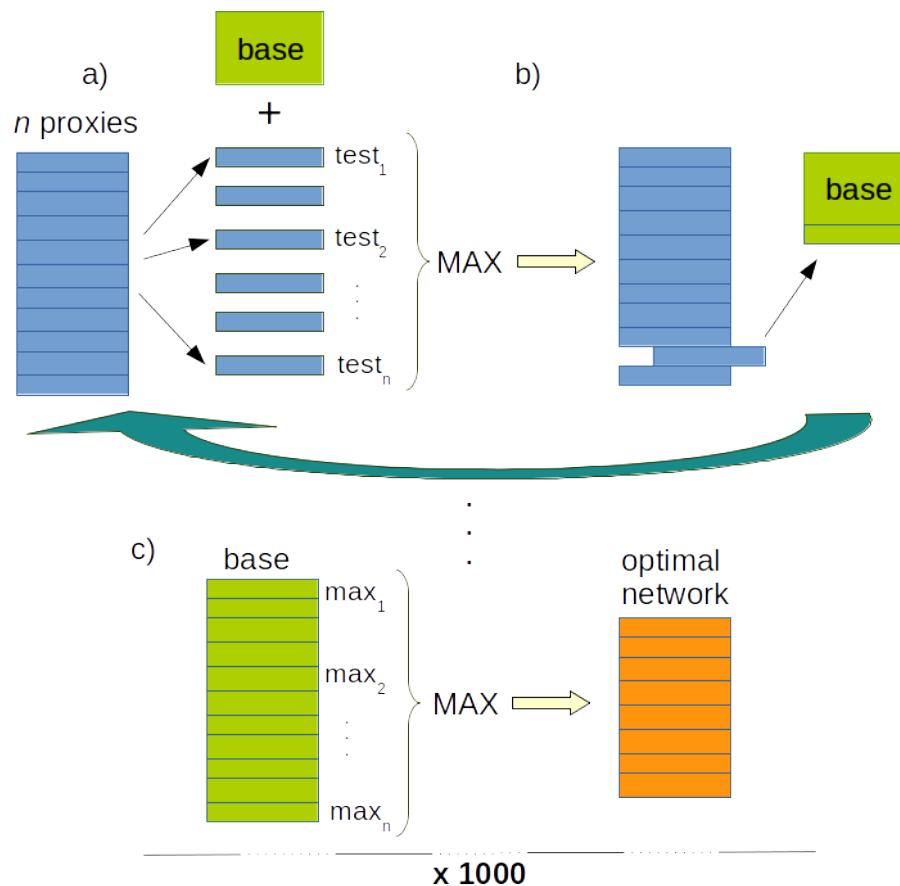


FIGURE 4.1: Overview of the network creation process. a) A new network is created from the base network (*base*) plus each pseudoproxy individually, and tested for its reconstructive power. This results in n test scores; b) the highest score (max_n) is selected and the associated proxy is moved from the test-proxies to *base*. This is repeated until all test-proxies are incorporated into *base*. c) The 'optimal' network is selected by cutting *base* where max_n was highest. The entire process is repeated 1000 times, with new noise realisations being added to the pseudoproxies at the start of each run.

4.3.5 Proxy ENSO ensemble

The 'optimal' networks that passed the R_{crit} test were used to create an ensemble of real proxy reconstructions of ENSO-like climate change. The proxy records were similarly Z-normalised and subjected to an ITS transform, before undergoing the same reconstruction process used in the network creation.

All ensemble members (s) were then re-normalised to ensure comparability. Although calibration to the instrumental period would potentially allow us to quantify the absolute amplitude, this was not done for two reasons. Firstly, the proxy data

coverage during the instrumental period and the preceding century was relatively low, reducing the confidence in the reconstruction during that period; calibrating to this period would thus increase the uncertainty on the rest of the reconstruction. Secondly, any calibration to the instrumental data are necessarily biased towards high-frequency trends (Mann et al., 2008). Within a 30-year averaged series, the number of comparison points with the instrumental period is extremely low. The final proxy reconstruction was calculated as the ensemble mean.

The last step in creating the reconstruction was calculating the final error range. Root mean square errors (RMSEs) were calculated for each network during validation, providing 1000 error estimates for each ensemble member. This was translated into ensemble member uncertainty limits by adding and subtracting the 1000 error series from the reconstruction timeseries (to get the maximum and minimum error limits respectively) and taking the 5-95th percentile over their full range. The uncertainty envelope around the final ENSO reconstruction (i.e. the ensemble mean) is thus a combination of the reconstruction ensemble range and the error ranges for individual ensemble members. This error estimation explicitly takes into account the impact of network choice as well as random error affecting the proxies.

4.3.6 LIA-MCA difference analysis

The absence of a known reference period to which the reconstructions can be calibrated precludes any absolute comparison of the result with recent trends. However, it is possible to ascertain whether the MCA and the LIA differ significantly in how 'El Niño-like' they are. Evaluating the LIA-MCA difference directly also removes the bias introduced by taking any reference period (Mann et al., 2009). To do this, the means over the two periods were taken and the MCA mean subtracted from the LIA mean. If the difference is significantly greater than zero, the LIA is more El Niño-like than the MCA; if the difference is significantly less than zero, the MCA is more El Niño-like than the LIA.

4.4 Results: ENSO reconstructions

The final ENSO reconstructions for precipitation and temperature and their proxy network density are shown in Figures 4.2 and 4.3. The final number of networks included in the precipitation ensemble is 1000, of which 999 are unique (Figure 4.2a). The total number of proxies used is 48, with a maximum of 40 for a single network. Proxy availability increases steadily throughout time, save a slight drop off in the most recent period (Figure 4.2b). Although there is spread in the ensemble, there are clear peaks and troughs visible. The within-ensemble coherence was tested by correlating 1000 randomly chosen pairs with each other. This confirmed that there is generally good agreement over the full period (100-1500 yrBP) as well as during the MCA and LIA individually (Figure 4.4).

The temperature reconstruction ensemble consists of 617 optimal networks, all of which are unique (Figure 4.3a). The within-ensemble correlations are lower than for precipitation in the LIA though still positive, and there is no distinct trend visible in the reconstruction. The total number of proxies used is 267, with a maximum of 116 for a single network. Despite the higher number of proxies available for temperature, the median proxy coverage (Figure 4.3b black line) is lower compared to the precipitation reconstruction; while roughly the most recent 1000 years of the precipitation reconstruction are based on a median of 8 or more proxies, this is only true for the last ~450 years of the temperature reconstruction. The steep increase in Figure 4.3b reflects the high number of tree ring and coral series, all but a handful of which are less than 600 years long (cf Mann et al., 2008, Tierney et al., 2015) and most of which are clustered in North America. The add-one-in method has mitigated some of the risk of co-varying, non-white noise in a subset of the proxies skewing the resulting reconstruction; testing showed that when all North American tree ring records were added to the reconstruction, a regional non-ENSO trend obscured the ENSO signal (Section 3.5). However, the relatively poor spatial coverage elsewhere and the lack of long proxies leaves the reconstruction prone to spurious noise-driven trends in the earlier period. Unlike the precipitation ensemble, the temperature ensemble members vary quite widely among them, particularly in the early period (Figure 4.4). Nevertheless, for both temperature and precipitation the error from proxy noise is overshadowed by the uncertainty associated with the choice of network – the ensemble spread makes up the bulk of the uncertainty envelope.

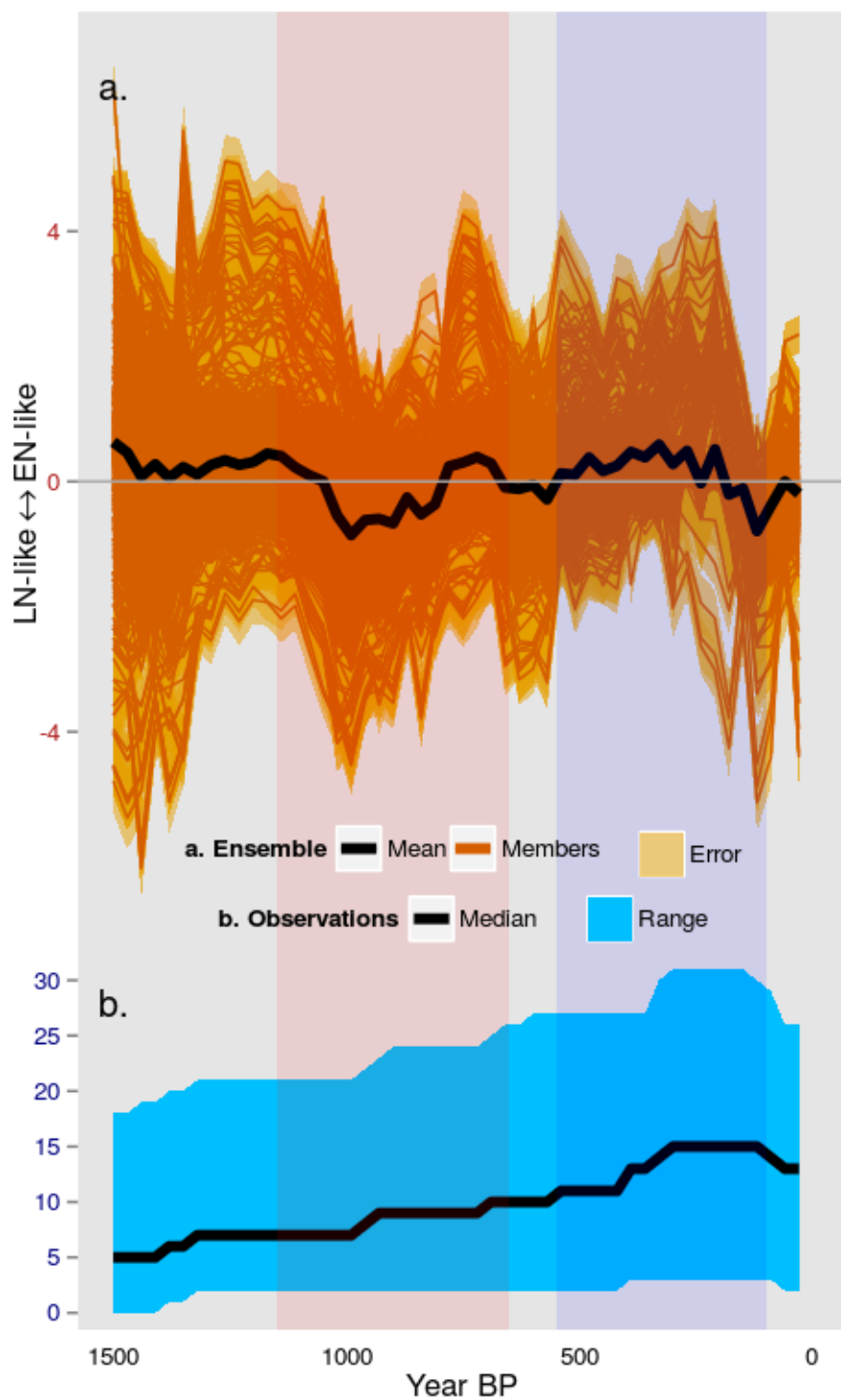


FIGURE 4.2: Precipitation ENSO ensembles. a) 30 year averaged precipitation reconstruction of ENSO-like climate change (black line). Individual network solutions are shown as orange lines, with the uncertainty envelope in orange shading. b) Number of proxies included in the ensemble over time, with the median in black and the range in blue. The pink and purple shaded periods are the MCA and LIA respectively.

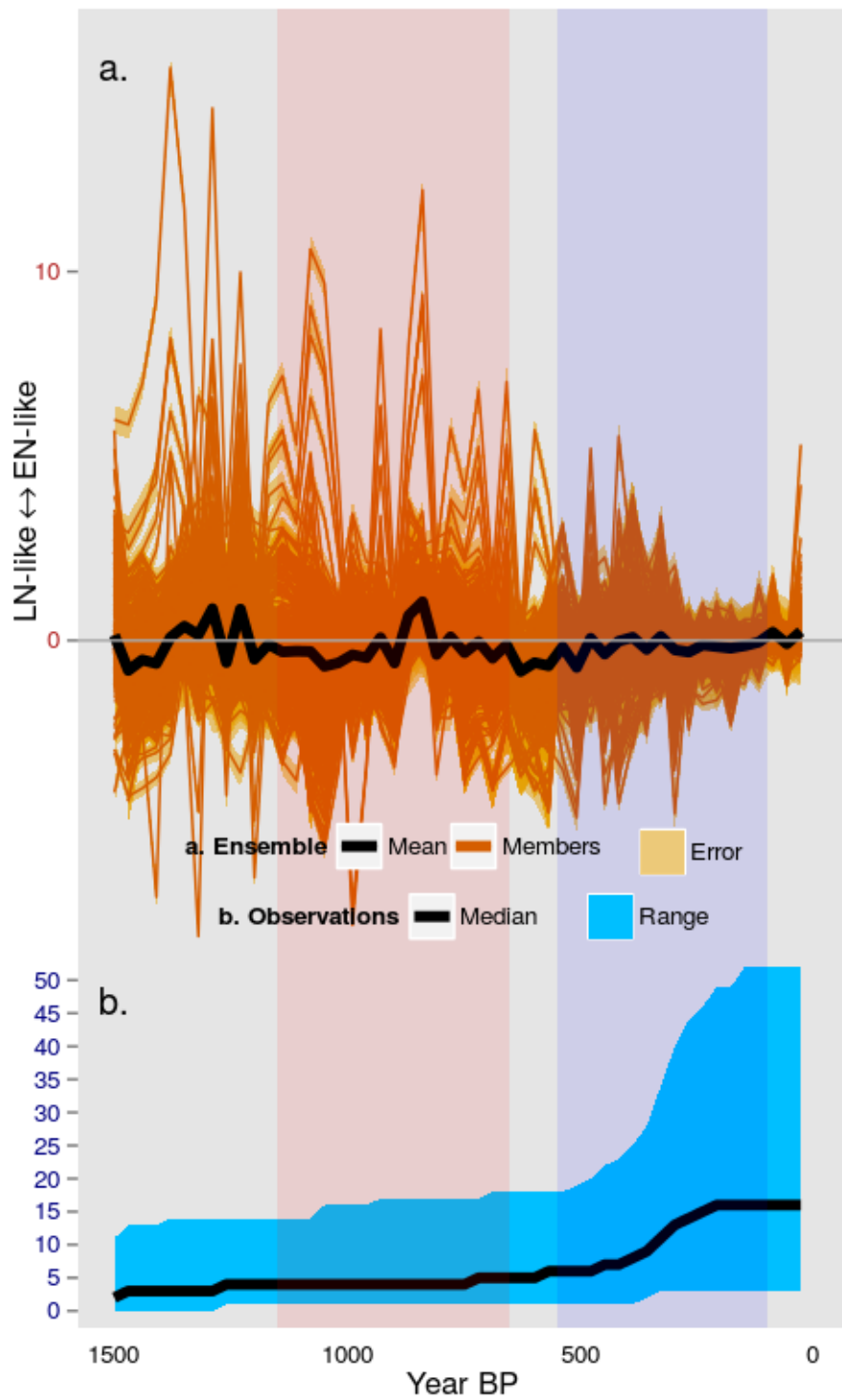


FIGURE 4.3: As Figure 4.2, but for temperature.

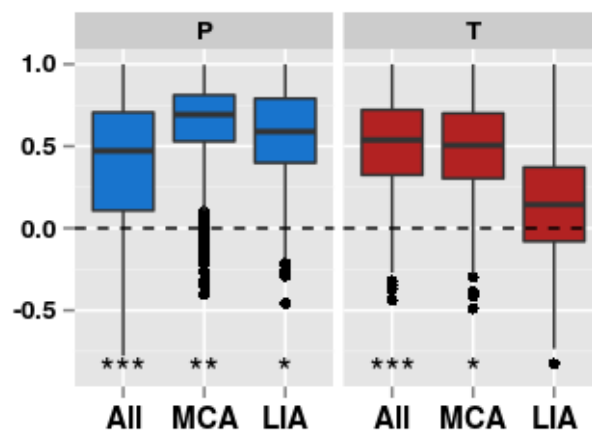


FIGURE 4.4: Correlations between 1000 pairs randomly chosen from the precipitation (blue) and temperature (red) ensembles. Box plots encapsulate the space between the first and third quartile with the median shown as a black line; whiskers indicate the ± 1.5 interquartile range; points are outliers. Statistical significance of the median value is indicated at the bottom: *** $p < 0.001$, ** $p < 0.01$, * $p < 0.05$, ^ $p < 0.1$, $p > 0.1$.

Figures 4.5 and 4.6 show the proxy locations plotted onto the precipitation and temperature EOF patterns, respectively. The proxies included in the precipitation ensemble members are well-distributed over the western and eastern side of the Pacific, though missing good coverage of the central Pacific. The relatively uniform size of the bubbles suggests that there is no immediate preference of any one proxy over the others. The spatial distribution of the temperature proxy locations, in contrast, is highly skewed towards North America (Figure 4.6), where most of the tree ring records are located, and again the central Pacific lacks coverage. The combination of this poor spatial coverage, low temporal coverage (Figure 4.2b) and wide ensemble range (about double that of precipitation) leads to the expectation that the temperature reconstruction is of lower quality than the precipitation reconstruction. There is no clear preference of any combination of proxies, with most proxies being selected equally often (i.e. equal bubble sizes). The fact that the similarity of the EOF patterns of GCM_{cal} and GCM_{val} to the 20CRv2c EOF pattern was lower for temperature than for precipitation (Section 4.3.1) further reduces confidence in the temperature reconstruction.

Figures 4.5 and 4.6 illustrate the benefit of using the pseudoproxy approach in creating the ‘optimal’ networks. There is no direct correlation between proxy weighting (indicated by the bubble colour) and frequency of use, suggesting that

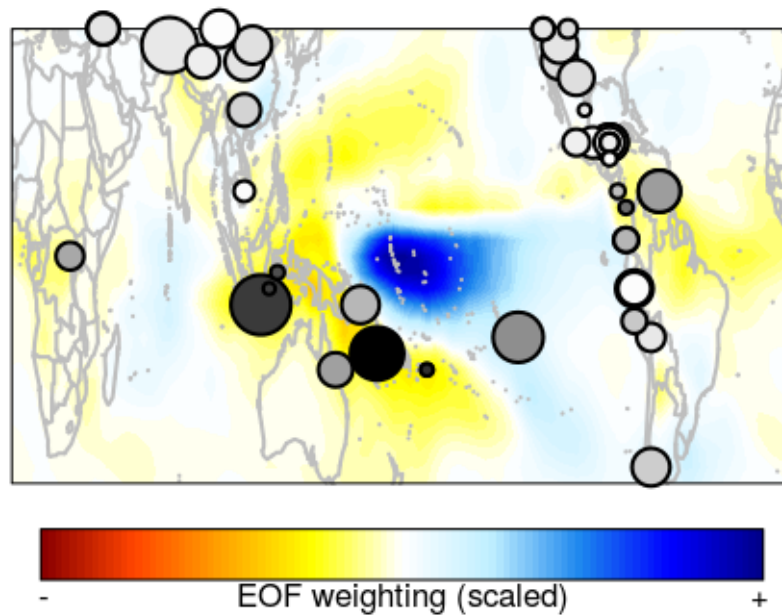


FIGURE 4.5: Precipitation EOF with proxy locations. Background colours are scaled EOF values. Bubbles are individual proxies; size is indicative of how often the proxy is included in the network ensemble, shading indicates relative weighting such that darker colours are more strongly positive or negative.

other aspects such as resolution, length and the relationship to other proxy locations played a significant role in determining the usefulness of a proxy which would be difficult to judge from the outset. The fact that the choice of proxy network is the dominant source of error is further evidence of the utility of the pseudoproxy 'optimal' network method. The high clustering of temperature tree ring records in North America is an example of where the add-one-in method has worked to reduce the risk that some co-varying, non-white noise in a subset of the proxies skews the resulting reconstruction; testing showed that when all North American tree ring records were added to the reconstruction, a regional non-ENSO trend obscured the ENSO signal (not shown).

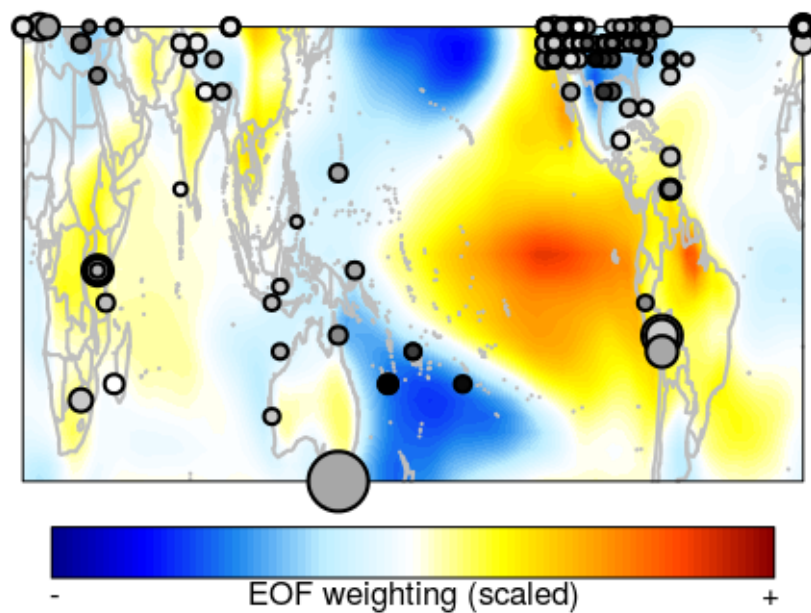


FIGURE 4.6: As Figure 4.5, but for temperature.

4.4.1 Comparing precipitation and temperature

Figure 4.7 shows the range of LIA-MCA differences for the individual members within the precipitation and temperature ensembles. The precipitation interquartile range indicates the LIA is more El Niño-like than the MCA, though the difference is statistically insignificant ($p = 0.22$). For temperature, there is no evidence of any difference between the ENSO-like state of the MCA and the LIA, with a median value very close to 0 ($p = 0.48$). There are also many more outliers (i.e. values outside the 95% confidence interval) compared to precipitation, again reflecting the high uncertainty on the temperature reconstruction.

Figure 4.8 shows the correlation between 1000 randomly chosen combinations of temperature and precipitation ensemble members as an indication of the agreement between the two climate variables. There is no correlation – positive or negative – apparent between the temperature and the precipitation reconstructions, neither over the entire 1500 years nor over the MCA or LIA individually. Whether this is a true physical phenomenon or simply a reflection of the high uncertainty on the reconstructions is difficult to separate. Therefore, it is not possible

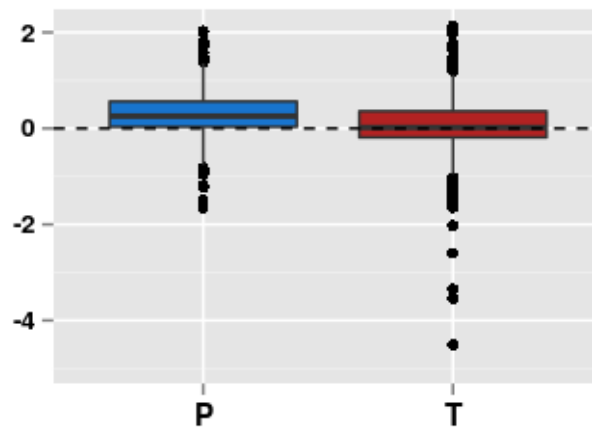


FIGURE 4.7: Difference between the means of the MCA and LIA calculated by subtracting μ_{MCA} from μ_{LIA} for each ensemble member. A positive value indicates LIA is more El Niño-like than MCA. Precipitation is on the left in blue, temperature is on the right in red. See Figure 4.4 for explanation of the box plots and significance.

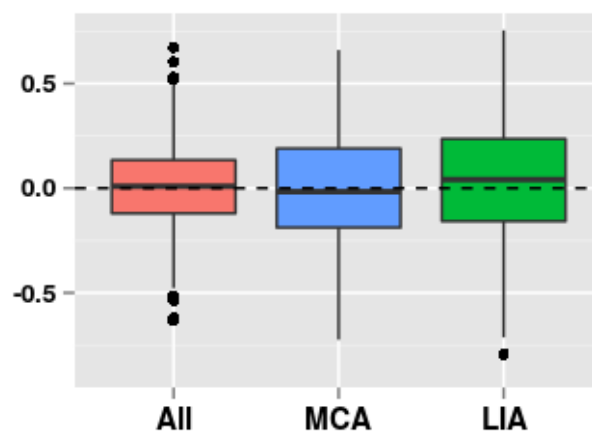


FIGURE 4.8: Correlations between the temperature and precipitation ensemble members based on 1000 randomly chosen pairs, for the period 100-1500 yrBP ('All') and the MCA and LIA individually. See Figure 4.4 for explanation of the box plots and significance.

to categorically determine a systematic difference between the ENSO signals in temperature and precipitation proxies.

The definitions of the MCA and the LIA used here are based on those given by Yan et al. (2011b); there are many alternative definitions, however (Jones & Mann, 2004). To test the sensitivity of the results to the definition of these periods, we recalculated the LIA-MCA difference using two widely used alternative

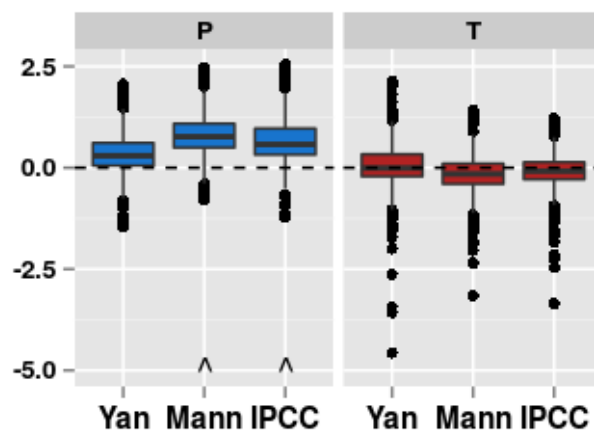


FIGURE 4.9: As Fig 4.7, done for the three MCA and LIA definitions listed in Sect 4.4. ‘Yan’ refers to the definition used in Yan et al. (2011b), ‘Mann’ in Mann et al. (2009), and ‘IPCC’ in Masson-Delmotte et al. (2013). See Figure 4.4 for explanation of the box plots and significance.

definitions: from Mann et al. (2009) (MCA = AD 950–1250, LIA = 1400–1700) and the Intergovernmental Panel on Climate Change (IPCC) Fifth Assessment Report (MCA = AD 950–1250, LIA = 1450–1850; Masson-Delmotte et al., 2013, Figure 4.9). For precipitation, the difference between the two period is more pronounced for the alternative definitions, with a weakly significantly more El Niño-like LIA ($p < 0.1$). For temperature there is very little change; although the median is negative for the alternative definitions, the interquartile range still encompasses zero. The precipitation reconstruction thus suggests that the LIA was more El Niño-like than the MCA, but our conclusion that there is no evidence for any precipitation–temperature correlation stands.

4.5 Discussion

An important question addressed in this study is whether the modern-day links between ENSO-like temperature and precipitation persist back in time. There is no concrete evidence in this study of any correlation between the precipitation and temperature reconstructions, whether positive (as in the modern day) or negative (as suggested by Yan et al., 2011b). This is contrary to expectations based on instrumental and modelling data, which both show a strong relationship between ENSO-like precipitation and temperature (Section 3.3). The fact that the

palaeodata apparently does not display this relationship over the past two millennia (cf Yan et al., 2011b, and this study) is thus interesting from a physical dynamical point of view as it contradicts our conventional understanding of long-term ENSO-like climate change.

There is also no evidence in the two reconstructions presented here that there was any significant difference in the mean ENSO-like climate state during the MCA and the LIA. This is contrary to the findings of Yan et al. (2011b). They create a SOI reconstruction (SOI_{pr}) from two precipitation proxies from the Galápagos (Conroy et al., 2008) and the Indo-Pacific Warm Pool (Oppo et al., 2009), weighting them according to the relationship of local rainfall to the instrumental SOI. Interestingly, SOI_{pr} shows broad trends opposite to the precipitation reconstruction presented here, with a more La Niña-like LIA compared to the MCA. While the two proxies used were considered for this study, they were both rejected due to high dating errors (average around 100 years). Several other precipitation (Tierney et al., 2010, Yan et al., 2011b) as well as temperature (Conroy et al., 2010) proxies supporting conclusions of the Yan et al. (2011b) study were similarly rejected due to high dating errors, as were proxies supporting the opposite conclusion (Conroy et al., 2009, Partin et al., 2007). Testing showed that applying the method described here using only the two proxies used by Yan et al. (2011b) produced highly similar results to their SOI reconstruction, suggesting it is not a methodological difference but rather related to proxy selection. A reconstruction based on only two (poorly dated) proxies is likely to be more vulnerable to spurious noise or other climatic influences distorting the signal, as is evidenced by the degradation back in time of the reconstructions presented in this study as the number of proxies declines. This highlights the need for more accurately dated proxy records, which remains an issue for low-resolution but long proxy archives such as marine sediments (Jones & Mann, 2004).

A number of other (non-temperature or precipitation) ENSO-sensitive proxies that were not included in our reconstructions provide evidence for a more La Niña-like climate state in the MCA compared to the LIA, although the mean state of the LIA appears inconsistent. Sedimentary sterol concentrations in marine sediment off the Peru coast Makou et al. (2010) suggest the MCA coincides with a reduction in El Niño activity, with both El Niño and La Niña activity increasing from the late MCA onwards. Based on a range of North American proxies Graham et al. (2007) conclude that the MCA was characterised by arid conditions in western

North America consistent with a La Niña-like state, followed by a wetter LIA. A basin ventilation record from the Western Pacific Warm Pool (WPWP; Langton et al., 2008) agrees particularly well with the earlier part of our precipitation reconstruction. It shows a peak in El Niño activity at ~ 1150 yrBP and a distinctive minimum during the MCA, followed by a more El Niño-like LIA characterised by a steady decline in activity. This decline is not apparent in our reconstruction, but is reflected in some other multi-millennial proxy records (Conroy et al., 2008, Moy et al., 2002, Stott et al., 2004).

Most multi-proxy reconstructions of ENSO variability are temperature-based, and focus on NINO regions. A NINO3 region (90°W – 150°W and 5°S – 5°N) temperature reconstruction by Mann et al. (2009) shows a slow millennial-scale warming trend (to a more El Niño-like state) from AD 1100 onwards, with relative cooling during the MCA compared to the LIA consistent with a La Niña-like state during the MCA. In contrast, Emile-Geay et al. (2013b) are unable to detect a systematic difference between the MCA and LIA in their Boreal winter NINO3.4 (120°W – 170°W and 5°S – 5°N) SST reconstruction, which is consistent with the findings of this study. The discrepancy between the two ENSO reconstructions may be due to the difference in proxy networks, particularly the use of lower-resolution proxies here and by Mann et al. (2009) which contribute a substantial part of the signal, due to the slightly different definition of the NINO regions, or the target season (Boreal winter versus annual). Other reasons may be related to the methodology or target instrumental dataset, particularly for low-frequency variability and amplitude. Work by Emile-Geay et al. (2013b) indicates that the results of many temperature reconstruction methods are sensitive to the target SST dataset used for calibration, and Wang et al. (2015) find that the La Niña-like pattern in the MCA evident in Mann et al. (2008) is not a robust feature across CFR methods. The fact that multi-proxy reconstructions are less likely to show strong differences between the ENSO-like state of the MCA and the LIA again highlights the potential sensitivity of individual records to non-physical trends, and suggests that conclusions drawn from single proxy records must be considered with caution. The lack of a coherent and strong difference between the ENSO-like state of the MCA and the LIA among (multi)proxy reconstructions may indicate that these periods indeed did not have a significant expression in ENSO-sensitive regions, as suggested by the lack of globally coherent warm and cool periods in regional temperature reconstructions (Consortium, 2013, Neukom et al., 2014). Conversely, it may

suggest that there is no direct relationship between long-term regional to global temperature anomalies and ENSO-like state of the climate. Further research into the physical and mechanistic interactions between global temperature and ENSO dynamics over long timescales is needed to throw more light on this. Comparative studies of the MCA and the LIA must thus be approached with caution for low-latitude and SH study areas, as their definitions are not necessarily rooted in real climatic events outside the NH.

There is some evidence that ENSO modulates the Pacific Decadal Oscillation (PDO; Zhang et al., 1997) on multidecadal timescales over the instrumental period (Newman et al., 2003) and further back in time (Verdon & Franks, 2006). The PDO is an SST anomaly pattern resembling ENSO located in the extratropical North Pacific ($20^{\circ}\text{N} - 45^{\circ}\text{N}$). Comparison of the precipitation reconstruction in this study with a reconstruction of the PDO over AD 993–1996 (MacDonald & Case, 2005) shows a slight tendency for the precipitation and PDO series to have the same sign over the MCA and LIA separately, although the relationships are not statistically significant (not shown). There is no indication of any relationship between the PDO and the temperature reconstructions, despite the fact that many of the temperature proxies are located in potentially PDO-sensitive areas (most notably North America). MacDonald & Case (2005) find a strongly negative PDO during the MCA (roughly equivalent to a La Niña-like spatial pattern), which corresponds to the qualitatively La Niña-like tendency of the precipitation reconstruction presented here. While there may be some conflation of ENSO and PDO signals in the reconstructions due to the similarity of their spatial patterns, it is not possible to distinguish these signals here. Moreover, the lack of correlation with the PDO reconstruction suggests the reconstructions presented here are distinct from the PDO. D'Arrigo & Wilson (2006) find no significant correlation between the 9-year smoothed reconstruction of the Asian expression of the PDO (based on East Asian tree rings as opposed to the often-used North American tree rings) and Boreal winter NINO3 SST, suggesting the ENSO-PDO link may be spatially variable.

An issue not addressed in this study is the role of different 'flavours' of ENSO patterns. A different type of ENSO pattern, first defined by Ashok et al. (2007) and dubbed ENSO Modoki, differs from the traditional ('canonical') ENSO pattern in the shift of positive SST anomalies from the western Pacific (mainly in NINO3 and NINO3.4) to the central Pacific (NINO4; $170^{\circ}\text{W} - 120^{\circ}\text{W}$ and $5^{\circ}\text{S} - 5^{\circ}\text{N}$), and its mid-latitude teleconnections. It is sometimes defined as the EOF2 of detrended

SST data (note that the data in this study was not detrended, hence here it would be EOF3; Ashok et al., 2007, Cai et al., 2015a,b), or a combination of EOF1 and EOF2 (Karamperidou et al., 2015, Takahashi et al., 2011). Some modelling studies suggest that ENSO Modoki will increase in frequency compared to canonical ENSO as a result of anthropogenic climate change (Cai et al., 2015a,b, Kim & Yu, 2012, Yeh et al., 2009), and there is some model evidence that ENSO Modoki was also more common in the mid-Holocene (Karamperidou et al., 2015). The difference in equatorial spatial pattern and teleconnections has implications for the interpretation of the proxy reconstructions in this study, as ENSO Modoki-like climate change may appear here as a reduction in ENSO-like activity.

The poor quality of the temperature reconstruction, which limits the statistical robustness of the precipitation–temperature comparison, is likely due to the low number and unequal distribution of available data locations. Most temperature proxies are located in teleconnected regions outside the ENSO source region, which have been shown to be subject to more temporal variability in precipitation–temperature relationships (Coats et al., 2013, Gallant et al., 2013, Lewis & Legrande, 2015, Wilson et al., 2010). A multi-region tree ring reconstruction of ENSO variability displays substantial variability in the strength of ENSO teleconnections over time and space (Li et al., 2013b). The authors find that the Pacific Northwest and Texas-Mexican regions show highly unstable teleconnections (although there is no discussion on whether this is related to the different ENSO flavours). This may explain the lack of signal in the temperature reconstruction presented here, as many of the temperature proxies are located in these teleconnected regions (Figure 4.6). If the strength of the teleconnection has indeed changed over time, the weightings based on modern-day ENSO patterns would not reflect this; thus this reconstruction should be regarded as an indication of change of the modern-day ENSO-like climate pattern only. Without proxies located in the centre of action or more robustly teleconnected areas, the loss of signal due to unstable teleconnections can be expected to be substantial as suggested by the results presented here.

An interesting observation of the EOF maps presented here (Figures 4.5 and 4.6) is the low to no correlation between EOF weighting (bubble shading) and how often proxies are used (bubble size). Correlations of temperature proxy frequency of occurrence versus GCM-derived and 20CRv2c-derived EOF weighting are 0.23 and 0.20, respectively ($p < 0.05$); there is no significant correlation for temperature

proxies ($p > 0.54$). Two possible explanations for this are i) the climatic noise in the high-occurrence but low-weighted areas is less spatially correlated with the noise elsewhere than in the low-occurrence but higher weighted areas; or ii) the length and resolution of the proxy records have a more important effect on a proxy's utility than its weighting. For instance, the proxies off the Australian coast and in the west Pacific islands are mostly short (< 500 years) coral records; while several of them have high weighting, their frequency of occurrence is very low. The proxy at the southern tip of Australia, in contrast, is a ~ 3600 year long tree ring record, and is the most frequently used temperature proxy. Overall, however, temperature proxy length is only very weakly correlated to occurrence frequency ($R = 0.17, p < 0.05$). The SNR assigned to the temperature pseudoproxies is similarly only very weakly correlated to frequency ($R = 0.13, p < 0.05$). In the precipitation case, neither length nor SNR are significantly correlated to how often the proxies occur in the ensemble. The selection process is likely driven by a combination of these factors rather than any single factor, and is modulated by the number of proxies available. More detailed analysis will be needed to elucidate this.

4.5.1 Reflections on the method

The method set out in this study is one of few which attempt to take into account the effect of real spatial *and* temporal patterns of proxy records, thus increasing our confidence in their ability to accurately evaluate the effectiveness of the networks. To our knowledge, this is the only study in which realistic temporal proxy resolution has been taken into account by the pseudoproxies, in addition to their length. This is an improvement of the pseudoproxy design used by, for example, Wang et al. (2014a), who take into consideration the declining proxy availability back in time but not their resolution. The authors find that this already significantly impacts the quality of multi-proxy reconstructions, so the inclusion of proxy resolution as done here is likely to have further impacts. More extensive research is needed to quantify this however.

The 'optimal' network creation still has scope for improvement. Although we have screened for maximum dating errors, its effect on the included proxies is

not explicitly assessed. This issue is often neglected in (multi) proxy reconstructions (but see Comboul et al., 2014, for a recent effort to address it systematically). Moreover, the noise simulation used here is relatively simplistic; the use of a wider noise spectrum (including red, and possibly even blue, noise) may alter the composition of the networks (Smerdon, 2012, and references therein). However, the issue remains that there is no easy way to determine the real noise spectrum of the proxies. With the advent of more isotope-enabled GCM simulations, further improvement could come from the use of proxy system models to estimate more accurately the proxy-climate relationships (cf Conroy et al., 2008, Dee et al., 2015, Evans et al., 2013, Russon et al., 2013, Stansell et al., 2013, Steinman et al., 2012, Sturm et al., 2010, Thompson et al., 2011, Tierney et al., 2011).

The choice of dataset from which to derive an EOF is also a source of uncertainty (cf Emile-Geay et al., 2013b), as differences in the EOF pattern will affect the weighting of the proxies. This is particularly pertinent for the precipitation reconstruction, as the modern-day ENSO precipitation signature is much less well-established than for temperature due to less and lower quality instrumental data. This is partially tested by using different GCMs to calibrate and validate the proxy networks. However, the true ENSO-like pattern has been non-stationary over time, as has been shown to be true in 20CRv2 for the NAO and Pacific North American (PNA) pattern, for example (Raible et al., 2014). We tested the stability of the 20CRv2c temperature EOF used in this study by recalculating it for a running 30-year window and found substantial variability in the spatial pattern and amount of variance captured by the EOF. Further investigation is necessary to explore whether this result is an artefact of internal variability, is due to uncertainties in the reanalysis dataset, or reflects real changes in the nature of ENSO. Nevertheless, it highlights the vulnerability of the majority of ENSO reconstructions (including ours) to the assumption that the modern-day ENSO is a good analogue for the past.

4.6 Conclusions

This chapter has presented two reconstructions of ENSO-like climate change, based on temperature- and precipitation-sensitive proxies respectively. The quality of the reconstructions degrades further back in time as there is less proxy data available, which is particularly detrimental to the temperature reconstruction. The main implications of these reconstructions are:

1. We find no evidence that temperature and precipitation proxies disagree over the ENSO-like state of the climate during the past two millennia. The two reconstructions in fact show little to no correlation, which is surprising as there is a strong relationship between temperature and precipitation ENSO behaviour at interannual timescales in instrumental/reanalysis data and GCMs.
2. The precipitation reconstruction shows a tendency for a more El Niño-like LIA compared to the MCA, but the difference is not statistically significant and is not apparent in the temperature reconstruction. This result is insensitive to the choice of definition for the MCA and LIA.
3. A major limitation on our ability to accurately reconstruct ENSO-like climate change back in time is the lack of high-quality, long proxy records in the tropical and subtropical latitude bands, and we reiterate the need for continued efforts to collect such data. The discrepancies between the two series presented here and many other interannual and (multi-)decadal ENSO reconstructions are more likely to be reconciled with denser proxy networks in the ENSO source region, along with resampling of existing locations to increase the signal to noise ratio (Wang et al., 2014a). The pseudoproxy experiments described in this paper can quite easily be adapted to search for optimal locations from which additional proxy information would be the most beneficial, as previously done specifically for corals by Evans et al. (1998) (see also Comboul et al., 2015, for a recent endeavour).
4. A final caveat is the reliance on modern-day ENSO patterns and the implicit assumption of its stationarity through time. Continued improvements in the ability of GCMs to accurately simulate and reproduce ENSO behaviour in

conjunction with more high-quality proxy data will give both the palaeocommunity and the modelling community an increasingly reliable foundation for creating, calibrating and evaluating palaeo-ENSO reconstructions.

Chapter 5

Precipitation and fire in the Indonesian region over the past two millennia

5.1 Introduction

Large-scale fire events and associated haze in the Indonesian region over the past few decades have had devastating effects on biodiversity, local and regional economies and human health (Field, 2004, Goldammer, 2007, Heil & Goldammer, 2001, Kovats et al., 2003, Wang, 2004) and have contributed significantly to atmospheric CO₂ (Page et al., 2002, van der Werf et al., 2008). Satellite data from the past few decades (Fuller & Murphy, 2006, Giglio et al., 2010, Wooster et al., 2012) suggests that on interannual timescales, the El Niño/Southern Oscillation (ENSO) plays a significant role in modulating fire behaviour in this region by influencing precipitation patterns. However, this period is also characterised by extensive anthropogenic impact, for example in the form of logging, peatland drainage and agricultural activity. This alters the fire regime by drying out peat forests, increasing dead fuel availability, and (accidentally or intentionally) igniting fires (Anshari et al., 2010, Hergoualc'h & Verchot, 2011, Langner & Siegert, 2009).

The question remains whether the current-day interannual relationship between precipitation and fire in the Indonesian region also occurs over timescales of centuries to millennia, and whether it has been altered significantly by human involvement. El Niño events are characterised by drought over Indonesia, which leads to drying out of the peat swamp forests and heightens the risk of fire. There is also evidence for increased lightning activity during these warm episodes (Kumar & Kamra, 2012, Sátori et al., 2009, Williams, 2005, Yoshida et al., 2007), which promotes natural ignition. However, these processes have only been assessed on seasonal to interannual scales; long-term biomass variability and links with the climate are less well understood. Global syntheses of millennial fire behaviour using charcoal data and simulated palaeo-precipitation point to a non-linear inverse relationship between biomass burning and precipitation, with highest fire activity at intermediate levels of rainfall (Daniau et al., 2012). A Holocene (12ka) regional analysis of the Asia-Monsoon region (10°N-45°N, 65°E-150°E) based on a comparison with one precipitation proxy (Marlon et al., 2013) similarly finds an increase of fire with decreasing moisture. This suggests that the modern day ENSO-induced fire variability in the Indonesian region mirrors long-term processes. However, there have been no comprehensive comparisons of charcoal and proxy precipitation records, despite the important role this area plays in the global carbon cycle and its apparent sensitivity to hydrological changes (Page & Hooijer, 2016, Page et al., 2002, Yu et al., 2011).

Much of the forest covering Indonesia is peat swamp forest, representing a major fraction of the world's tropical peatlands (Yu et al., 2011) and storing an estimated 57 GtC (Page et al., 2011). In their pristine state, these forests have a dense canopy and are characterised by a high water table (Page & Hooijer, 2016). Both contribute to moisture retention, making the forest highly resistant to fire (Bowman et al., 2011). Fires in dense, tall vegetation stands are more likely to start in the understory, only transferring to the canopy in severe fires. This stands in contrast with savannah and shrubland, which is much more susceptible to widespread and total burning. Generally, fire regimes in tropical forests are largely modulated by fuel moisture, whereas savannah fires are constrained mostly by fuel availability (Krawchuk & Moritz, 2011).

The recovery time after a fire event is much longer for trees than for ground vegetation. The severity and frequency of fires can thus alter the vegetation composition of an area (Cochrane, 2003). During small or intermediate fire events,

it is likely that only the understory of a forest is lost. In this case, fire risk may be temporarily suppressed due to lack of flammable material until the understory vegetation has recovered, although post-fire mortality due to damage could increase the amount of dead wood and litter sooner. Small and frequent fires can be sustained in a forested area, and may even be beneficial as they prevent fuel build-up, clear the forest floor, return nutrients to the soil, can kill disease and open up habitats for wildlife (Fredericksen & Fredericksen, 2002).

Low-intensity and low-frequency fire regimes have been shown to allow peat forests to recover through secondary succession (Page et al., 2009a). If the fires are severe and/or frequent enough, however, it will have a long-lasting impact on the post-fire vegetation composition. Grasses, shrubs and other non-woody vegetation are the first to recolonise a burnt area before the more slow-growing trees. If the damage to the forest is extreme enough, the area may get locked into a positive feedback loop (Cochrane, 2003); the flammable grass promotes fire, which in turn encourages more extensive grass coverage leading to more fire and little chance of forest recovery (Hoscilo et al., 2011, Page et al., 2009b).

The density of tropical forest fires results in a relatively small burnt area relative to the fuel consumed, and high CO₂ emissions per unit area. A review of biomass burning fuel consumption rates (Van Leeuwen et al., 2014) found that fuel consumption in tropical forests can be an order of magnitude higher than in savannah. The high C content of the Indonesian peat soils gives this tropical peatland biome the highest fuel consumption rates in the world, further increasing the potential CO₂ emissions from fires in this region (Page et al., 2013, Van Leeuwen et al., 2014). Tropical savannah is prone to frequent fires due to high flammability of its vegetation in combination with lightning and fire-promoting weather conditions (a combination of low humidity, warmth and windiness; Bowman et al., 2011). Estimates of global fire frequency in savannah biomes between 2001-2009 show an average burning of up to once every four years (Van Der Werf et al., 2010). The high fire frequency limits woody growth, which in turn lowers fuel consumption and CO₂ emissions.

This chapter explores the question of long-term (centennial) relationships between precipitation and biomass burning over the Indonesian region. The past two millennia have been punctuated by several significant climatic upheavals, including the Medieval Climate Anomaly (MCA, AD 800–1300) and the Little Ice

Age (LIA, AD 1400–1850; definitions based on Yan et al., 2011b). These two long-term climate anomalies are widely acknowledged to be at least NH phenomena, although whether they were global events is disputed (Consortium, 2013, Jones & Mann, 2004, Neukom et al., 2014, see also 2.3.3.3, 4.5). Focusing on this period enables an evaluation of the impact of climatic variability on fire regimes, and exploring potential feedbacks on the carbon cycle. Using networks of charcoal records and precipitation proxies, the fire and hydrological histories are reconstructed and their relationship elucidated.

Section 5.2 describes the data and methodology employed in this chapter. The results are presented and discussed in 5.3, before highlighting the main issues and remaining questions in 5.4.

5.2 Data and methods

The focus of this study is the wider Indonesian region, which is defined here as 30°S–15°N, 100°E–200°E, and where ENSO alters the hydroclimate (As-syakur et al., 2014, Climate Prediction Center Internet Team, 2012). These boundaries also maximise the number of proxy records available whilst minimising influence of the South Asian Monsoon. The study region precipitation regime is dominated by two monsoonal systems, the East Asian Summer Monsoon (EASM) in the north and the Australian Summer Monsoon (ASM) in the south. The EASM is strongest during the boreal summer (JJA), while the ASM is most active in the austral summer (DJF). Both monsoon systems are driven by seasonal shifts in the intertropical convergence zone (ITCZ).

5.2.1 Data selection

The Global Charcoal Database Version 3.0.5 (GCDv3.0.5; <http://www.paleofire.org/>) made available by the Global Palaeofire Working Group (GPWG; <http://www.gpwg.paleofire.org/>), is a collection of terrestrial and marine sedimentary charcoal records and provides metadata including dating methods, site characteristics, and sampling methods. This database has formed the basis for a number of global (Daniau et al., 2012, Marlon et al., 2008, 2013, Power et al.,

2008) and regional (Mooney et al., 2011, Power et al., 2013a, Vanniere et al., 2011) syntheses of past biomass burning at centennial to millennial scales.

The recently developed `paleofire` package (Blarquez et al., 2014) for open-source programming language R (R Core Team, 2016) is designed to extract charcoal data from the GCDv3.0.5 and perform various forms of analysis to reconstruct past biomass burning (Marlon et al., 2008, Power et al., 2008). This package was used in this study to extract charcoal data and perform the bulk of the analysis.

Sedimentary charcoal records from the wider Indonesian region were extracted from the GCDv3.0.5 and screened to ensure all records have data after 1000yr BP, resulting in 74 records. Fourteen precipitation records for the same region were downloaded from the NOAA Paleoclimate Database (<https://www.ncdc.noaa.gov/data-access/paleoclimatology-data>) and screened for the same temporal requirements. These are a subsection of the precipitation proxies used in Chapter 4 (see also Appendix A). The precipitation data files were formatted such that they were compatible with the `paleofire` package, enabling identical processing of the charcoal and precipitation data.

5.2.2 Data transformation

The charcoal and precipitation records were first standardised to homogenise their units and enable comparison. Charcoal records given in concentrations were first converted to influx values by multiplying the data by sediment accumulation rates (cm yr^{-1}) derived from their respective age-depth models. All converted charcoal series and precipitation proxy series were then subjected to a minimax rescaling, which rescales the values of each record to fall between 0 – 1 (Section 3.5.1, Eq. 3.13).

The data were then transformed to a normal distribution using a Box-Cox transformation (Sect. 3.5.2; Box & Cox, 1964), which serves to homogenise the variance of the data:

$$c_i^* = \begin{cases} \frac{(c_i + \alpha)^\lambda - 1}{\lambda} & \text{if } \lambda \neq 0 \\ \log(c_i + \alpha) & \text{if } \lambda = 0 \end{cases} \quad (5.1)$$

α was set to 0.01, and λ was estimated by maximum likelihood (Venables & Ripley, 2002).

This was followed by another minimax transformation (to ensure identical λ values necessary for comparability between Box-Cox transformed series; Blarquez et al., 2014, Marlon et al., 2008) prior to Z-score calculation (Section 3.5.1, Eq 3.14). The base period for the Z-score calculation was set to 100–2000 yr BP. The most recent \sim 200 years were excluded from the base period to reduce the influence of anthropogenic activity on the fire record (Power et al., 2008). The choice of base period and standardisation of the data has been shown to have an insignificant effect on the signal of the data (Marlon et al., 2008, Power et al., 2010).

5.2.3 Compositing and smoothing

The standardised data were used to create two composite series: a simple binned series (BIN) and a smoothed curve (LOW). The BIN series was created by taking the mean of all individual records over 200-year non-overlapping windows, equivalent to the method used by (Power et al., 2008). Following the method described by (Marlon et al., 2008) and (Daniau et al., 2012), the LOW curve was created in two stages: first, individual records were pre-binned over 20-year non-overlapping windows. This serves to reduce the influence of high-resolution records and prevents interpolation of low-resolution records. Section 3.6.1 provides more detail on binning techniques and parameter sensitivity.

The pre-binned series were then smoothed using a locally weighted scatterplot smoothing (LOWESS; Cleveland, 1979, see also 3.6.2) regression with a fixed 200-year smoothing window. To calculate confidence intervals, the pre-binned series were bootstrap re-sampled and fitted with a LOWESS curve for 1000 iterations. The confidence intervals at each target point were defined by the 5 – 95th percentile of the bootstrap results. To correct for the edge effect potentially introduced by the LOWESS, a ‘minimum slope’ constraint (Mann, 2004) was applied prior to fitting the regression. This involved padding both ends of each resampled series with 10% of the data reversed in time, which pulls the smoothing slope towards zero near the time boundaries (Blarquez et al., 2014, Mann, 2004).

5.2.4 Statistical fire - precipitation models

As the relationship between charcoal abundance and precipitation is known to be non-linear (Daniau et al., 2012, Marlon et al., 2013), we fitted generalised additive models (GAMs; 3.6.3) to the charcoal and precipitation curves using the `gam` and `gamm` routines from the R package `mgcv` (Wood, 2006, 2011). GAMs are flexible, empirically fitted statistical models which create smooth functions linking a response variable (in this case, the charcoal composite) with one or more predictors (the precipitation composite). More mathematical background on GAMs and some parameter choices applied in this section are given in 3.6.3. The equation for GAMs (Eq. 3.20) is recalled here:

$$g(\mu_i) = \mathbf{X}_i^* \boldsymbol{\theta} + \sum_{j=1}^p f_j(\mathbf{X}_j) + \varepsilon \quad (5.2)$$

Three subsets of the charcoal and precipitation curves were tested: 1) the full (0–2000yr BP) period (2ka), 2) the MCA period, and 3) the LIA period. Following the method of (Marlon et al., 2013), the 200-year smoothed series were first binned over 60-year intervals to reduce pseudoreplication prior to fitting a GAM to each subset. The value of basis dimension k was determined by firstly maximising Aikake’s Information Criterion (AIC):

$$AIC = -2LL + (2K) \quad (5.3)$$

Where LL is the model Log Likelihood and K is the number of model parameters. If the resultant estimated degrees of freedom (df) of the smoothing function were estimated to be too close to $k - 1$ (which generally occurs when k is too small and makes the model prone to over-smoothing), the preliminary estimation of optimal k was followed by manual adjustment. The suitability of k was tested using the `gam.check` function from `mgcv` (a manual check can also be performed by fitting the same smooth to the deviance residuals of the original model using a substantially larger k to check whether any pattern in the residuals could potentially be explained by increasing k).

If the GAM residuals were serially autocorrelated, the model was updated to a generalised additive mixed model (GAMM), which allows for autoregressive error

structures (Wood, 2006). The general autoregressive-moving average model (ARMA Davison & Hinkley, 1997) was applied to achieve this. More mathematical detail is provided in 3.6.3; for clarity equations are repeated here for GAMMs:

$$g(\mu_i^b) = \mathbf{X}_i\boldsymbol{\beta} + \sum_{j=1}^p f_j(\mathbf{X}_j) + \mathbf{Z}_i\mathbf{b} + \phi_i \quad (5.4)$$

and for ARMA:

$$\phi_t = \sum_{i=1}^p \alpha_i \phi_{t-i} + \varepsilon_t + \sum_{i=1}^q \beta_i \varepsilon_{t-i} \quad (5.5)$$

5.3 Results and discussion

5.3.1 Data characteristics

The charcoal and precipitation records used in this study are listed in Appendix B. The data are unevenly distributed, with a higher concentration of records on the island of New Guinea and along the coast of Western Australia (Figure 5.1). The paucity of records in the rest of Indonesia and central Australia is likely due to difficult field work conditions and a lack of suitable conditions for charcoal preservation (Mooney et al., 2011). The climatic and vegetational characteristics of the charcoal records are reasonably representative of this region, although there is a slight bias towards forested biomes compared to lower-density grassland and shrubland. However, this does not compromise the results as the main area of interest here is the impact of fire on tropical forest and peatlands in Indonesia. Roughly 43% (16 out of 37) of charcoal records located in the Southeast Asian section of the study region (north of 10°S) are explicitly recorded in GCDv3.0.5 as having a peaty site type (marsh, mire, bog or fen; see Table B.1).

The precipitation data is much sparser, but similarly provides a reasonable coverage of the main biomes of the region. The temporal coverage of the records varies mostly between charcoal and precipitation, with nearly all charcoal records starting before 1500 yr BP while roughly half the precipitation records start after

1000 yr BP (Figure 5.2). The longest precipitation records are favourably located for this study, on the Indonesian islands of Sulawesi and Java.

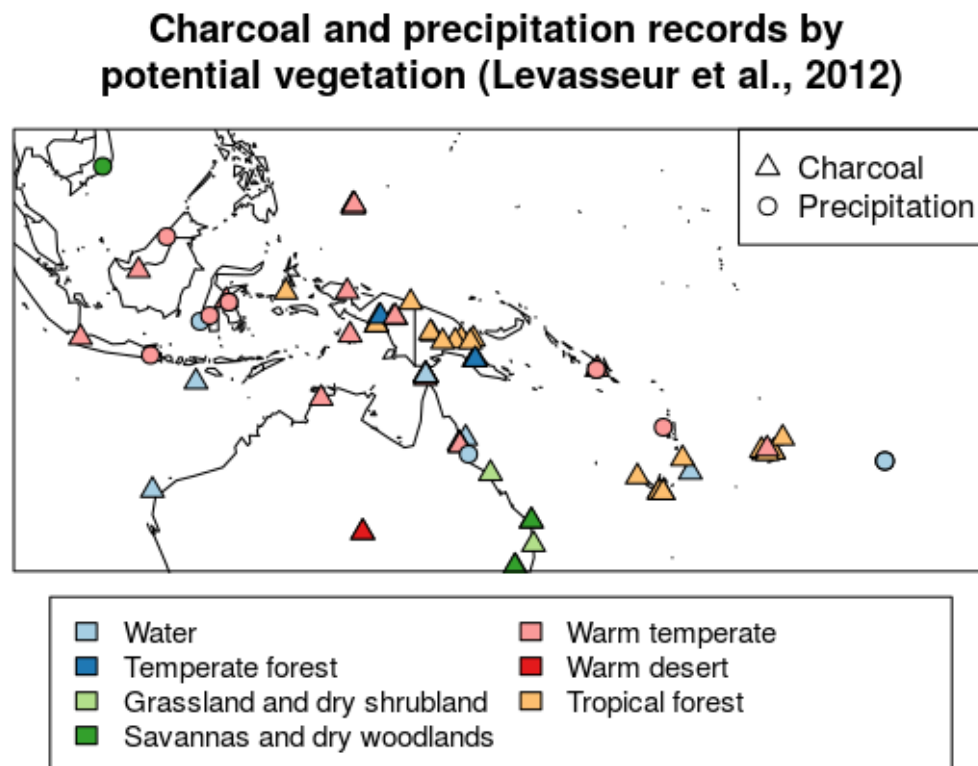


FIGURE 5.1: Potential vegetation maps (based on Levasseur et al., 2012) at charcoal (triangle) and precipitation (circle) record locations.

5.3.1.1 Vegetation

Most charcoal sites in the Southeast Asian part of the study region are in highly forested locations (Table 5.1). The Australian sites, in contrast, mostly fall in savannah or shrubland.

The forested parts of the study region have likely been characterised by persistent forest cover over the past 2000 years, with the most dramatic vegetation changes being driven by recent anthropogenic activities (Anshari et al., 2004, Cole et al., 2015). The Australian landscape has similarly been stable (Harrison & Dodson,

Charcoal and precipitation records by starting age

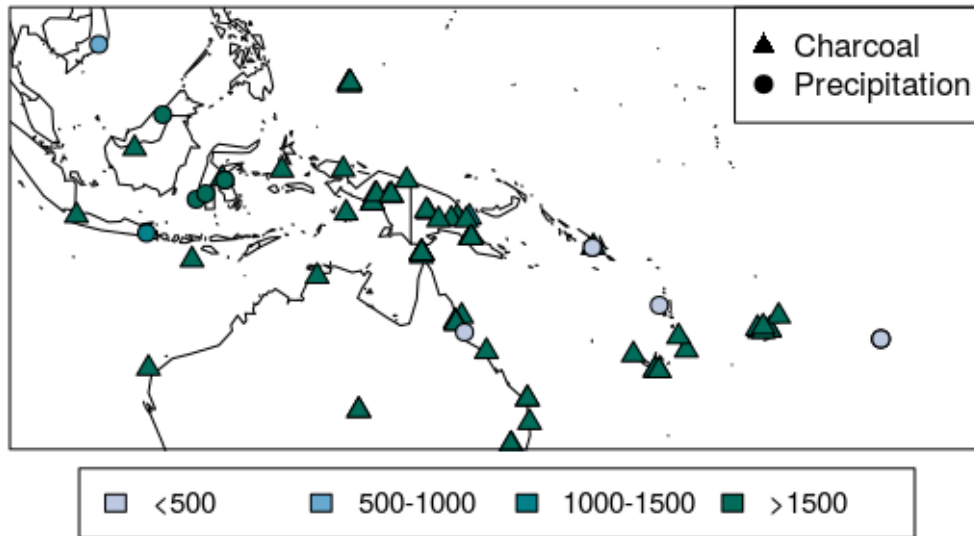


FIGURE 5.2: Starting age of charcoal and precipitation records. Ages are in yr BP.

1993, Pickett et al., 2004), although there is some debate regarding early aboriginal impacts on fire regimes (Haberle, 2005, Mooney et al., 2011, Williams et al., 2015).

5.3.1.2 Precipitation regimes

At a seasonal level, a change in precipitation during the wet season is likely to have a greater impact on fuel load and moisture than changes during the dry season. While only two of the precipitation proxies used in this study have seasonal resolution, they are all likely to be most sensitive to wet season variability as this is when the highest levels of deposition and accretion rates occur (e.g. Maupin

Density Biome		All	SE Asia	Australia
Low	barren	10	2	8
	desert	3	2	1
	tropical savannah	1	0	1
	tropical xerophytic shrubland	4	4	0
	Total	18	8	10
High	temperate evergreen needleleaf forest	4	4	0
	tropical deciduous broadleaf forest and woodland	9	0	9
	tropical evergreen broadleaf	23	17	6
	tropical semi-evergreen broadleaf	3	0	3
	warm-temperate evergreen broadleaf and mixed	12	8	4
	Total	51	29	22
Other	marine	3	0	3
	not known	1	0	1
	Total	4	0	4

TABLE 5.1: Summary of biomes at charcoal sites (from Table B.1). “SE Asia” is north and “Australia” is south of 10°S. The biomes are divided into low and high density vegetation types, which roughly separates savannah/shrubland from forest.

et al., 2014, Rasbury & Aharon, 2006, Rodysill et al., 2012). With the exception of the Buckley et al. (2010) tree ring record, all precipitation proxies are from ASM-sensitive locations. The composite record is thus likely largely a reflection of changes in austral summer precipitation, which coincides with the peak of ENSO activity (NOAA Earth System Research Laboratory, 2016). Several of the proxies are reported to be sensitive to ENSO variability on interannual scales (Buckley et al., 2010, Hendy et al., 2003, Rasbury & Aharon, 2006). Some are located in the South Pacific convergence zone (SPCZ) (Maupin et al., 2014, Partin et al., 2013, Rasbury & Aharon, 2006), which is influenced both by ENSO and Pacific decadal variability (PDV).

5.3.2 Temporal trends

The sedimentary charcoal record for the wider Indonesian region displays no overall trend, but does vary at centennial scales (Figure 5.3). The period of ~1700–800 yr BP is relatively stable, before increasing to a maximum at the start of the MCA (~800 yr BP). The MCA is characterised by a negative trend, followed

by an increase over the LIA. The precipitation record shows many similarities to the charcoal record, except for a strong negative excursion around ~ 1700 yr BP which is not present in the charcoal record. There is an upturn in biomass burning around 200 yr BP, concurrent with the global increase in biomass burning noted by Marlon et al. (2008). Estimates of population density and cropland and pasture area from the HYDE3.1 dataset (Klein Goldewijk et al., 2010, 2011) shows a sharp increase in all three variables synchronous with this post-industrial spike in biomass burning (Figure 5.7). The precipitation record, in contrast, is relatively flat over the last two centuries, which may suggest that anthropogenic influence, in the form of human-induced ignitions and increasing atmospheric CO_2 concentrations, are driving or exacerbating factors behind this increase in biomass burning (Mooney et al., 2011).

5.3.2.1 ENSO and the ITCZ

The charcoal curve presented here is very similar to an ITCZ region composite compiled by Mooney et al. (2011), which is unsurprising as the two study areas largely cover the same region ($20^\circ\text{S} - 20^\circ\text{N}$, $100^\circ\text{E} - 183^\circ\text{E}$ for the ITCZ composite). The two curves notably diverge between ~ 1800 - 1300 yr BP, however. Where our charcoal curve is relatively flat during this period, the ITCZ curve shows a peak roughly coinciding with the negative peak in the precipitation curve presented here. The main difference in terms of data is that the ITCZ excludes records from the 30 - 20°S band, which largely fall in savannah, grassland and dry shrubland vegetation zones (Figure 5.1). This suggests that these dryland records record less biomass burning than the tropical forest records. In terms of fire, this could be explained by relatively humid conditions suppressing fire activity, or conversely prolonged drought conditions (as hinted at by the precipitation curve) keeping the fuel load low. The low number of precipitation records contributing to the curve for the early time period precludes any definitive interpretations, however.

On decadal to centennial timescales, proxy (Haug et al., 2001, Hodell et al., 2005, Rustic et al., 2015, Sachs et al., 2009) and modelling (Broccoli et al., 2006) evidence points to a potential NH temperature forcing on the ITCZ, causing it to shift southwards in response to cooler NH temperatures. This hypothesis has been

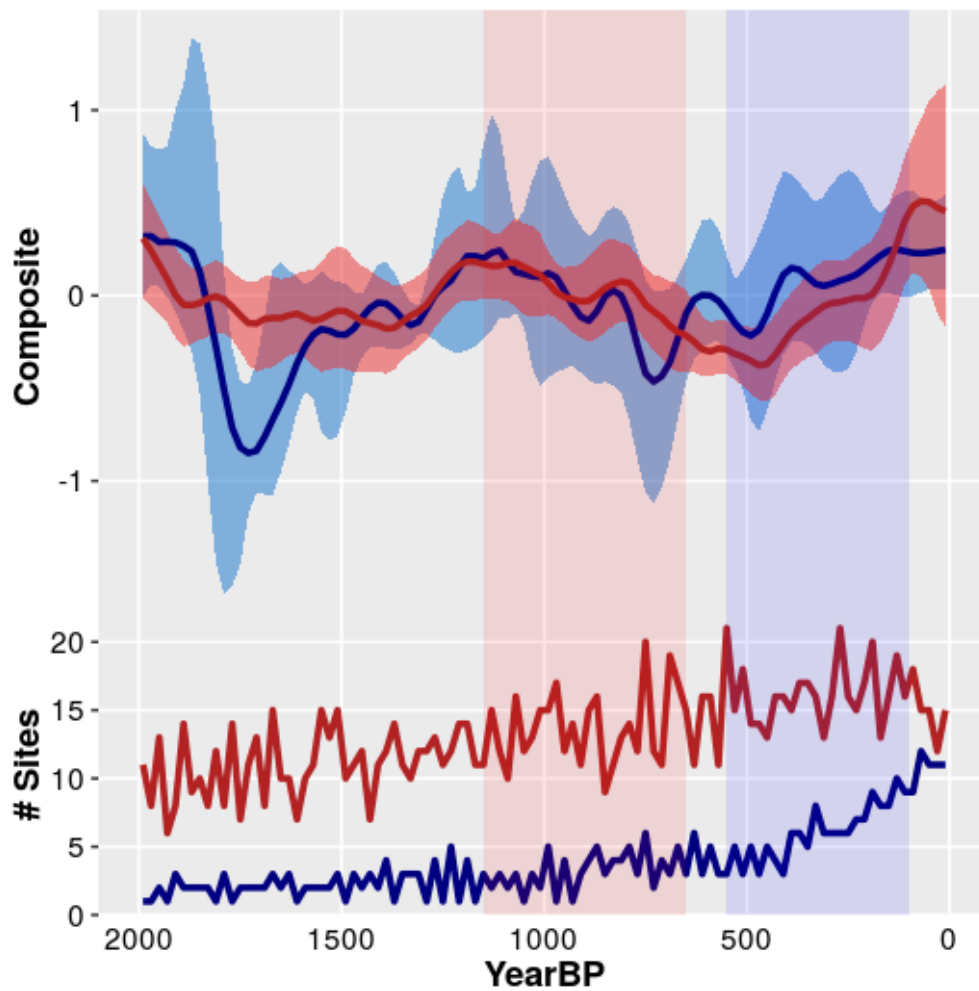


FIGURE 5.3: 200-year LOWESS smoothed composite curves (top) and sample density (bottom) for precipitation (blue) and biomass burning (red). Confidence intervals denote 5 – 95th percentiles of the bootstrapped series. Pink and blue shaded bands indicate the MCA and LIA intervals, respectively.

invoked to explain an apparent southward shift of the ITCZ during the LIA (Hodell et al., 2005, Rustic et al., 2015, Sachs et al., 2009). Similarly, there is evidence for a northward shift of the ITCZ during the MCA (Oppo et al., 2009, Sachs et al., 2009, Tierney et al., 2010, Wang et al., 2005, Zhang et al., 2008). A southward shift is analogous to an El Niño-like state (Deser & Wallace, 1990, Haug et al., 2001, Ivanochko et al., 2005), suggesting the MCA was characterised by a La Niña-like climate state and the LIA by an El Niño-like state. However, recent studies hint at an expansion and contraction of the ITCZ during the MCA and LIA respectively (Griffiths et al., 2016, Yan et al., 2015), which throws into question the degree to which these periods are ENSO-like. A contraction of the ITCZ is coupled with a strengthening of the Pacific Walker Circulation (PWC), and thus indicates a La Niña-like state during the LIA.

The precipitation reconstruction presented in Figure 5.3 shows a decreasing trend over the MCA followed by an increase over the LIA. If the same relationship between interannual ENSO and precipitation is assumed for ENSO-like state and precipitation on centennial timescales, this would suggest a slow oscillation from La Niña-like towards El Niño-like, followed by a return to a La Niña-like state over these two periods. The trends in Figure 5.3 are similar to the multiproxy reconstruction of East Indonesian hydroclimate in Griffiths et al. (2016, Figure 2; these data were not used to make the composite), which could be taken as corroboration of the contracting ITCZ hypothesis, though this is tentative without additional reconstructions from the EEP. There is rough resemblance between the precipitation composite and the precipitation reconstruction of ENSO-like climate change in Chapter 4 Figure 4.2, which suggests that the variations in the precipitation composite in Figure 5.3 indeed represent some long-term ENSO-like change (which supports a latitudinal shift in the ITCZ).

5.3.3 Fire and precipitation interactions

GAMs (Sections 3.6.3 and 5.2.4) were fitted to the 2ka, MCA and LIA datasets with respective basis dimensions (k) of 6, 4 and 4. The MCA and LIA model residuals showed no autocorrelation or partial autocorrelation. However, the 2ka GAM residuals were mildly autocorrelated, thus a GAMM was applied instead. After

testing ARMA(p, q) models for $0 \leq p, q \leq 3$, the optimal estimation of autoregressive-moving average model ϕ was found to be ARMA(1, 1). The test results are displayed in Table 5.2; note not all combinations of p and q are represented as some failed to converge. A lower AIC score indicates a more parsimonious (hence better) model. The p-value indicates whether the difference between two tested models (indicated under Test) is significant. The goal is to find the ARMA with lowest values of p and q which still significantly improves the model, hence the hierarchical process of testing ARMAs. A comparison of the original GAM and the GAMM using ARMA(1, 1) is shown at the bottom of the table. The difference is highly significant ($p \ll 0.001$) and reduces AIC from -8.2 to -22.7. The normalised residuals of the resulting GAMM were uncorrelated for the Box-Pierce test (Box & Pierce, 1970) and Box-Ljung test (Ljung & Box, 1978) ($p > 0.5$; Figure 5.4).

	Model	df	AIC	BIC	logLik	Test	L.Ratio	p-value
1	ARMA(0,1)	5	-19.899	-14.222	14.950			
2	ARMA(0,2)	6	-22.312	-15.499	17.156	1 vs 2	4.413	0.036
3	ARMA(0,3)	7	-19.738	-11.789	16.869	2 vs 3	0.574	0.449
4	ARMA(1,0)	5	-20.252	-14.574	15.126	3 vs 4	3.486	0.175
5	ARMA(1,1)	6	-22.727	-15.914	17.364	4 vs 5	4.475	0.034
6	ARMA(2,0)	6	-21.512	-14.699	16.756			
7	ARMA(2,1)	7	-20.814	-12.866	17.407	6 vs 7	1.303	0.254
8	ARMA(2,2)	8	-20.209	-11.125	18.105	7 vs 8	1.395	0.238
9	ARMA(3,0)	7	-20.114	-12.166	17.057	8 vs 9	2.095	0.148
10	ARMA(3,1)	8	-18.830	-9.746	17.415	9 vs 10	0.716	0.398
11	ARMA(3,2)	9	-20.630	-10.411	19.315	10 vs 11	3.800	0.051

	Model	df	AIC	BIC	logLik	Test	L.Ratio	p-value
1	ARMA(0,0)	4	-8.220	-3.676	8.110			
2	ARMA(1,1)	6	-22.727	-15.914	17.364	1 vs 2	18.507	$\ll 0.001$

TABLE 5.2: Comparison of different ARMA(p, q) models. df is degrees of freedom, AIC is Aikake's Information Criterion (Eq. 5.3), BIC is the Bayesian Information Criterion, logLik is the log-likelihood, Test indicates which two models are being compared (a vs b), L.Ratio is the likelihood ratio between models a and b , and p-value is the significance level of the improvement of model b over model a . Lower values of AIC, BIC, and p-value, and higher values of logLik and L.Ratio indicate better models. The best model ARMA(1, 1) is shown in bold, and comparison between this model and the original GAM (i.e. ARMA(0, 0)) is shown in the bottom two lines.

The models for all three periods show a significant ($p < 0.02$) relationship between biomass burning and precipitation (Figure 5.6). Daniau et al. (2012) use the fully coupled three-dimensional atmosphere-ocean-sea ice model ECBILT-CLIO

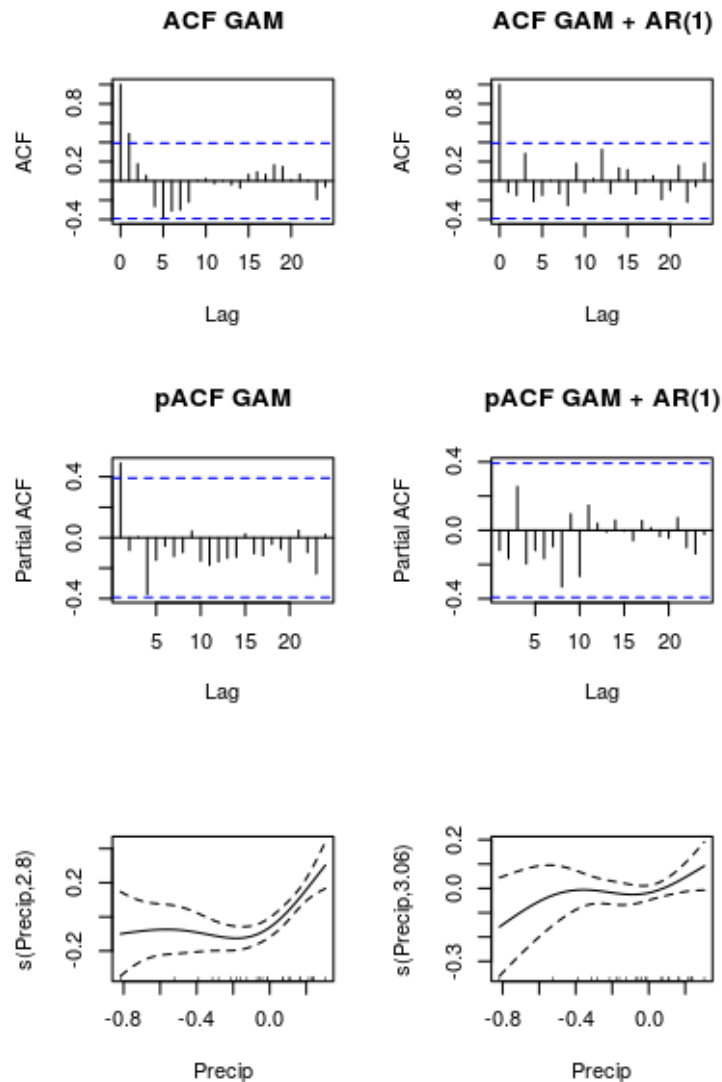


FIGURE 5.4: correlograms (ACF), partial correlograms (pACF) and model splines for the 2ka GAM (left; Eq. 5.2) and GAMM (right; Eq. 5.4). Blue dotted lines indicate estimated 95% confidence levels; data should only exceed this limit for the first lag in ACF, and not at all for pACF.

		2ka	MCA	LIA
Intercept	Estimate	0.034	0.036	-0.114
	Std. Error	0.092	0.023	0.041
	T-value	0.369	1.540	-2.824
	Pr(> t)	0.716	0.184	0.051
s(P)	edf	3.055	1.000	1.223
	F	9.325	17.930	12.820
	p-value	≪0.001	0.008	0.019
	R_{adj}^2	0.138	0.738	0.789
	-REML		-4.935	-1.650
	Deviance explained		0.782	0.841
	Scale est.	0.044	0.004	0.010
	n	25	7	6
ARMA(1,1)	α	0.652		
	β	1.000		

TABLE 5.3: Model summaries for the three fitted models. ‘s(P)’ is the smoothing spline, ‘edf’ is the estimated degrees of freedom for the model terms. ‘ R_{adj}^2 ’ is the adjusted R^2 , ‘REML’ gives the negative REML (only applicable for GAMs). α and β are the AR and MA model parameters (Eq. 3.25).

to produce a transient simulation of run-off (precipitation minus evaporation; P-E) and mean annual temperature (MAT) over the past 21ka, combining this with charcoal data over the same period to develop GAMs (Figure 5.5). The strength of the 2ka precipitation–biomass burning relationship presented in Figure 5.6 and Table 5.3 is the same in strength ($R_{adj}^2 = 0.14$) as the relationship between global simulated P-E and standardised charcoal found by Daniau et al. (2012), despite the differences in smoothing window (4000 years versus 200 years in this thesis), the time period considered (21ka versus 2ka), and the spatial scale (global versus Indonesian region). Similarly, a GAM model fitted by the same authors to annual CRU CL 2.0 P-E and GFED v3.1 burnt-area for 1996-2008 gives an R^2 -value of 0.17. This suggests that the *strength* of the precipitation-biomass burning relationship is relatively constant at different spatiotemporal scales, even if the *shape* of the relationship may not be. The shape of 21ka GAM cross-sections showing charcoal across P-E values (Figure 5.5c) is visually similar to the 2ka GAM spline, but the 2ka model shows stronger responses at both ends of the precipitation range. As standardised precipitation increases, so does charcoal abundance. At mid-range precipitation levels, the interaction with fire appears to be more muted, with a relatively steady fire response. The curvilinear nature of the model spline

is influenced by the precipitation dip around 1700yr BP, as confirmed by a re-fit of the model to a dataset truncated to 1500yr BP (not shown). Excluding the earliest 500 years from the model gives a much more monotonic positive relationship similar to those seen for the MCA and LIA (Figure 5.6 centre and right). The fire–precipitation relationship is much stronger over the MCA and LIA individually, with respective R_{adj}^2 values of 0.74 and 0.79. Using a GAM instead of a GAMM for the 2ka period, or assuming a linear relationship by calculating Pearson product-moment correlations directly from the curves, suggests a much stronger relationship ($R \sim 0.5$, not shown). This highlights the importance of taking into account autocorrelation when interpreting such composite curves (Daniau et al., 2012, Marlon et al., 2013, Wood, 2006).

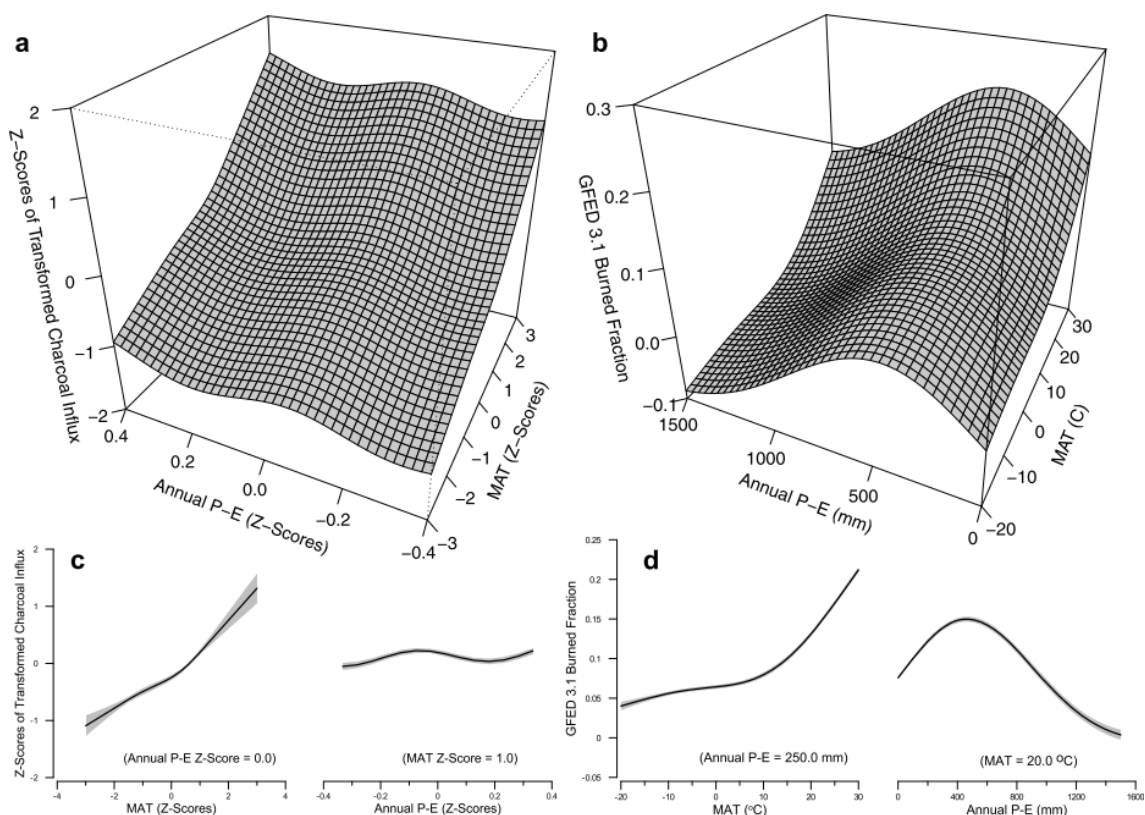


FIGURE 5.5: Daniau et al. (2012) GAMs showing global climate-biomass burning relationships over 21ka and in the modern day. a) 21ka GAM using palaeo-charcoal and ECBILT-CLIO simulated P-E and MAT (pre-binned to 20 years and LOWESS smoothed with a 4000-year window); b) GAM using GFEDv3.1 burnt area and CRU CL 2.0 P-E and MAT (annual resolution). c) and d) are cross-sections of a) and b), respectively, at constant P-E (left) and constant MAT (right).

As temperature variability in the tropics is small compared to the global average, moisture availability is likely the controlling factor for biomass burning (Krawchuk

& Moritz, 2011, and 5.3.1.2). In a review of Holocene biomass burning, Marlon et al. (2013) present a charcoal composite for the Australia–Monsoon region, which is slightly larger than the present study area, alongside a speleothem-derived precipitation proxy for the past 12ka. Although there is no formal comparison in the paper, the curves do not show similar behaviour over this timescale. For the Eastern Asian region further north, in contrast, they report a strong negative curvilinear relationship between biomass burning and moisture, in line with the findings of Daniau et al. (2012). The fact that the relationship found here is similar to the global analysis of Daniau et al. (2012) but not to the East Asian analysis of Marlon et al. (2013) may be related to various factors. Firstly, the present study region is strongly influenced by ENSO timescales, although it is not clear how this affects decadal to centennial biomass burning. It also encompasses the full latitudinal range of the ITCZ, which has been shown to have shifted and/or contracted at decadal to centennial scales (see 5.3.1.2; Griffiths et al., 2016, Rustic et al., 2015, Yan et al., 2015).

Secondly, the seasonality of the precipitation anomalies could alter the fire response, as rainfall changes in the dry period will set up different fuel availability, soil and ambient moisture levels, vegetation distribution and even ignition factors compared to a change to wet season rainfall. The East Asian region is strongly influenced by the EASM, whereas most of the precipitation proxies used here are more likely to reflect ASM-related rainfall (see 5.3.1.2). Moreover, the vegetation composition plays a pivotal role in determining fire activity under any given precipitation regime (see 5.3.1.1). The inclusion of savannah in the study region here has altered the charcoal composite curve, as highlighted in 5.3.2. The East Asian region is likely to be more homogeneous in its vegetational composition.

5.4 Fire-climate interactions over different timescales

As these results show, fire regimes are determined by complex interactions between climatic stimuli, vegetation dynamics and ignition. Over centennial timescales, precipitation is positively correlated with fire in the study region. This is in contrast to the short-term modern-day relationship, as discussed in 5.5. It is unclear why this relationship changes at different timescales. This section explores how the

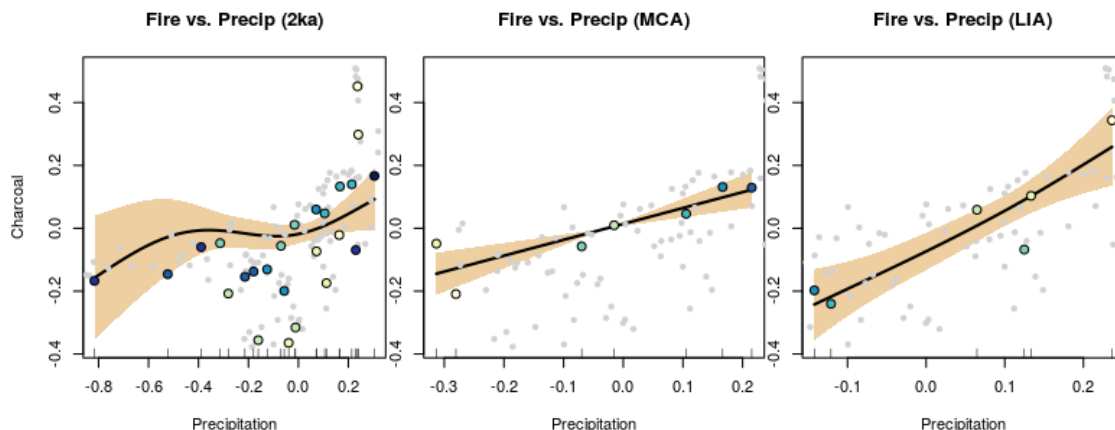


FIGURE 5.6: The 2ka GAMM (left), and the MCA (centre) and LIA (right) GAMs. Orange shading show the associated 95% confidence intervals. Small gray points are the original data, larger coloured points are predicted partial residuals. The colours indicate age, ranging from dark blue (oldest) through green to yellow (youngest) scaled individually for each plot. Note that the precipitation axes differ.

dominance of some of the main fire mechanisms changes at different temporal resolutions.

In many fire-prone regions such as Australia and Canada, fire indices (e.g. McArthur's Forest Fire Danger Index, the Canadian Forest Fire Weather Index) have been developed to determine immediate (short-term) fire risk (Forestry Canada Fire Danger Group, 1992, McArthur et al., 1967). These rely on daily or even hourly observations of moisture and temperature and are usually optimised to certain types of vegetation rather than incorporating fuel type or load as a variable.

This balance between moisture and temperature is undoubtedly paramount at any time scale, but as one moves from (sub-)daily towards seasonal or interannual resolution, concomitant changes in vegetation become increasingly influential in driving subsequent fire behaviour. On these timescales, vegetation has sufficient time to recover from fire disturbance, creating a transient system. The climatic driving factors also shift from daily weather fluctuations to regional climate oscillations (monsoons and ENSO), where longer-term averaged, more sustained conditions dominate the vegetation and fire response on the same timescales.

Up to interannual resolution, there are observational climate and fire data available to analyse and quantify these interactions. The Global Fire Emissions Database

(GFED; Giglio et al., 2013, 2010), for example, provides 3-hourly to annual data derived from various satellite products. Various climate datasets are available for precipitation and temperature, the longest of which (20CRv2c) goes back to 1851 (Compo et al., 2011, Section 3.2.2). On interannual timescales, precipitation over Indonesia is strongly modulated by ENSO, with El Niño characterised by anomalously low precipitation rates. A comparison of Global Precipitation Climatology Project (GPCP) precipitation estimates over Indonesia with the Southern Oscillation Index (SOI, which represents the atmospheric component of ENSO and is negative during El Niño events), shows that annual precipitation is strongly correlated with SOI ($R = 0.67$, $p < 0.001$; see also 3.3.3).

There are a number of studies that explore links between ENSO and Indonesian fire during the satellite era, with the overarching conclusion that fire occurrence in the Indonesian region is significantly higher during El Niño years. Satellite data suggests the SOI is significantly negatively correlated with fire occurrence (Fuller & Murphy, 2006) and burnt area (Giglio et al., 2010). El Niño years are also characterised by higher CO₂ emissions (Field et al., 2009, van der Werf et al., 2008), and more haze clouds (Field, 2004, Field et al., 2009, Heil & Goldammer, 2001, Wang, 2004), both of which support stronger fire activity. A direct inverse relationship between precipitation and fire has also been shown using satellite data (van der Werf et al., 2008), and potentially higher lightning strike rates (Chronis et al., 2008, Dowdy, 2016, Hamid, 2001, Kumar & Kamra, 2012, Sători et al., 2009, Sători & Zieger, 1999), both of which could explain this ENSO-fire coupling through their effect on fuel moisture, availability and ignition.

However, the limitation of fire data to the satellite era (~30 years) precludes meaningful analysis on longer timescales. The reliance on palaeodata presents several difficulties: the records may not be complete, they tend to have low resolution, the extent, timing and location of fires is not always clear, and the distinction between size and frequency of fire events is blurred.

At decadal to millennial timescales, the vegetation response to fire may move beyond recovery to adaptation, significantly altering its composition and the subsequent fire regime. It is not well understood how the hourly fluctuations (so important for the fire danger indices) and interannual variability (such as ENSO) play a role in long-term fire behaviour. As 5.3.3 highlights, the relationship between fire and climate varies depending on spatial scales (Daniau et al., 2012,

Marlon et al., 2013) and vegetation composition. Compounding these complexities is the potentially non-linear transformation of these relationships as the focus shifts from short-term (daily to interannual) to long-term (centennial to millennial) timescales.

5.5 Humans and fire

An additional complication is the fact that the satellite era is also punctuated by unprecedented human activity in the region, which has influenced fire in a multitude of ways and confounds the natural interactions. To understand natural fire-climate interactions, untangling the anthropogenic factor from the instrumental measurements is crucial.

A significant anthropogenic impact on recent fire activity has been demonstrated over recent decades for various study sites across the Indonesian islands (Bowman et al., 2011, Field et al., 2009, Page & Hooijer, 2016). Deforestation and logging is rife in Indonesia, with large swathes of peat swamp forest being cleared for pulp and palm oil plantations and timber harvesting. Tropical rainforest is being lost at an increasing rate in Indonesia; forest cover fell from 80-90% a century ago to ~50% in 1997 (Brown & Jacobson, 2005), with a ~40% loss between 1950-2000 (FWI/GFW, 2002) alone. Logging disrupts the below-canopy microclimate which keeps pristine forest relatively cool and moist, resulting in heightened flammability of the vegetation above and below ground, while the dead wood left behind increases fuel availability (Cochrane, 2003, Page & Hooijer, 2016). An analysis of fire occurrence in East Kalimantan after the extreme 1997-98 El Niño event (Siegert et al., 2001) found that the extent of fire damage was significantly higher in logged forest (59%) than in undisturbed forest (5.7%). If the logged areas are not converted to farm land or other land uses, they are likely to be repopulated initially by grasses and other quick-growing pioneer species, before the slow-growing tropical hardwood returns (Brown & Jacobson, 2005). These quick-growing species are more flammable and are unable to retain ambient moisture like a full-grown forest would. The conversion of tropical peatlands to agricultural land impacts the fire regime in several ways. Where an area is cleared for agriculture, drainage channels are usually dug to dry out the underlying peatlands. This not only produces large amounts of CO₂ emissions through switching from

CO₂ burial and sequestration to heightened aerobic respiration and fluvial organic C transport (Section 2.5.2), it also increases the flammability of the C-rich peat soils. Once peat is ignited, it is extremely difficult to extinguish and can burn for years underground, reigniting aboveground fires repeatedly.

The increasing presence of humans in previously virtually unexplored forests also poses a significant risk of increased fire ignition, whether accidental or intentional. Fires started as part of slash-and-burn, practised by smallholders as well as large plantation firms, can easily spread to surrounding forested areas (Siegert et al., 2001). During the extreme fire season in September 2015, coinciding with the “Godzilla” El Niño (Kintisch, 2016), an estimated 37% of fires in Sumatra were located on pulpwood concessions, many others occurring near or on land used for the production of palm oil (Balch, 2015); 38% of fires were on peatlands (Johnston et al., 2015). Human activity can also suppress fire activity, for example through fragmentation of the landscape or more proactive interventions (preventative burning, pre-wetting, fire-fighting).

The low resolution of the biomass burning reconstruction presented here, and the fact that it ends in AD 1950, precludes any substantial analysis of recent anthropogenic impact on the charcoal records. Investigations of human impact on fire at centennial to millennial timescales show mixed results, with some finding indications of non-climatically induced changes in charcoal abundance (cf Anshari et al., 2004, Hope et al., 2005) while others find no evidence for human-driven changes in fire regimes (cf Marlon et al., 2008, Mooney et al., 2011). The current population pressure on natural ecosystems is unprecedented, however, and the combined effects of recent human intervention in fuel structure, type, flammability and ignition described above have significantly altered fire behaviour. The divergence in precipitation and biomass burning since ~200 yr BP seen in Figure 5.3 coincides with a sharp increase in estimated population, cropland area and pasture area across the study region (Klein Goldewijk et al., 2010, 2011, <http://themasites.pbl.nl/tridion/en/themasites/hyde/download/index-2.html>). While ENSO-induced drought certainly plays a significant role in driving biomass burning trends in the Indonesian region, the anthropogenic activities have an amplifying effect on the region’s sensitivity to the climatic drivers. More work must be done to resolve what role temporal resolution (centennial versus interannual) plays in the different fire-climate relationships seen in the palaeo and modern

data. Nonetheless, it is highly likely that the recent relationship between ENSO (precipitation) and fire has been significantly altered by the presence of humans.

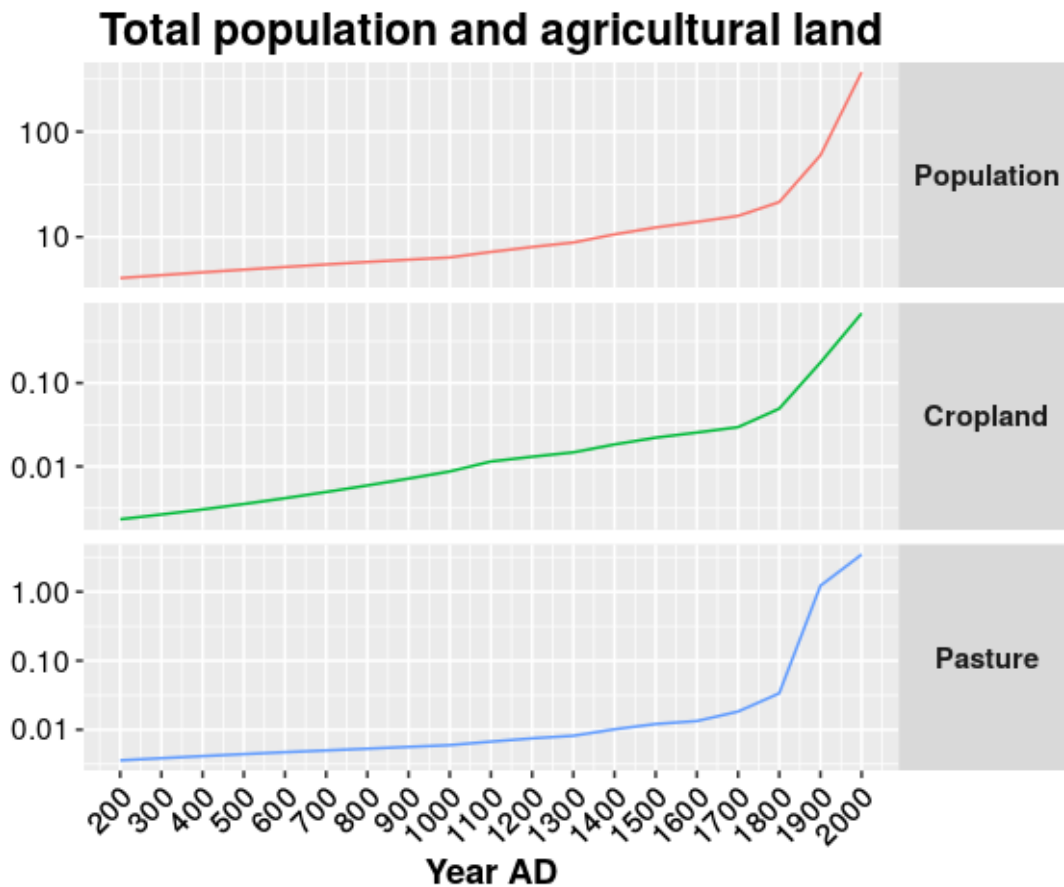


FIGURE 5.7: Total population (millions), cropland area (million km²) and pasture area (million km²) in the study region estimated from the HYDE3.1 database (Klein Goldewijk et al., 2010, 2011, <http://themasites.pbl.nl/tridion/en/themasites/hyde/download/index-2.html>). Note the y-axes are on a log scale.

5.6 Conclusions

In this chapter, charcoal records and precipitation proxy records were synthesised to compare reconstructed rainfall and biomass burning over the Indonesian region for the past 2ka. The results presented here point to a positive correlation between precipitation and fire. This is in contrast with the modern-day observed relationship, where El Niño-induced drought is associated with increased fire occurrence. This discrepancy has highlighted the complex nature of fire-climate

interactions and feedbacks to vegetation dynamics and C cycling. Addressing the role of timescales on these interactions to bridge the gap between instrumental and palaeo-data has not been done extensively in the literature (Bistinas et al., 2014, Daniau et al., 2012), and is hampered greatly by both a lack of high resolution proxy data and a lack of mechanistic understanding of how the dominance of the multitudinous variables changes at different temporal resolutions (Hantson et al., 2016a).

These complexities are compounded by the heavy influence of humans over the instrumental period. There is evidence that anthropogenic activities have had, and continue to have, a profound detrimental effect on the stability of the Indonesian forests and their susceptibility to fire (Page & Hooijer, 2016). The key question, then, is whether the difference between the reconstructed and observed relationships between fire and precipitation are due to a fundamental ecological shift in long and short term responses to precipitation changes, or whether the observed relationship has evolved as a result of anthropogenically induced disequilibrium. The sharp upturn in biomass burning from 200 yr BP visible in the charcoal reconstruction (Figure 5.3) concurrent with exponential population growth (Klein Goldewijk et al., 2010, 2011), and studies comparing pristine and human-degraded forests (Cattau et al., 2016, Siegert et al., 2001), suggest that humans have indeed significantly altered the fire dynamics in the region. This has serious implications for understanding future fire risk and associated impacts on the global C cycle, air quality and ecological biodiversity.

Further research, including the use of fire models, can help us better understand the physical mechanisms that underpin fire responses to variations in climate and vegetation. The development of these models has made much progress in recent years, and the first comprehensive effort to compare existing fire models was initiated in 2014 with the creation of the Fire Model Intercomparison Project (FireMIP; Hantson et al., 2016a). Targeted modelling experiments, combined with new palaeo-records and more comprehensive multi-variable syntheses, will improve our understanding of fire behaviour on different temporal scales and strengthen projections of future changes under different scenarios of climate and human activity.

Chapter 6

Conclusion

This thesis has focused on understanding long term tropical hydrological variability and ENSO-like climate change from palaeorecords and their interactions with fire. Using a wide range of instrumental, proxy and model datasets, it has drawn inferences about the consequences of this long term variability on tropical C cycles, with an emphasis on peatlands, over the past two millennia. An overarching theme has been the role of varying timescales on the strength and direction of these relationships, contrasting modern-day short-term analyses with long-term reconstructions. This chapter revisits the main aims and objectives, bringing together the primary findings and their limitations, and drawing out the still unresolved questions. It concludes with a proposed avenue for further research, laying out some potential modelling experiments.

6.1 Revisiting aims and objectives

The research presented in this thesis can be divided into three strands, roughly reflected by the structure of the main data chapters. The first strand addresses methodological issues in palaeoclimatic research, and throws up questions of robustness and subjectivity of method and data selection. This is explored in detail in Chapter 3, with additional major insights in Chapter 4. The second strand, covered in Chapter 4, is concerned with long-term ENSO-like variability in the tropics and subtropics, and how this is expressed in precipitation and temperature proxies. Finally, Chapter 5 relates hydrological change and variability to fire

behaviour in the Indonesian region, which has profound implications for tropical peatlands and their C cycle. The following sections reiterate the main findings for each strand, discuss their relevance in the wider context, and identify priorities for future research.

6.1.1 Methodological issues in palaeoclimatology

The nature of palaeoclimatological research makes it inherently difficult; proxy record collection is often physically challenging, and the quality of proxy datasets varies widely in terms of spatial and temporal resolution, non-linearities, multivariate responses, dating errors, and length. Chapter 3 laid out a number of existing transformation (Section 3.5) and smoothing (Section 3.6) methods that enable more statistically sound comparisons and aggregation of different proxy records. These methods address issues such as non-linearity in individual proxy records and differences in temporal resolution, and provide relatively simple ways of synthesising a set of records into a single reconstruction (e.g. using LOWESS) or modelling the relationship between two sets of data (using GA(M)Ms), and have been applied widely in the palaeoclimate literature (e.g. Blarquez et al., 2014, Daniau et al., 2012, Emile-Geay & Tingley, 2016, Trouet et al., 2013).

However, even the use of established statistical methods is a subjective process, and the choice of methods and parameters can significantly alter the results. This was illustrated in the sensitivity exercise in 3.6.1, where the effects of pre-smoothing bin width, bin placement and smoothing window were examined. Such parameter choices (and their robustness) are often not clearly reported in the literature (e.g. GAM parameters in Marlon et al., 2013), despite the fact that this issue is relevant from interpreting individual data series (e.g. peak detection in high-resolution charcoal records; Higuera et al., 2010) to creating multiproxy reconstructions (e.g. CFR sensitivity to proxy noise and spatial sampling; Mann et al., 2007). Several studies have compared the effect of methodology on multiproxy reconstruction, both for full climate fields (Emile-Geay et al., 2013a, Mann et al., 2007, 2005, Wang et al., 2015, 2014a) and for specific climatic phenomena such as ENSO (McGregor et al., 2010, Wilson et al., 2010).

A significant limiting factor particularly pertinent to palaeoclimate reconstructions is the increasing sparsity of data further back in time. This was evident in the

temperature reconstruction presented in Chapter 4, which suffered from low data density compounded by the poor spatial distribution of the available proxies. The fact that the inclusion of all proxies further away from the ENSO source region (particularly the North American tree rings) significantly degraded the reconstructive power of the proxy network is a strong indicator of the importance of intelligent data selection. The ‘add-one-in’ method introduced and implemented in Chapter 4 presents a sophisticated algorithm to objectively and automatically search for the best combinations of proxy records. The fact that the resultant network ensembles were so diverse (999 precipitation and 617 temperature networks were unique out of the 1000 created) highlights how sensitive a reconstruction can be to the data included. This raises serious concerns about the fidelity of reconstructions that rely on single or very few proxy records (cf Conroy et al., 2010, Yan et al., 2011b), which may be highly sensitive to noise, unduly high dating errors, and other sources of uncertainty.

The improved simulation of palaeodata through pseudoproxies (Smerdon, 2012), and the advent of pseudoproxy system models (PSMs; Evans et al., 2013), is an extremely promising avenue for further improvements to reconstruction methods and their validation. This thesis introduced and employed relatively simplistic ways of creating pseudoproxies, including mimicking the temporal coverage of the real proxies and lowering the signal-to-noise ratio (SNR; 3.4.3), as well as the more sophisticated, process-based, VS-Lite model for creating pseudo-TRW (Section 3.4.2, Breitenmoser et al., 2014, Evans et al., 2014, Tolwinski-Ward et al., 2013, 2011). This model accounts for the fact that tree ring widths are expressions of both moisture availability and temperature variability, rather than representing a straightforward univariate response to a single environmental stimulus. The multivariate response of many proxy archives is widely acknowledged in the palaeo-community (Jones et al., 2009), but is still largely ignored when interpreting the data. A standard approach is to evaluate the relative influence of one or more variables by examining the modern-day relationship between proxy and variable, if possible using the proxy data points that overlap with the instrumental period, or taking real-time, *in situ* measurements for comparison with instrumental data. However, this is often where the interrogation ends, despite the potentially severe implications of potential non-linearities and non-stationarity in the relationships between proxy and variable (and between the variable of interest and other variables). For instance, an isotope-enabled GCM study (Russon et al.,

2013) found that $\delta^{18}O_{sw}$ variability in the western Pacific accounted for 50% of the model $\delta^{18}O_{coral}$ variance, and that the relationship between $\delta^{18}O_{sw}$ and SST was non-stationary. Assuming a western Pacific $\delta^{18}O_{coral}$ record represents SST may, as a result, overestimate variability by up to 20%. In the case of low-resolution records, there is an added complication of climate-proxy relationships changing at different timescales, as is apparent in the discussions on fire and precipitation in Chapter 5. Clemens & Prell (2003) highlight this in the context of organic carbon and lithogenic accumulation in a marine core from the northern Arabian Sea; both proxies are highly correlated to summer monsoon strength at the seasonal level, but over geological time scales the influence of glacial-interglacial cycles dominates their variability. Similar timescale-dependencies of climate-proxy relationships have been found in coral records (and have been taken into account in the proxy selection procedure for Chapter 4; see the list of excluded coral records in Appendix A).

It is important to note here that while the proxy pre-screening procedure, pseudoproxy development and 'add-one-in' methodology applied in Chapter 4 constitute significant efforts to address these issues of nonlinear and multivariate proxy responses, there is scope for further improvement. An obvious next step would be the use of PSMs for simulating the non-tree ring proxies, which was not done here as the method depends on runs from (at least) two separate GCMs with the same parameters. While there are several isotope-enabled GCMs available (Sturm et al., 2010), as yet none appear to provide both control and past 1000 runs (both of which are necessary for the 'add-one-in' method calibration and validation). An adapted calibration-validation approach would have to be devised to deal with this. There is additional scope for improvement on a larger scale by extending isotope-enabled GCMs to model other environmental variables relevant to the palaeoclimate community. In terms of PSMs, a promising development is the creation of the open-source modelling framework for proxy systems, PRYSM (Dee et al., 2015). This framework lays the groundwork for a systematic approach to PSMs, which have existed for decades but have thus far been scattered throughout the literature and rely on a range of programmes and data types which makes their implementation difficult when working with a wide range of proxy types. The continued improvement of PSMs and multiproxy reconstructions is a combined effort, as PSMs (as well as isotope-enabled GCMs) rely on deepening our mechanistic understanding of proxy-environment interactions (which is

necessarily partially driven by palaeo-reconstructions), while proxy interpretations and uncertainty quantification will be aided by PSM-based pseudoproxy experiments.

6.1.2 Long-term ENSO-like precipitation and temperature

Changes in the ENSO-like state of the climate over the past two millennia are poorly understood, with apparent discrepancies between the temperature and precipitation signals captured in proxy records (Yan et al., 2011b). Comparing the ENSO-like state during the Medieval Climate Anomaly (MCA) and Little Ice Age (LIA) may shed light on potential links between hemispheric to global scale temperatures and ENSO, which has relevance to interpreting and projecting future climates under elevated CO₂ concentrations. Using an EOF-based weighting method, a precipitation and a temperature reconstruction of ENSO-like climate change over the past millennium were presented in Chapter 4. The main questions addressed were 1) whether the precipitation and temperature reconstructions of ENSO-like climate change were consistent with each other, and 2) whether they showed any systematic difference in the ENSO-like state during the MCA compared to the LIA. However, as touched upon in the previous section, there is a scarcity of temperature proxies in crucial ENSO-sensitive regions, which prevented a robust comparison between the two reconstructions. The precipitation reconstruction suggested a slightly more El Niño-like LIA compared to the MCA, although this difference was not statistically significant.

The lack of similarity between the precipitation and temperature reconstructions of long-term ENSO-like climate change are not in line with modern-day observed relationships. As shown in 3.3.1 and 3.3.2, instrumental, reanalysis and GCM data all show a strong positive correlation between the precipitation and temperature responses to ENSO on interannual timescales. Nevertheless, these results also do not support the contention of Yan et al. (2011b) that they show opposing trends over the past millennium. It is impossible to determine to what extent the lack of correlation found in the research presented here is solely due to the low quality of the temperature reconstruction, or whether it is (partly) representative of the true state of the past climate. Based on these results, there is no evidence

that there was a dynamical difference in the relationship between precipitation temperature.

As highlighted in 4.5, the lack of long temperature proxies in the ENSO source region complicates the interpretation of the reconstruction, as ENSO teleconnections have likely been non-stationary over time (Coats et al., 2013, Gallant et al., 2013, Lewis & Legrande, 2015, Wilson et al., 2010). In addition, the long-term ENSO signal is possibly conflated with the PDO as most of the tree ring records lie in PDO-sensitive North America (MacDonald & Case, 2005). Since most of the proxy records have decadal or lower resolution (Table A.2), it is not possible to separate the two here. This again raises the issue of how individual proxies are interpreted, and potentially changing proxy-climate relationships at different timescales (Section 6.1.1). Many proxy records of low resolution have been interpreted as ENSO reconstructions (cf Moy et al., 2002, Nelson et al., 2011, Yan et al., 2011b) based on modern-day climate-proxy interactions, just as the reconstructions presented in this thesis are based on modern-day (inter-annual) spatial ENSO patterns. The interactions between the PDO – and similar (pseudo)oscillations such as the Interdecadal Pacific Oscillation (IPO) – and ENSO are still not well understood beyond a statistical relationship (Wang et al., 2014b), with some studies suggesting that these decadal oscillations are essentially integrated long-term expressions of ENSO (Newman et al., 2003, Power & Colman, 2006). However, the lack of significant correlations between the precipitation and temperature reconstructions presented here and the MacDonald & Case (2005) PDO reconstruction for AD 993-1996 suggests that they are indeed different phenomena. The latter is supported by comparisons between ENSO and a reconstruction of the Asian expression of the PDO (D'Arrigo & Wilson, 2006) and a recent IPO reconstruction (Henley et al., 2015).

With regard to the difference between the MCA and the LIA, there is no strong shift in ENSO-like tendency evident in either the temperature or precipitation reconstruction. The precipitation reconstruction shows a slight, but statistically insignificant tendency for a more El Niño-like LIA compared to the MCA, while there is no difference whatsoever apparent in the temperature reconstruction 4.7. This result is insensitive to the choice of definition for the MCA and LIA, suggesting it is a robust conclusion. Therefore there is no clear evidence of ENSO-driven global temperature changes at long timescales.

Conversely, the lack of distinction between the MCA and LIA in these reconstructions could be seen as confirmation that these events were not global (Consortium, 2013, Neukom et al., 2014). This result is partly consistent with the multiproxy NINO3.4 reconstruction by Emile-Geay et al. (2013b), which finds no systematic difference between the two periods, and with the La Niña-like pattern during the MCA found in the multiproxy reconstruction by Mann et al. (2009). On the other hand, numerous reconstructions based on one or two proxy records (cf Oppo et al., 2009, Rustic et al., 2015, Yan et al., 2011a) do report a significant difference, although as Yan et al. (2011b) highlight, the sign of the difference varies. This is another indication of the possible vulnerability of single-proxy reconstructions to over-interpretation, the danger of over-extrapolation, and ‘cherry-picking’ of supporting evidence. This is illustrated by the contrasting conclusions drawn by recent publications on the behaviour of the ITCZ over the past millennium. Based on a multiproxy ocean sediment core from the Galápagos, Rustic et al. (2015) conclude that the ITCZ shifted southwards during the transition from MCA to LIA (suggesting a more El Niño-like LIA). An analysis of two western Pacific speleothems (Griffiths et al., 2016), contrastingly, proposes a contraction of the ITCZ during the LIA. Both contentions are supported by (qualitative) comparisons with a set of other previously published proxy records spanning the Pacific, but only two of these records are common to both sets. It must be noted that the point here is not to disparage the work of these authors, nor to dismiss the utility of single proxy records. Rather, this is an illustration of the potential pitfalls of selective and qualitative comparisons between individual proxy records. The strength of the ‘add-one-in’ approach employed in this thesis is that the proxy selection is largely automated (aside from basic pre-screening), removing some of the bias from the process. As proxy reconstruction and interpretation methods become more sophisticated, it should also become easier to resolve conflicting hypotheses (e.g. migrating versus contracting ITCZ).

The interactions between climate oscillations such as ENSO, the PDO and the ITCZ, and their potentially non-stationary nature, is a key area for further research, particularly on timescales that cannot be evaluated in the relatively short instrumental datasets. The collection of additional proxy data in key locations must be a priority for the palaeoclimate community, alongside the methodological advancements discussed in Section 6.1.1 to maximise the information that can be gleaned from existing records.

6.1.3 Long-term Indonesian precipitation and fire

The sensitivity of the Indonesian region to ENSO-related increases in fire occurrence evident over the past few decades not only has significant detrimental socio-economic and health impacts, it also leads to major GHG emissions from the vast swathes of the C-rich peat swamp forests (Page & Hooijer, 2016). There is evidence that anthropogenic activities have exacerbated the region's vulnerability, but a lack of instrumental data prior to significant deforestation and land use conversion makes it difficult to separate the 'natural' fire regime and associated vegetation responses from human-induced changes. Gaining a better understanding of interactions between climate and fire are paramount to improving our understanding of potential future changes, peatland management, and fire modelling. Chapter 5 presented regional syntheses of reconstructed biomass burning (using charcoal records) and precipitation variability over the past 2,000 years. These centennial-resolution reconstructions suggested a significant positive correlation between precipitation and biomass burning. Modern-day observations, in contrast, show that interannual (ENSO-induced) drought leads to increased fire activity. This difference suggests that fire-precipitation relationships in this region are non-stationary over different timescales. This may be linked to differences between interannual ENSO variability and long-term ENSO-like climate states, and associated fire responses, or may point to a significant human-caused disruption of the natural fire dynamics in the region.

The relationships between precipitation and three ENSO indices (Section 3.3.3) confirm that ENSO significantly influences interannual precipitation variability in this region. This, combined with previous studies indicating a strong ENSO-driven modulation of fire activity in the most recent three decades (Sections 2.4.3 and 5.4), served as a starting point for untangling decadal to millennial relationships between precipitation, ENSO and biomass burning. The drought conditions brought on by El Niño events in the region amplify the fire risk by lowering moisture content of the vegetation and the soil, which increases fuel flammability and could increase fuel availability through drought-related mortality. This negative precipitation-fire correlation is not evident in the 2ka reconstructions (Figures 5.3), however, and the fitted GA(M)M models (Figure 5.6) show a largely positive relationship. A fundamental question emerging from these results is whether the difference between the reconstructed and observed relationships between fire

and precipitation are due to a fundamental ecological shift in long and short term responses to precipitation changes, or whether the observed relationship has evolved as a result of anthropogenic disruption of the natural fire system.

The interactions and feedbacks between fire, climate and vegetation are highly complex, and it is still not clear how they change from (sub-)daily to millennial timescales. As with ENSO variability, the short-term (up to interannual scales) can be examined in modern datasets such as GFED (Giglio et al., 2013), while long-term analyses depend on spatiotemporally incomplete proxy data. In the most general terms, the balance between moisture and temperature is key to fire activity, as they determine vegetation distribution, fuel availability and fuel flammability (Kloster et al., 2015). Although there have been some efforts to link long-term biomass burning to changes in climate and human activity at global (Daniau et al., 2012, Marlon et al., 2013) and regional (Carcaillet et al., 2002, Mooney et al., 2011, Power et al., 2008, 2013a, Vanniere et al., 2011) level, the issue of varying temporal scales is not clearly addressed. This is partly due to lack of sufficient high-resolution proxy data of biomass burning, vegetation, climate and human activity. The comparison presented in this thesis is the first, to the author's knowledge, to use a multiproxy precipitation reconstruction alongside the charcoal reconstruction. As emphasised in 6.1.1, the use of a single proxy record to represent a large region (for example the single Borneo precipitation record used by Marlon et al., 2013, to represent their 'Australia-Monsoon' region) is problematic. A more rigorous approach such as presented here, in combination with statistical modelling (Daniau et al., 2012, Marlon et al., 2013), is a key consideration for future work.

The resolution and timespan of the reconstructions presented here do not allow for robust inferences about recent human interventions in fire behaviour, although a comparison with the estimated population and cropland trends from the HYDE3.1 database (Figure 5.7) show increases over the last 200 years concurrent with biomass burning but not with precipitation. This recent upturn is also reported for other regional and global reconstructions (Marlon et al., 2013), and has been interpreted as post-industrial anthropogenic impact. In the Indonesian region, forest degradation through land-clearance, fragmentation and selective logging has accelerated since at least AD 1950 (FWI/GFW, 2002). This has been

shown to have significantly affected fire likelihood (Siegert et al., 2001), distribution (Cattau et al., 2016), spread (Knorr et al., 2016), and frequency (Page et al., 2013).

Worryingly, a large fraction of the degraded forests are on or near peatlands, which are a major C store (Page et al., 2002). Degradation of peatlands through drainage, land use conversion, logging and burning destabilise these C pools and lead to significant emissions (Hooijer et al., 2010, Page & Hooijer, 2016). Figure 6.1 shows the extent of Indonesian peatlands in 2013, alongside the change in forest cover between 1990-2013. It is clear that large swathes of peatland have been deforested in this period, particularly on Sumatra and Kalimantan. A comparison of soil properties in peat forests, logged over peat forest, industrial timber plantation, community agriculture, and oil palms found a significantly higher rate of peat decomposition in oil palm and agriculture sites (Anshari et al., 2010). Another comparison between oil palm plantation and virgin peat swamp forest (Hergoualc'h & Verchot, 2011) estimated an annual peat C loss of $10.8 \pm 3.5 \text{ Mg C ha}^{-1}$, representing 63% of total C loss (the other loss being from biomass). In addition to increasing C respiration (2.5.2.2) and fluvial C loss (2.5.2.3), the drainage and conversion of peat swamp forests highly increases the risk of fire (Konecny et al., 2016), which can cause immense CO_2 releases in a relatively short period of time due to the C density of the peat. In an assessment of the 1997 Indonesian fire season, Page et al. (2002) finds that on average, a layer of 51 cm of peat was lost over the study area, equivalent to an estimated emission of 2.18 to 2.57 GtC. A more recent estimate found an average peat burning depth of 26 cm during Sept-Oct 2015 (Huijnen et al., 2016). They attribute this decrease in burning depth to previous fire occurrences, speculating that the fuel consumption per unit area on peatlands decreases with fire frequency. This is corroborated by Konecny et al. (2016), who report a shallowing with each recurrent fire on peatland which means a possible overestimation of peatland emissions. However, Wijedasa (2016) points out the bulk density of peat changes with fire, which could counteract the shallowing effect. Gaveau et al. (2014) suggest that the ENSO-fire link detected over the past few decades is showing signs of breaking down as forest degradation continues, with extreme air pollution episodes no longer restricted to (ENSO) drought years. Considering that an additional 6-9 Mha of Indonesian peatland are projected to be converted to plantations by the year 2020 (Miettinen

et al., 2012), this is a major cause for concern for global efforts to stabilise GHG emissions (Hooijer et al., 2010).

While about 43% of the charcoal records used to make the biomass burning reconstruction in Chapter 5, it is unclear whether the charcoal preserved in these sediment cores originate from aboveground vegetation or from peat burning. It can be assumed that peat burning leaves behind little evidence in the form of charcoal, as smouldering (the main form of combustion in subsurface peat) consumes the char it produces (Rein, 2013, Zaccone et al., 2014). Some recent work has been done to find alternative identifiers of peat burning, including charred decayed organic aggregates (New et al., 2016) and ash content, pH, C/N ratios, and total nitrogen (Zaccone et al., 2014). However, particularly the latter indicators are also associated with other environmental factors (such as dust deposition and vegetation), complicating their interpretation. Even once robust indicators of peat burning have been developed, much additional analysis will have to be done on the existing palaeo-archives as well as expanding the proxy network to achieve better spatiotemporal coverage.

The clear anthropogenic impact on recent fire-climate correlations discussed above call for a better mechanistic understanding of the interplay between the multitude of factors in order to separate human and natural drivers of fire regimes. As with pseudoproxy development (Section 6.1.1), this requires a collaboration between the palaeoclimate and modelling community (Marlon, 2016). Observational data, proxy data and vegetation/fire models each contribute crucial understanding of the interplay of climate, vegetation, human intervention and fire, but it is only when they are combined that we are able to address these issues over all spatial and temporal scales (Figure 6.2). A 2015 workshop on “Paleofire Data-Model Comparisons for the Past Millennium” (Kehrwald et al., 2016) resulted in several proposals for achieving better integration, including: a modern Global Carbon Database with fire proxy data of the past century for better calibration of fire proxy data with observations; a statistical process model for improving understanding of how changes in various fire-regime characteristics are reflected in sedimentary charcoal; and the estimation of pre-industrial baseline levels of biomass burning for initialising models. The following section examines briefly the current state of peat and/or fire models, and sets out next steps for further investigation into the reasons behind the discrepancy between the modern-day and reconstructed 2ka relationship between fire and precipitation.

6.2 Moving forward: untangling fire mechanisms using models

The research presented in this thesis has highlighted the importance of taking into account timescales when defining relationships between environmental variables. While ENSO on seasonal to interannual timescales presents a tight coupling between precipitation and temperature responses, it is still unclear whether this is also true for ENSO-like climate change at centennial or millennial scales. This is complicated by interactions with other climatic phenomena such as the PDO/IPO and the ITCZ, whose behaviour have changed concomitantly with ENSO.

Similarly, the intricate nature of climate-fire-vegetation feedbacks complicates the interpretation of the results in Chapter 5. Observational data can only illuminate short-term processes and interactions, while the low temporal resolution of most charcoal records only allows for estimations of long-term, average fire behaviour. The continued improvement and structured comparison of fire models through the FireMIP initiative (Hantson et al., 2016a,b) will hopefully enable the scientific community to bridge this gap in timescales, and provide a more mechanistic understanding of what drives these interactions between climate, fire and vegetation.

Accurate representation of peat fires in particular continues to be a point of weakness for many models, as many neglect to incorporate peatland altogether (Limpens et al., 2008). There are several models of varying complexity specifically designed to simulate, for example, peat development (Baird et al., 2012, Morris et al., 2012, Parry et al., 2012), extent (Gumbrecht et al., 2017), fire emissions (Rossi et al., 2016, Yin et al., 2016), and C (and/or N) cycling (Kurnianto et al., 2015). To maximise their utility, however, it would be beneficial to move towards incorporating these independent models into GCMs or DGVMs so that they can be compared and combined more effectively on all spatial and temporal scales. Wania et al. (2009a,b) incorporate permafrost dynamics, peatland hydrology, and peatland vegetation processes for the northern high latitudes into a DGVM, and find that this significantly alters simulated soil carbon stocks. Spahni et al. (2013) further incorporate dynamic C and N cycles, which substantially improves agreement with observed and reconstructed soil C inventories. While this is promising, it is likely that more complex processes will need to be included to simulate tropical

peatland as their vegetation composition tends to be much more diverse (Page et al., 2009b). An empirical approach is taken by Li et al. (2013a), who incorporate a parametrisation into an ESM for simulating peat fires based on climate, peat cover, and water table level. This approach is computationally much less intensive while still providing improvements in the simulation of peat fire emissions. Conversely, it is limited by the available calibration data, such as peatland extent (and temporal variability thereof), burned area, and fire carbon emissions. Moreover, nuances such as the burning depth of peat and various anthropogenic impacts are lost. The lack of observational calibration data is currently also an issue for process-based approaches, which is why better integration of palaeo-data and models holds much promise (as evidenced by Schmidt et al., 2014, who show that palaeoclimate data can be used to constrain CMIP5 future projections).

Returning to the biomass burning reconstruction presented in Chapter 5, the use of a fire-enabled DGVM or ESM could allow a systematic examination of vegetation and fire responses to different hydrological changes. This can illuminate whether the positive precipitation-fire relationship observed in the palaeorecords in this thesis are likely to be linked to ENSO-like precipitation changes (i.e. an ENSO-like pattern of change) or more homogeneous changes. Other possible avenues of questioning are the influence of ENSO frequency, amplitude and variability (many consecutive El Niños or large swings from El Niño to La Niña?) on fire and vegetation response. Such a model can also potentially elucidate the relative importance of other drivers of fire, such as the vegetation composition, other climatic variables, or even the anthropogenic influence. Two ways of approaching the modelling exercise could be to ask 1) which model configurations reproduce the palaeo-results, or 2) how does modelled fire respond when the reconstructed precipitation series is used as input? The former is an examination of possible drivers behind the palaeo-results, while the latter acts as a validation of the model performance (see Brücher et al., 2014, for a different approach to fire model-data comparison). Since both palaeo data and climate/fire models have uncertainties, there is no clear advantage of one approach over the other as both have an implied assumption that either the proxy data or the model data are correct. Nevertheless, both modelling exercises would be valuable for improving our understanding of fire dynamics, as the proxy-model intercomparison can highlight where both datasets agree and where discrepancies point to weaknesses in either of the datasets. This ultimately will contribute to more robust fire simulations

necessary for preparing for future changes in wildfire risk (Hantson et al., 2016a).

6.3 Concluding remarks

The overarching theme of variable relationships on different timescales has punctuated the findings in this thesis, and call for a better mechanistic and physical-dynamical understanding of the interactions between climate and proxy records. The advent of 'Big Data' has hugely benefited the academic community as access to large datasets opens up the possibility of large-scale analyses using a diverse set of data types. The application of rigorous statistical techniques to these data and strong collaborations with modelling communities should be priorities for the palaeo-community, and lay the groundwork for more robust projections of future changes in climate and fire risk.

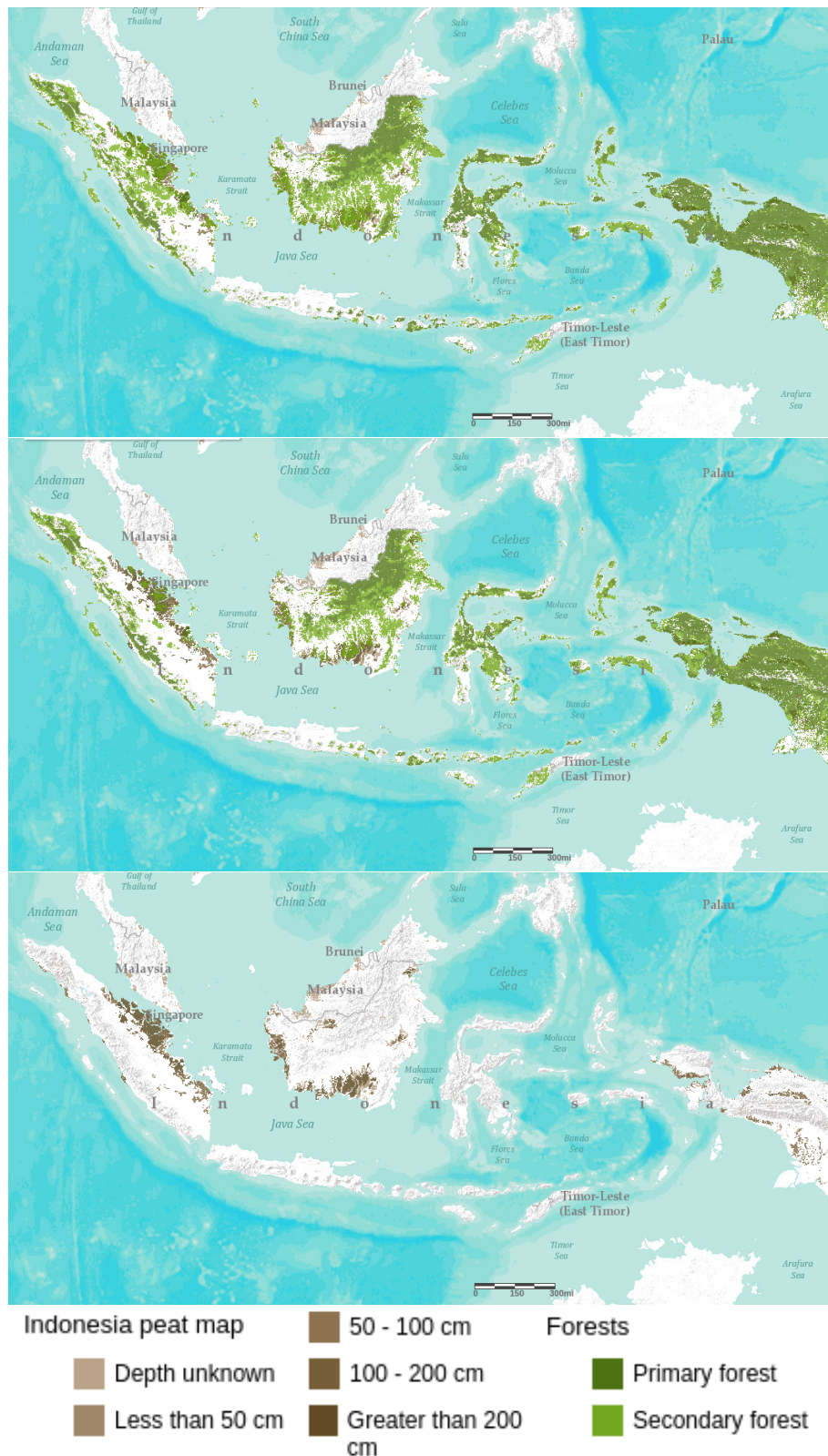


FIGURE 6.1: Maps showing Indonesian forest cover in 1990 (top) and 2013 (middle), and peat extent and depth in 2013 (bottom). Maps were created using the Greenpeace online interactive map (Greenpeace, 2017) powered by Global Forest Watch data (<http://data.globalforestwatch.org/>). Note that the forest cover data does not extend to Malaysia, while the peat data does.

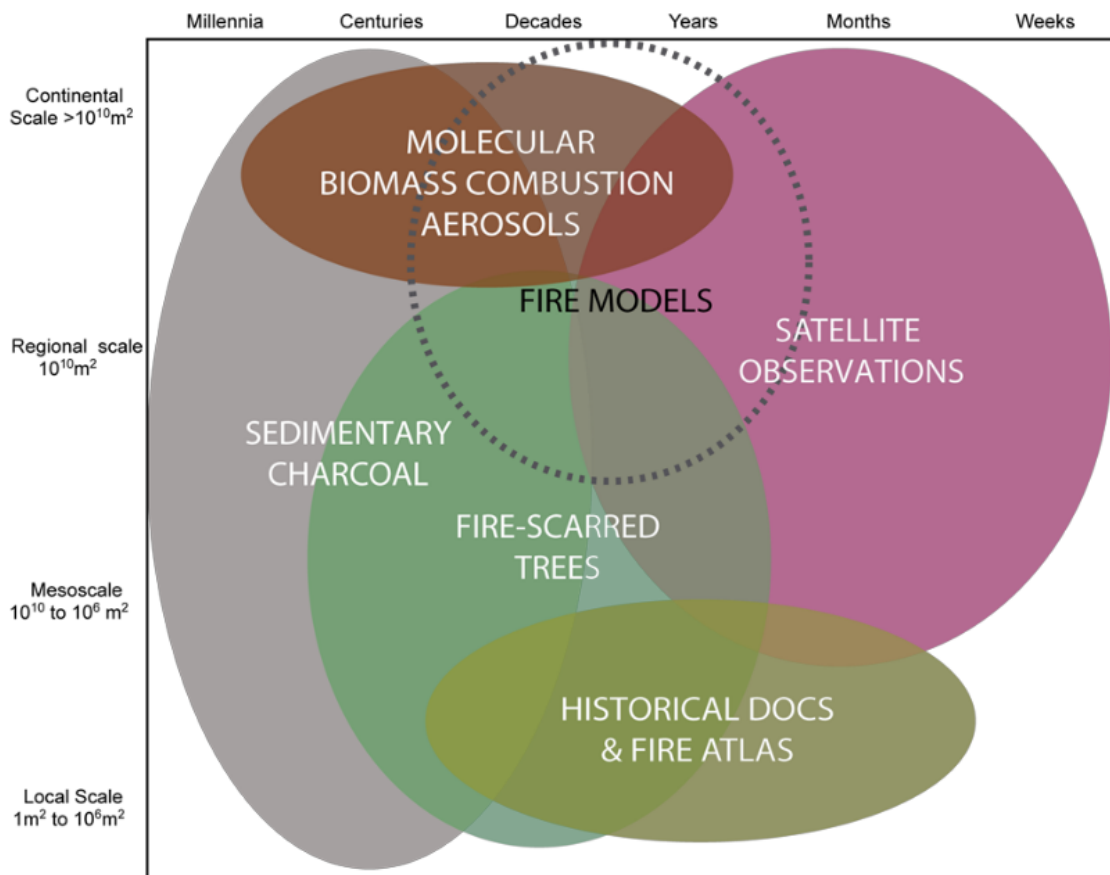


FIGURE 6.2: Overview of the spatiotemporal extent of the various data sources of fire history (figure from Kehrwald et al., 2016).

Appendix A

Proxy data used in Chapter 4

A.1 Proxy data details

Tables A.1 and A.2 provide an overview of the proxy records collected for this study. Where a proxy was rejected, the reason is given. ‘AOI’ refers to a proxy not being selected for any networks by the ‘add-one-in’ algorithm. This could be due to poor ability to capture the EOF pattern related to location or time resolution. Records from the NOAA Paleoclimate Database are identified by original publications. Where there are multiple timeseries from one publication, an identifier suffix is added. The naming of this identifier is based on the naming in the original database files or the proxy type (e.g. $\delta^{18}O$, Sr/Ca, etc.).

Most tree ring records were taken from the dataset used by Mann et al. (2008), which is a reduced set derived from the International tree ring Data Bank (ITRDB, version 5.03; [www.ncdc.noaa.gov/paleo/tree ring.html](http://www.ncdc.noaa.gov/paleo/tree%20ring.html)). The naming for these series has not changed from the original (an abbreviated location followed by a core number). The tree ring series were subject to the following selection criteria (Mann et al., 2008):

- (i) series must cover at least the interval 1750 to 1970, (ii) correlation between individual cores for a given site must be 0.50 for this period, (iii) there must be at least eight samples during the screened period 1800–1960 and for every year used. Series that were redundant with other compilations [used in the Mann et al. (2008) study]

were not included. Four other series were not included because of site-specific problems [...]. Of the remaining series, [some] had to be replaced because of format errors in the chronology file on the ITRDB [...], or because sample depth data were missing from the chronology file. [...] When sample depth data were absent, the raw ring-width data from ITRDB were used to recalculate the chronology using program ARSTAN (Version 6.05P), with the following settings: a) a single detrending fitting a cubic spline of 50% variance reduction function at 66.6% the length of each sample, no stabilization of variance or autoregressive modeling, indices computed as ratio, that is measurement divided by curve, and chronology calculated as biweight robust mean estimate.

The Tierney et al. (2015) coral dataset is a comprehensive compilation of coral data covering the last ~400 years. Most of the records in this database were used in this study as temperature proxies, with the following exceptions:

- DeLong et al. (2014, 2012, 2013) were replaced by the coral-derived SST series as presented in original publications
- Kuhnert et al. (1999), Zinke et al. (2004) were replaced by the coral-derived SST series as presented in Zinke et al. (2014)
- Goodkin et al. (2008) $\delta^{18}O$ and Sr/Ca were replaced by the coral-derived SST series as presented in the original publication
- Pfeiffer et al. (2004) was excluded as the original publication shows that advection-induced SSS changes dominates over temperature in the coral $\delta^{18}O$ on interannual timescales
- Swart et al. (1996b) was excluded as the original authors find no interannual $\delta^{18}O$ -temperature relationship
- Swart et al. (1996a) was excluded as the original publication shows SSS dominates the interannual $\delta^{18}O$ signal and the $\delta^{18}O$ -precipitation relationship is unstable

- For Abram et al. (2008), Cole et al. (1993), Nakamura et al. (2009), the coral $\delta^{18}O$ signal is not clearly dominated by temperature but is a combination of T and P
- For Cobb et al. (2003), Felis et al. (2000, 2009), Gorman et al. (2012), Linsley et al. (2006), Urban et al. (2000), Zinke et al. (2008), the coral $\delta^{18}O$ signal is not clearly dominated by temperature but is a combination of T and SSS
- Linsley et al. (1994) is interpreted as a precipitation record as the original study shows the $\delta^{18}O$ signal is 80% precipitation influence
- Felis et al. (2009) Sr/Ca and $\delta^{18}O$, Kuhnert et al. (2005) Sr/Ca , Quinn et al. (1996), Quinn et al. (2006) Sr/Ca , Kilbourne et al. (2008) Sr/Ca and Druffel & Griffin (1999) $\delta^{18}O$ were excluded as their correlations with SST reported in Tierney et al. (2015) were of opposite sign to what is expected (i.e. positive when the physical processes should lead to a negative correlation)

Additional tree ring and coral records were retrieved from the NOAA Paleoclimatology Database (<http://www.ncdc.noaa.gov/data-access/paleoclimatology-data/datasets>) and were used as presented there. Where available, temperature or precipitation reconstructions were used (i.e. where the raw proxy series has already been converted). This was done to minimise biases due to nonlinearities in the raw proxy data which are accounted for in the conversion process. In some cases, two precipitation series were available for different seasons; these were summed (or averaged, depending on the type of data) to get a better approximate of an annual signal. While this may not be entirely accurate, annual signals are more desirable for the purpose of this study. Moreover, summing the records as opposed to treating them as individual records makes very little difference due to the nature of the method (weighting and summing the series). For corals, spliced records were used where available to maximise their length.

Proxy records with dating errors > 60 years were excluded from the analysis. The dating error was taken from the original publications where it was reported; otherwise it was derived from the age model results in the raw data files. In the latter case, the maximum error reported for the past 2000 years was used; larger errors further back in time were thus not taken into account as they are irrelevant for this study.

A.2 Precipitation records

Reference	Longitude (°E)	Latitude (°N)	Proxy (m)	SNR	EOF	Start (years)	End (years)	Resolution (years)	Dating error (years)	Included?
Anchukaitis & Evans (2010)	275	10	tree ring	N/A	N/A	50	-53	1	2	No; Length
Anderson (2011)	68	29	lake	0.40	0.32	>1500	-58	14	50	Yes
Apastegui et al. (2014)	76	13	speleothem	0.40	-0.03	413	22	5	15	Yes
Asmerom et al. (2007)	255	32	speleothem	N/A	N/A	>1500	-15	17	550	No; Dating error
Baker et al. (2009)	78	10	lake	0.40	-0.22	>1500	127	10	30	Yes
Bird et al. (2011)	76	11	lake	0.40	0.52	>1500	-57	20	60	Yes
Bonnefille & Chalie (2000)	356	30	pollen	N/A	N/A	>1500	0	23	110	No; Dating error
Buckley et al. (2010)	29	19	tree ring	0.37	0.04	920	-58	1	1	Yes
Chen et al. (2009)	26	29	lake	0.40	-0.02	960	-52	10	60	Yes
Christie et al. (2011)	78	2	tree ring	0.35	0.48	604	-52	1	1	Yes
Cleaveland et al. (2003)	29	24	tree ring	0.40	0.42	564	-43	1	1	Yes
Conroy et al. (2008) C/N	271	-1	lake	N/A	N/A	>1500	-54	10	70	No; Dating error
Conroy et al. (2008) clay	271	-1	lake	N/A	N/A	>1500	-54	10	70	No; Dating error
Conroy et al. (2008) sand	271	-1	lake	N/A	N/A	>1500	-54	10	70	No; Dating error
Conroy et al. (2008) silt	271	-1	lake	N/A	N/A	>1500	-54	10	70	No; Dating error
Curtis et al. (1996) gastropod	73	22	lake	0.40	0.16	>1500	-43	6	50	Yes
Curtis et al. (1996) ostracod	73	22	lake	0.40	0.16	>1500	-43	6	50	Yes
Denniston et al. (2015)	62	10	speleothem	0.40	1.08	>1500	-36	1	30	Yes
Díaz et al. (2002)	69	26	tree ring	1.10	0.32	303	-42	1	1	Yes
Faulstich et al. (2013)	67	28	tree ring	0.46	0.26	353	-58	1	1	Yes
Griffin et al. (2013)	67	27	tree ring	0.40	0.31	411	-58	1	1	Yes
Haug et al. (2001) Fe	79	19	marine	0.40	-0.93	>1500	110	5	50	Yes
Haug et al. (2001) Ti	79	19	marine	0.40	-0.93	>1500	110	5	50	Yes
Hendy et al. (2003)	40	8	coral	0.86	-0.90	338	-35	1	1	Yes
Hodell et al. (1995) gastropod	73	22	lake	0.40	0.16	>1500	-10	25	60	Yes
Hodell et al. (1995) ostracod	73	22	lake	0.40	0.16	>1500	-10	25	60	Yes
Hodell et al. (1995) s	73	22	lake	0.40	0.16	>1500	157	25	60	Yes
Kennett et al. (2012)	73	21	speleothem	0.40	0.00	>1500	-54	1	19	Yes

Continued on next page

Table A.1 – continued from previous page

Reference	Longitude (°E)	Latitude (°N)	Proxy (m)	SNR	EOF	Start (years)	End (years)	Resolution (years)	Dating error (years)	Included?
Linsley et al. (1994) $\delta^{18}O$	75	18	coral	0.10	-1.38	242	-35	1	1	Yes
Maupin et al. (2014) 10fc	43	12	speleothem	2.35	-0.68	527	-60	1	6	Yes
Maupin et al. (2014) 5fc	160	-10	speleothem	N/A	N/A	70	-26	1	5	No; Length
Medina-Elizalde et al. (2010)	73	22	speleothem	0.79	0.16	1463	-54	2	10	Yes
Metcalfe et al. (2010)	69	22	lake	0.40	-0.16	>1500	-51	1	24	Yes
Moy et al. (2002)	75	16	lake	0.40	0.70	>1500	-27	1	60	Yes
Nelson et al. (2011)	65	29	lake	0.40	0.24	>1500	101	5	60	Yes
Oppo et al. (2009) $\delta^{18}O_{sw}$	32	13	marine	0.40	-1.82	>1500	-5	11	50	Yes
Partin et al. (2007)	115	4	speleothem	N/A	N/A	>1500	0	45	300	No; Dating error
Partin et al. (2013)	45	9	speleothem	1.10	-2.42	393	-55	1	11	Yes
Pohl et al. (2003)	70	24	tree ring	1.01	0.18	168	-50	1	1	Yes
Rasbury & Aharon (2006) asm1	51	8	speleothem	0.40	-1.97	121	-51	1	7	Yes
Rasbury & Aharon (2006) asm2	51	8	speleothem	0.40	-1.97	190	-51	1	5	Yes
Rasbury & Aharon (2006) asm3	190	-19	speleothem	N/A	N/A	76	-51	1	13	No; Length
Reuter et al. (2009) a	283	-6	speleothem	N/A	N/A	47	-56	1	9	No; Length
Reuter et al. (2009) d	76	13	speleothem	0.40	-0.03	861	43	1	9	Yes
Rodbell (1999) old	75	16	lake	0.40	0.70	>1500	802	1	10	No; AOI
Rodbell (1999) recent	75	16	lake	0.40	0.70	662	-27	1	10	Yes
Rodysill et al. (2012)	31	12	lake	0.40	-1.86	1290	-59	55	60	Yes
Russell et al. (2014) $\delta^{13}C_{wax}$	33	14	lake	0.40	-1.67	>1500	630	220	57	Yes
Russell et al. (2014) TiO	33	14	lake	0.40	-1.67	>1500	669	220	57	No; AOI
Russell & Johnson (2007)	8	15	lake	0.40	-0.83	1399	-24	3	10	Yes
Stahle et al. (2011)	71	22	tree ring	0.79	0.00	1179	-58	1	1	Yes
Stansell et al. (2013)	74	19	lake	0.40	-0.61	>1500	-54	5	10	Yes
Steinman et al. (2012) Castor	65	29	lake	1.43	0.24	1450	-50	5	60	Yes
Tan et al. (2009)	29	27	speleothem	0.42	-0.27	701	-33	3	8	Yes
Thompson et al. (2006) c2an	24	27	ice core	0.40	-0.16	349	-46	10	50	Yes
Tierney et al. (2010)	120	-4	marine	N/A	N/A	>1500	-48	30	65	No; Dating error
Tierney et al. (2015) bc1 δD_{wax}	12	29	marine	0.40	0.24	322	-50	9	25	Yes
Tierney et al. (2015) p δD_{wax}	12	29	marine	0.40	0.24	>1500	-30	20	25	Yes

Continued on next page

Table A.1 – continued from previous page

Reference	Longitude (°E)	Latitude (°N)	Proxy (m)	SNR	EOF	Start (years)	End (years)	Resolution (years)	Dating error (years)	Included?
Treydte et al. (2006)	20	28	tree ring	0.61	0.22	950	-48	1	1	Yes
Yan et al. (2011a) dy2	113	17	lake	N/A	N/A	926	-46	15	70	No; Dating error
Yan et al. (2011a) dy4	113	17	lake	N/A	N/A	926	-46	20	70	No; Dating error
Yan et al. (2011a) dy6	113	17	lake	N/A	N/A	926	-53	10	70	No; Dating error
Yi et al. (2012)	30	28	tree ring	0.40	-0.29	350	-50	1	1	Yes

TABLE A.1: Precipitation proxy used in Chapter 4. ‘Reference’ is the original publication optionally followed by a further identifier, or in the case of Mann et al. (2008) tree rings, consists of an abbreviated location followed by a core number as applied in the original database. ‘SNR’ gives the signal-to-noise ratio used to make the pseudoproxies. ‘EOF’ gives the (unscaled) 20CRV2c EOF value used to weight the proxy. ‘Start’ and ‘End’ are starting and ending years in YearBP. ‘Res’ is proxy resolution, rounded to the nearest integer; sub-annual proxies are listed as having a 1-year resolution. ‘Dating’ refers to dating error. ‘Included?’ indicates whether the proxy contributed to the final ENSO reconstruction; if not, the reason for exclusion is listed (‘Dating error’ and ‘Length’ are *a priori* conditions which the proxies failed to meet. ‘AOI’ indicates it passed pre-processing screening, but was not selected during the add-one-in process).

A.3 Temperature records

Reference	Longitude (°E)	Latitude (°N)	Proxy (m)	SNR	EOF	Start (years)	End (years)	Resolution (years)	Dating error (years)	Included?
Alibert & Kinsley (2008) Sr/Ca	151	-3	coral	0.26	-0.73	127	-47	1	1	Yes
ar018	266	35	tree ring	0.40	-1.63	300	-29	1	1	Yes
ar024	266	36	tree ring	0.40	-1.07	225	-29	1	1	Yes
ar030	267	35	tree ring	0.40	-1.42	214	-29	1	1	Yes
ar042	268	35	tree ring	0.40	-1.42	428	-29	1	1	Yes
ar048	269	36	tree ring	0.40	-0.94	533	-29	1	1	Yes
ar050	269	35	tree ring	0.40	-0.94	931	-30	1	1	Yes
ar055	267	36	tree ring	0.40	-0.94	591	-42	1	1	Yes
ar056	267	36	tree ring	0.40	-0.94	280	-42	1	1	Yes
ar057	267	36	tree ring	0.40	-0.94	330	-43	1	1	Yes
ar058	266	36	tree ring	0.40	-1.07	271	-42	1	1	Yes
ar060	268	36	tree ring	0.40	-0.94	313	-43	1	1	Yes
ar061	267	37	tree ring	0.40	-0.94	258	-43	1	1	Yes
ar064	266	34	tree ring	0.40	-1.63	292	-41	1	1	Yes
ar072	266	36	tree ring	0.40	-1.07	325	-41	1	1	Yes
Asami (2005) $\delta^{18}O$	145	13	coral	0.71	-0.76	160	-50	1	1	Yes
aust002	11	47	tree ring	0.40	-0.56	384	-21	1	1	Yes
az080	251	36	tree ring	0.40	0.42	352	-21	1	1	Yes
az081	251	36	tree ring	0.40	0.42	349	-21	1	1	Yes
az082	251	36	tree ring	0.40	0.42	574	-22	1	1	Yes
az084	250	36	tree ring	0.40	0.42	480	-21	1	1	Yes
az086	249	37	tree ring	0.40	0.42	585	-21	1	1	Yes
az089	250	34	tree ring	0.40	0.20	354	-22	1	1	Yes
az091	248	36	tree ring	0.40	0.42	261	-22	1	1	Yes
az098	248	36	tree ring	0.40	0.42	302	-22	1	1	Yes
az099	250	35	tree ring	0.40	0.20	263	-23	1	1	Yes
az102	250	37	tree ring	0.40	0.42	460	-22	1	1	Yes
az104	246	37	tree ring	0.40	0.51	356	-21	1	1	Yes

Continued on next page

Table A.2 – continued from previous page

Reference	Longitude (°E)	Latitude (°N)	Proxy (m)	SNR	EOF	Start (years)	End (years)	Resolution (years)	Dating error (years)	Included?
az106	248	36	tree ring	0.40	0.42	502	-25	1	1	Yes
az109	247	35	tree ring	0.40	0.51	352	-21	1	1	Yes
az127	248	37	tree ring	0.40	0.42	369	-26	1	1	Yes
az129	248	37	tree ring	0.40	0.42	468	-26	1	1	Yes
az135	246	35	tree ring	0.40	0.51	381	-21	1	1	Yes
az143	247	36	tree ring	0.40	0.51	307	-22	1	1	Yes
az144	248	37	tree ring	0.40	0.42	469	-25	1	1	Yes
az505	248	36	tree ring	0.40	0.42	257	-25	1	1	Yes
az510	248	36	tree ring	0.40	0.42	1402	-33	1	1	Yes
az527	249	34	tree ring	0.40	0.20	320	-36	1	1	Yes
az542	250	34	tree ring	0.40	0.20	320	-36	1	1	Yes
Bagnato et al. (2005) $\delta^{18}O$	179	-17	coral	0.16	-1.56	174	-51	1	1	Yes
Barron (2003)	235	42	marine	N/A	N/A	15804	158	100	90	No; Dating error
Berke et al. (2012)	37	3	lake	N/A	N/A	173	-40	6	6	No; AOI
Berke et al. (2012)	37	3	lake	N/A	N/A	2529	477	44	60	No; AOI
Black et al. (2007)	295	11	marine	0.40	0.89	729	-40	2	5	Yes
Boiseau et al. (1999) $\delta^{18}O$	210	-18	coral	N/A	N/A	98	-41	1	1	No; Length
ca051	243	34	tree ring	0.40	0.90	1992	-20	1	1	Yes
ca066	239	40	tree ring	0.40	0.40	479	-30	1	1	Yes
ca067	239	40	tree ring	0.40	0.40	466	-30	1	1	Yes
ca089	242	35	tree ring	0.40	0.39	445	-31	1	1	Yes
ca092	241	37	tree ring	0.40	0.39	516	-31	1	1	Yes
ca094	242	36	tree ring	0.40	0.39	422	-31	1	1	Yes
ca514	242	36	tree ring	0.40	0.39	343	-31	1	1	Yes
ca528	242	37	tree ring	0.40	0.39	1052	-37	1	1	Yes
ca529	241	37	tree ring	0.40	0.39	1251	-37	1	1	Yes
ca530	242	37	tree ring	0.40	0.39	1033	-37	1	1	Yes
ca531	242	37	tree ring	0.40	0.39	923	-37	1	1	Yes
ca532	241	37	tree ring	0.40	0.39	900	-37	1	1	Yes
ca536	243	34	tree ring	0.40	0.90	296	-38	1	1	Yes

Continued on next page

Table A.2 – continued from previous page

Reference	Longitude (°E)	Latitude (°N)	Proxy (m)	SNR	EOF	Start (years)	End (years)	Resolution (years)	Dating error (years)	Included?
ca544	243	34	tree ring	0.40	0.90	243	-38	1	1	Yes
ca546	243	34	tree ring	0.40	0.90	209	-38	1	1	Yes
ca547	243	34	tree ring	0.40	0.90	266	-38	1	1	Yes
ca552	243	34	tree ring	0.40	0.90	322	-38	1	1	Yes
ca555	237	40	tree ring	0.40	0.40	773	-38	1	1	Yes
ca609	243	34	tree ring	0.40	0.90	390	-45	1	1	Yes
ca612	241	35	tree ring	0.40	0.90	480	-43	1	1	Yes
ca619	238	40	tree ring	0.40	0.40	587	-54	1	1	Yes
ca621	241	36	tree ring	0.40	0.39	365	-53	1	1	Yes
ca625	239	37	tree ring	0.40	0.63	440	-53	1	1	Yes
ca626	239	37	tree ring	0.40	0.63	373	-53	1	1	Yes
ca628	239	40	tree ring	0.40	0.40	500	-48	1	1	Yes
Charles (1997) $\delta^{18}O$	55	-5	coral	0.71	0.25	103	-45	1	1	No; AOI
Charles et al. (2003) Bali	116	-8	coral	0.46	-0.55	168	-40	1	1	Yes
Charles et al. (2003) Bunaken	125	2	coral	N/A	N/A	90	-41	1	1	No; Length
co066	252	38	tree ring	0.40	-0.29	493	-28	1	1	Yes
co067	252	38	tree ring	0.40	-0.29	680	-28	1	1	Yes
co511	254	40	tree ring	0.40	0.02	781	-39	1	1	Yes
co526	255	40	tree ring	0.40	0.02	300	-30	1	1	Yes
co532	254	40	tree ring	0.40	0.02	310	-37	1	1	Yes
co533	255	40	tree ring	0.40	0.02	400	-37	1	1	Yes
co538	255	41	tree ring	0.40	0.02	280	-37	1	1	Yes
co542	255	40	tree ring	0.40	0.02	260	-37	1	1	Yes
co543	254	40	tree ring	0.40	0.02	380	-37	1	1	Yes
co544	254	40	tree ring	0.40	0.02	520	-37	1	1	Yes
co545	255	40	tree ring	0.40	0.02	620	-37	1	1	Yes
co547	254	40	tree ring	0.40	0.02	880	-37	1	1	Yes
co548	255	39	tree ring	0.40	-0.79	300	-38	1	1	Yes
co549	254	40	tree ring	0.40	0.02	440	-37	1	1	Yes
co550	255	40	tree ring	0.40	0.02	260	-37	1	1	Yes

Continued on next page

Table A.2 – continued from previous page

Reference	Longitude (°E)	Latitude (°N)	Proxy (m)	SNR	EOF	Start (years)	End (years)	Resolution (years)	Dating error (years)	Included?
co551	255	40	tree ring	0.40	0.02	200	-37	1	1	Yes
co563	254	40	tree ring	0.40	0.02	252	-51	1	1	Yes
co568	257	37	tree ring	0.40	-1.27	322	-48	1	1	Yes
co569	256	37	tree ring	0.40	-1.27	486	-47	1	1	Yes
co572	255	40	tree ring	0.40	0.02	1056	-48	1	1	Yes
co579	254	40	tree ring	0.40	0.02	630	-52	1	1	Yes
co581	253	41	tree ring	0.40	0.02	411	-50	1	1	Yes
Cole (2000)	40	-3	coral	N/A	N/A	149	-44	1	1	No; AOI
Conroy et al. (2009)	271	-1	lake	N/A	N/A	1219	-54	5	70	No; Dating error
Cook et al. (2000)	146	-42	tree ring	0.53	-0.71	3550	-41	1	1	Yes
Cronin et al. (2003)	284	38	marine	N/A	N/A	2134	-45	8	80	No; Dating error
Cronin et al. (2005)	284	38	marine	N/A	N/A	2127	-45	8	80	No; Dating error
Damassa et al. (2006) $\delta^{18}O$	40	-8	coral	0.66	0.54	328	-48	1	5	Yes
DeLong et al. (2012)	167	-23	coral	0.61	-2.06	301	-50	1	1	Yes
DeLong et al. (2014)	277	25	coral	0.93	-0.57	216	-59	1	1	Yes
Dunbar et al. (1994)	269	0	coral	N/A	N/A	343	-31	1	1	No; AOI
Felis et al. (2010) UCa	142	27	coral	N/A	N/A	77	-44	1	1	No; Length
Goni et al. (2006) Cariaco	295	11	marine	0.40	0.89	256	-46	8	60	Yes
Goni et al. (2006) Guaymas	248	28	marine	0.40	0.79	223	-38	5	60	Yes
Goodkin et al. (2008)	296	32	coral	0.40	-0.45	168	-48	1	1	Yes
Guilderson & Schrag (1999) $\delta^{18}O$	166	-30	coral	N/A	N/A	53	-46	1	1	No; Length
Heiss (1994)	35	29	coral	0.29	-1.06	161	-43	1	1	Yes
Hetzinger et al. (2010) $\delta^{18}O$	-422	16	coral	N/A	N/A	54	-49	1	1	No; Length
Hetzinger et al. (2010) Sr/Ca	-422	16	coral	N/A	N/A	54	-49	1	1	No; Length
ia003	268	41	tree ring	0.40	-0.41	235	-31	1	1	Yes
id002	244	48	tree ring	0.40	0.63	278	-26	1	1	Yes
il010	270	40	tree ring	0.40	-0.55	279	-30	1	1	Yes
il011	272	39	tree ring	0.40	-0.55	276	-30	1	1	Yes
il013	271	38	tree ring	0.40	-0.99	295	-31	1	1	Yes
il014	271	38	tree ring	0.40	-0.99	298	-31	1	1	Yes

Continued on next page

Table A.2 – continued from previous page

Reference	Longitude (°E)	Latitude (°N)	Proxy (m)	SNR	EOF	Start (years)	End (years)	Resolution (years)	Dating error (years)	Included?
indi002	74	35	tree ring	0.40	-0.23	346	-30	1	1	Yes
indi006	76	35	tree ring	0.40	-0.34	296	-31	1	1	Yes
ital023	12	47	tree ring	0.40	-0.75	476	-40	1	1	Yes
Keigwin (1996)	302	34	marine	0.77	-0.41	3125	25	50	50	Yes
Kellerhals et al. (2010)	292	-17	ice core	0.40	0.71	1595	-45	10	20	Yes
Khider et al. (2014) SST	126	7	marine	N/A	N/A	9960	199	15	262	No; Dating error
Kilbourne et al. (2008) $\delta^{18}O$	293	18	coral	0.30	0.47	199	-54	1	1	Yes
Krusic et al. (2015)	91	27	tree ring	0.40	-0.66	574	-63	1	1	Yes
ks007	264	38	tree ring	0.40	-1.07	212	-29	1	1	Yes
Kuhnert et al. (2000)	114	-22	coral	N/A	N/A	71	-45	1	1	No; AOI
Kuhnert et al. (2005) $\delta^{18}O$	295	33	coral	0.11	-0.77	83	-33	1	1	Yes
ky003	277	37	tree ring	0.40	-1.12	290	-32	1	1	Yes
Linsley et al. (2000) Clipperton	251	10	coral	N/A	N/A	55	-44	1	1	No; Length
Linsley et al. (2006) Rarotonga Sr/Ca	201	-22	coral	0.15	-1.99	223	-47	1	1	Yes
Linsley et al. (2006) Savusavu Sr/Ca	179	-17	coral	0.28	-1.56	168	-47	1	1	Yes
Marchitto et al. (2010)	247	25	marine	0.40	2.06	13812	832	50	50	No; AOI
me019	292	46	tree ring	0.40	-0.80	253	-31	1	1	Yes
mi009	275	47	tree ring	0.40	-0.83	440	-33	1	1	Yes
mo003	269	37	tree ring	0.40	-0.94	257	-31	1	1	Yes
mo005	270	38	tree ring	0.40	-0.94	242	-32	1	1	Yes
mo018	266	37	tree ring	0.40	-1.07	226	-29	1	1	Yes
mo033	267	37	tree ring	0.40	-0.94	254	-42	1	1	Yes
mo036	266	37	tree ring	0.40	-1.07	261	-29	1	1	Yes
mo037	270	37	tree ring	0.40	-0.94	765	-42	1	1	Yes
mo038	268	37	tree ring	0.40	-0.94	397	-42	1	1	Yes
mo039	268	38	tree ring	0.40	-0.94	286	-42	1	1	Yes
mo040	269	37	tree ring	0.40	-0.94	257	-43	1	1	Yes
mo043	269	37	tree ring	0.40	-0.94	812	-40	1	1	Yes
morc002	355	35	tree ring	0.40	0.34	318	-34	1	1	Yes

Continued on next page

Table A.2 – continued from previous page

Reference	Longitude (°E)	Latitude (°N)	Proxy (m)	SNR	EOF	Start (years)	End (years)	Resolution (years)	Dating error (years)	Included?
Moustafa (2000)	34	28	coral	N/A	N/A	52	-43	1	1	No; Length
nc002	277	36	tree ring	0.40	-1.12	392	-33	1	1	Yes
nc003	278	36	tree ring	0.40	-1.09	390	-33	1	1	Yes
nc006	277	35	tree ring	0.40	-1.12	273	-33	1	1	Yes
nc007	278	36	tree ring	0.40	-1.09	333	-27	1	1	Yes
nc009	283	37	tree ring	0.40	-1.11	426	-34	1	1	Yes
nj001	285	41	tree ring	0.40	-0.76	330	-32	1	1	Yes
nj002	285	41	tree ring	0.40	-0.76	276	-32	1	1	Yes
nm021	252	37	tree ring	0.40	-0.29	395	-21	1	1	Yes
nm023	252	37	tree ring	0.40	-0.29	375	-21	1	1	Yes
nm024	253	37	tree ring	0.40	-0.29	307	-21	1	1	Yes
nm025	252	36	tree ring	0.40	-0.29	569	-22	1	1	Yes
nm026	254	36	tree ring	0.40	-0.29	588	-22	1	1	Yes
nm031	252	35	tree ring	0.40	-0.29	472	-22	1	1	Yes
nm033	252	35	tree ring	0.40	-0.29	414	-22	1	1	Yes
nm034	252	35	tree ring	0.40	-0.52	288	-22	1	1	Yes
nm038	254	36	tree ring	0.40	-0.29	394	-22	1	1	Yes
nm040	254	36	tree ring	0.40	-0.29	371	-22	1	1	Yes
nm047	257	37	tree ring	0.40	-1.27	310	-24	1	1	Yes
nm051	253	36	tree ring	0.40	-0.29	263	-26	1	1	Yes
nm053	252	36	tree ring	0.40	-0.29	321	-26	1	1	Yes
nm055	253	37	tree ring	0.40	-0.29	356	-21	1	1	Yes
nm118	254	35	tree ring	0.40	-0.29	386	-32	1	1	Yes
nm500	254	36	tree ring	0.40	-0.29	242	-22	1	1	Yes
nm501	254	36	tree ring	0.40	-0.29	223	-22	1	1	Yes
nm529	251	36	tree ring	0.40	0.42	298	-27	1	1	Yes
nm548	255	37	tree ring	0.40	-0.29	358	-31	1	1	Yes
nm549	255	37	tree ring	0.40	-0.29	311	-37	1	1	Yes
nm550	253	36	tree ring	0.40	-0.29	418	-36	1	1	Yes
nm551	255	36	tree ring	0.40	-0.29	250	-31	1	1	Yes

Continued on next page

Table A.2 – continued from previous page

Reference	Longitude (°E)	Latitude (°N)	Proxy (m)	SNR	EOF	Start (years)	End (years)	Resolution (years)	Dating error (years)	Included?
nm552	255	36	tree ring	0.40	-0.29	369	-31	1	1	Yes
nm554	255	36	tree ring	0.40	-0.29	260	-36	1	1	Yes
nm555	253	36	tree ring	0.40	-0.29	346	-36	1	1	Yes
nm556	253	36	tree ring	0.40	-0.29	378	-36	1	1	Yes
nm557	254	36	tree ring	0.40	-0.29	395	-36	1	1	Yes
nm558	253	36	tree ring	0.40	-0.29	297	-37	1	1	Yes
nm559	255	37	tree ring	0.40	-0.29	559	-37	1	1	Yes
nm560	255	37	tree ring	0.40	-0.29	1113	-39	1	1	Yes
nm575	256	37	tree ring	0.40	-1.27	238	-48	1	1	Yes
nm576	256	37	tree ring	0.40	-1.27	324	-48	1	1	Yes
nm577	256	36	tree ring	0.40	-1.27	355	-48	1	1	Yes
Nurhati et al. (2009)	198	6	coral	N/A	N/A	64	-48	1	1	No; AOI
nv048	245	40	tree ring	0.40	0.63	447	-28	1	1	Yes
nv506	245	37	tree ring	0.40	0.51	345	-27	1	1	Yes
nv507	245	39	tree ring	0.40	0.63	485	-26	1	1	Yes
nv509	245	39	tree ring	0.40	0.63	399	-26	1	1	Yes
nv510	244	36	tree ring	0.40	0.51	1150	-34	1	1	Yes
nv512	245	40	tree ring	0.40	0.63	1630	-35	1	1	Yes
nv513	246	39	tree ring	0.40	0.63	1125	-33	1	1	Yes
nv514	245	41	tree ring	0.40	0.63	1648	-35	1	1	Yes
nv516	246	39	tree ring	0.40	0.63	1950	-34	1	1	Yes
nv517	244	36	tree ring	0.40	0.51	1630	-34	1	1	Yes
oh003	276	40	tree ring	0.40	-0.83	288	-35	1	1	Yes
oh006	279	40	tree ring	0.40	-0.90	325	-48	1	1	Yes
ok001	265	37	tree ring	0.40	-1.07	275	-29	1	1	Yes
ok004	264	37	tree ring	0.40	-1.07	213	-29	1	1	Yes
ok007	264	36	tree ring	0.40	-1.07	339	-45	1	1	Yes
ok013	262	36	tree ring	0.40	-1.37	270	-29	1	1	Yes
ok016	264	35	tree ring	0.40	-1.07	205	-29	1	1	Yes
ok019	265	34	tree ring	0.40	-1.63	326	-29	1	1	Yes

Continued on next page

Table A.2 – continued from previous page

Reference	Longitude (°E)	Latitude (°N)	Proxy (m)	SNR	EOF	Start (years)	End (years)	Resolution (years)	Dating error (years)	Included?
ok025	262	34	tree ring	0.40	-1.99	259	-45	1	1	Yes
ok028	261	35	tree ring	0.40	-1.99	264	-29	1	1	Yes
ok031	265	34	tree ring	0.40	-1.63	265	-32	1	1	Yes
Oppo et al. (2009) SST	119	-5	marine	0.40	-0.38	1925	-5	11	50	Yes
or040	242	46	tree ring	0.40	0.25	275	-41	1	1	Yes
pa001	282	41	tree ring	0.40	-0.75	341	-31	1	1	Yes
pa005	280	40	tree ring	0.40	-0.90	327	-31	1	1	Yes
pa007	282	40	tree ring	0.40	-0.75	415	-31	1	1	Yes
pa009	284	40	tree ring	0.40	-0.75	319	-31	1	1	Yes
pa012	282	40	tree ring	0.40	-0.75	338	-31	1	1	Yes
Powers et al. (2011)	34	-10	lake	N/A	N/A	667	-46	41	50	No; AOI
Quinn et al. (1998)	167	-23	coral	0.33	-2.06	292	-43	1	1	Yes
Quinn et al. (2006) $\delta^{18}O$	152	4	coral	N/A	N/A	83	-48	1	1	No; Length
Richey et al. (2009) Fisk	268	28	marine	0.40	-1.33	702	-50	19	35	Yes
Richey et al. (2009) Garrison	266	27	marine	0.40	-1.64	529	-50	33	45	Yes
Saenger et al. (2009) ext	281	26	coral	0.73	-0.14	398	-41	1	1	Yes
Saenger et al. (2011) ggc	284	33	marine	0.40	-1.22	1500	100	100	45	Yes
Saenger et al. (2011) mc	284	33	marine	0.40	-1.22	1700	100	100	40	Yes
spai009	358	40	tree ring	0.40	0.23	262	-38	1	1	Yes
spai011	358	40	tree ring	0.40	0.23	465	-38	1	1	Yes
spai013	0	40	tree ring	0.40	-0.18	265	-42	1	1	Yes
spai016	355	41	tree ring	0.40	0.23	283	-38	1	1	Yes
spai018	355	40	tree ring	0.40	0.23	263	-39	1	1	Yes
spai019	356	41	tree ring	0.40	0.23	427	-38	1	1	Yes
spai029	358	40	tree ring	0.40	0.23	239	-33	1	1	Yes
spai036	356	41	tree ring	0.40	0.23	201	-33	1	1	Yes
spai037	356	41	tree ring	0.40	0.23	289	-35	1	1	Yes
spai038	356	41	tree ring	0.40	0.23	351	-34	1	1	Yes
spai041	1	40	tree ring	0.40	-0.18	269	-35	1	1	Yes
spai045	358	40	tree ring	0.40	0.23	312	-35	1	1	Yes

Continued on next page

Table A.2 – continued from previous page

Reference	Longitude (°E)	Latitude (°N)	Proxy (m)	SNR	EOF	Start (years)	End (years)	Resolution (years)	Dating error (years)	Included?
spai046	358	40	tree ring	0.40	0.23	306	-35	1	1	Yes
Stott et al. (2002) <i>G.Ruber</i>	126	6	marine	0.40	-0.46	67592	89	25	50	Yes
Sundqvist et al. (2013)	29	-24	speleothem	0.46	0.45	315	-43	1	3	Yes
Thompson et al. (1995)	282	-9	ice core	0.40	0.92	19100	0	100	20	Yes
Thompson & et Al. (1997)	82	35	ice core	0.40	-0.13	1946	-34	10	20	Yes
Thompson et al. (2002) furt	37	-3	ice core	0.40	0.62	270	30	10	20	Yes
Thompson et al. (2002) knif2	37	-3	ice core	0.40	0.62	1490	0	10	20	Yes
Thompson et al. (2002) knif3	37	-3	ice core	0.40	0.62	1490	0	10	20	Yes
Thompson et al. (2002) ksif1	37	-3	ice core	0.40	0.62	1270	0	10	20	Yes
Thompson et al. (2002) ksif2	37	-3	ice core	0.40	0.62	1470	0	10	20	Yes
Thompson et al. (2003) Dasuopu	86	28	ice core	0.40	-0.07	940	-47	10	20	Yes
Thompson et al. (2003) Dundee	96	38	ice core	0.40	0.14	940	-37	10	20	Yes
Thompson et al. (2006) c1 $\delta^{18}O$	89	34	ice core	N/A	N/A	1946	-44	5	95	No; Dating error
Thompson et al. (2006) c2 $\delta^{18}O$	89	34	ice core	0.40	-0.66	1946	-44	5	50	Yes
Thompson et al. (2006) Dundee an	96	38	ice core	0.40	0.14	344	-31	5	20	Yes
Thompson et al. (2006) Dundee $\delta^{18}O$	96	38	ice core	0.40	0.14	1426	-32	10	20	Yes
Thompson et al. (2013) nd	289	-14	ice core	0.40	0.43	945	-45	10	10	Yes
Thompson et al. (2013) sd	289	-14	ice core	0.66	0.43	1724	-59	1	10	Yes
Tierney et al. (2015) bc1 SST	44	45	marine	0.40	-0.69	322	-50	9	25	Yes
Tierney et al. (2015) p SST	44	45	marine	0.40	-0.69	1819	-30	20	25	Yes
Tiwari et al. (2015)	74	13	marine	0.40	0.11	4772	154	62	45	Yes
tn008	276	36	tree ring	0.40	-1.12	317	-30	1	1	Yes
Tudhope et al. (2001) Laing	145	-4	coral	N/A	N/A	65	-43	1	1	No; Length
Tudhope et al. (2001) Madang	146	-5	coral	N/A	N/A	69	-43	1	1	No; Length
turk001	31	40	tree ring	0.40	-1.23	658	-51	1	1	Yes
turk005	30	37	tree ring	0.40	-1.13	580	-38	1	1	Yes
turk006	30	37	tree ring	0.40	-1.13	590	-38	1	1	Yes
ut013	250	41	tree ring	0.40	0.73	517	-21	1	1	Yes
ut018	251	39	tree ring	0.40	0.73	461	-22	1	1	Yes
ut020	250	38	tree ring	0.40	0.42	505	-21	1	1	Yes

Continued on next page

Table A.2 – continued from previous page

Reference	Longitude (°E)	Latitude (°N)	Proxy (m)	SNR	EOF	Start (years)	End (years)	Resolution (years)	Dating error (years)	Included?
ut021	249	37	tree ring	0.40	0.42	385	-21	1	1	Yes
ut023	250	38	tree ring	0.40	0.42	603	-22	1	1	Yes
ut024	250	38	tree ring	0.40	0.42	674	-20	1	1	Yes
ut501	250	41	tree ring	0.40	0.73	315	-21	1	1	Yes
va008	281	38	tree ring	0.40	-0.90	290	-28	1	1	Yes
va009	281	38	tree ring	0.40	-1.09	363	-32	1	1	Yes
va010	281	38	tree ring	0.40	-1.09	419	-32	1	1	Yes
va012	278	37	tree ring	0.40	-1.09	305	-32	1	1	Yes
Hengstum et al. (2015) whc4	295	32	marine	0.40	-0.77	2792	-56	30	35	Yes
Vasquez-Bedoya et al. (2012) ext	273	21	coral	1.04	-0.20	177	-59	1	1	Yes
wa048	238	47	tree ring	0.40	0.40	664	-29	1	1	Yes
wa056	239	47	tree ring	0.40	0.40	691	-29	1	1	Yes
wa057	239	48	tree ring	0.40	0.40	520	-30	1	1	Yes
wa058	237	48	tree ring	0.40	0.40	533	-30	1	1	Yes
wa063	239	47	tree ring	0.40	0.40	364	-30	1	1	Yes
wa065	239	48	tree ring	0.40	0.40	408	-32	1	1	Yes
wa085	239	47	tree ring	0.40	0.40	435	-37	1	1	Yes
Wörheide (1998)	146	-15	coral	0.40	-0.96	398	-40	10	10	Yes
Wu et al. (2013) Sr/Ca	186	-20	coral	N/A	N/A	159	-53	1	1	No; AOI
Wurtzel et al. (2013)	295	11	marine	0.40	0.89	2010	-58	1	60	Yes
wv002	281	39	tree ring	0.40	-0.90	440	-29	1	1	Yes
Zhao et al. (2000)	240	34	marine	0.40	1.05	653	9	1	5	Yes
Zinke et al. (2014) AC	44	-23	coral	0.40	0.00	290	-44	1	1	Yes
Zinke et al. (2014) HAI	114	-29	coral	0.88	-0.46	155	-60	1	1	Yes
Zinke et al. (2015) Ning	114	-22	coral	N/A	N/A	71	-58	1	1	No; Length
Zinke et al. (2015) Rowley	119	-17	coral	0.63	-0.63	152	-59	1	1	Yes

TABLE A.2: As Table A.1, but for temperature proxies.

Appendix B

Proxy data used in Chapter 5

193

B.1 Charcoal records

Site Name	Latitude (°N)	Longitude (°E)	Elevation (m)	Biome	Site Type	Length (years)	Resolution (years)
ODP Site 820	-16.6	146.3	0	marine	marine	99636	898
Core Fr10.95-GC-17	-22	113.5	0	marine	marine	101639	1037
Boggy Swamp	-30	151.5	1160	warm-temperate evergreen broadleaf and mixed	terrestrial, mire, bog	12535	149
Butchers Swamp	-30	151.5	1230	warm-temperate evergreen broadleaf and mixed	terrestrial, mire, bog	14257	446
Haeapugua	-5.8	142.8	1650	tropical evergreen broadleaf	terrestrial marsh	25319	309
Noreikora Swamp	-6.3	145.8	1750	tropical evergreen broadleaf	terrestrial marsh	6497	271
Rawa Danau	-6.2	106	100	tropical evergreen broadleaf	lacustrine	16483	532
Whitehaven Swamp	-20.3	148.9	45	tropical deciduous broadleaf forest and woodland	terrestrial, mire, bog	8072	152

Continued on next page

Table B.1 – continued from previous page

Site Name	Latitude (°N)	Longitude (°E)	Elevation (m)	Biome	Site Type	Length (years)	Resolution (years)
Lake Habbema	-4.1	138.7	3120	tropical xerophytic shrubland	lacustrine	11181	254
Tugupugua	-5.7	142.6	2300	tropical evergreen broadleaf	terrestrial, mire, fen	18322	291
Ijomba	-4	137.2	3630	tropical evergreen broadleaf	terrestrial, mire, fen	17485	397
Laukutu Swamp	-9.5	160.1	20	desert	terrestrial, mire, bog	3938	303
Pemerak Swamp	0.8	112.1	40	tropical evergreen broadleaf	terrestrial, mire, bog	35427	1222
Lake Majo	-1.5	127.5	140	barren	lacustrine	5596	233
Lac Suprin	-22.2	166.6	230	barren	lacustrine	33175	706
Voli Voli	-18.2	177.5	2	tropical evergreen broadleaf	terrestrial, mire, bog	5873	140
Supulah Hill	-4.1	139	1580	tropical xerophytic shrubland	terrestrial, mire, bog	39000	1054
Wanda	-2.3	121.2	440	tropical evergreen broadleaf	terrestrial, mire, bog	49202	895
Lake Euramoo	-17.2	145.6	718	tropical semi-evergreen broadleaf	lacustrine, volcanic lake, explosion crater	23527	31
Argan Swamp	-10.1	142.1	3	tropical deciduous broadleaf forest and woodland	coastal	5457	52
Talita Kupai	-10.1	142.1	33	tropical deciduous broadleaf forest and woodland	coastal, estuarine	2414	20
Waruid	-10.4	142.1	5	tropical deciduous broadleaf forest and woodland	coastal	7126	48
Tiam Point	-10.1	142.2	3	tropical deciduous broadleaf forest and woodland	coastal, salt marsh	7501	156
Boigu Gawat Core 1	-10.1	142.1	10	tropical deciduous broadleaf forest and woodland	coastal	4569	91
Bar20	-10.1	142.1	18	tropical deciduous broadleaf forest and woodland	coastal	2733	48
Zurath Islet	-10.2	142.1	3	tropical deciduous broadleaf forest and woodland	coastal	11825	370
Allom Lake	-25.2	153.2	100	warm-temperate evergreen broadleaf and mixed	lacustrine	56986	467
Quambie Lagoon	-12.5	131.2	20	tropical savanna	lacustrine	6386	67
Xere Wapo C	-22.3	167	220	barren	lacustrine	78799	281
Ajkwa 1	-4.9	137	1.3	tropical evergreen broadleaf	coastal	6161	228
Ajkwa 2	-4.9	137	1.3	tropical evergreen broadleaf	coastal	10427	171
Ajkwa 3	-4.9	137	1.3	tropical evergreen broadleaf	coastal	2964	72
Ajkwa 4	-4.9	137	1.3	tropical evergreen broadleaf	coastal	5553	206
Ajkwa 5	-4.9	137	1.3	tropical evergreen broadleaf	coastal	5553	135
Anggi Lake	-1.4	133.9	1945	temperate evergreen needleleaf forest	lacustrine, natural open-water, tectonic lake	26084	2898
Anumon Swamp	-20.2	169.8	45	barren	terrestrial, mire, fen	1817	227

Continued on next page

Table B.1 – continued from previous page

Site Name	Latitude (°N)	Longitude (°E)	Elevation (m)	Biome	Site Type	Length (years)	Resolution (years)
Aru	-5.9	134.2	1	barren	terrestrial	6890	383
Hogayaku	-4	137.4	3580	tropical xerophytic shrubland	lacustrine, natural open-water, glacial origin, morainally dammed lake	5368	96
Lake Hordorli	-2.5	140.6	680	tropical evergreen broadleaf	terrestrial, mire, bog	63347	1056
Koumac	-20.7	164.3	2	desert	coastal, salt marsh	6039	1006
Doge Doge	-17.9	177.3	8	tropical evergreen broadleaf	fluvial	8325	520
Plum Swamp	-22.3	166.6	40	barren	terrestrial, mire, bog	23100	296
Saint Louis Lac	-22.2	166.6	5	barren	terrestrial, mire, bog	7236	117
Kelela Swamp	-4	138.9	1650	tropical xerophytic shrubland	terrestrial, mire, bog	11701	316
Kosipe A	-8.5	147.2	1960	warm-temperate evergreen broadleaf and mixed	terrestrial marsh	33386	1151
Kosipe C	-8.5	147.2	1960	warm-temperate evergreen broadleaf and mixed	terrestrial marsh	55030	1251
Laravita	-8.4	147.4	3570	warm-temperate evergreen broadleaf and mixed	terrestrial, mire, bog	16139	521
Aguai Ramata	-6.6	145.2	1950	tropical evergreen broadleaf	lacustrine, volcanic lake	15775	30
Sondambile	-6.3	147.1	2850	tropical evergreen broadleaf	lacustrine, natural open-water, glacial origin	1334	4
Wanum	-6.6	146.8	35	tropical evergreen broadleaf	lacustrine, natural open-water	3895	14
Yawi Ti	-6.6	143.9	1150	tropical evergreen broadleaf	terrestrial, mire, bog	16835	145
Xere Wapo B	-22.3	167	220	barren	lacustrine	126089	1910
Native Companion La- goon	-27.7	153.4	20	tropical semi-evergreen broadleaf	coastal	34450	594
Bonatoa	-18.1	178.5	4	tropical evergreen broadleaf	terrestrial, mire, bog	5437	194
Navatu	-18.1	178.5	4	tropical evergreen broadleaf	terrestrial, mire, bog	8338	417
Sari	-16.6	179.5	67	barren	terrestrial, mire, bog	6427	279
Vunimoli	-18.2	177.9	251	tropical evergreen broadleaf	terrestrial, mire, bog	4710	471
Lombok Ridge Core G6-4	-10.8	118.1	0	marine	marine	375041	2778
Lake Coomboo	-25.2	153.2	90	warm-temperate evergreen broadleaf and mixed	lacustrine	201782	3203
Dalhousie Springs	-26.4	135.5	150	Not known	terrestrial mound spring or spring	1760	93
Evoran Pond	-18.8	169	194	barren	lacustrine	2563	92

Continued on next page

Table B.1 – continued from previous page

Site Name	Latitude (°N)	Longitude (°E)	Elevation (m)	Biome	Site Type	Length (years)	Resolution (years)
Nadrau	-17.8	177.9	680	tropical evergreen broadleaf	terrestrial	2250	73
Nekkeng	7.5	134.5	9	warm-temperate evergreen broadleaf and mixed	terrestrial	8287	1184
Ngardmau	7.6	134.6	10	temperature evergreen needleleaf forest	terrestrial	5199	325
Ngerchau	7.6	134.5	9	temperature evergreen needleleaf forest	terrestrial	4494	375
Ngerdok 2	7.5	134.6	25	warm-temperate evergreen broadleaf and mixed	lacustrine, natural open-water	3547	114
Olbed 1	7.5	134.5	20	warm-temperate evergreen broadleaf and mixed	terrestrial	7987	380
Yano	7.4	134.5	40	warm-temperate evergreen broadleaf and mixed	terrestrial	7200	257
Ngerkell	7.6	134.6	10	temperature evergreen needleleaf forest	terrestrial	4007	501
Mela Swamp	-9.5	160.1	20	desert	terrestrial, mire, bog	4981	383
Lynchs Crater (Holocene core)	-17.4	145.7	760	tropical semi-evergreen broadleaf	lacustrine, volcanic lake	7385	284
Neon	-8.5	147.3	2875	warm-temperate evergreen broadleaf and mixed	terrestrial, mire, bog	13010	651
Boigu Gawat Core 2	-10.1	142.1	10	tropical deciduous broadleaf forest and woodland	coastal	13824	276

TABLE B.1: Charcoal records from the Indonesian region used in Chapter 5.

B.2 Precipitation records

Site Name	Latitude (°N)	Longitude (°E)	Elevation (m)	Archive	Proxy	Length (years)	Resolution (years)	Reference
Bidoup Nui Ba National Park	11.6	108.3	1700	tree ring	PDSI	977	1	Buckley et al. (2010)
Great Barrier Reef	-18.3	146.6	0	coral	luminescence	373	1	Hendy et al. (2003)
Forestry Cave 10FC-02	-9.5	160	200	speleothem	$\delta^{18}O$	587	0.3	Maupin et al. (2014)
Forestry Cave 05FC-04	-9.5	160	200	speleothem	$\delta^{18}O$	96	0.2	Maupin et al. (2014)
Makassar Strait	-4.5	118.5	0	marine sediment	$\delta^{18}O_{sw}$	1930	10	Oppo et al. (2009)
Gunung Buda National Park	4.3	115	150	speleothem	$\delta^{18}O$	26420	54	Partin et al. (2007)
Espiritu Santo	-15.5	167	230	speleothem	$\delta^{18}O$	446	0.3	Partin et al. (2013)
Avaiki Cave ASM1	-19	190.2	2-4	speleothem	layer thickness	172	1	Rasbury & Aharon (2006)
Avaiki Cave ASM2	-19	190.2	2-4	speleothem	layer thickness	175	1	Rasbury & Aharon (2006)
Avaiki Cave ASM3	-19	190.2	2-4	speleothem	layer thickness	127	1	Rasbury & Aharon (2006)
Lake Logung	-8	113.3	215	lake sediment	$\delta^{13}C$	1382	16	Rodysill et al. (2012)
Lake Towuti $\delta^{13}C_{wax}$	-2.5	121.5	293	lake sediment	$\delta^{13}C$	59706	412	Russell et al. (2014)
Lake Towuti TiO	-2.5	121.5	293	lake sediment	TiO	59656	615	Russell et al. (2014)
West Sulawesi margin	-3.9	119.5	0	marine sediment	δD_{wax}	2329	32	Tierney et al. (2010)

TABLE B.2: Precipitation records from the Indonesian region used in this Chapter 5.

Appendix C

R scripts

C.1 VS-Lite bugs and corrections

```
1 # Bug corrections to the VSLite R code at https://github.com/suztolwinskiward/VSLiteR
   # made 21/03/2016 by Lilo Henke (University of Exeter)
3
   ## VSLite.R line 113:
5   width(cyear)
7
   # uses wrong bracket types and gives error:
   ' > Error: could not find function "width" '
9
   # Fixed by changing to square brackets:
11  width[cyear]
13
   ## In leakybucket.monthly.R line 112–115:
   # error-catching:
15   if (M[t,cyear] <= Mmin) {M[t,cyear] <- Mmin;}
   if (M[t,cyear] >= Mmax) {M[t,cyear] <- Mmax;}
17   if (is.na(M[t,cyear])==1){ M[t,cyear] <- Mmin;}
19
   # fails when M[t, year] is NA/NaN:
   ' Error in if (M[t, cyear] <= Mmin) { :
21   missing value where TRUE/FALSE needed '
23
   # Fixed by switching them so that it checks for NA first and only
   checks other conditions if is.na is FALSE:
```

```

# error-catching:
25   if (is.na(M[t,cyear])==1){ M[t,cyear] <- Mmin;} else
    if (M[t,cyear] <= Mmin) {M[t,cyear] <- Mmin;} else
27   if (M[t,cyear] >= Mmax) {M[t,cyear] <- Mmax;}

```

C.2 Inverse Transform Sampling (ITS)

```

1  ## gaussianize.R
   # Adapted 17/02/2016 by Lilo Henke (University of Exeter) from the
   # matlab code at https://github.com/CommonClimate/common-climate/
   # blob/master/gaussianize.m
3  #does inverse transform on time series

5  erfinv <- function (x) qnorm((1 + x)/2)/sqrt(2)

7

9  gaussianize=function(X) {
   n<-nrow(X)
   p<-ncol(X)
11
   Xn<-matrix(NA,n,p)
13   for (j in 1:p)
   {
15     # % Sort the data in ascending order and retain permutation indices
       Z<-X[,j]; nz<-!is.na(Z)
17     sorted<-sort(Z[nz])
       index<-order(Z[nz])
19     ni<-length(Z[nz])
       # % Make 'rank' the rank number of each observation
21     rank<-order(index)
       # % The cumulative distribution function
23     CDF = rank/ni - 1/(2*ni)
       # % Apply the inverse Rosenblatt transformation
25     Xn[nz,j]<-sqrt(2)*erfinv(2*CDF - 1) # % Xn is now normally
       distributed

27   #   Xn[,j]<-Xn[index,j]
       }
29   Xn<-data.frame(Xn)

```

```
31   names(Xn) <- names(X)
    return(Xn)
}
```


Appendix D

Data acknowledgements

Many thanks to the Databases of the NOAA World Data Center for Paleoclimatology and Pangaea, and the Global Charcoal Database, and all contributing authors for making available the proxy data used in this thesis.

The GPCP and 20th Century Reanalysis V2 data were provided by the NOAA/OAR/ESRL PSD, Boulder, Colorado, USA, from their Web site at <http://www.esrl.noaa.gov/psd/>.

Support for the Twentieth Century Reanalysis Project dataset is provided by the U.S. Department of Energy, Office of Science Innovative and Novel Computational Impact on Theory and Experiment (DOE INCITE) program, and Office of Biological and Environmental Research (BER), and by the National Oceanic and Atmospheric Administration Climate Program Office.

The GPCP combined precipitation data were developed and computed by the NASA/Goddard Space Flight Center's Laboratory for Atmospheres as a contribution to the GEWEX Global Precipitation Climatology Project.

We acknowledge the World Climate Research Programme's Working Group on Coupled Modelling, which is responsible for CMIP, and we thank the climate modeling groups listed in 3.2.3 for producing and making available their model output. For CMIP the U.S. Department of Energy's Program for Climate Model Diagnosis and Intercomparison provides coordinating support and led development of software infrastructure in partnership with the Global Organization for Earth System Science Portals.

Charcoal records listed in Table B.1 were obtained from the Global Charcoal Database (<http://www.paleofire.org>), and the work of the data contributors and the Global Palaeofire Working Group is gratefully acknowledged.

Lilo Henke was supported by a University of Exeter Climate Change and Sustainable Futures studentship.

Bibliography

- Abram, N. J., Gagan, M. K., Cole, J. E., Hantoro, W. S., & Mudelsee, M. (2008). Recent intensification of tropical climate variability in the Indian Ocean. *Nat. Geosci.*, *1*(12), 849–853.
- Abram, N. J., McGregor, H. V., Gagan, M. K., Hantoro, W. S., & Suwargadi, B. W. (2009). Oscillations in the southern extent of the Indo-Pacific Warm Pool during the mid-Holocene. *Quat. Sci. Rev.*, *28*(25-26), 2794–2803.
- Adler, R. F., Huffman, G. J., Chang, A., Ferraro, R., Xie, P.-P., Janowiak, J., Rudolf, B., Schneider, U., Curtis, S., Bolvin, D., Gruber, A., Susskind, J., Arkin, P., & Nelkin, E. (2003). The Version-2 Global Precipitation Climatology Project (GPCP) Monthly Precipitation Analysis (1979–Present). *J. Hydrometeorol.*, *4*(6), 1147–1167.
- Alibert, C., & Kinsley, L. (2008). A 170-year Sr/Ca and Ba/Ca coral record from the western Pacific warm pool: 1. What can we learn from an unusual coral record? *J. Geophys. Res. Ocean.*, *113*(4), 1–13.
- Allen, M. R., & Ingram, W. J. (2002). Constraints on future changes in climate and the hydrologic cycle. *Nature*, *419*(September), 224–232.
- Anchukaitis, K. J., & Evans, M. N. (2010). Tropical cloud forest climate variability and the demise of the Monteverde golden toad. *Proc. Natl. Acad. Sci. U. S. A.*, *107*(11), 5036–5040.
- Anderson, L. (2011). Holocene record of precipitation seasonality from lake calcite $\delta^{18}\text{O}$ in the central Rocky Mountains, United States. *Geology*, *39*, 211–214.
- Anderson, L. (2012). Rocky Mountain hydroclimate: Holocene variability and the role of insolation, ENSO, and the North American Monsoon. *Glob. Planet. Change*, *92-93*, 198–208.
- Andrews, T., Forster, P. M., Boucher, O., Bellouin, N., & Jones, A. (2010). Precipitation, radiative forcing and global temperature change. *Geophys. Res. Lett.*, *37*(14).

- Anshari, G., Kershaw, A. P., van der Kaars, S., & Jacobsen, G. (2004). Environmental change and peatland forest dynamics in the Lake Sentarum area, West Kalimantan, Indonesia. *J. Quat. Sci.*, *19*, 637–655.
- Anshari, G. Z., Afifudin, M., Nuriman, M., Gusmayanti, E., Arianie, L., Susana, R., Nusantara, R. W., Sugardjito, J., & Rafiastanto, A. (2010). Drainage and land use impacts on changes in selected peat properties and peat degradation in West Kalimantan Province, Indonesia. *Biogeosciences*, *7*(11), 3403–3419.
- Apastegui, J., Cruz, F. W., Sifeddine, A., Vuille, M., Espinoza, J. C., Guyot, J. L., Khodri, M., Strikis, N., Santos, R. V., Cheng, H., Edwards, L., Carvalho, E., & Santini, W. (2014). Hydroclimate variability of the northwestern Amazon Basin near the Andean foothills of Peru related to the South American Monsoon System during the last 1600 years. *Clim. Past*, *10*(6), 1967–1981.
- Arora, V. K., & Boer, G. J. (2005). Fire as an interactive component of dynamic vegetation models. *J. Geophys. Res. Biogeosciences*, *110*(G2).
- As-syakur, A. R., Adnyana, I. W. S., Mahendra, M. S., Arthana, I. W., Merit, I. N., Kasa, I. W., Ekayanti, N. W., Nuarsa, I. W., & Sunarta, I. N. (2014). Observation of spatial patterns on the rainfall response to ENSO and IOD over Indonesia using TRMM Multisatellite Precipitation Analysis (TMPA). *Int. J. Climatol.*, *34*(15), 3825–3839.
- Asami, R. (2005). Interannual and decadal variability of the western Pacific sea surface condition for the years 1787–2000: Reconstruction based on stable isotope record from a Guam coral. *J. Geophys. Res.*, *110*(C5), C05018.
- Ashok, K., Behera, S. K., Rao, S. A., Weng, H., & Yamagata, T. (2007). El Niño Modoki and its possible teleconnection. *J. Geophys. Res. Ocean.*, *112*(11), 1–27.
- Asmerom, Y., Polyak, V., Burns, S. J., & Rasmussen, J. (2007). Solar forcing of Holocene climate: New insights from a speleothem record, southwestern United States. *Geology*, *35*(1), 1–4.
- Badjeck, M.-C., Allison, E. H., Halls, A. S., & Dulvy, N. K. (2010). Impacts of climate variability and change on fishery-based livelihoods. *Mar. Policy*, *34*(3), 375–383.
- Bagnato, S., Linsley, B. K., Howe, S. S., Wellington, G. M., & Salinger, J. (2005). Coral oxygen isotope records of interdecadal climate variations in the South Pacific Convergence Zone region. *Geochemistry, Geophys. Geosystems*, *6*(6), 1–8.

- Baird, A. J., Morris, P. J., & Belyea, L. R. (2012). The DigiBog peatland development model 1: Rationale, conceptual model, and hydrological basis. *Ecohydrology*, *5*, 242–255.
- Baker, A., Bradley, C., Phipps, S. J., Fischer, M., Fairchild, I. J., Fuller, L., Spötl, C., & Azcurra, C. (2012). Millennial-length forward models and pseudoproxies of stalagmite $\delta^{18}O$: an example from NW Scotland. *Clim. Past*, *8*(4), 1153–1167.
- Baker, P. A., Fritz, S. C., Burns, S. J., Ekdahl, E., & Rigsby, C. A. (2009). The Nature and Origin of Decadal to Millennial Scale Climate Variability in the Southern Tropics of South America: The Holocene Record of Lago Umayo, Peru. In *Past Clim. Var. South Am. Surround. Reg. From Last Glacial Maximum to Holocene*, Developments in Paleoenvironmental Research 14, (pp. 301–322). Springer.
- Bala, G., Caldeira, K., & Nemani, R. (2009). Fast versus slow response in climate change: implications for the global hydrological cycle. *Clim. Dyn.*, *35*(2-3), 423–434.
- Balch, O. (2015). Indonesia's forest fires: everything you need to know.
- Barbour, M. M., Roden, J. S., Farquhar, G. D., & Ehleringer, J. R. (2004). Expressing leaf water and cellulose oxygen isotope ratios as enrichment above source water reveals evidence of a Péclet effect. *Oecologia*, *138*(3), 426–435.
- Barron, J. A. (2003). High-resolution climatic evolution of coastal northern California during the past 16,000 years. *Paleoceanography*, *18*(1).
- Barron, J. A., & Anderson, L. (2011). Enhanced Late Holocene ENSO/PDO expression along the margins of the eastern North Pacific. *Quat. Int.*, *235*(1-2), 3–12.
- Bellenger, H., Guilyardi, E., Leloup, J., Lengaigne, M., & Vialard, J. (2014). ENSO representation in climate models: From CMIP3 to CMIP5. *Clim. Dyn.*, *42*, 1999–2018.
- Berke, M. A., Johnson, T. C., Werne, J. P., Schouten, S., & Sinninghe Damsté, J. S. (2012). A mid-Holocene thermal maximum at the end of the African Humid Period. *Earth Planet. Sci. Lett.*, *351-352*, 95–104.
- Bickel, P. J., & Doksum, K. A. (1981). An analysis of transformations revisited. *J. Am. Stat. Assoc.*, *76*(374), 296–311.
- Bird, B. W., Abbott, M. B., Rodbell, D. T., & Vuille, M. (2011). Holocene tropical South American hydroclimate revealed from a decadal resolved lake sediment $\delta^{18}O$ record. *Earth Planet. Sci. Lett.*, *310*(3-4), 192–202.

- Bistinas, I., Harrison, S. P., Prentice, I. C., & Pereira, J. M. C. (2014). Causal relationships versus emergent patterns in the global controls of fire frequency. *Biogeosciences*, *11*(18), 5087–5101.
- Björnsson, H., & Venegas, S. A. (1997). A Manual for EOF and SVD Analysis of Climatic Data. *CCGCR Rep.*, *97*, 52.
- Black, D. E., Abahazi, M. A., Thunell, R. C., Kaplan, A., Tappa, E. J., & Peterson, L. C. (2007). An 8-century tropical Atlantic SST record from the Cariaco Basin: Baseline variability, twentieth-century warming, and Atlantic hurricane frequency. *Paleoceanography*, *22*(4), 1–10.
- Blarquez, O., Vanni ere, B., Marlon, J. R., Daniau, A.-L., Power, M. J., Brewer, S., & Bartlein, P. J. (2014). paleofire: An R package to analyse sedimentary charcoal records from the Global Charcoal Database to reconstruct past biomass burning. *Comput. Geosci.*, *72*, 255–261.
- Boardman, C. P., Gauci, V., Watson, J. S., Blake, S., & Beerling, D. J. (2011). Contrasting wetland CH₄ emission responses to simulated glacial atmospheric CO₂ in temperate bogs and fens. *New Phytol.*, *192*(4), 898–911.
- Boiseau, M., Ghil, M., & Juillet-leclerc, A. (1999). Climatic trends and interdecadal variability from South-Central Pacific coral records. *Geophys. Res. Lett.*, *26*(18), 2881–2884.
- Bonnefille, R., & Chalief, F. (2000). Pollen-inferred precipitation time-series from equatorial mountains, Africa, the last 40 kyr BP. *Glob. Planet. Change*, *26*, 25–50.
- Bony, S., Bellon, G., Klocke, D., Sherwood, S., Fermepin, S., & Denvil, S. (2013). Robust direct effect of carbon dioxide on tropical circulation and regional precipitation. *Nat. Geosci.*, *6*(6), 447–451.
- Bowman, D. M. J. S., Balch, J., Artaxo, P., Bond, W. J., Cochrane, M. A., D'Antonio, C. M., Defries, R., Johnston, F. H., Keeley, J. E., Krawchuk, M. A., Kull, C. A., Mack, M., Moritz, M. A., Pyne, S., Roos, C. I., Scott, A. C., Sodhi, N. S., & Swetnam, T. W. (2011). The human dimension of fire regimes on Earth.
- Box, G., & Cox, R. (1964). An Analysis of Transformations. *J. R. Stat. Soc. Ser. B*, *26*(2), 211–252.
- Box, G., & Pierce, D. (1970). Distribution of Residual Autocorrelations in Autoregressive Integrated moving Average Time Series Models. *J. Am. Stat. Assoc.*, *65*(332), 1509–1526.

- Braconnot, P., Harrison, S. P., Kageyama, M., Bartlein, P. J., Masson-Delmotte, V., Abe-Ouchi, A., Otto-Bliesner, B., & Zhao, Y. (2012). Evaluation of climate models using palaeoclimatic data. *Nat. Clim. Chang.*, *2*(6), 417–424.
- Braconnot, P., Harrison, S. P., Otto-Bliesner, B. L., Abe-Ouchi, A., Jungclaus, J. H., & Peterschmitt, J.-Y. (2011). The Paleoclimate Modeling Intercomparison Project contribution to CMIP5. *CLIVAR Exch. Newsl.*, *16*(56, No. 2), 15–19.
- Braganza, K., Gergis, J. L., Power, S. B., Risbey, J. S., & Fowler, A. M. (2009). A multiproxy index of the El Niño-Southern Oscillation, A.D. 1525-1982. *J. Geophys. Res. Atmos.*, *114*, 1–17.
- Breitenmoser, P., Brönnimann, S., & Frank, D. (2014). Forward modelling of tree-ring width and comparison with a global network of tree-ring chronologies. *Clim. Past*, *10*(2), 437–449.
- Briffa, K. R., Osborn, T. J., Schweingruber, F. H., Harris, I. C., Jones, P. D., Shiyatov, S. G., & Vaganov, E. A. (2001). Low-frequency temperature variations from a northern tree ring density network. *J. Geophys. Res.*, *106*(D3), 2929–2941.
- Broccoli, A. J., Dahl, K. A., & Stouffer, R. J. (2006). Response of the ITCZ to Northern Hemisphere cooling. *Geophys. Res. Lett.*, *33*(1).
- Brook, G., Sheen, S.-W., Rafter, M., Railsback, L., & Lundberg, J. (1999). A high-resolution proxy record of rainfall and ENSO since AD 1550 from layering in stalagmites from Anjohibe Cave, Madagascar. *The Holocene*, *9*, 695–705.
- Brown, E., & Jacobson, M. F. (2005). *Cruel Oil: How Palm Oil Harms Health, Rainforest and Wildlife*. Washington, DC: Center for Science in the Public Interest.
- Brücher, T., Brovkin, V., Kloster, S., Marlon, J. R., & Power, M. J. (2014). Comparing modelled fire dynamics with charcoal records for the Holocene. *Clim. Past*, *10*(2), 811–824.
- Buckley, B. M., Anchukaitis, K. J., Penny, D., Fletcher, R., Cook, E. R., Sano, M., Nam, L. C., Wichienkeo, A., Minh, T. T., & Hong, T. M. (2010). Climate as a contributing factor in the demise of Angkor, Cambodia. *Proc. Natl. Acad. Sci. U. S. A.*, *107*, 6748–6752.
- Bürger, G. (2007). On the verification of climate reconstructions. *Clim. Past Discuss.*, *3*(1), 249–284.

- Cai, W., Santoso, A., Wang, G., Yeh, S.-w., An, S.-i., Cobb, K. M., Collins, M., Guilyardi, E., Jin, F.-f., Kug, J.-s., Lengaigne, M., & McPhaden, M. J. (2015a). ENSO and greenhouse warming. *Nat. Publ. Gr.*, *5*(9), 849–859.
- Cai, W., Wang, G., Santoso, A., McPhaden, M. J., Wu, L., Jin, F.-F., Timmermann, A., Collins, M., Vecchi, G., Lengaigne, M., England, M. H., Dommenges, D., Takahashi, K., & Guilyardi, E. (2015b). Increased frequency of extreme La Niña events under greenhouse warming. *Nat. Clim. Chang.*, *5*(January), 132–137.
- Cane, M. A. (2005). The evolution of El Niño, past and future. *Earth Planet. Sci. Lett.*, *230*, 227–240.
- Carcaillet, C., Almquist, H., Asnong, H., Bradshaw, R., Carrión, J., Gaillard, M.-J., Gajewski, K., Haas, J., Haberle, S., Hadorn, P., Müller, S., Richard, P., Richoz, I., Rösch, M., Sánchez Goñi, M., von Stedingk, H., Stevenson, A., Talon, B., Tardy, C., Tinner, W., Tryterud, E., Wick, L., & Willis, K. (2002). Holocene biomass burning and global dynamics of the carbon cycle. *Chemosphere*, *49*(8), 845–863.
- Carré, M., Bentaleb, I., Fontugne, M., & Lavallée, D. (2005). Strong El Niño events during the early Holocene: stable isotope evidence from Peruvian sea shells. *The Holocene*, *15*, 42–47.
- Cattau, M. E., Harrison, M. E., Shinyo, I., Tungau, S., Uriarte, M., & DeFries, R. (2016). Sources of anthropogenic fire ignitions on the peat-swamp landscape in Kalimantan, Indonesia. *Glob. Environ. Chang.*, *39*, 205–219.
- Charles, C. D. (1997). Interaction Between the ENSO and the Asian Monsoon in a Coral Record of Tropical Climate. *Science* (80-.), *227*, 925–928.
- Charles, C. D., Cobb, K. M., Moore, M. D., & Fairbanks, R. G. (2003). Monsoon-tropical ocean interaction in a network of coral records spanning the 20th century. *Mar. Geol.*, *201*(1-3), 207–222.
- Chen, J., Chen, F., Zhang, E., Brooks, S. J., Zhou, A., & Zhang, J. (2009). A 1000-year chironomid-based salinity reconstruction from varved sediments of Sugan Lake, Qaidam Basin, arid Northwest China, and its palaeoclimatic significance. *Chinese Sci. Bull.*, *54*(40721061), 3749–3759.
- Chen, Y., Morton, D. C., Andela, N., Giglio, L., & Randerson, J. T. (2016). How much global burned area can be forecast on seasonal time scales using sea surface temperatures? *Environ. Res. Lett.*, *11*(4), 45001.

- Chen, Y., Randerson, J. T., Morton, D. C., DeFries, R. S., Collatz, G. J., Kasibhatla, P. S., Giglio, L., Jin, Y., & Marlier, M. E. (2011). Forecasting Fire Season Severity in South America Using Sea Surface Temperature Anomalies. *Science (80-.)*, *334*(6057), 787–791.
- Christie, D. A., Boninsegna, J. A., Cleaveland, M. K., Lara, A., Le Quesne, C., Morales, M. S., Mudelsee, M., Stahle, D. W., & Villalba, R. (2011). Aridity changes in the Temperate-Mediterranean transition of the Andes since AD 1346 reconstructed from tree-rings. *Clim. Dyn.*, *36*, 1505–1521.
- Chronis, T. G., Goodman, S. J., Cecil, D., Buechler, D., Robertson, P. F. J., Pittman, J., & Blakeslee, R. J. (2008). Global lightning activity from the ENSO perspective. *Geophys. Res. Lett.*, *35*(April), 2–6.
- Cleaveland, M. K., Stahle, D. W., Therrell, M. D., Villanueva-Diaz, J., & Burns, B. T. (2003). Tree-ring reconstructed winter precipitation and tropical teleconnections in Durango, Mexico. *Clim. Change*, *59*, 369–388.
- Clemens, S. C., & Prell, W. L. (2003). A 350,000 year summer-monsoon multi-proxy stack from the Owen Ridge, Northern Arabian Sea. *Mar. Geol.*, *201*(1-3), 35–51.
- Clement, A. C. (1999). Orbital controls on ENSO and the tropical climate. *Paleoceanography*, *14*(4), 441–456.
- Clement, A. C., Cane, M. A., & Seager, R. (2001). An Orbitally Driven Tropical Source for Abrupt Climate Change. *J. Clim.*, *14*(11), 2369–2375.
- Clement, A. C., Saeger, R., & Cane, M. A. (2000). Suppression of El Niño during the mid-Holocene by changes in Earth's orbit. *Paleoceanography*, *15*(6), 731–737.
- Cleveland, W. S. (1979). Robust Locally Weighted Regression and Smoothing Scatterplots. *J. Am. Stat. Assoc.*, *74*(368), 829–836.
- Climate Prediction Center Internet Team (2012). Warm (El Niño/Southern Oscillation - ENSO) Episodes in the Tropical Pacific.
- Coats, S., Smerdon, J. E., Cook, B. I., & Seager, R. (2013). Stationarity of the tropical pacific teleconnection to North America in CMIP5/PMIP3 model simulations. *Geophys. Res. Lett.*, *40*(18), 4927–4932.
- Cobb, K. M., Charles, C. D., Cheng, H., & Edwards, R. L. (2003). El Niño/Southern Oscillation and tropical Pacific climate during the last millennium. *Nature*, *424*(July), 271–276.

- Cochrane, M. A. (2003). Fire science for rainforests. *Nature*, 421(6926), 913–919.
- Cole, J. E. (2000). Tropical Pacific Forcing of Decadal SST Variability in the Western Indian Ocean over the Past Two Centuries. *Science (80-.)*, 287, 617–619.
- Cole, J. E., Fairbanks, R. G., & Shen, G. T. (1993). Recent variability in the southern oscillation: isotopic results from a tarawa atoll coral. *Science (80-.)*, 260(5115), 1790–1793.
- Cole, L. E. S., Bhagwat, S. A., & Willis, K. J. (2015). Long-term disturbance dynamics and resilience of tropical peat swamp forests. *J. Ecol.*, 103(1), 16–30.
- Collins, M. (2005). El Niño- or La Niña-like climate change? *Clim. Dyn.*, 24(1), 89–104.
- Collins, M., Knutti, R., Arblaster, J., Dufresne, J.-L., Fichet, T., Friedlingstein, P., Gao, X., Gutowski, W. J., Johns, T., Krinner, G., Shongwe, M., Tebaldi, C., Weaver, A. J., & Wehner, M. (2013). Long-term Climate Change: Projections, Commitments and Irreversibility. *Clim. Chang. 2013 Phys. Sci. Basis. Contrib. Work. Gr. I to Fifth Assess. Rep. Intergov. Panel Clim. Chang.*, (pp. 1029–1136).
- Comboul, M., Emile-Geay, J., Evans, M. N., Mirnategui, N., Cobb, K. M., & Thompson, D. M. (2014). A probabilistic model of chronological errors in layer-counted climate proxies: Applications to annually banded coral archives. *Clim. Past*, 10, 825–841.
- Comboul, M., Emile-Geay, J., Hakim, G. J., & Evans, M. N. (2015). Paleoclimate Sampling as a Sensor Placement Problem. *J. Clim.*, 28, 7717–7740.
- Compo, G. P., Whitaker, J. S., Sardeshmukh, P. D., Matsui, N., Allan, R. J., Yin, X., Gleason, B. E., Vose, R. S., Rutledge, G., Bessemoulin, P., Bronnimann, S., Brunet, M., Crouthamel, R. I., Grant, A. N., Groisman, P. Y., Jones, P. D., Kruk, M. C., Kruger, A. C., Marshall, G. J., Mauerer, M., Mok, H. Y., Nordli, O., Ross, T. F., Trigo, R. M., Wang, X. L., Woodruff, S. D., & Worley, S. J. (2011). The Twentieth Century Reanalysis Project. *Q. J. R. Meteorol. Soc.*, 137(January), 1–28.
- Conroy, J., Overpeck, J. T., & Cole, J. E. (2010). El Niño/Southern Oscillation and changes in the zonal gradient of tropical Pacific sea surface temperature over the last 1.2 ka. *PAGES News*, (pp. 1–5).
- Conroy, J. L., Overpeck, J. T., Cole, J. E., Shanahan, T. M., & Steinitz-Kannan, M. (2008). Holocene changes in eastern tropical Pacific climate inferred from a Galápagos lake sediment record. *Quat. Sci. Rev.*, 27, 1166–1180.

- Conroy, J. L., Restrepo, A., Overpeck, J. T., Steinitz-Kannan, M., Cole, J. E., Bush, M. B., & Colinvaux, P. A. (2009). Unprecedented recent warming of surface temperatures in the eastern tropical Pacific Ocean. *Nat. Geosci.*, *2*(1), 46–50.
- Consortium, P. (2013). Continental-scale temperature variability during the past two millennia. *Nat. Geosci.*, *6*(6), 503–503.
- Cook, E. R., Briffa, K. R., & Jones, P. D. (1994). Spatial regression methods in dendroclimatology: A review and comparison of two techniques. *Int. J. Climatol.*, *14*, 379–402.
- Cook, E. R., Briffa, K. R., Meko, D. M., Graybill, D. A., & Funkhouser, G. (1995). The 'segment length curse' in long tree-ring chronology development for palaeoclimatic studies. *The Holocene*, *5*(2), 229–237.
- Cook, E. R., Buckley, B. M., D'Arrigo, R. D., & Peterson, M. J. (2000). Warm-season temperatures since 1600 BC reconstructed from Tasmanian tree rings and their relationship to large-scale sea surface temperature anomalies. *Clim. Dyn.*, *16*, 79–91.
- Corrège, T., Delcroix, T., Récy, J., Beck, W., Cabioch, G., & Le Cornec, F. (2000). Evidence for stronger El Niño-Southern Oscillation (ENSO) events in a mid-Holocene massive coral. *Paleoceanography*, *15*(4), 465–470.
- Crausbay, S. D., Russell, J. M., & Schnurrenberger, D. W. (2006). A ca. 800-year lithologic record of drought from sub-annually laminated lake sediment, East Java. *J. Paleolimnol.*, *35*(3), 641–659.
- Cronin, T. M., Dwyer, G. S., Kamiya, T., Schwede, S., & Willard, D. A. (2003). Medieval Warm Period, Little Ice Age and 20th century temperature variability from Chesapeake Bay. *Glob. Planet. Change*, *36*, 17–29.
- Cronin, T. M., Thunell, R., Dwyer, G. S., Saenger, C., Mann, M. E., Vann, C., & Seal, I. R. (2005). Multiproxy evidence of Holocene climate variability from estuarine sediments, eastern North America. *Paleoceanography*, *20*(4).
- Cubasch, U., Wuebbles, D., Chen, D., Facchini, M. C., Frame, D., Mahowald, N., & Winther, J.-G. (2013). Introduction in Climate Change 2013. *Intergov. Panel Clim. Chang. 2013 Phys. Sci. Basis. Contrib. Work. Gr. I to Fifth Assess. Rep. Intergov. Panel Clim. Chang.*, (pp. 119–158).
- Curtis, J. H., Hodell, D. A., & Brenner, M. (1996). Climate Variability on the Yucatan Peninsula (Mexico) during the Past 3500 Years , and Implications for Maya Cultural Evolution. *Quat. Res.*, *46*, 37–47.

- Damassa, T. D., Cole, J. E., Barnett, H. R., Ault, T. R., & McClanahan, T. R. (2006). Enhanced multidecadal climate variability in the seventeenth century from coral isotope records in the western Indian Ocean. *Paleoceanography*, *21*(2), PA2016.
- Daniau, A.-L., Bartlein, P. J., Harrison, S. P., Prentice, I. C., Brewer, S., Friedlingstein, P., Harrison-Prentice, T. I., Inoue, J., Izumi, K., Marlon, J. R., Mooney, S., Power, M. J., Stevenson, J., Tinner, W., Andrič, M., Atanassova, J., Behling, H., Black, M., Blarquez, O., Brown, K. J., Carcaillet, C., Colhoun, E. A., Colombaroli, D., Davis, B. A. S., D'Costa, D., Dodson, J., Dupont, L., Eshetu, Z., Gavin, D. G., Genries, A., Haberle, S., Hallett, D. J., Hope, G., Horn, S. P., Kassa, T. G., Katamura, F., Kennedy, L. M., Kershaw, P., Krivonogov, S., Long, C., Magri, D., Marinova, E., McKenzie, G. M., Moreno, P. I., Moss, P., Neumann, F. H., Norström, E., Paitre, C., Rius, D., Roberts, N., Robinson, G. S., Sasaki, N., Scott, L., Takahara, H., Terwilliger, V., Thevenon, F., Turner, R., Valsecchi, V. G., Vannièrè, B., Walsh, M., Williams, N., & Zhang, Y. (2012). Predictability of biomass burning in response to climate changes. *Global Biogeochem. Cycles*, *26*(4).
- D'Arrigo, R., & Wilson, R. (2006). On the Asian expression of the PDO. *Int. J. Climatol.*, *26*(12), 1607–1617.
- Davidson, E. A., & Janssens, I. A. (2006). Temperature sensitivity of soil carbon decomposition and feedbacks to climate change. *Nature*, *440*(March), 165–173.
- Davison, A. C., & Hinkley, D. V. (1997). *Bootstrap Methods and their Application*. Cambridge: Cambridge University Press, 1 ed.
- Dee, S., Emile-Geay, J., Evans, M. N., Allam, A., Steig, E. J., & Thompson, D. M. (2015). PRYSM: An open-source framework for PRoxY System Modeling, with applications to oxygen-isotope systems. *J. Adv. Model. Earth Syst.*, *7*, 1220–1247.
- DeLong, K. L., Flannery, J. A., Poore, R. Z., Quinn, T. M., Maupin, C. R., Lin, K., & Shen, C. C. (2014). A reconstruction of sea surface temperature variability in the southeastern Gulf of Mexico from 1734 to 2008 C.E. using cross-dated Sr/Ca records from the coral *Siderastrea siderea*. *Paleoceanography*, *29*(5), 403–422.
- DeLong, K. L., Quinn, T. M., Taylor, F. W., Lin, K., & Shen, C.-C. (2012). Sea surface temperature variability in the southwest tropical Pacific since AD 1649. *Nat. Clim. Chang.*, *2*(11), 799–804.
- DeLong, K. L., Quinn, T. M., Taylor, F. W., Shen, C. C., & Lin, K. (2013). Improving coral-base paleoclimate reconstructions by replicating 350years of coral Sr/Ca variations. *Palaeogeogr. Palaeoclimatol. Palaeoecol.*, *373*, 6–24.

- Denniston, R. F., Villarini, G., Gonzales, A. N., Wyrwoll, K.-H., Polyak, V. J., Ummenhofer, C. C., Lachniet, M. S., Wanamaker, A. D., Humphreys, W. F., Woods, D., & Cugley, J. (2015). Extreme rainfall activity in the Australian tropics reflects changes in the El Niño/Southern Oscillation over the last two millennia. *Proc. Natl. Acad. Sci. U. S. A.*, *112*(15), 4576–4581.
- Deser, C., & Wallace, J. M. (1990). Large-Scale Atmospheric Circulation Features of Warm and Cold Episodes in the Tropical Pacific. *J. Clim.*, *3*(11), 1254–1281.
- Díaz, S. C., Therrell, M. D., Stahle, D. W., & Cleaveland, M. K. (2002). Chihuahua (Mexico) winter-spring precipitation reconstructed from tree-rings, 1647-1992. *Clim. Res.*, *22*(1995), 237–244.
- Dommain, R., Couwenberg, J., & Joosten, H. (2011). Development and carbon sequestration of tropical peat domes in south-east Asia: Links to post-glacial sea-level changes and Holocene climate variability. *Quat. Sci. Rev.*, *30*(7-8), 999–1010.
- Donders, T. H., Wagner, F., Dilcher, D. L., & Visscher, H. (2005). Mid- to late-Holocene El Niño-Southern Oscillation dynamics reflected in the subtropical terrestrial realm. *Proc. Natl. Acad. Sci. U. S. A.*, *102*(31), 10904–10908.
- Donders, T. H., Wagner-Cremer, F., & Visscher, H. (2008). Integration of proxy data and model scenarios for the mid-Holocene onset of modern ENSO variability. *Quat. Sci. Rev.*, *27*, 571–579.
- Dowdy, A. J. (2016). Seasonal forecasting of lightning and thunderstorm activity in tropical and temperate regions of the world. *Sci. Rep.*, *6*(February), 20874.
- Druffel, E. R. M., & Griffin, S. (1999). Variability of surface ocean radiocarbon and stable isotopes in the southwestern Pacific. *J. Geophys. Res. Ocean.*, *104*(C10), 23607–23613.
- Duchon, J. (1977). Splines minimizing rotation-invariant semi-norms in Sobolev spaces. *Constr. Theory Funct. Sev. Var. Oberwolfach 1976*, *571/1977*(571), 85–100.
- Dunbar, R. B., Wellington, G. M., Colgan, M. W., & Glynn, P. W. (1994). Eastern Pacific sea surface temperature since 1600 A.D.: The $\delta^{18}\text{O}$ record of climate variability in Galápagos Corals. *Paleoceanography*, *9*(2), 291–315.
- Duplessy, J. C., Cortijo, E., & Kallel, N. (2005). Marine records of Holocene climatic variations. *Comptes Rendus - Geosci.*, *337*, 87–95.

- Emile-Geay, J., Cobb, K. M., Mann, M. E., & Wittenberg, A. T. (2013a). Estimating central equatorial pacific SST variability over the past millennium. Part I: Methodology and validation. *J. Clim.*, *26*, 2302–2328.
- Emile-Geay, J., Cobb, K. M., Mann, M. E., & Wittenberg, A. T. (2013b). Estimating central equatorial pacific SST variability over the past millennium. Part II: Reconstructions and Implications. *J. Clim.*, *26*, 2302–2328.
- Emile-Geay, J., & Tingley, M. (2016). Inferring climate variability from nonlinear proxies. Application to paleo-ENSO studies. *Clim. Past*, *12*, 31–50.
- Esper, J., Cook, E. R., & Schweingruber, F. H. (2002). Low-frequency signals in long tree-ring chronologies for reconstructing past temperature variability. *Science*, *295*(5563), 2250–2253.
- Evans, M. N. (2007). Toward forward modeling for paleoclimatic proxy signal calibration: A case study with oxygen isotopic composition of tropical woods. *Geochemistry, Geophys. Geosystems*, *8*(7).
- Evans, M. N., Kaplan, A., & Cane, M. A. (1998). Optimal sites for coral-based reconstruction of global sea surface temperature. *Paleoceanography*, *13*(5), 502.
- Evans, M. N., Smerdon, J. E., Kaplan, A., Tolwinski-Ward, S. E., & González-Rouco, J. F. (2014). Climate field reconstruction uncertainty arising from multivariate and nonlinear properties of predictors. *Geophys. Res. Lett.*, *41*(24), 9127–9134.
- Evans, M. N., Tolwinski-Ward, S. E., Thompson, D. M., & Anchukaitis, K. J. (2013). Applications of proxy system modeling in high resolution paleoclimatology. *Quat. Sci. Rev.*, *76*, 16–28.
- Faulstich, H. L., Woodhouse, C. A., & Griffin, D. (2013). Reconstructed cool- and warm-season precipitation over the tribal lands of northeastern Arizona. *Clim. Change*, *118*, 457–468.
- Felis, T., Patzold, J., Loya, Y., Fine, M., Nawar, A. H., & Wefer, G. (2000). A coral oxygen isotope record from the northern Red Sea documenting NAO, ENSO, and North Pacific teleconnections on Middle East climate variability since the year 1750. *Paleoceanography*, *15*(6), 679–694.
- Felis, T., Suzuki, A., Kuhnert, H., Dima, M., Lohmann, G., & Kawahata, H. (2009). Sub-tropical coral reveals abrupt early-twentieth-century freshening in the western North Pacific Ocean. *Geology*, *37*(6), 527–530.

- Felis, T., Suzuki, A., Kuhnert, H., Rimbu, N., & Kawahata, H. (2010). Pacific decadal oscillation documented in a coral record of North Pacific winter temperature since 1873. *Geophys. Res. Lett.*, *37*, 2000–2005.
- Field, R. (2004). A drought-based predictor of recent haze events in western Indonesia. *Atmos. Environ.*, *38*(13), 1869–1878.
- Field, R. D., van der Werf, G. R., & Shen, S. S. P. (2009). Human amplification of drought-induced biomass burning in Indonesia since 1960.
- Fletcher, I. N. (2014). *Empirical models of the incidence and spread of tropical fires*. Ph.D. thesis, University of Exeter.
- Fletcher, I. N., Murray-totarolo, G., & Friedlingstein, P. (2013). Fire emissions in tropical forests: refining the SPITFIRE model using remote sensing data. *An. XVI Simpósio Bras. Sensoriamento Remoto - SBSR, 13-18 Apri*, 7337–7344.
- Forestry Canada Fire Danger Group (1992). Development of the Canadian Forest Fire Behavior Prediction System.
- Fredericksen, N. J., & Fredericksen, T. S. (2002). Terrestrial wildlife responses to logging and fire in a Bolivian tropical humid forest. *Biodivers. Conserv.*, *11*(1), 27–38.
- Freeman, E., Woodruff, S. D., Worley, S. J., Lubker, S. J., Kent, E. C., Angel, W. E., Berry, D. I., Brohan, P., Eastman, R., Gates, L., Gloeden, W., Ji, Z., Lawrimore, J., Rayner, N. A., Rosenhagen, G., & Smith, S. R. (2016). ICOADS Release 3.0: A major update to the historical marine climate record. *Int. J. Climatol.*
- Fritts, H. C. (2001). *Tree rings and climate*. Blackburn Press.
- Fuller, D. O., & Murphy, K. (2006). The ENSO-fire dynamic in insular Southeast Asia. *Clim. Change*, *74*(4), 435–455.
- FWI/GFW (2002). *The State of the Forest*. Bogor, Indonesia: Forest Watch Indonesia, and Washington DC: Global Forest Watch.
- Gallant, A. J. E., Phipps, S. J., Karoly, D. J., Mullan, A. B., & Lorrey, A. M. (2013). Nonstationary Australasian teleconnections and implications for paleoclimate reconstructions. *J. Clim.*, *26*(22), 8827–8849.
- Gaveau, D. L. a., Salim, M. a., Hergoualc'h, K., Locatelli, B., Sloan, S., Wooster, M., Marlier, M. E., Molidena, E., Yaen, H., DeFries, R., Verchot, L., Murdiyarso, D., Nasi, R., Holmgren, P., & Sheil, D. (2014). Major atmospheric emissions from peat fires in

- Southeast Asia during non-drought years: evidence from the 2013 Sumatran fires. *Sci. Rep.*, 4(6112), 1–7.
- Gedney, N., Cox, P. M., & Huntingford, C. (2004). Climate feedback from wetland methane emissions. *Geophys. Res. Lett.*, 31, 1–4.
- Giese, B. S., Seidel, H. F., Compo, G. P., & Sardeshmukh, P. D. (2016). An ensemble of ocean reanalyses for 1815–2013 with sparse observational input. *J. Geophys. Res. Ocean.*, 121(9), 6891–6910.
- Giglio, L., Randerson, J. T., & Van Der Werf, G. R. (2013). Analysis of daily, monthly, and annual burned area using the fourth-generation global fire emissions database (GFED4). *J. Geophys. Res. Biogeosciences*, 118(1), 317–328.
- Giglio, L., Randerson, J. T., van der Werf, G. R., Kasibhatla, P. S., Collatz, G. J., Morton, D. C., & DeFries, R. S. (2010). Assessing variability and long-term trends in burned area by merging multiple satellite fire products. *Biogeosciences*, 7, 1171–1186.
- Goldammer, J. G. (2007). History of equatorial vegetation fires and fire research in Southeast Asia before the 1997–98 episode: A reconstruction of creeping environmental changes. *Mitig. Adapt. Strateg. Glob. Chang.*, 12(1), 13–32.
- Gomez, B., Carter, L., Trustrum, N. A., Palmer, A. S., & Roberts, A. P. (2004). El Niño–Southern Oscillation signal associated with middle Holocene climate change in inter-correlated terrestrial and marine sediment cores, North Island, New Zealand. *Geology*, 32(8), 653–656.
- Goni, M. A., Thunell, R. C., Woodworth, M. P., & Müller-Karger, F. E. (2006). Changes in wind-driven upwelling during the last three centuries: Interocean teleconnections. *Geophys. Res. Lett.*, 33(15), 3–6.
- Goodkin, N. F., Hughen, K. A., Curry, W. B., Doney, S. C., & Ostermann, D. R. (2008). Sea surface temperature and salinity variability at Bermuda during the end of the Little Ice Age. *Paleoceanography*, 23(3), 1–13.
- Gorman, M. K., Quinn, T. M., Taylor, F. W., Partin, J. W., Cabioch, G., Austin, J. A., Pelletier, B., Ballu, V., Maes, C., & Sastrup, S. (2012). A coral-based reconstruction of sea surface salinity at Sabine Bank, Vanuatu from 1842 to 2007 CE. *Paleoceanography*, 27(3), 1–13.
- Goto, S., & Yamano, M. (2010). Reconstruction of the 500-year ground surface temperature history of northern Awaji Island, southwest Japan, using a layered thermal property model. *Phys. Earth Planet. Inter.*, 183(3–4), 435–446.

- Graham, N. E., Hughes, M. K., Ammann, C. M., Cobb, K. M., Hoerling, M. P., Kennett, D. J., Kennett, J. P., Rein, B., Stott, L., Wigand, P. E., & Xu, T. (2007). Tropical Pacific - Mid-latitude teleconnections in medieval times. *Clim. Change*, *83*, 241–285.
- Grau, H. R., & Veblen, T. T. (2000). Rainfall variability, fire and vegetation dynamics in neotropical montane ecosystems in north-western Argentina. *J. Biogeogr.*, *27*(5), 1107–1121.
- Greenpeace (2017). Protecting forests & peatlands in Indonesia.
URL <http://www.greenpeace.org/seasia/id/Global/seasia/Indonesia/Code/Forest-Map/en/index.html{#}>
- Griffin, D., Woodhouse, C. A., Meko, D. M., Stahle, D. W., Faulstich, H. L., Carrillo, C., Touchan, R., Castro, C. L., & Leavitt, S. W. (2013). North American monsoon precipitation reconstructed from tree-ring latewood. *Geophys. Res. Lett.*, *40*(5), 954–958.
- Griffiths, M. L., Kimbrough, A. K., Gagan, M. K., Drysdale, R. N., Cole, J. E., Johnson, K. R., Zhao, J.-X., Cook, B. I., Hellstrom, J. C., & Hantoro, W. S. (2016). Western Pacific hydroclimate linked to global climate variability over the past two millennia. *Nat. Commun.*, *7*, 11719.
- Grissino-Mayer, H., & Swetnam, T. (2000). Century-scale climate forcing of fire regimes in the American Southwest. *The Holocene*, *10*(2), 213–220.
- Guilderson, T. P., & Schrag, D. P. (1999). Reliability of coral isotope records from the Western Pacific Warm Pool: A comparison using age-optimized records. *Paleoceanography*, *14*(4), 457.
- Guilyardi, E., Wittenberg, A., Fedorov, A., Collins, M., Wang, C., Capotondi, A., van Oldenborgh, G. J., & Stockdale, T. (2009). Understanding El Niño in ocean-atmosphere general circulation models: Progress and challenges. *Bull. Am. Meteorol. Soc.*, *90*(march), 325–340.
- Gumbrecht, T., Roman-Cuesta, R. M., Verchat, L., Herold, M., Wittmann, F., Householder, E., Herold, N., & Murdiyarso, D. (2017). An expert system model for mapping tropical wetlands and peatlands reveals South America as the largest contributor. *Glob. Chang. Biol.*, (pp. 1–19).
- Haberle, S. G. (2005). A 23,000-yr pollen record from Lake Euramoo, Wet Tropics of NE Queensland, Australia. *Quat. Res.*, *64*(3), 343–356.

- Haberle, S. G., & Ledru, M.-P. (2001). Correlations among Charcoal Records of Fires from the Past 16,000 Years in Indonesia, Papua New Guinea, and Central and South America. *Quat. Res.*, *55*(1), 97–104.
- Hamid, Y. (2001). El Niño Event on Lightning. *Event (London)*, *28*(1), 147–150.
- Hansen, M. C., Potapov, P. V., Moore, R., Hancher, M., Turubanova, S. a., Tyukavina, A., Thau, D., Stehman, S. V., Goetz, S. J., Loveland, T. R., Kommareddy, A., Egorov, A., Chini, L., Justice, C. O., & Townshend, J. R. G. (2013). High-Resolution Global Maps of 21st-Century Forest Cover Change. *Science (80-.)*, *342*(6160), 850–853.
- Hantson, S., Arneth, A., Harrison, S. P., Kelley, D. I., Prentice, I. C., Rabin, S. S., Archibald, S., Mouillot, F., Arnold, S. R., Artaxo, P., Bachelet, D., Ciais, P., Forrest, M., Friedlingstein, P., Hickler, T., Kaplan, J. O., Kloster, S., Knorr, W., Lasslop, G., Li, F., Mangeon, S., Melton, J. R., Meyn, A., Sitch, S., Spessa, A., van der Werf, G. R., Voulgarakis, A., & Yue, C. (2016a). The status and challenge of global fire modelling. *Biogeosciences*, *13*, 3359–3375.
- Hantson, S., Kloster, S., Coughlan, M., Daniau, A. L., Vannièrè, B., Brücher, T., Kehrwald, N., & Magi, B. I. (2016b). Fire in the earth system: Bridging data and modeling research. *Bull. Am. Meteorol. Soc.*, *97*(6), 1069–1072.
- Harrison, S. P., & Dodson, J. R. (1993). Climates of Australia and New Guinea since 18 000 yr BP. In *Glob. Clim. since Last Glacial Maximum*, chap. 11, (pp. 265–293). University of Minnesota Press.
- Hastie, T., & Loader, C. (1993). [Local Regression: Automatic Kernel Carpentry]: Rejoinder. *Stat. Sci.*, *8*(2), 139–143.
- Hastie, T. J., & Tibshirani, R. J. (1990). *Generalized Additive Models*. Chapman & Hall/CRC Monographs on Statistics & Applied Probability. London: Chapman and Hall.
- Haug, G. H., Hughen, K. a., Sigman, D. M., Peterson, L. C., & Röhl, U. (2001). Southward migration of the intertropical convergence zone through the Holocene. *Science*, *293*(2001), 1304–1308.
- Hegerl, G. C., Zwiers, F. W., Braconnot, P., Gillett, N. P., Luo, Y., Marengo Orsini, J. A., Nicolls, N., Penner, J. E., & Stott, P. A. (2007). Understanding and Attributing Climate Change. In *Clim. Chang. 2007 Phys. Sci. Basis. Contrib. Work. Gr. I to Fourth Assess. Rep. Intergov. Panel Clim. Chang. [Solomon, S., D. Qin, M. Manning, Z. Chen, M. Marquis, K.B. Averyt, M. Tignor H.L. Mill.*, (p. 84). Cambridge: Cambridge University Press.

- Heil, A., & Goldammer, J. G. (2001). Smoke-haze pollution: a review of the 1997 episode in Southeast Asia. *Reg. Environ. Chang.*, 2, 24–37.
- Heiss, G. A. (1994). Coral reefs in the Red Sea: Growth, production and stable isotopes. *GEOMAR Rep.*, 32(January 1994), 1–141.
- Held, I. M., & Soden, B. J. (2006). Robust responses of the hydrological cycle to global warming (vol 19, pg 5686, 2006). *J. Clim.*, 19, 5686–5699.
- Hendon, H. H. (2003). Indonesian rainfall variability: Impacts of ENSO and local air-sea interaction. *J. Clim.*, 16, 1775–1790.
- Hendy, E. J., Gagan, M. K., & Lough, J. M. (2003). Chronological control of coral records using luminescent lines and evidence for non-stationary ENSO teleconnections in northeast Australia. *The Holocene*, 13, 187–199.
- Hengstum, P. J. V., Donnelly, J. P., Kingston, A. W., Williams, B. E., Scott, D. B., Reinhardt, E. G., Little, S. N., & Patterson, W. P. (2015). Low-frequency storminess signal at Bermuda linked to cooling events in the North Atlantic region. *Paleoceanography*, (pp. 52–76).
- Henke, L. M. K., Lambert, F. H., & Charman, D. J. (2017). Was the Little Ice Age more or less El Niño-like than the Medieval Climate Anomaly? Evidence from hydrological and temperature proxy data. *Clim. Past*, 13(3), 267–301.
- Henley, B. J., Gergis, J., Karoly, D. J., Power, S., Kennedy, J., & Folland, C. K. (2015). A Tripole Index for the Interdecadal Pacific Oscillation. *Clim. Dyn.*, 45(11-12), 3077–3090.
- Henley, B. J., Thyer, M. A., Kuczera, G., & Franks, S. W. (2011). Climate-informed stochastic hydrological modeling: Incorporating decadal-scale variability using paleo data. *Water Resour. Res.*, 47(11), 1–14.
- Hergoualc'h, K., & Verchot, L. V. (2011). Stocks and fluxes of carbon associated with land use change in Southeast Asian tropical peatlands: A review. *Global Biogeochem. Cycles*, 25(January).
- Hetzinger, S., Pfeiffer, M., Dullo, W. C., Garbe-Schonberg, D., & Halfar, J. (2010). Rapid 20th century warming in the Caribbean and impact of remote forcing on climate in the northern tropical Atlantic as recorded in a Guadeloupe coral. *Palaeogeogr. Palaeoclimatol. Palaeoecol.*, 296(1-2), 111–124.

- Higuera, P. E., Gavin, D. G., Bartlein, P. J., & Hallett, D. J. (2010). Peak detection in sediment-charcoal records: Impacts of alternative data analysis methods on fire-history interpretations. *Int. J. Wildl. Fire*, 19(8), 996–1014.
- Hirahara, S., Ishii, M., & Fukuda, Y. (2014). Centennial-Scale Sea Surface Temperature Analysis and Its Uncertainty. *J. Clim.*, 27(1), 57–75.
- Hirano, T., Segah, H., Harada, T., Limin, S., June, T., Hirata, R., & Osaki, M. (2007). Carbon dioxide balance of a tropical peat swamp forest in Kalimantan, Indonesia. *Glob. Chang. Biol.*, 13, 412–425.
- Hjelle, B., & Glass, G. E. (2000). Outbreak of hantavirus infection in the Four Corners region of the United States in the wake of the 1997-1998 El Niño-Southern Oscillation. *J. Infect. Dis.*, 181(5), 1569–1573.
- Hodell, D. A., Brenner, M., Curtis, J. H., Medina-González, R., Ildefonso-Chan Can, E., Albornaz-Pat, A., & Guilderson, T. P. (2005). Climate change on the Yucatan Peninsula during the Little Ice Age. *Quat. Res.*, 63(2), 109–121.
- Hodell, D. A., Curtis, J. H., & Brenner, M. (1995). Possible role of climate in the collapse of Classic Maya civilization. *Nature*, 375(6530), 391–394.
- Hodson, E. L., Poulter, B., Zimmermann, N. E., Prigent, C., & Kaplan, J. O. (2011). The El Niño-Southern Oscillation and wetland methane interannual variability. *Geophys. Res. Lett.*, 38(March), 3–6.
- Hooijer, A., Page, S. E., Canadell, J. G., Silvius, M., Kwadijk, J., Wösten, H., & Jauhiainen, J. (2010). Current and future CO₂ emissions from drained peatlands in Southeast Asia. *Biogeosciences*, 7, 1505–1514.
- Hope, G., Chokkalingam, U., & Anwar, S. (2005). The stratigraphy and fire history of the Kutai Peatlands, Kalimantan, Indonesia. *Quat. Res.*, 64(3), 407–417.
- Hoscilo, A., Page, S. E., Tansey, K. J., & Rieley, J. O. (2011). Effect of repeated fires on land-cover change on peatland in southern Central Kalimantan, Indonesia, from 1973 to 2005. *Int. J. Wildl. Fire*, 20(4), 578–588.
- Huang, J., Van Den Dool, H. M., & Georgakakos, K. P. (1996). Analysis of model-calculated soil moisture over the United States (1931-1993) and applications to long-range temperature forecasts. *J. Clim.*, 9(6), 1350–1362.
- Huffman, G. J., Adler, R. F., Bolvin, D. T., & Gu, G. (2009). Improving the global precipitation record: GPCP Version 2.1. *Geophys. Res. Lett.*, 36(17), 1–5.

- Huijnen, V., Wooster, M. J., Kaiser, J. W., Gaveau, D. L. A., Flemming, J., Parrington, M., Inness, A., Murdiyarso, D., Main, B., & van Weele, M. (2016). Fire carbon emissions over maritime southeast Asia in 2015 largest since 1997. *Sci. Rep.*, 6(1), 26886.
- Hurley, J. V., Vuille, M., & Hardy, D. R. (2016). Forward modeling of $\delta^{18}O$ in Andean ice cores. *Geophys. Res. Lett.*, 43(15), 8178–8188.
- Ivanochko, T. S., Ganeshram, R. S., Brummer, G. J. a., Ganssen, G., Jung, S. J. A., Moreton, S. G., & Kroon, D. (2005). Variations in tropical convection as an amplifier of global climate change at the millennial scale. *Earth Planet. Sci. Lett.*, 235, 302–314.
- Jaenicke, J., Rieley, J., Mott, C., Kimman, P., & Siegert, F. (2008). Determination of the amount of carbon stored in Indonesian peatlands. *Geoderma*, 147(3-4), 151–158.
- John, J. A., & Draper, N. R. (1980). An Alternative Family of Transformations. *J. R. Stat. Soc. Ser. C (Applied Stat.)*, 29(2), 190–197.
- Johnston, L., Samadhi, T. N., Minnemeyer, S., & Sizer, N. (2015). Indonesia's Forest Fires Reignite, Threatening Protected Areas and Peatlands.
URL <http://www.wri.org/blog/2015/07/indonesia%E2%80%99s-forest-fires-reignite-threatening-protected-areas-and-peatlands>
- Jones, P., Briffa, K., Osborn, T., Lough, J., van Ommen, T., Vinther, B., Luterbacher, J., Wahl, E., Zwiars, F., Mann, M. E., Schmidt, G., Ammann, C., Buckley, B., Cobb, K., Esper, J., Goosse, H., Graham, N., Jansen, E., Kiefer, T., Kull, C., Kuttel, M., Mosley-Thompson, E., Overpeck, J., Riedwyl, N., Schulz, M., Tudhope, A., Villalba, R., Wanner, H., Wolff, E., & Xoplaki, E. (2009). High-resolution palaeoclimatology of the last millennium: a review of current status and future prospects. *The Holocene*, 19(1), 3–49.
- Jones, P. D., & Mann, M. E. (2004). Climate over past millennia. *Rev. Geophys.*, 42(2003), 1–42.
- Kantzas, E., Lomas, M., & Quegan, S. (2013). Fire at high latitudes: Data-model comparisons and their consequences. *Global Biogeochem. Cycles*, 27(3), 677–691.
- Karamperidou, C., Di Nezio, P. N., Timmermann, A., Jin, F. F., & Cobb, K. M. (2015). The response of ENSO flavors to mid-Holocene climate: Implications for proxy interpretation. *Paleoceanography*, (pp. 527–547).
- Kehrwald, N., Aleman, J., Coughlan, M., Courtney-Mustalphi, C., Githumbi, E., Magi, B. I., Marlon, J. R., & Power, M. J. (2016). One thousand years of fires: Integrating proxy and model data. *Front. Biogeogr.*, 8(1), e29606.

- Keigwin, L. D. (1996). The Little Ice Age and Medieval Warm Period in the Sargasso Sea. *Science (80-.)*, 274(5292), 1504–1508.
- Keller, J. K. (2011). Wetlands and the global carbon cycle: What might the simulated past tell us about the future? *New Phytol.*, 192, 789–792.
- Kellerhals, T., Brüttsch, S., Sigl, M., Knüsel, S., Gäggeler, H. W., & Schwikowski, M. (2010). Ammonium concentration in ice cores: A new proxy for regional temperature reconstruction? *J. Geophys. Res. Atmos.*, 115(16), 1–8.
- Kennett, D., Breitenbach, S., Aquino, V., Asmerom, Y., Awe, J., Baldini, J., Bartlein, P., Culleton, B., Ebert, C., Jazwa, C., Macri, M., Marwan, N., Polyak, V., Prufer, K., Ridley, H., Sodemann, H., Winterhalder, B., & Haug, G. (2012). Development and disintegration of Maya political systems in response to climate change. *Science (80-.)*, 788(2012), 788–791.
- Khider, D., Jackson, C. S., & Stott, L. D. (2014). Assessing millennial-scale variability during the Holocene: A perspective from the western tropical Pacific. *Paleoceanography*, 29, 143–159.
- Kilbourne, K. H., Quinn, T. M., Webb, R., Guilderson, T., Nyberg, J., & Winter, A. (2008). Paleoclimate proxy perspective on Caribbean climate since the year 1751: Evidence of cooler temperatures and multidecadal variability. *Paleoceanography*, 23(3), 1–14.
- Kim, S. T., & Yu, J. Y. (2012). The two types of ENSO in CMIP5 models. *Geophys. Res. Lett.*, 39(11), 1–6.
- Kimeldorf, G. S., & Wahba, G. (1970). A Correspondence Between Bayesian Estimation on Stochastic Processes and Smoothing by Splines. *Ann. Math. Stat.*, 41(2), 495–502.
- Kintisch, E. (2016). How a *Godzilla* El Niño shook up weather forecasts. *Science (80-.)*, 352(6293), 1501–1502.
- Kitzberger, T., Swetnam, T. W., & Veblen, T. T. (2001). Inter-hemispheric synchrony of forest fires and the El Niño-Southern Oscillation. *Glob. Ecol. Biogeogr.*, 10, 315–326.
- Klein, S. a., Soden, B. J., & Lau, N. C. (1999). Remote Sea Surface Temperature Variations during ENSO: Evidence for a Tropical Atmospheric Bridge. *J. Clim.*, 12, 917–932.
- Klein Goldewijk, K., Beusen, A., & Janssen, P. (2010). Long-term dynamic modeling of global population and built-up area in a spatially explicit way: HYDE 3.1. *The Holocene*, 20(4), 565–573.

- Klein Goldewijk, K., Beusen, A., Van Drecht, G., & De Vos, M. (2011). The HYDE 3.1 spatially explicit database of human-induced global land-use change over the past 12,000 years. *Glob. Ecol. Biogeogr.*, *20*(1), 73–86.
- Kloster, S., Brücher, T., Brovkin, V., & Wilkenskjeld, S. (2015). Controls on fire activity over the Holocene. *Clim. Past*, *11*(5), 781–788.
- Kloster, S., Mahowald, N. M., Randerson, J. T., & Lawrence, P. J. (2012). The impacts of climate, land use, and demography on fires during the 21st century simulated by CLM-CN. *Biogeosciences*, *9*(1), 509–525.
- Knorr, W., Jiang, L., & Arneeth, A. (2016). Climate, CO₂ and human population impacts on global wildfire emissions. *Biogeosciences*, *13*(1), 267–282.
- Konecny, K., Ballhorn, U., Navratil, P., Jubanski, J., Page, S. E., Tansey, K., Hooijer, A., Vernimmen, R., & Siegert, F. (2016). Variable carbon losses from recurrent fires in drained tropical peatlands. *Glob. Chang. Biol.*, *22*(4), 1469–1480.
- Koutavas, A., DeMenocal, P. B., Olive, G. C., & Lynch-Stieglitz, J. (2006). Mid-Holocene El Niño-Southern Oscillation (ENSO) attenuation revealed by individual foraminifera in eastern tropical Pacific sediments. *Geology*, *34*(12), 993–996.
- Kovats, R. S., Bouma, M. J., Hajat, S., Worrall, E., & Haines, A. (2003). El Niño and health. *Lancet*, *362*, 1481–1489.
- Krawchuk, M. A., & Moritz, M. A. (2011). Constraints on global fire activity vary across a resource gradient. *Ecology*, *92*(1), 121–132.
- Krusic, P. J., Cook, E. R., Dukpa, D., Putnam, A. E., Rupper, S., & Schaefer, J. (2015). Six hundred thirty-eight years of summer temperature variability over the Bhutanese Himalaya. *Geophys. Res. Lett.*, *42*, 2988–2994.
- Kuhnert, H., Crüger, T., & Pätzold, J. (2005). NAO signature in a Bermuda coral Sr/Ca record. *Geochemistry, Geophys. Geosystems*, *6*(4).
- Kuhnert, H., Patzold, J., Hatcher, B., Wyrwoll, K. H., Eisenhauer, A., Collins, L. B., Zhu, Z. R., & Wefer, G. (1999). A 200-year coral stable oxygen isotope record from a high-latitude reef off Western Australia. *Coral Reefs*, *18*(1), 1–12.
- Kuhnert, H., Petzold, J., Wyrwoll, K. H., & Wefer, G. (2000). Monitoring climate variability over the past 116 years in coral oxygen isotopes from Ningaloo Reef, Western Australia. *Int. J. Earth Sci.*, *88*(4), 725–732.

- Kumar, P. R., & Kamra, A. K. (2012). Variability of lightning activity in South/Southeast Asia during 1997-98 and 2002-03 El Niño/La Niña events. *Atmos. Res.*, *118*, 84–102.
- Kurnianto, S., Warren, M., Talbot, J., Kauffman, B., Murdiyarso, D., & Frohking, S. (2015). Carbon accumulation of tropical peatlands over millennia: a modeling approach. *Glob. Chang. Biol.*, *21*(1), 431–444.
- Langner, A., & Siegert, F. (2009). Spatiotemporal fire occurrence in Borneo over a period of 10 years. *Glob. Chang. Biol.*, *15*(1), 48–62.
- Langton, S. J., Linsley, B. K., Robinson, R. S., Rosenthal, Y., Oppo, D. W., Eglinton, T. I., Howe, S. S., Djajadihardja, Y. S., & Syamsudin, F. (2008). 3500 yr record of centennial-scale climate variability from the Western Pacific Warm Pool. *Geology*, *36*(10), 795–798.
- Le Quéré, C., Raupach, M. R., Canadell, J. G., Marland et al., G., Le Quéré et al., C., Le Quéré et al., C., Raupach, M. R., Canadell, J. G., Marland, G., Bopp, L., Ciais, P., Conway, T. J., Doney, S. C., Feely, R. A., Foster, P., Friedlingstein, P., Gurney, K., Houghton, R. A., House, J. I., Huntingford, C., Levy, P. E., Lomas, M. R., Majkut, J., Metzl, N., Ometto, J. P., Peters, G. P., Prentice, I. C., Randerson, J. T., Running, S. W., Sarmiento, J. L., Schuster, U., Sitch, S., Takahashi, T., Viovy, N., van der Werf, G. R., & Woodward, F. I. (2009). Trends in the sources and sinks of carbon dioxide. *Nat. Geosci.*, *2*(12), 831–836.
- Lea, D. W., Pak, D. K., & Spero, H. J. (2000). Climate Impact of Late Quaternary Equatorial Pacific Sea Surface Temperature Variations. *Holocene*, *289*(September), 1719–1724.
- Lehmann, C. E. R., Anderson, T. M., Sankaran, M., Higgins, S. I., Archibald, S., Hoffmann, W. A., Hanan, N. P., Williams, R. J., Fensham, R. J., Felfili, J., Hutley, L. B., Ratnam, J., San Jose, J., Montes, R., Franklin, D., Russell-Smith, J., Ryan, C. M., Durigan, G., Hiernaux, P., Haidar, R., Bowman, D. M. J. S., & Bond, W. J. (2014). Savanna Vegetation-Fire-Climate Relationships Differ Among Continents. *Science* (80-), *343*(6170), 548–552.
- Lenton, T. M., Held, H., Kriegler, E., Hall, J. W., Lucht, W., Rahmstorf, S., & Schellnhuber, H. J. (2008). Tipping elements in the Earth's climate system. *Proc. Natl. Acad. Sci.*, *105*(6), 1786–1793.
- Levavasseur, G., Vrac, M., Roche, D. M., & Paillard, D. (2012). Statistical modelling of a new global potential vegetation distribution. *Environ. Res. Lett.*, *7*(4), 044019.

- Lewis, S. C., & Legrande, A. N. (2015). Stability of ENSO and its tropical Pacific teleconnections over the Last Millennium. *Clim. Past*, *11*(10), 1347–1360.
- Li, F., Levis, S., & Ward, D. S. (2013a). Quantifying the role of fire in the Earth system - Part 1: Improved global fire modeling in the Community Earth System Model (CESM1). *Biogeosciences*, *10*(4), 2293–2314.
- Li, J., Xie, S.-P., Cook, E. R., Morales, M. S., Christie, D. A., Johnson, N. C., Chen, F., D'Arrigo, R., Fowler, A. M., Gou, X., & Fang, K. (2013b). El Niño modulations over the past seven centuries. *Nat. Clim. Chang.*, *3*(9), 822–826.
- Li, W., Dickinson, R. E., Fu, R., Niu, G. Y., Yang, Z. L., & Canadell, J. G. (2007). Future precipitation changes and their implications for tropical peatlands. *Geophys. Res. Lett.*, *34*, 1–6.
- Limpens, J., Berendse, F., Blodau, C., Canadell, J., Freeman, C., Holden, J., Roulet, N. T., Rydin, H., & Schaepman-Strub, G. (2008). Peatlands and the carbon cycle: from local processes to global implications - a synthesis. *Biogeosciences*, *5*, 1475–1491.
- Linsley, B. K., Dunbar, R. B., Wellington, G. M., & Mucciarone, A. (1994). A coral-based reconstruction of Intertropical Convergence Zone variability over Central America since 1707 on a massive season in Panamfi , the is reduced on average from Secas Island against t data indicate that seasonal rainfall induced variations in se. *Geology*, *99*, 9977–9994.
- Linsley, B. K., Kaplan, A., Gouriou, Y., Salinger, J., DeMenocal, P. B., Wellington, G. M., & Howe, S. S. (2006). Tracking the extent of the South Pacific Convergence Zone since the early 1600s. *Geochemistry, Geophys. Geosystems*, *7*(5), 1–15.
- Linsley, B. K., Ren, L., Dunbar, R. B., & Howe, S. S. (2000). El Niño Southern Oscillation (ENSO) and decadal-scale climate variability at 10°N in the eastern Pacific from 1893 to 1994: A coral-based reconstruction from Clipperton Atoll. *Paleoceanography*, *15*(3), 322–335.
- Ljung, G. M., & Box, G. E. (1978). On a measure of lack of fit in time series models. *Biometrika*, *65*(2), 297–303.
- Loader, C. (1999). *Local Regression and Likelihood*. Statistics and Computing. Springer New York.
- MacDonald, G. M., & Case, R. A. (2005). Variations in the Pacific Decadal Oscillation over the past millennium. *Geophys. Res. Lett.*, *32*(8), 1–4.

- Makou, M. C., Eglinton, T. I., Oppo, D. W., & Hughen, K. A. (2010). Postglacial changes in El Niño and La Niña behavior. *Geology*, *38*, 43–46.
- Manley, G. (1974). Central England temperatures: Monthly means 1659 to 1973. *Q. J. R. Meteorol. Soc.*, *100*(425), 389–405.
- Manly, B. F. J. (1976). Exponential data transformations. *J. R. Stat. Soc. Ser. D (The Stat.)*, *25*(1), 37–42.
- Mann, M. E. (2002). Climate reconstruction using ‘Pseudoproxies’. *Geophys. Res. Lett.*, *29*(10), 10–13.
- Mann, M. E. (2004). On smoothing potentially non-stationary climate time series. *Geophys. Res. Lett.*, *31*(7), 18–21.
- Mann, M. E., Rutherford, S., Wahl, E., & Ammann, C. (2007). Robustness of proxy-based climate field reconstruction methods. *J. Geophys. Res. Atmos.*, *112*(January), 1–18.
- Mann, M. E., Rutherford, S., Wahl, E. R., & Ammann, C. M. (2005). Testing the fidelity of methods used in proxy-based reconstructions of past climate. *J. Clim. Lett.*, *18*, 4097–4107.
- Mann, M. E., Zhang, Z., Hughes, M. K., Bradley, R. S., Miller, S. K., Rutherford, S., & Ni, F. (2008). Proxy-based reconstructions of hemispheric and global surface temperature variations over the past two millennia. *Proc. Natl. Acad. Sci. U. S. A.*, *105*(36), 13252–13257.
- Mann, M. E., Zhang, Z., Rutherford, S., Bradley, R. S., Hughes, M. K., Shindell, D., Ammann, C., Faluvegi, G., & Ni, F. (2009). Global Signatures and Dynamical Origins of the Little Ice Age and Medieval Climate Anomaly. *Science* (80-.), *326*(5957), 1256–1260.
- Marchitto, T. M., Muscheler, R., Ortiz, J. D., Carriquiry, J. D., & van Geen, A. (2010). Dynamical response of the tropical Pacific Ocean to solar forcing during the early Holocene. *Science*, *330*, 1378–1381.
- Marlon, J. R. (2016). Reconstructions of biomass burning from sediment-charcoal records to improve data – model comparisons. *Biogeosciences*, *13*, 3225–3244.
- Marlon, J. R., Bartlein, P. J., Carcaillet, C., Gavin, D. G., Harrison, S. P., Higuera, P. E., Joos, F., Power, M. J., & Prentice, I. C. (2008). Climate and human influences on global biomass burning over the past two millennia. *Nat. Geosci.*, *1*, 697–702.

- Marlon, J. R., Bartlein, P. J., Daniau, A.-L., Harrison, S. P., Maezumi, S. Y., Power, M. J., Tinner, W., & Vanni re, B. (2013). Global biomass burning: a synthesis and review of Holocene paleofire records and their controls. *Quat. Sci. Rev.*, *65*, 5–25.
- Masson-Delmotte, V., Schulz, M., Abe-Ouchi, A., Beer, J., Ganopolski, A., Gonz lez Rouco, J. F., Jansen, E., Lambeck, K., Luterbacher, J., Naish, T., Osborn, T., Otto-Bliesner, B., Quinn, T., Ramesh, R., Rojas, M., Shao, X., Timmermann, A., & Rouco, J. F. G. (2013). Information from Paleoclimate Archives. In T. Stocker, D. Qin, G.-K. Plattner, M. Tignor, S. K. Allen, J. Boschung, A. Nauels, Y. Xia, V. Bex, & P. Midgley (Eds.) *Clim. Chang. 2013 Phys. Sci. Basis. Contrib. Work. Gr. I to Fifth Assess. Rep. Intergov. Panel Clim. Chang.*, (pp. 383–464). Cambridge, United Kingdom and New York, NY, USA: Cambridge University Press.
- Maupin, C. R., Partin, J. W., Shen, C.-C., Quinn, T. M., Lin, K., Taylor, F. W., Banner, J. L., Thirumalai, K., & Sinclair, D. J. (2014). Persistent decadal-scale rainfall variability in the tropical South Pacific Convergence Zone through the past six centuries. *Clim. Past*, *10*, 1319–1332.
- McArthur, A. G., Australia, F., Bureau, T., & McArthur, A. G. (1967). *Fire behaviour in eucalypt forests*. Canberra: Forestry and Timber Bureau.
- McCulloch, M., Mortimer, G., Esat, T., Xianhua, L., Pillans, B., & Chappell, J. (1996). High resolution windows into early Holocene climate: SrCa coral records from the Huon Peninsula. *Earth Planet. Sci. Lett.*, *138*(95), 169–178.
- McGregor, H. V., Gagan, M. K., McCulloch, M. T., Hodge, E., & Mortimer, G. (2008). Mid-Holocene variability in the marine 14C reservoir age for northern coastal Papua New Guinea. *Quat. Geochronol.*, *3*, 213–225.
- McGregor, S., Timmermann, A., & Timm, O. (2010). A unified proxy for ENSO and PDO variability since 1650. *Clim. Past*, *6*, 1–17.
- Medina-Elizalde, M., Burns, S. J., Lea, D. W., Asmerom, Y., von Gunten, L., Polyak, V., Vuille, M., & Karmalkar, A. (2010). High resolution stalagmite climate record from the Yucat n Peninsula spanning the Maya terminal classic period. *Earth Planet. Sci. Lett.*, *298*(1-2), 255–262.
- Melling, L., Hatano, R., & Goh, K. J. (2005). Soil CO₂ flux from three ecosystems in tropical peatland of Sarawak, Malaysia. *Tellus, Ser. B Chem. Phys. Meteorol.*, *57*, 1–11.

- Metcalfe, S., Jones, M., Davies, S., Noren, A., & MacKenzie, A. (2010). Climate variability over the last two millenia in the North American Monsoon region, recorded in laminated lake sediments from Labuna de Juanacatlan, Mexico. *The Holocene*, *20*(8), 1195–1206.
- Miettinen, J., Hooijer, A., Shi, C., Tollenaar, D., Vernimmen, R., Liew, S. C., Malins, C., & Page, S. E. (2012). Extent of industrial plantations on Southeast Asian peatlands in 2010 with analysis of historical expansion and future projections. *GCB Bioenergy*, *4*(6), 908–918.
- Mitra, S., Wassmann, R., & Vlek, P. L. G. (2005). An appraisal of global wetland area and its organic carbon stock. *Curr. Sci.*, *88*, 25–35.
- Mooney, S. D., Harrison, S. P., Bartlein, P. J., Daniiau, A. L., Stevenson, J., Brownlie, K. C., Buckman, S., Cupper, M., Luly, J., Black, M., Colhoun, E., D'Costa, D., Dodson, J., Haberle, S., Hope, G. S., Kershaw, P., Kenyon, C., McKenzie, M., & Williams, N. (2011). Late Quaternary fire regimes of Australasia. *Quat. Sci. Rev.*, *30*(1-2), 28–46.
- Moore, S., Evans, C. D., Page, S. E., Garnett, M. H., Jones, T. G., Freeman, C., Hooijer, A., Wiltshire, A. J., Limin, S. H., & Gauci, V. (2013). Deep instability of deforested tropical peatlands revealed by fluvial organic carbon fluxes. *Nature*, *493*(7434), 660–3.
- Morris, P. J., Baird, A. J., & Belyea, L. R. (2012). The DigiBog peatland development model 2: Ecohydrological simulations in 2D. *Ecohydrology*, *5*, 256–268.
- Moustafa, Y. A. (2000). Paleoclimatic reconstructions of the northern Red Sea during the Holocene inferred from stable isotope records of modern and fossil corals and molluscs. *Berichte aus dem Fachbereich Geowissenschaften, Univ. Bremen*, *153*, 1–102.
- Moy, A. D., Seltzer, G. O., Rodbell, D. T., & Andersons, D. M. (2002). Variability of El Niño/Southern Oscillation activity at millennial timescales during the Holocene epoch. *Nature*, *420*, 162–165.
- Nakamura, N., Kayanne, H., Iijima, H., McClanahan, T. R., Behera, S. K., & Yamagata, T. (2009). Mode shift in the Indian Ocean climate under global warming stress. *Geophys. Res. Lett.*, *36*(23), 3–7.
- Nelson, D. B., Abbott, M. B., Steinman, B. A., Polissar, P. J., Stansell, N. D., Ortiz, J. D., Rosenmeier, M. F., Finney, B. P., & Riedel, J. (2011). Drought variability in the Pacific Northwest from a 6,000-yr lake sediment record. *Proc. Natl. Acad. Sci. U. S. A.*, *108*, 3870–3875.

- Neukom, R., Gergis, J. L., & Karoly, D. J. (2014). Inter-hemispheric temperature variability over the past millennium. *Nat. Clim. Chang.*, 4(May), 1–6.
- New, S., Belcher, C., Hudspith, V., & Gallego-Sala, A. (2016). Holocene fire history: can evidence of peat burning be found in the palaeo-archive? *Mires Peat*, 18(26), 1–11.
- Newman, M., Compo, G. P., & Alexander, M. A. (2003). ENSO-forced variability of the Pacific decadal oscillation. *J. Clim.*, 16(23), 3853–3857.
- NOAA Earth System Research Laboratory, P. S. D. (2016). El Niño Southern Oscillation (ENSO).
URL http://www.esrl.noaa.gov/psd/enso/enso_101.html
- NOAA/OAR/ESRL PSD (2011). ENSO Response Comparison Plots.
URL <http://www.esrl.noaa.gov/psd/enso/compare/>
- Nurhati, I. S., Cobb, K. M., Charles, C. D., & Dunbar, R. B. (2009). Late 20th century warming and freshening in the central tropical Pacific. *Geophys. Res. Lett.*, 36(21), 1–4.
- Oppo, D. W., Rosenthal, Y., & Linsley, B. K. (2009). 2,000-year-long temperature and hydrology reconstructions from the Indo-Pacific warm pool. *Nature*, 460(7259), 1113–1116.
- Page, S., Hoscilo, A., Wösten, H., Jauhiainen, J., Silvius, M., Rieley, J., Ritzema, H., Tansey, K., Graham, L., Vasander, H., & Limin, S. (2009a). Restoration ecology of lowland tropical peatlands in Southeast Asia: Current knowledge and future research directions. *Ecosystems*, 12(6), 888–905.
- Page, S. E., & Hooijer, A. (2016). In the line of fire: the peatlands of Southeast Asia. *Philos. Trans. R. Soc. B Biol. Sci.*, 371(1696), 20150176.
- Page, S. E., Rieley, J., Hoscilo, A., Spessa, A., & Weber, U. (2013). Current Fire Regimes , Impacts and the Likely Changes – IV : Tropical Southeast Asia. In *Veg. Fires Glob. Chang. – Challenges Concert. Int. Action A White Pap. Dir. to United Nations Int. Organ.*, chap. 7, (pp. 89–99). Kessel.
- Page, S. E., Rieley, J. O., & Banks, C. J. (2011). Global and regional importance of the tropical peatland carbon pool. *Glob. Chang. Biol.*, 17(2), 798–818.
- Page, S. E., Siegert, F., Rieley, J. O., Boehm, H.-D. V., Jaya, A., & Limin, S. (2002). The amount of carbon released from peat and forest fires in Indonesia during 1997. *Nature*, 420(1), 61–65.

- Page, S. E., Wüst, R., Weiss, D., Rieley, J., Shotyk, W., & Limin, S. H. (2009b). A record of Late Pleistocene and Holocene carbon accumulation and climate change from an equatorial peat bog (Kalimantan, Indonesia): implications for past, present and future carbon dynamics. *J. Quat. Sci.*, *19*, 625–635.
- Parnell, A. C., Haslett, J., Sweeney, J., Doan, T. K., Allen, J. R., & Huntley, B. (2016). Joint palaeoclimate reconstruction from pollen data via forward models and climate histories. *Quat. Sci. Rev.*, *151*, 111–126.
- Parry, L. E., Charman, D. J., & Noades, J. P. W. (2012). A method for modelling peat depth in blanket peatlands. *Soil Use Manag.*, *28*(December), 614–624.
- Partin, J. W., Cobb, K. M., Adkins, J. F., Clark, B., & Fernandez, D. P. (2007). Millennial-scale trends in west Pacific warm pool hydrology since the Last Glacial Maximum. *Nature*, *449*(September), 452–455.
- Partin, J. W., Quinn, T. M., Shen, C. C., Emile-Geay, J., Taylor, F. W., Maupin, C. R., Lin, K., Jackson, C. S., Banner, J. L., Sinclair, D. J., & Huh, C. A. (2013). Multidecadal rainfall variability in south pacific convergence zone as revealed by stalagmite geochemistry. *Geology*, *41*(September), 1143–1146.
- Pfeiffer, M., Spessa, A., & Kaplan, J. O. (2013). A model for global biomass burning in preindustrial time: LPJ-LMfire (v1.0). *Geosci. Model Dev.*, *6*(3), 643–685.
- Pfeiffer, M., Timm, O., Dullo, W. C., & Podlech, S. (2004). Oceanic forcing of interannual and multidecadal climate variability in the southwestern Indian Ocean: Evidence from a 160 year coral isotopic record (La Réunion, 55°E, 21°S). *Paleoceanography*, *19*(4), 1–14.
- Pickett, E. J., Harrison, S. P., Hope, G., Harle, K., Dodson, J. R., Peter Kershaw, A., Colin Prentice, I., Backhouse, J., Colhoun, E. A., D'Costa, D., Flenley, J., Grindrod, J., Haberle, S., Hassell, C., Kenyon, C., Macphail, M., Martin, H., Martin, A. H., McKenzie, M., Newsome, J. C., Penny, D., Powell, J., Ian Raine, J., Southern, W., Stevenson, J., Sutra, J.-P., Thomas, I., Kaars, S., & Ward, J. (2004). Pollen-based reconstructions of biome distributions for Australia, Southeast Asia and the Pacific (SEAPAC region) at 0, 6000 and 18,000 14C yr BP. *J. Biogeogr.*, *31*(9), 1381–1444.
- Pohl, K., Therrell, M. D., Blay, G. S., Ayotte, N., Hernandez, J. J. C., Castro, S. D., Oviedo, E. C., Elvir, J. A., Elizondo, M. G., Opland, D., Park, J., Pederson, G., Salazar, S. B., Selem, L. V., Diaz, J. V., & Stahle, D. S. (2003). A cool season precipitation reconstruction for Saltillo, Mexico. *Tree-ring Res.*, *59*(1), 11–19.

- Power, M. J., Marlon, J. R., Bartlein, P. J., & Harrison, S. P. (2010). Fire history and the global charcoal database: A new tool for hypothesis testing and data exploration. *Palaeogeogr. Palaeoclimatol. Palaeoecol.*, *291*(1-2), 52–59.
- Power, M. J., Marlon, J. R., Ortiz, N., Bartlein, P. J., Harrison, S. P., Mayle, F. E., Ballouche, A., Bradshaw, R. H. W., Carcaillet, C., Cordova, C., Mooney, S., Moreno, P. I., Prentice, I. C., Thonicke, K., Tinner, W., Whitlock, C., Zhang, Y., Zhao, Y., Ali, A. A., Anderson, R. S., Beer, R., Behling, H., Briles, C., Brown, K. J., Brunelle, A., Bush, M., Camill, P., Chu, G. Q., Clark, J., Colombaroli, D., Connor, S., Daniau, A.-L., Daniels, M., Dodson, J., Doughty, E., Edwards, M. E., Finsinger, W., Foster, D., Frechette, J., Gaillard, M.-J., Gavin, D. G., Gobet, E., Haberle, S., Hallett, D. J., Higuera, P., Hope, G., Horn, S., Inoue, J., Kaltenrieder, P., Kennedy, L., Kong, Z. C., Larsen, C., Long, C. J., Lynch, J., Lynch, E. A., McGlone, M., Meeks, S., Mensing, S., Meyer, G., Minckley, T., Mohr, J., Nelson, D. M., New, J., Newnham, R., Noti, R., Oswald, W., Pierce, J., Richard, P. J. H., Rowe, C., Sanchez Goñi, M. F., Shuman, B. N., Takahara, H., Toney, J., Turney, C., Urrego-Sanchez, D. H., Umbanhowar, C., Vandergoes, M., Vanni re, B., Vescovi, E., Walsh, M., Wang, X., Williams, N., Wilmschurst, J., & Zhang, J. H. (2008). Changes in fire regimes since the Last Glacial Maximum: an assessment based on a global synthesis and analysis of charcoal data. *Clim. Dyn.*, *30*(7-8), 887–907.
- Power, M. J., Mayle, F. E., Bartlein, P. J., Marlon, J. R., Anderson, R. S., Behling, H., Brown, K. J., Carcaillet, C., Colombaroli, D., Gavin, D. G., Hallett, D. J., Horn, S. P., Kennedy, L. M., Lane, C. S., Long, C. J., Moreno, P. I., Paitre, C., Robinson, G., Taylor, Z., & Walsh, M. K. (2013a). Climatic control of the biomass-burning decline in the Americas after AD 1500. *The Holocene*, *23*(1), 3.
- Power, S., & Colman, R. (2006). Multi-year predictability in a coupled general circulation model. *Clim. Dyn.*, *26*(2-3), 247–272.
- Power, S., Delage, F., Chung, C., Kociuba, G., & Keay, K. (2013b). Robust twenty-first-century projections of El Ni o and related precipitation variability. *Nature*, *502*(7472), 541–5.
- Powers, L. A., Johnson, T. C., Werne, J. P., Casta eda, I. S., Hopmans, E. C., Sinninghe Damst , J. S., & Schouten, S. (2011). Organic geochemical records of environmental variability in Lake Malawi during the last 700 years, Part I: The TEX86 temperature record. *Palaeogeogr. Palaeoclimatol. Palaeoecol.*, *303*(1-4), 133–139.
- Prentice, I. C., Kelley, D. I., Foster, P. N., Friedlingstein, P., Harrison, S. P., & Bartlein, P. J. (2011). Modeling fire and the terrestrial carbon balance. *Global Biogeochem. Cycles*, *25*(3).

- Price, C. (2009). Will a drier climate result in more lightning? *Atmos. Res.*, *91*(2-4), 479–484.
- Quinn, T. M., Crowley, T. J., & Taylor, F. W. (1996). New stable isotope results from a 173-year coral from Espiritu Santo, Vanuatu. *Geophys. Res. Lett.*, *23*(23), 3413–3416.
- Quinn, T. M., Crowley, T. J., Taylor, F. W., Henin, C., Joannot, P., & Join, Y. (1998). A multicentury stable isotope record from a New Caledonia coral: Interannual and decadal sea surface temperature variability in the southwest Pacific since 1657 A.D. *Paleoceanography*, *13*(4), 412–426.
- Quinn, T. M., Taylor, F. W., & Crowley, T. J. (2006). Coral-based climate variability in the Western Pacific Warm Pool since 1867. *J. Geophys. Res.*, *111*(C11), 1–11.
- R Core Team (2016). *R: A Language and Environment for Statistical Computing*. R Foundation for Statistical Computing, Vienna, Austria.
- Raible, C. C., Lehner, F., González-Rouco, J. F., & Fernández-Donado, L. (2014). Changing correlation structures of the Northern Hemisphere atmospheric circulation from 1000 to 2100 AD. *Clim. Past*, *10*, 537–550.
- Randerson, J. T., van der Werf, G. R., Giglio, L., Collatz, G. J., & Kasibhatla, P. S. (2015). Global Fire Emissions Database, Version 4, (GFEDv4).
- Rasbury, M., & Aharon, P. (2006). ENSO-controlled rainfall variability records archived in tropical stalagmites from the mid-ocean island of Niue, South Pacific. *Geochemistry, Geophys. Geosystems*, *7*(December 2005).
- Rein, G. (2013). Smouldering Fires and Natural Fuels. In C. M. Belcher (Ed.) *Fire Phenom. Earth Syst.*, chap. 2, (pp. 15–33). Oxford: John Wiley & Sons.
- Reiss, P. T., & Todd Ogden, R. (2009). Smoothing parameter selection for a class of semiparametric linear models. *J. R. Stat. Soc. Ser. B Stat. Methodol.*, *71*(2), 505–523.
- Reuter, J., Stott, L., Khider, D., Sinha, A., Cheng, H., & Edwards, R. L. (2009). A new perspective on the hydroclimate variability in northern South America during the Little Ice Age. *Geophys. Res. Lett.*, *36*, 1–5.
- Richey, J. N., Poore, R. Z., Flower, B. P., Quinn, T. M., & Hollander, D. J. (2009). Regionally coherent Little Ice Age cooling in the Atlantic Warm Pool. *Geophys. Res. Lett.*, *36*(21), 3–7.
- Rodbell, D. T. (1999). An 15,000-Year Record of El Niño-Driven Alluviation in Southwestern Ecuador. *Science (80-.)*, *283*(1999), 516–520.

- Roden, J. S., Lin, G., & Ehleringer, J. R. (2000). A mechanistic model for interpretation of hydrogen and oxygen isotope ratios in tree-ring cellulose. *Geochim. Cosmochim. Acta*, 64(1), 21–35.
- Rodysill, J. R., Russell, J. M., Bijaksana, S., Brown, E. T., Safiuddin, L. O., & Eggermont, H. (2012). A paleolimnological record of rainfall and drought from East Java, Indonesia during the last 1,400 years. *J. Paleolimnol.*, 47, 125–139.
- Román-Cuesta, R. M., Carmona-Moreno, C., Lizcano, G., New, M., Silman, M., Knoke, T., Malhi, Y., Oliveras, I., Asbjornsen, H., & Vuille, M. (2014). Synchronous fire activity in the tropical high Andes: an indication of regional climate forcing. *Glob. Chang. Biol.*, 20(6), 1929–42.
- Román-Cuesta, R. M., Gracia, M., & Retana, J. (2003). Environmental and Human Factors Influencing Fire Trends in ENSO and Non-ENSO Years in Tropical Mexico. Environmental And Human Factors Influencing Fire Trends In Enso And Non-ENSO Years In Tropical Mexico. *Ecol. Appl.*, 13(4), 1177–1192.
- Rosenblatt, M. (1952). Remarks on a Multivariate Transformation. *Ann. Math. Stat.*, 23(3), 470–472.
- Rossi, S., Tubiello, F. N., Prosperi, P., Salvatore, M., Jacobs, H., Biancalani, R., House, J. I., & Boschetti, L. (2016). FAOSTAT estimates of greenhouse gas emissions from biomass and peat fires. *Clim. Change*, 135(3-4), 699–711.
- Russell, J. M., & Johnson, T. C. (2007). Little ice age drought in equatorial Africa: Intertropical convergence zone migrations and El Niño-Southern oscillation variability. *Geology*, 35, 21–24.
- Russell, J. M., Vogel, H., Konecky, B. L., Bijaksana, S., Huang, Y., Melles, M., Wattrus, N., Costa, K., & King, J. W. (2014). Glacial forcing of central Indonesian hydroclimate since 60,000 y B.P. *Proc. Natl. Acad. Sci. U. S. A.*, 111, 5100–5.
- Russon, T., Tudhope, A. W., Hegerl, G. C., Collins, M., & Tindall, J. (2013). Inter-annual tropical Pacific climate variability in an isotope-enabled CGCM: Implications for interpreting coral stable oxygen isotope records of ENSO. *Clim. Past*, 9(4), 1543–1557.
- Rustic, G. T., Koutavas, A., Marchitto, T. M., & Linsley, B. K. (2015). Dynamical excitation of the tropical Pacific Ocean and ENSO variability by Little Ice Age cooling. *Science*, 350(6267), 1537–41.
- Sachs, H. M., Webb, T., & Clarck, D. R. (1977). Paleocological transfer functions. *Annu. Rev. Earth Planet. Sci.*, 5, 159–178.

- Sachs, J. P., Sachse, D., Smittenberg, R. H., Zhang, Z., Battisti, D. S., & Golubic, S. (2009). Southward movement of the Pacific intertropical convergence zone AD 1400–1850. *Nat. Geosci.*, *2*(7), 519–525.
- Saenger, C., Came, R. E., Oppo, D. W., Keigwin, L. D., & Cohen, A. L. (2011). Regional climate variability in the western subtropical North Atlantic during the past two millennia. *Paleoceanography*, *26*(2), 1–12.
- Saenger, C., Cohen, A. L., Oppo, D. W., Halley, R. B., & Carilli, J. E. (2009). Surface-temperature trends and variability in the low-latitude North Atlantic since 1552. *Nat. Geosci.*, *2*(7), 492–495.
- Sakia, R. M. (1992). The Box-Cox Transformation Technique: A Review. *J. R. Stat. Soc. Ser. D (The Stat.)*, *41*(2), 169–178.
- Sátori, G., Williams, E., & Lemperger, I. (2009). Variability of global lightning activity on the ENSO time scale. *Atmos. Res.*, *91*(2-4), 500–507.
- Sátori, G., & Zieger, B. (1999). El Niño related meridional oscillation of global lightning activity. *Geophys. Res. Lett.*, *26*(10), 1365.
- Schmidt, G. A., Annan, J. D., Bartlein, P. J., Cook, B. I., Guilyardi, E., Hargreaves, J. C., Harrison, S. P., Kageyama, M., LeGrande, A. N., Konecky, B., Lovejoy, S., Mann, M. E., Masson-Delmotte, V., Risi, C., Thompson, D., Timmermann, A., Tremblay, L.-B., & Yiou, P. (2014). Using palaeo-climate comparisons to constrain future projections in CMIP5. *Clim. Past*, *10*(1), 221–250.
- Scott, A. C., & Glasspool, I. J. (2006). The diversification of Paleozoic fire systems and fluctuations in atmospheric oxygen concentration. *Proc. Natl. Acad. Sci. U. S. A.*, *103*(29), 10861–10865.
- Settele, J., Scholes, R. J., Betts, R. A., Bunn, S., Leadley, P., Nepstad, D., Overpeck, J. T., & Tobaoda, M. A. (2014). Terrestrial and inland water systems. In *Clim. Chang. 2014 Impacts, Adapt. Vulnerability. Part A Glob. Sect. Asp. Contrib. Work. Gr. II to Fifth Assess. Rep. Intergov. Panel Clim. Chang.*, (pp. 271–359). Cambridge, United Kingdom and New York, NY, USA: Cambridge University Press.
- Shadish, W. R., Zuur, A. F., & Sullivan, K. J. (2014). Using generalized additive (mixed) models to analyze single case designs. *J. Sch. Psychol.*, *52*(2), 149–178.
- Shanahan, T. M., Overpeck, J. T., Sharp, W. E., Scholz, C. A., & Arko, J. A. (2007). Simulating the response of a closed-basin lake to recent climate changes in tropical West Africa (Lake Bosumtwi, Ghana). *Hydrol. Process.*, *21*(13), 1678–1691.

- Shi, F., Yang, B., Mairesse, A., Von Gunten, L., Li, J., Bräuning, A., Yang, F., & Xiao, X. (2013). Northern Hemisphere temperature reconstruction during the last millennium using multiple annual proxies. *Clim. Res.*, *56*(3), 231–244.
- Shin, S. I., Sardeshmukh, P. D., Webb, R. S., Oglesby, R. J., & Barsugli, J. J. (2006). Understanding the mid-Holocene climate. *J. Clim.*, *19*, 2801–2817.
- Siegert, F., Ruecker, G., Hinrichs, A., & Hoffmann, A. A. (2001). Increased damage from fires in logged forests during droughts caused by El Niño. *Nature*, *414*(6862), 437–440.
- Singarayer, J. S., Valdes, P. J., Friedlingstein, P., Nelson, S., & Beerling, D. J. (2011). Late Holocene methane rise caused by orbitally controlled increase in tropical sources. *Nature*, *470*(7332), 82–85.
- Smerdon, J. E. (2012). Climate models as a test bed for climate reconstruction methods: Pseudoproxy experiments. *Wiley Interdiscip. Rev. Clim. Chang.*, *3*(February), 63–77.
- Spahni, R., Joos, F., Stocker, B. D., Steinacher, M., & Yu, Z. C. (2013). Transient simulations of the carbon and nitrogen dynamics in northern peatlands: from the Last Glacial Maximum to the 21st century. *Clim. Past*, *9*(3), 1287–1308.
- Stahle, D. W., Diaz, J. V., Burnette, D. J., Paredes, J. C., Heim, R. R., Fye, F. K., Soto, R. A., Therrell, M. D., & Cleaveland, M. K. (2011). Major Mesoamerican droughts of the past millennium. *Geophys. Res. Lett.*, *38*(January), 2–5.
- Stansell, N. D., Steinman, B. A., Abbott, M. B., Rubinov, M., & Roman-Lacayo, M. (2013). Lacustrine stable isotope record of precipitation changes in Nicaragua during the Little Ice Age and Medieval Climate Anomaly. *Geology*, *41*, 151–154.
- Steinman, B. A., Abbott, M. B., Mann, M. E., Stansell, N. D., & Finney, B. P. (2012). 1,500 year quantitative reconstruction of winter precipitation in the Pacific Northwest. *Proc. Natl. Acad. Sci.*, *109*(6), 11619–11623.
- Stoll, H. M., Müller, W., & Prieto, M. (2012). I-STAL, a model for interpretation of Mg/Ca, Sr/Ca and Ba/Ca variations in speleothems and its forward and inverse application on seasonal to millennial scales. *Geochemistry, Geophys. Geosystems*, *13*(9), 1–27.
- Stott, L., Cannariato, K., Thunell, R., Haug, G. H., Koutavas, A., & Lund, S. (2004). Decline of surface temperature and salinity in the western tropical Pacific Ocean in the Holocene epoch. *Nature*, *431*(September 2004), 56–59.
- Stott, L., Poulsen, C., Lund, S., & Thunell, R. (2002). Super ENSO and global climate oscillations at millennial time scales. *Science*, *297*(2002), 222–226.

- Sturm, C., Zhang, Q., & Noone, D. (2010). An introduction to stable water isotopes in climate models: benefits of forward proxy modelling for paleoclimatology. *Clim. Past*, 6, 115–129.
- Sundqvist, H. S., Holmgren, K., Fohlmeister, J., Zhang, Q., Matthews, M. B., Spötl, C., & Körnich, H. (2013). Evidence of a large cooling between 1690 and 1740 AD in southern Africa. *Sci. Rep.*, 3, 1–6.
- Swart, P. K., Dodge, R. E., & Hudson, H. J. (1996a). A 240-year stable oxygen and carbon isotopic record in a coral from South Florida: implications for the prediction of precipitation in Southern Florida. *Palaios*, 11(4), 362–375.
- Swart, P. K., Healy, G., Dodge, R. E., Kramer, P., Hudson, J. H., Halley, R. B., & Robblee, M. B. (1996b). The stable oxygen and carbon isotopic record of climatic and anthropogenic influence. *Palaeogeogr., Palaeoclim., Palaeoecol.*, 123, 219–237 [4–5].
- Swetnam, T. W. (1990). Fire history and climate in the Southwestern United States. In *Proc. Symp. Eff. Fire Manag. Southwest. Nat. Resour. Gen. Tech. Rep. RM-191. US For. Serv.*, (pp. 6–17).
- Swetnam, T. W. (1993). Fire History and Climate Change in Sequoia Groves. *Science* (80-), 262, 885–889.
- Swetnam, T. W., & Betancourt, J. L. (1990). El Niño-Southern Oscillation (ENSO) phenomena and forest fires in the southwestern United States. In *Proc. Sixth Annu. Pacific Clim. Work.*, (pp. 129–134). Asilomar Conference Center, Pacific Grove, CA.
- Takahashi, K., Montecinos, A., Goubanova, K., & Dewitte, B. (2011). ENSO regimes: Reinterpreting the canonical and Modoki El Niño. *Geophys. Res. Lett.*, 38(10), 1–5.
- Tan, L., Cai, Y., Cheng, H., An, Z., & Edwards, R. L. (2009). Summer monsoon precipitation variations in central China over the past 750 years derived from a high-resolution absolute-dated stalagmite. *Palaeogeogr. Palaeoclimatol. Palaeoecol.*, 280(3-4), 432–439.
- Taylor, K. E., Stouffer, R. J., & Meehl, G. A. (2012). An overview of CMIP5 and the experiment design. *Bull. Am. Meteorol. Soc.*, 93(4), 485–498.
- Thompson, D. M., Ault, T. R., Evans, M. N., Cole, J. E., & Emile-Geay, J. (2011). Comparison of observed and simulated tropical climate trends using a forward model of coral $\delta^{18}O$. *Geophys. Res. Lett.*, 38(14), 1–6.

- Thompson, L. G., & et Al. (1997). Tropical climate instability: the last glacial cycle from a Qinghai - Tibetan ice core. *Science (80-.)*, 276(June), 1821–1825.
- Thompson, L. G., Mosley-Thompson, E., Davis, M. E., Henderson, K. A., Brecher, H. H., Zagorodnov, V. S., Mashiotta, T. A., Lin, P.-n., Mikhailenko, V. N., Hardy, D. R., & Beer, J. (2002). Kilimanjaro ice core records: evidence of holocene climate change in tropical Africa. *Science (80-.)*, 298(5593), 589–593.
- Thompson, L. G., Mosley-thompson, E., Davis, M. E., Lin, P., Henderson, K., & Mashiotta, T. A. (2003). Tropical glacier and ice core evidence of climate change on annual to millennial time scales. *Clim. Change*, 59, 137–155.
- Thompson, L. G., Mosley-Thompson, E., Davis, M. E., Lin, P.-N., Henderson, K. A., Cole-Dai, J., Bolzan, J. F., & Liu, K.-b. (1995). Late Glacial Stage and Holocene Tropical Ice Core Records from Huascarán, Peru. *Science (80-.)*, 269.
- Thompson, L. G., Mosley-Thompson, E., Davis, M. E., Zagorodnov, V. S., Howat, I. M., Mikhailenko, V. N., & Lin, P.-N. (2013). Annually resolved ice core records of tropical climate variability over the past ~1800 years. *Science*, 340(2013), 945–950.
- Thompson, L. G., Yao, T., Davis, M. E., Mosley-Thompson, E., Mashiotta, T. A., Lin, P. N., Mikhailenko, V. N., & Zagorodnov, V. S. (2006). Holocene climate variability archived in the Puruogangri ice cap on the central Tibetan Plateau. *Ann. Glaciol.*, 43(February), 61–69.
- Tierney, J. E., Abram, N. J., Anchukaitis, K. J., Evans, M. N., Giry, C., Kilbourne, K. H., Saenger, C. P., Wu, H. C., & Zinke, J. (2015). Tropical sea surface temperatures for the past four centuries reconstructed from coral archives. *Paleoceanography*, 30(October), 226–252.
- Tierney, J. E., Lewis, S. C., Cook, B. I., LeGrande, A. N., & Schmidt, G. A. (2011). Model, proxy and isotopic perspectives on the East African Humid Period. *Earth Planet. Sci. Lett.*, 307(1-2), 103–112.
- Tierney, J. E., Oppo, D. W., Rosenthal, Y., Russell, J. M., & Linsley, B. K. (2010). Coordinated hydrological regimes in the Indo-Pacific region during the past two millennia. *Paleoceanography*, 25(1), 1–7.
- Tierney, J. E., & Tingley, M. P. (2014). A Bayesian, spatially-varying calibration model for the TEX86 proxy. *Geochim. Cosmochim. Acta*, 127, 83–106.

- Tingley, M. P., Craigmile, P. F., Haran, M., Li, B., Mannshardt, E., & Rajaratnam, B. (2012). Piecing together the past: Statistical insights into paleoclimatic reconstructions. *Quat. Sci. Rev.*, *35*, 1–22.
- Tiwari, M., Nagoji, S. S., & Ganeshram, R. S. (2015). Multi-centennial scale SST and Indian summer monsoon precipitation variability since mid-Holocene and its nonlinear response to solar activity. *The Holocene*, *25*(9), 1415–1424.
- Tolwinski-Ward, S. E., Anchukaitis, K. J., & Evans, M. N. (2013). Bayesian parameter estimation and interpretation for an intermediate model of tree-ring width. *Clim. Past*, *9*(4), 1481–1493.
- Tolwinski-Ward, S. E., Evans, M. N., Hughes, M. K., & Anchukaitis, K. J. (2011). An efficient forward model of the climate controls on interannual variation in tree-ring width. *Clim. Dyn.*, *36*(11-12), 2419–2439.
- Treydte, K. S., Schleser, G. H., Helle, G., Frank, D. C., Winiger, M., Haug, G. H., & Esper, J. (2006). The twentieth century was the wettest period in northern Pakistan over the past millennium. *Nature*, *440*(7088), 1179–1182.
- Trouet, V., Diaz, H. F., Wahl, E. R., Viau, A. E., Graham, R., Graham, N., & Cook, E. R. (2013). A 1500-year reconstruction of annual mean temperature for temperate North America on decadal-to-multidecadal time scales. *Environ. Res. Lett.*, *8*(2), 024008.
- Trouet, V., Esper, J., Graham, N. E., Baker, A., Scourse, J. D., & Frank, D. C. (2009). Persistent positive North Atlantic oscillation mode dominated the Medieval Climate Anomaly. *Science*, *324*, 78–80.
- Trouet, V., Scourse, J. D., & Raible, C. C. (2012). North Atlantic storminess and Atlantic Meridional Overturning Circulation during the last Millennium: Reconciling contradictory proxy records of NAO variability. *Glob. Planet. Change*, *84-85*, 48–55.
- Truebe, S. A., Ault, T. R., & Cole, J. E. (2010). A forward model of cave dripwater $\delta^{18}O$ and application to speleothem records. *IOP Conf. Ser. Earth Environ. Sci.*, *9*.
- Tudhope, A. W., Chilcott, C. P., McCulloch, M. T., Cook, E. R., Chappell, J., Ellam, R. M., Lea, D. W., Lough, J. M., & Shimmield, G. B. (2001). Variability in the El Niño-Southern Oscillation through a glacial-interglacial cycle. *Science*, *291*(February), 1511–1517.
- Turney, C. S. M., Kershaw, A. P., Clemens, S. C., Branch, N., Moss, P. T., & Fifield, L. K. (2004). Millennial and orbital variations of El Niño / Southern Oscillation and high-latitude climate in the last glacial period. *Nature*, *428*(March), 306–310.

- Urban, F. E., Cole, J. E., & Overpeck, J. T. (2000). Influence of mean climate change on climate variability from a 155-year tropical Pacific coral record. *Nature*, *407*(October), 989–993.
- Vaganov, E., Anchukaitis, K., & Evans, M. (2011). *Dendroclimatology*, vol. 11 of *Developments in Paleoenvironmental Research*. Dordrecht: Springer Netherlands.
- Vaganov, E. A., Hughes, M. K., & Shashkin, A. V. (2006). *Growth Dynamics of Conifer Tree Rings: Images of Past and Future Environments*, vol. 183. Springer-Verlag Berlin Heidelberg.
- van Albada, S. J., & Robinson, P. A. (2007). Transformation of arbitrary distributions to the normal distribution with application to EEG test-retest reliability. *J. Neurosci. Methods*, *161*(2), 205–211.
- van den Dool, H. (2003). Performance and analysis of the constructed analogue method applied to U.S. soil moisture over 1981–2001. *J. Geophys. Res.*, *108*(D16), 8617.
- van der Werf, G. R., Dempewolf, J., Trigg, S. N., Randerson, J. T., Kasibhatla, P. S., Giglio, L., Murdiyarso, D., Peters, W., Morton, D. C., Collatz, G. J., Dolman, A. J., & DeFries, R. S. (2008). Climate regulation of fire emissions and deforestation in equatorial Asia. *Proc. Natl. Acad. Sci. U. S. A.*, *105*(51), 20350–20355.
- Van Der Werf, G. R., Randerson, J. T., Giglio, L., Collatz, G. J., Mu, M., Kasibhatla, P. S., Morton, D. C., Defries, R. S., Jin, Y., & Van Leeuwen, T. T. (2010). Global fire emissions and the contribution of deforestation, savanna, forest, agricultural, and peat fires (1997–2009). *Atmos. Chem. Phys.*, *10*(23), 11707–11735.
- Van Leeuwen, T. T., Van Der Werf, G. R., Hoffmann, A. A., Detmers, R. G., Rücker, G., French, N. H. F., Archibald, S., Carvalho, J. A., Cook, G. D., De Groot, W. J., Hély, C., Kasischke, E. S., Kloster, S., McCarty, J. L., Pettinari, M. L., Savadogo, P., Alvarado, E. C., Boschetti, L., Manuri, S., Meyer, C. P., Siegert, F., Trollope, L. A., & Trollope, W. S. W. (2014). Biomass burning fuel consumption rates: A field measurement database. *Biogeosciences*, *11*(24), 7305–7329.
- van Oldenborgh, G. J., Philip, S. Y., & Collins, M. (2005). El Niño in a changing climate : a multi-model study. *Ocean Sci.*, *1*, 81–95.
- Vanniere, B., Power, M. J., Roberts, N., Tinner, W., Carrion, J., Magny, M., Bartlein, P., Colombaroli, D., Daniau, A. L., Finsinger, W., Gil-Romera, G., Kaltenrieder, P., Pini, R., Sadori, L., Turner, R., Valsecchi, V., & Vescovi, E. (2011). Circum-Mediterranean fire activity and climate changes during the mid-Holocene environmental transition (8500–2500 cal. BP). *The Holocene*, *21*(1), 53–73.

- Vasquez-Bedoya, L. F., Cohen, A. L., Oppo, D. W., & Blanchon, P. (2012). Corals record persistent multidecadal SST variability in the Atlantic Warm Pool since 1775 AD. *Paleoceanography*, 27(3), 1–9.
- Vecchi, G. A., & Wittenberg, A. T. (2010). El Niño and our future climate: Where do we stand? *Wiley Interdiscip. Rev. Clim. Chang.*, 1(2), 260–270.
- Venables, W. N., & Ripley, B. D. (2002). *Modern Applied Statistics with S*. Statistics and Computing. New York, NY: Springer New York, 4 ed.
- Verdon, D. C., & Franks, S. W. (2006). Long-term behaviour of ENSO: Interactions with the PDO over the past 400 years inferred from paleoclimate records. *Geophys. Res. Lett.*, 33(6), 1–5.
- Visser, K., Thunell, R. C., & Stott, L. D. (2003). Magnitude and timing of temperature change in the Indo-Pacific warm pool during deglaciation. *Nature*, 421(January), 152–155.
- Vuille, M., Bradley, R. S., Healy, R., Werner, M., Hardy, D. R., Thompson, L. G., & Keimig, F. (2003). Modeling $\delta^{18}O$ in precipitation over the tropical Americas: 2. Simulation of the stable isotope signal in Andean ice cores. *J. Geophys. Res. Atmos.*, 108(D6), 4175.
- Wahba, G. (1985). A Comparison of GCV and GML for Choosing the Smoothing Parameter in the Generalized Spline Smoothing Problem. *Ann. Math. Stat.*, 13(4), 1378–1402.
- Wallace, J. G. (1997). Meteorological Observations at the Radcliffe Observatory, Oxford: 1815-1995. *Oxford Geogr. Res. Pap.*, 53.
- Wang, H. J., Zhang, R. H., Cole, J. E., & Chavez, F. (1999). El Niño and the related phenomenon Southern Oscillation (ENSO): the largest signal in interannual climate variation. *Proc. Natl. Acad. Sci. U. S. A.*, 96(September), 11071–11072.
- Wang, J., Emile-Geay, J., Guillot, D., McKay, N. P., & Rajaratnam, B. (2015). Fragility of reconstructed temperature patterns over the Common Era: Implications for model evaluation. *Geophys. Res. Lett.*, 42(17), 7162–7170.
- Wang, J., Emile-Geay, J., Guillot, D., Smerdon, J. E., & Rajaratnam, B. (2014a). Evaluating climate field reconstruction techniques using improved emulations of real-world conditions. *Clim. Past*, 10, 1–19.
- Wang, S., Huang, J., He, Y., & Guan, Y. (2014b). Combined effects of the Pacific Decadal Oscillation and El Niño-Southern Oscillation on Global Land Dry–Wet Changes. *Sci. Rep.*, 4, 6651.

- Wang, Y. (2004). Trends in atmospheric haze induced by peat fires in Sumatra Island, Indonesia and El Niño phenomenon from 1973 to 2003. *Geophys. Res. Lett.*, *31*(4), L04103.
- Wang, Y., Cheng, H., Edwards, R. L., He, Y., Kong, X., An, Z., Wu, J., Kelly, M. J., Dykoski, C. A., & Li, X. (2005). The Holocene Asian Monsoon: Links to Solar Changes and North Atlantic Climate. *Science* (80-.), *308*(5723), 854–857.
- Wania, R., Ross, I., & Prentice, I. C. (2009a). Integrating peatlands and permafrost into a dynamic global vegetation model: 1. Evaluation and sensitivity of physical land surface processes. *Global Biogeochem. Cycles*, *23*(3).
- Wania, R., Ross, I., & Prentice, I. C. (2009b). Integrating peatlands and permafrost into a dynamic global vegetation model: 2. Evaluation and sensitivity of vegetation and carbon cycle processes. *Global Biogeochem. Cycles*, *23*(3).
- Wanner, H., Beer, J., Bütikofer, J., Crowley, T. J., Cubasch, U., Flückiger, J., Goosse, H., Grosjean, M., Joos, F., Kaplan, J. O., Küttel, M., Müller, S. A., Prentice, I. C., Solomina, O., Stocker, T. F., Tarasov, P., Wagner, M., & Widmann, M. (2008). Mid- to Late Holocene climate change: an overview. *Quat. Sci. Rev.*, *27*, 1791–1828.
- Ward, D. S., Kloster, S., Mahowald, N. M., Rogers, B. M., Randerson, J. T., & Hess, P. G. (2012). The changing radiative forcing of fires: global model estimates for past, present and future. *Atmos. Chem. Phys.*, *12*(22), 10857–10886.
- Wijedasa, L. S. (2016). Peat soil bulk density important for estimation of peatland fire emissions. *Glob. Chang. Biol.*, *22*(9), 2959–2959.
- Williams, A. N., Mooney, S. D., Sisson, S. A., & Marlon, J. R. (2015). Exploring the relationship between Aboriginal population indices and fire in Australia over the last 20,000years. *Palaeogeogr. Palaeoclimatol. Palaeoecol.*, *432*, 49–57.
- Williams, E. R. (2005). Lightning and climate: A review. *Atmos. Res.*, *76*(272-287), 402–404.
- Wilson, R., Cook, E. R., D'Arrigo, R. D., Riedwyl, N., Evans, M. N., Tudhope, A., & Allan, R. (2010). Reconstructing ENSO: the influence of method, proxy data, climate forcing and teleconnections. *J. Quat. Sci.*, *25*(1), 62–78.
- Withers, C. S., & Nadarajah, S. (2013). Simple alternatives for Box-Cox transformations. *Metrika*, *77*(2), 297–315.

- Wolter, K., & Timlin, M. S. (2011). El Niño/Southern Oscillation behaviour since 1871 as diagnosed in an extended multivariate ENSO index (MEI.ext). *Int. J. Climatol.*, *31*(7), 1074–1087.
- Wood, S. N. (2003). Thin plate regression splines. *J. R. Stat. Soc. Ser. B Stat. Methodol.*, *65*(1), 95–114.
- Wood, S. N. (2006). Generalized additive models : an introduction with R. *Texts Stat. Sci.*, (pp. xvii, 392 p.).
- Wood, S. N. (2011). Fast stable restricted maximum likelihood and marginal likelihood estimation of semiparametric generalized linear models. *J. R. Stat. Soc. Ser. B Stat. Methodol.*, *73*(1), 3–36.
- Wooster, M. J., Perry, G. L. W., & Zoumas, A. (2012). Fire, drought and El Niño relationships on Borneo (Southeast Asia) in the pre-MODIS era (1980-2000). *Biogeosciences*, *9*(1), 317–340.
- Wörheide, G. (1998). The reef cave dwelling ultraconservative coralline demosponge *Astrosclera willeyana* Lister 1900 from the Indo-Pacific. *Facies*, *38*(1), 1–88.
- Wu, H. C., Linsley, B. K., Dassié, E. P., Schiraldi, B., & Demenocal, P. B. (2013). Oceanographic variability in the south pacific convergence zone region over the last 210 years from multi-site coral Sr/Ca records. *Geochemistry, Geophys. Geosystems*, *14*(5), 1435–1453.
- Wurtzel, J. B., Black, D. E., Thunell, R. C., Peterson, L. C., Tappa, E. J., & Rahman, S. (2013). Mechanisms of southern Caribbean SST variability over the last two millennia. *Geophys. Res. Lett.*, *40*, 5954–5958.
- Xi, X. (2014). A Review of Water Isotopes in Atmospheric General Circulation Models: Recent Advances and Future Prospects. *Int. J. Atmos. Sci.*, *2014*(1), 16pp.
- Yan, H., Sun, L., Oppo, D. W., Wang, Y., Liu, Z., Xie, Z., Liu, X., & Cheng, W. (2011a). South China Sea hydrological changes and Pacific Walker Circulation variations over the last millennium. *Nat. Commun.*, *2*, 293.
- Yan, H., Sun, L., Wang, Y., Huang, W., Qiu, S., & Yang, C. (2011b). A record of the Southern Oscillation Index for the past 2,000 years from precipitation proxies. *Nat. Geosci.*, *4*(9), 611–614.
- Yan, H., Wei, W., Soon, W., An, Z., Zhou, W., Liu, Z., Wang, Y., & Carter, R. M. (2015). Dynamics of the intertropical convergence zone over the western Pacific during the Little Ice Age. *Nat. Geosci.*, *8*(April), 8–13.

- Yang, F., Wang, N., Shi, F., Ljungqvist, F. C., Zhao, S., & Liu, T. (2016). The spatial distribution of precipitation over the West Qinling region, China, AD 1470–2000. *Palaeogeogr. Palaeoclimatol. Palaeoecol.*, *443*, 278–285.
- Yeh, S.-W., Kug, J.-S., Dewitte, B., Kwon, M.-H., Kirtman, B. P., & Jin, F.-F. (2009). El Niño in a changing climate. *Nature*, *461*(7263), 511–514.
- Yi, L., Yu, H., Ge, J., Lai, Z., Xu, X., Qin, L., & Peng, S. (2012). Reconstructions of annual summer precipitation and temperature in north-central China since 1470 AD based on drought/flood index and tree-ring records. *Clim. Change*, *110*, 469–498.
- Yin, Y., Ciais, P., Chevallier, F., van der Werf, G. R., Fanin, T., Broquet, G., Boesch, H., Cozic, A., Hauglustaine, D., Szopa, S., & Wang, Y. (2016). Variability of fire carbon emissions in equatorial Asia and its nonlinear sensitivity to El Niño. *Geophys. Res. Lett.*, *43*(19), 10,472–10,479.
- Yoshida, S., Morimoto, T., Ushio, T., & Kawasaki, Z. (2007). ENSO and convective activities in Southeast Asia and western Pacific. *Geophys. Res. Lett.*, *34*(21), 1–6.
- Yu, Z., Beilman, D. W., Frohking, S., MacDonald, G. M., Roulet, N. T., Camill, P., & Charman, D. J. (2011). Peatlands and Their Role in the Global Carbon Cycle. *Eos, Trans. Am. Geophys. Union*, *92*(12), 97.
- Yu, Z., Loisel, J., Brosseau, D. P., Beilman, D. W., & Hunt, S. J. (2010). Global peatland dynamics since the Last Glacial Maximum. *Geophys. Res. Lett.*, *37*, 1–5.
- Zaccone, C., Rein, G., D’Orazio, V., Hadden, R. M., Belcher, C. M., & Miano, T. M. (2014). Smouldering fire signatures in peat and their implications for palaeoenvironmental reconstructions. *Geochim. Cosmochim. Acta*, *137*, 134–146.
- Zebiak, S., & Cane, M. A. (1987). A Model El Niño-Southern Oscillation. *Mon. Weather Rev.*, *115*(1985), 2262–2278.
- Zhang, P., Cheng, H., Edwards, R. L., Chen, F., Wang, Y., Yang, X., Liu, J., Tan, M., Wang, X., Liu, J., An, C., Dai, Z., Zhou, J., Zhang, D., Jia, J., Jin, L., & Johnson, K. R. (2008). A Test of Climate, Sun, and Culture Relationships from an 1810-Year Chinese Cave Record. *Science* (80-.), *322*(5903), 940–942.
- Zhang, Y., Wallace, J. M., & Battisti, D. S. (1997). ENSO-like interdecadal variability: 1900-93. *J. Clim.*, *10*(5), 1004–1020.
- Zhao, M., Read, G., & Schimmelmann, A. (2000). An alkenone (UK37) quasi-annual sea surface temperature record (A.D. 1440 to 1940) using varved sediments from the Santa Barbara Basin. *Org. Geochem.*, *31*, 903–917.

- Zinke, J., Dullo, W. C., Heiss, G. A., & Eisenhauer, A. (2004). ENSO and Indian Ocean subtropical dipole variability is recorded in a coral record off southwest Madagascar for the period 1659 to 1995. *Earth Planet. Sci. Lett.*, *228*, 177–194.
- Zinke, J., Hoell, A., Lough, J. M., Feng, M., Kuret, A. J., Clarke, H., Ricca, V., Rankenburg, K., & McCulloch, M. T. (2015). Coral record of southeast Indian Ocean marine heatwaves with intensified Western Pacific temperature gradient. *Nat. Commun.*, *6*(October), 8562.
- Zinke, J., Pfeiffer, M., Timm, O., Dullo, W. C., Kroon, D., & Thomassin, B. A. (2008). Mayotte coral reveals hydrological changes in the western Indian Ocean between 1881 and 1994. *Geophys. Res. Lett.*, *35*(23), 1–5.
- Zinke, J., Rountrey, A., Feng, M., Xie, S.-P., Dissard, D., Rankenburg, K., Lough, J. M., & McCulloch, M. T. (2014). Corals record long-term Leeuwin current variability including Ningaloo Niño/Niña since 1795. *Nat. Commun.*, *5*, 3607.